Development and Characterization of Nanostructured Carbon Adsorbents for Carbon Dioxide Capture

Thesis
Submitted in partial fulfillment for the award of degree
of

Doctor of Philosophy

By

CHITRAKSHI GOEL
(Registration No.: 901101001)

Under the guidance of

Prof. Pramod K. Bajpai
Distinguished Professor
Department of Chemical Engineering,
Thapar University, Patiala

Prof. Haripada Bhunia
Professor
Department of Chemical Engineering,
Thapar University, Patiala

Department of Chemical Engineering
Thapar University
Patiala – 147004, Punjab
www.thapar.edu

March 2016

Dedicated

To

My Parents

Mr. Suresh Kumar Goel & Mrs. Renu Goel

And

My sister

Ms. Pragya Goel

Certificate

This is to certify that the thesis entitled **"Development and Characterization of Nanostructured Carbon Adsorbents for Carbon Dioxide Capture"** being submitted by Ms. Chitrakshi Goel to Department of Chemical Engineering, Thapar University, Patiala for the award of degree of **Doctor of Philosophy**, is a record of bonafide research work carried out by her under our guidance and supervision and has fulfilled the requirements for the submission of this thesis, which to our knowledge has reached the requisite standard.

The results embodied in the thesis have not been submitted in part or full to any other University or Institute for the award of any degree or diploma.

25.03.2016

(Pramod K. Bajpai)
Distinguished Professor
Department of Chemical Engineering,
Thapar University, Patiala

25-3-2016

(Haripada Bhunia)
Professor
Department of Chemical Engineering,
Thapar University, Patiala

Acknowledgements

I would like to express my sincerest regards and gratitude to my supervisors **Prof. Pramod K. Bajpai** and **Prof. Haripada Bhunia**, Department of Chemical Engineering, Thapar University, for providing me such a valuable research opportunity and for their countless guidance, knowledge and motivation during the course of my research. They have been invaluable in the constructive input to this work. It's been a great honour to work under their guidance.

I am extremely thankful to **Prof. Prakash Gopalan**, Director, Thapar University, **Prof. O. P. Pandey**, Dean of Research & Sponsored Projects, Thapar University and **Dr. Raj K. Gupta**, Head, Department of Chemical Engineering, Thapar University for extending the opportunity to undertake this doctoral research.

I am also thankful to my doctoral committee members **Dr. Sanghamitra Barman**, Associate Professor, Department of Chemical Engineering, Thapar University; **Dr. Vijaya Kumar Bulasara**, Assistant Professor, Department of Chemical Engineering, Thapar University and **Prof. Bonamali Pal**, Professor and Head, School of Chemistry & Biochemistry, Thapar University for advising and guiding me towards the right direction. The generous support of all the staff members of Department of Chemical Engineering, Thapar University is greatly appreciated.

My sincere thanks to **Dr. Bhaskar Chandra Mohanty**, Assistant Professor, School of Physics and Material Science, Thapar University for helping me with XPS analysis and to **Dr. Debabrata Deb**, Assistant Professor, School of Physics and Material Science, Thapar University for helping me with MATLAB coding.

I would like to thank my colleagues **Ms. Kimi Jain**, **Mr. Kumar Uddipto**, **Mr. Nipun Dogra**, **Ms. Arshdeep Kaur**, **Ms. Harleen Kaur** and **Ms. Ronjish Chugh** for providing all the encouragement and support at various stages of my work.

I express my deepest gratitude to my parents **Mr. Suresh Kumar Goel** and **Mrs. Renu Goel** and my sister **Ms. Pragya Goel** for their love, never ending support, and encouragement and would like to dedicate this thesis to them.

I would like to gratefully acknowledge the financial support from **Department of Science & Technology (DST)**, Government of India and **DST-Innovation in Science Pursuit for Inspired Research (INSPIRE) under its Assured Opportunity for Research Careers (AORC) scheme**, Government of India throughout the course of this work.

Above all, I express my indebtedness to the "**ALMIGHTY**" for all His blessing and kindness.

Chitrakshi Goel

Chitrakshi Goel

Abstract

The growing concern over global climate change because of increasing anthropogenic carbon dioxide (CO_2) emissions has triggered the requirement to develop technologies for reduction of these emissions. Capture of CO_2 by solid adsorbents has received attention because of its ability to reduce energy penalty associated with capture process. This calls for the development of adsorbent materials with high adsorption capacity, selectivity and fast kinetics coupled with good thermal and mechanical stability. Carbon based adsorbents have been extensively used for adsorption of CO_2. Synthesis of carbon materials, having specific pore structure, from nanocasting technique have been reported by many research groups but their application to CO_2 adsorption is very limited. The objectives of the present work are to develop nanostructured carbon adsorbents having specific pore structure, from nanocasting technique, for their application in CO_2 capture under simulated flue gas conditions by dynamic method and to investigate adsorption kinetics, binary system adsorption equilibria and thermodynamics.

In the present work, two different types of nanostructured carbons have been developed by nanocasting technique by using different starting materials. Two polymeric materials namely melamine-formaldehyde resin and resorcinol-formaldehyde resin have been synthesized and were used as polymeric precursors for nanocasting method with mesoporous silica as hard template. A series of adsorbents were developed by varying the carbonization temperature followed by their thorough characterization. Fixed-bed experiments were carried out, under different adsorption temperature and inlet concentrations, to evaluate their CO_2 adsorption potential, selectivity and regenerability. Pure component adsorption isotherms for CO_2 and N_2 on the prepared carbons were also evaluated at four different temperatures ranging from 30–100 °C and were then correlated with three pure component adsorption isotherm models namely Langmuir, Sips, and dual-site Langmuir (DSL) models. Adsorption equilibria of binary CO_2-N_2 adsorption was then predicted by extending Sips and DSL equations empirically along with usage of ideal adsorbed solution theory and was compared with experimental data obtained from the breakthrough curves through various phase diagrams. Thermodynamic functions such as molar Gibbs free energy change, entropy change, and enthalpy change were evaluated numerically for pure component system. Finally, energy duty for desorption of adsorbed CO_2 was also estimated.

Mesoporous carbons having high nitrogen content were obtained from melamine-formaldehyde resin as polymeric precursor. Carbonization temperature controlled the textural parameters of nitrogen doped porous carbon adsorbents in consort with evolution of functional groups associated with oxygen and nitrogen heteroatoms. Carbonization at 700 °C produced porous carbons having maximum specific surface area of 266 $m^2 g^{-1}$ with nitrogen amount of 21 wt% and surface basicity of 4.07 meq g^{-1}. X-ray diffraction analysis and transmission electron micrographs confirmed the development of nanostructured carbons with partial amorphous character. CO_2 capture performance of the prepared carbons was investigated in a fixed-bed adsorption study set up at different temperatures (30 °C to 100 °C) under varying CO_2 concentrations (5–12.5%). Multiple cycles of adsorption-desorption were also carried out to examine the reusability of the prepared carbons. Adsorbent synthesized at 700 °C exhibited the highest dynamic CO_2 adsorption capacity of 0.83 mmol g^{-1} at 30 °C under 12.5% CO_2 feed concentration in N_2. Breakthrough time and CO_2 equilibrium adsorption capacity were investigated from the breakthrough curves and were found to decline as the adsorption temperature increased. Experimental CO_2 uptake data at all adsorption temperatures was fitted to three kinetic models with fractional order model giving the best fit to the experimental data over the entire range of adsorption with maximum error of 5% between data predicted by kinetic models and data obtained from breakthrough experiments. From three isotherms models used to analyze the equilibrium data of pure component system, Sips and dual-site Langmuir isotherm models presented a nearly perfect fit implying the heterogeneous adsorbent surface. But their extended forms along with ideal adsorbed solution theory failed in explaining binary CO_2 adsorption equilibria. Thermodynamic parameters confirmed the feasibility of adsorption process and indicated the formation of more ordered configuration of CO_2 molecules on adsorbent surface and hence exhibited higher heats of adsorption as compared to N_2. Additionally, isosteric heat of adsorption was found to vary with surface coverage implying heterogeneous adsorbent surface with an average value of 17 kJ mol^{-1}.

Silica templated nanostructured carbons were developed from resorcinol-formaldehyde polymeric precursor by varying the carbonization temperature from 400 °C to 800 °C. Prepared carbons were characterized thoroughly for their textural, chemical and surface properties followed by dynamic CO_2 capture performance at various adsorption temperatures from 30 °C to 100 °C under simulated flue gas conditions. Both the textural properties and surface chemistry had an effect on the CO_2 adsorption performance of the prepared carbons. RF-700

exhibited the highest dynamic CO_2 uptake of 0.761 mmol g^{-1} at 30 °C in a binary mixture of 12.5% CO_2 in N_2 attributing to well-developed porous structure and high surface basicity of 1.93 meq g^{-1}. It also demonstrated high selectivity towards CO_2 over N_2 and stable adsorption capacity over multiple adsorption-desorption cycles. CO_2 adsorption on prepared carbons was well described by fractional order kinetic model. Mixed-gas adsorption equilibria of CO_2 and N_2 on RF derived carbons could not be explained by various isotherm models and IAST which was due to dissimilar adsorbate molecules, adsorptive strengths and adsorbent heterogeneity. Total and partial adsorbed amounts and selectivity towards CO_2 were highly under estimated by these isotherm equations. Thermodynamics of CO_2 adsorption on carbon material suggested exothermic and spontaneous nature of the process. Thermal energy required for desorption of CO_2 was also estimated to be around 1.9 MJ per kg CO_2 with average isosteric heat of adsorption of 15.74 kJ mol^{-1}.

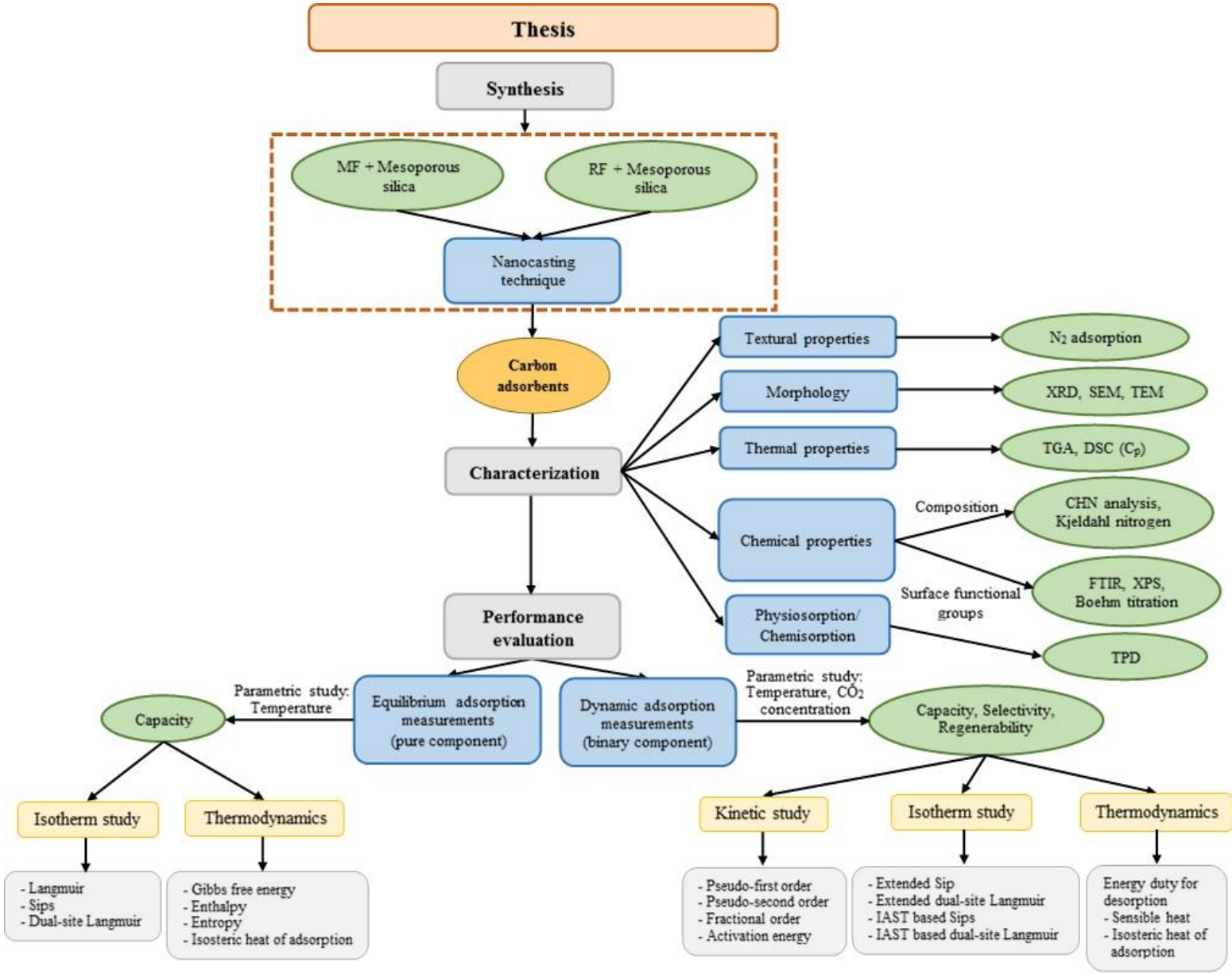
Thesis
Synthesis
MF + Mesoporous silica
RF + Mesoporous silica
Nanocasting technique
Carbon adsorbents
Characterization
Textural properties
N2 adsorption
Morphology
XRD, SEM, TEM
Thermal properties
TGA, DSC (Cp)
Chemical properties
Composition
CHN analysis, Kjeldahl nitrogen
FTIR, XPS, Boehm titration
Surface functional groups
Physiosorption/ Chemisorption
TPD
Performance evaluation
Parametric study: Temperature
Equilibrium adsorption measurements (pure component)
Dynamic adsorption measurements (binary component)
Parametric study: Temperature, CO2 concentration
Capacity
Capacity, Selectivity, Regenerability
Isotherm study
Thermodynamics
- Langmuir
- Sips
- Dual-site Langmuir
- Gibbs free energy
- Enthalpy
- Entropy
- Isosteric heat of adsorption
Kinetic study
Isotherm study
Thermodynamics
- Pseudo-first order
- Pseudo-second order
- Fractional order
- Activation energy
- Extended Sip
- Extended dual-site Langmuir
- IAST based Sips
- IAST based dual-site Langmuir
Energy duty for desorption
- Sensible heat
- Isosteric heat of adsorption

Publications

1. Peer-Reviewed (SCI) Journals

1.1 Related to Ph. D. work

1. **Chitrakshi Goel**, Haripada Bhunia, and Pramod K. Bajpai, "Mesoporous carbon adsorbents from melamine-formaldehyde resin using nanocasting technique for CO_2 adsorption", *Journal of Environmental Sciences*, **2015**, *32*, 238-248.
2. **Chitrakshi Goel**, Haripada Bhunia, and Pramod K. Bajpai, "Synthesis of nitrogen doped mesoporous carbons for carbon dioxide capture", *RSC Advances*, **2015**, *5 (58)*, 46568-46582.
3. **Chitrakshi Goel**, Haripada Bhunia, and Pramod K. Bajpai, "Development of nitrogen enriched nanostructured carbon adsorbents for CO_2 capture", *Journal of Environmental Management*, **2015**, *162*, 20-29.
4. **Chitrakshi Goel**, Haripada Bhunia, and Pramod K. Bajpai, "Resorcinol-formaldehyde based nanostructured carbons for CO_2 adsorption: kinetics, isotherm and thermodynamic studies", *RSC Advances*, **2015**, *5 (113)*, 93563-93578.

1.2 In related area

1. **Chitrakshi Goel**, Haripada Bhunia, and Pramod K. Bajpai, "Novel nitrogen enriched porous carbon adsorbents for CO_2 capture: Breakthrough adsorption study", *Journal of Environmental Chemical Engineering*, **2016**, *4 (1)*, 346-356.
2. **Chitrakshi Goel**, Harleen Kaur, Haripada Bhunia, and Pramod K. Bajpai, "Carbon dioxide adsorption on nitrogen enriched carbon adsorbents: Experimental, kinetics, isothermal and thermodynamic", *Journal of CO_2 Utilization* (Under review).

2. Conferences

2.1 Related to Ph. D. work

(i) International

1. **Chitrakshi Goel**, Haripada Bhunia, and Pramod K. Bajpai, "Nanostructured carbon adsorbents for CO_2 capture", *66th Annual Session of Indian Institute of Chemical Engineers & Joint Indo North American Symposium, CHEMCON 2013*, Institute of Chemical Technology (ICT), Mumbai, December 27-30, 2013, 22.

2. **Chitrakshi Goel**, Haripada Bhunia, and Pramod K. Bajpai, "Development of high surface area nitrogen enriched nanostructured carbon adsorbents", *9th World Congress of Chemical Engineering Incorporating 15th Asian Pacific Confederation of Chemical Engineering Congress (WCCE9 & APCChE 2013)*, Seoul, Korea, August 18-23, 2013, 284.

(ii) National

1. **Chitrakshi Goel**, Nipun Dogra, Haripada Bhunia, and Pramod K. Bajpai, "Nanostructured carbon for environmental applications", *National Conference on Nanomaterials and Devices (NCONAD)*, National Institute of Technology Srinagar, Kashmir, October 3-5, 2013, 56.
2. **Chitrakshi Goel**, Haripada Bhunia, and Pramod K. Bajpai, "Developments in carbon dioxide capture by adsorption", *Theory and Practice of Separation Processes Including Modern Techniques*, Haldia Institute of Technology, Haldia, January 16-18, 2013, 60-63.

2.2 In related area

(i) International

1. Ronjish Chugh, **Chitrakshi Goel**, Haripada Bhunia, and Pramod K. Bajpai, "Adsorption kinetics of carbon dioxide on copper benzene-1, 3, 5-tricarboxylate metal-organic framework", *67th Annual Session of Indian Institute of Chemical Engineers, CHEMCON 2014*, Panjab University, Chandigarh, December 27-30, 2014, 80-81.

(ii) National

1. **Chitrakshi Goel**, Pramod K. Bajpai, and Haripada Bhunia, "Development of nanostructured carbons for CO_2 capture", *2nd Conference on Microscopy in Materials Science (AMST-2016)*, Thapar University, Patiala, February 25-27, 2016, 33.
2. Ronjish Chugh, **Chitrakshi Goel**, Haripada Bhunia, and Pramod K. Bajpai, "Kinetic study of carbon dioxide capture on Copper benzene-1, 3, 5-tricarboxylate metal-organic framework", *Technological Advances in Chemical, Petroleum & Natural Gas Engineering*, Chandigarh University, April 10-11, 2015, 32.
3. Harleen Kaur, **Chitrakshi Goel**, Haripada Bhunia, Pramod K. Bajpai, "Activated carbon based adsorption of 3,4-dichlorophenol", *National Conference on Innovation*

and Development in Chemical Technology (IDCT-2014), Guru Gobind Singh Indra Prastha University, Dwarka, February 28- March 1, 2014, 58-63.

4. Harleen Kaur, **Chitrakshi Goel**, Haripada Bhunia, Pramod K. Bajpai, "Kinetic and isothermal studies on adsorption of 3,4 dichlorophenol by activated carbon", *National Conference on Innovative Molecules for Sustainable Future (NCIMSF)*, Thapar University, Patiala, October 24-26, 2013, 39.

Table of Contents

Certificate iii

Acknowledgements iv

Abstract vi

Publications x

Table of Contents xiii

List of Figures xviii

List of Tables xxii

List of Symbols xxiv

List of Abbreviations xxvii

Chapter 1 – Introduction 1

1.1 Greenhouse gases and global warming 1

1.2 Mitigation pathways 3

1.3 Carbon dioxide capture and sequestration 3

1.3.1 CO_2 capture technologies 4

1.4 Post-combustion capture technologies 5

1.5 The scope and objectives of thesis 7

1.6 Thesis overview 8

Chapter 2 – Literature Review 10

2.1 Adsorption technology 10

2.2 Types of adsorbents 11

2.2.1 Zeolites 11

2.2.2 Silica based adsorbents 13

2.2.3 Carbon based adsorbents 15

2.2.3.1 Commercial activated carbons 15

2.2.3.2 Carbon adsorbents from renewable resources 15

2.2.3.3 Carbon adsorbents from synthetic polymers 17

2.2.3.3.1 Template free synthesis 17

2.2.3.3.2 Carbons from nanocasting technique 19

2.2.3.4 Carbon nanotubes 21

Chapter 3 – Experimental Methods, Kinetics and Isotherm Models 23
3.1 Materials 23
3.2 Characterization techniques 23
3.2.1 Surface area and pore size distribution 23
3.2.2 X-ray diffraction analysis 24
3.2.3 Transmission electron microscopy 24
3.2.4 Scanning electron microscopy 24
3.2.5 Thermal analysis 24
3.2.5.1 Thermogravimetric analysis (TGA) 24
3.2.5.2 Differential scanning calorimetry (DSC) 24
3.2.6 Elemental composition 24
3.2.7 Fourier transform infrared (FTIR) spectroscopy 25
3.2.8 X-ray photoelectron spectroscopy 25
3.2.9 Surface basicity by Boehm titration 25
3.2.10 Temperature programmed desorption 25
3.3 Performance evaluation of adsorbents 26
3.3.1 Fixed-bed adsorption study setup 26
3.3.2 Dynamic CO_2 adsorption measurements 28
3.3.3 Equilibrium sorption measurements 29
3.4 Kinetic study 29
3.4.1 Pseudo-first order model 29
3.4.2 Pseudo-second order model 30
3.4.3 Fractional order model 30
3.4.4 Error calculation 31
3.4.5 Activation energy 31
3.5 Isotherm study 32
3.5.1 Pure component isotherm 32
3.5.1.1 Langmuir isotherm model 32
3.5.1.2 Sips isotherm model 33
3.5.1.3 Dual-site Langmuir model 33
3.5.1.4 Error calculation 34
3.5.2 Binary component isotherm 34

3.5.2.1 Extended Sips isotherm model 35
3.5.2.2 Extended dual-site Langmuir isotherm model 35
3.5.2.3 Ideal adsorbed solution theory (IAST) 36
3.5.2.4 IAST based Sips and dual-site Langmuir models 38
3.5.2.5 Selectivity 38
3.6 Thermodynamic study 39
3.6.1 Thermodynamic parameters 39
3.6.2 Energy duty for desorption 39
3.7 Software used 40
Chapter 4 - Nitrogen Doped Mesoporous Carbons for Carbon Dioxide Capture 42
4.1 Introduction 42
4.2 Adsorbent synthesis 42
4.2.1 Templated resin synthesis 42
4.2.2 Carbonization of templated resin 44
4.2.3 Removal of template 44
4.3 Adsorbent characterization 45
4.3.1 Surface area and pore size distribution 45
4.3.2 X-ray diffraction analysis 48
4.3.3 Transmission electron microscopy 49
4.3.4 Scanning electron microscopy 50
4.3.5 Thermogravimetric analysis 52
4.3.6 Elemental composition 52
4.3.7 Fourier transform infrared (FTIR) spectroscopy 53
4.3.8 X-ray photoelectron spectroscopy 54
4.3.9 Surface basicity by Boehm titration 63
4.4 CO_2 adsorption performance 64
4.4.1 Effect of carbonization temperature 64
4.4.2 Effect of adsorption temperature and CO_2 feed concentration 67
4.4.3 CO_2 selectivity 70
4.4.4 Cyclic adsorption-desorption study 71
4.5 Equilibrium sorption measurements 72
4.6 Kinetic study 74

4.7 Isotherm study 79
4.7.1 Pure component isotherm 79
4.7.2 Binary component isotherm 83
4.8 Thermodynamic study 89
4.8.1 Thermodynamic parameters 89
4.8.2 Energy duty for desorption of CO_2 92
4.9 Conclusions 94
Chapter 5 – Resorcinol-Formaldehyde Based Nanostructured Carbons for Carbon Dioxide Capture 96
5.1 Introduction 96
5.2 Synthesis of porous carbons 96
5.2.1 Templated RF resin synthesis 96
5.2.2 Carbonization of templated RF resin 98
5.2.3 Template removal 98
5.3 Characterization of porous carbons 98
5.3.1 Surface area and pore size distribution 98
5.3.2 X-ray diffraction analysis 100
5.3.3 Transmission electron microscopy 102
5.3.4 Scanning electron microscopy 103
5.3.5 Thermogravimetric analysis 104
5.3.6 Elemental composition 105
5.3.7 Fourier transform infrared (FTIR) spectroscopy 106
5.3.8 X-ray photoelectron spectroscopy 107
5.3.9 Surface functional groups by Boehm titration 113
5.4 CO_2 capture performance 114
5.4.1 Adsorption capacity with carbonization temperature 114
5.4.2 Adsorption capacity with adsorption temperature and CO_2 feed concentration 116
5.4.3 Adsorbent selectivity and regenerability 118
5.5 Equilibrium sorption measurements 120
5.6 Kinetic study 121
5.7 Isotherm study 127

5.7.1 Pure component isotherm 127
5.7.2 Binary component isotherm 131
5.8 Thermodynamic study 136
5.8.1 Thermodynamic parameters 136
5.8.2 Energy duty for desorption of CO_2 138
5.9 Conclusions 140
Chapter 6 - Conclusions and Recommendations for Future Work 142
6.1 Conclusions 142
6.2 Recommendations for future work 144
References 145

List of Figures

Figure No.	Title	Page No.
Figure 1.1	Global greenhouse gas emissions during 1970-2010	1
Figure 1.2	Schematic diagram of CO_2 capture processes	4
Figure 3.1	Schematic diagram of the experimental setup	27
Figure 3.2	Adsorption study set up coupled with gas chromatograph	28
Figure 4.1	Block diagram of templated resin synthesis process	43
Figure 4.2	MF resin synthesis setup	44
Figure 4.3	(a) N_2 adsorption (closed symbols) - desorption (open symbols) isotherms at -196 °C of prepared carbons and mesoporous silica, (b) pore size distribution of nitrogen doped mesoporous carbon adsorbents	46
Figure 4.4	XRD patterns of nitrogen doped carbon adsorbents	48
Figure 4.5	TEM images of prepared nitrogen doped carbons	50
Figure 4.6	SEM images of nitrogen doped carbons (a) MF-500, (b) MF-600, (c, d) MF-700, (e) MF-800, and (f) MF-C	51
Figure 4.7	Thermogravimetric profiles of nitrogen doped mesoporous carbon adsorbents	52
Figure 4.8	FTIR spectra of nitrogen doped mesoporous carbons	54
Figure 4.9	XPS survey scan spectra of MF-based carbons	55
Figure 4.10	Deconvoluted XPS spectra of C1s region of nitrogen doped carbons	56
Figure 4.11	Deconvoluted XPS spectra of N1s region of nitrogen doped carbons	59
Figure 4.12	Deconvoluted XPS spectra of O1s region of nitrogen doped carbons	62
Figure 4.13	(a) Breakthrough profiles of CO_2 adsorption, and (b) CO_2 adsorption capacity of nitrogen doped carbon adsorbents at 30 °C and 10% CO_2 inlet concentration	65

Figure 4.14	Breakthrough curves of MF-700 as a function of adsorption temperature at (a) 5%, (b) 7.5%, (c) 10%, and (d) 12.5 % feed CO_2 concentration in N_2	67
Figure 4.15	Adsorption capacity of MF-700 as a function of CO_2 feed concentration at different temperatures	68
Figure 4.16	Breakthrough curves of CO_2 and N_2 for 12.5% CO_2 rest N_2 on MF-700 at (a) 30 °C, and (b) 50 °C	70
Figure 4.17	(a) Multi-cycle adsorption-desorption concentration profile for adsorption at 30 °C & 12.5% CO_2, and (b) Adsorption capacity over 4 consecutive adsorption-desorption cycles as a function of temperature at 12.5% CO_2 concentration	71
Figure 4.18	CO_2-Temperature programmed desorption profile of MF-700	72
Figure 4.19	Adsorption (closed symbols) - desorption (open symbols) isotherms of (a) CO_2, and (b) N_2 on MF-700 at different adsorption temperatures (30–100 °C) as function of pressure	73
Figure 4.20	Experimental uptake of CO_2 on MF-700 carbon along with corresponding fit to adsorption kinetic models at different adsorption temperatures and CO_2 inlet concentrations	74
Figure 4.21	Arrhenius plot for fractional order kinetic rate constant of CO_2 adsorption on MF-700	79
Figure 4.22	Experimental adsorption isotherms of (a) CO_2, and (b) N_2 on MF-700 at different temperatures and their corresponding isotherm model fits	80
Figure 4.23	Binary adsorption isotherms for CO_2-N_2 mixture on MF-700 at (a) 30 °C, (b) 50 °C, (c) 75 °C, and (d) 100 °C (symbols represent experimental data and lines represent model predicted data)	84
Figure 4.24	*x-y* diagram for binary adsorption of CO_2 and N_2 on MF-700 at (a) 30 °C, (b) 50 °C, (c) 75 °C, and (d) 100 °C	86
Figure 4.25	Thermodynamic functions $(\Delta G, \Delta H$ and $\Delta S \times T)$ for CO_2 (closed symbols) and N_2 (open symbols) on MF-700 at 30 °C	90
Figure 4.26	Isosteric heat of adsorption of pure CO_2 from equilibrium isotherms on MF-700	91
Figure 4.27	Isosteric heat of adsorption of CO_2 on MF-700	93

Figure 5.1	Templated RF resin synthesis process diagram	97
Figure 5.2	(a) N_2 adsorption (closed symbols) and desorption (open symbols) isotherms, and (b) pore size distribution of nanostructured carbons	99
Figure 5.3	Powder XRD patterns of synthesized carbons	101
Figure 5.4	TEM images of nanostructured carbons (a) RF-600, (b, c) RF-700, (d) RF-800, and (e) RF-C	103
Figure 5.5	SEM images of nanostructured carbons (a) RF-500, (b) RF-600, (c, d) RF-700, (e) RF-800, and (f) RF-C	104
Figure 5.6	Thermogravimetric profiles of RF-derived carbons	105
Figure 5.7	FTIR spectra of porous carbons obtained from RF resin	107
Figure 5.8	Survey scan spectra of RF derived carbons	108
Figure 5.9	Deconvoluted C1s spectra of RF based carbons	109
Figure 5.10	Deconvoluted O1s spectra of RF derived carbons	112
Figure 5.11	(a) CO_2 breakthrough profiles, and (b) CO_2 adsorption capacity of RF-derived carbons at 30 °C and 10% CO_2 feed concentration	115
Figure 5.12	Breakthrough profiles for CO_2 adsorption on RF-700 under (a) 5%, (b) 7.5%, (c) 10%, and (d) 12.5 % CO_2 concentration at different adsorption temperatures	116
Figure 5.13	CO_2 adsorption capacity of RF-700 at different adsorption temperatures as a function of inlet CO_2 concentration	118
Figure 5.14	(a) Breakthrough curves of N_2 (open symbols) and CO_2 (closed symbols) on RF-700 at 30 °C and 50 °C for 12.5% CO_2 feed concentration, and (b) CO_2 adsorption capacity of RF-700 over multiple cycles of adsorption-desorption at 10% CO_2 feed concentration as a function of temperature	119
Figure 5.15	Temperature programmed desorption profile of CO_2 from RF-700	120
Figure 5.16	Pure component adsorption (closed symbols) - desorption (open symbols) isotherms of (a) CO_2, and (b) N_2 on RF-700 at different adsorption temperatures	121

Figure 5.17	Comparison of kinetic models for CO_2 uptake on RF-700 at different adsorption temperatures as a function of feed concentration	123
Figure 5.18	Arrhenius plot for kinetic rate constants obtained from fractional order kinetic model	126
Figure 5.19	Measured and correlated adsorption isotherms of pure (a) CO_2, and (b) N_2 on RF-700 at different adsorption temperatures	128
Figure 5.20	Total and partial adsorbed amounts of CO_2 and N_2 binary adsorption on RF-700 at (a) 30 °C, (b) 50 °C, (c) 75 °C, and (d) 100 °C (symbols represent experimental data and lines represent model predicted data)	132
Figure 5.21	*x-y* diagram for CO_2 and N_2 binary adsorption on RF-700 at (a) 30 °C, (b) 50 °C, (c) 75 °C, and (d) 100 °C	133
Figure 5.22	Three functions ΔG, ΔH and $\Delta S \times T$ for pure CO_2 (closed symbols) and N_2 (open symbols) adsorption on RF-700 at (a) 30 °C, and (b) 50 °C	137
Figure 5.23	Isosteric heat of adsorption of pure CO_2 on RF-700 carbon	138
Figure 5.24	Isosteric heat of adsorption with surface coverage on RF-700	140

List of Tables

Table No.	Title	Page No.
Table 4.1	Textural properties of nitrogen doped mesoporous carbon adsorbents	47
Table 4.2	Structural parameters of nitrogen doped carbons	49
Table 4.3	Chemical properties of mesoporous carbon adsorbents	53
Table 4.4	Deconvolution of XPS spectra of C1s region of nitrogen doped carbons	57
Table 4.5	Deconvolution of XPS spectra of N1s region of nitrogen doped carbons	60
Table 4.6	Deconvolution of XPS spectra of O1s region of nitrogen doped carbons	63
Table 4.7	Surface acidity and basicity by Boehm titration of the carbon adsorbents	64
Table 4.8	CO_2 adsorption capacity of MF-700 at different adsorption temperatures	69
Table 4.9	Kinetic model parameters for adsorption of CO_2 on MF-700 at different CO_2 feed concentrations and adsorption temperatures	76
Table 4.10	Parameters of Arrhenius equation for adsorption of CO_2 on MF-700	79
Table 4.11	Langmuir isotherm model parameters for pure component adsorption on MF-700 at different temperatures	81
Table 4.12	Sips isotherm model parameters for pure component adsorption on MF-700 at different temperatures	82
Table 4.13	Dual-site Langmuir isotherm model parameters for pure component adsorption on MF-700 at different temperatures	82
Table 4.14	Comparison of experimental and predicted binary system CO_2 adsorption capacities on MF-700 based on binary component adsorption isotherms	85
Table 4.15	Experimental and isotherm model predicted selectivities for CO_2-N_2 binary system on MF-700	87

Table 5.1	Textural parameters of RF derived nanostructured carbons	100
Table 5.2	Structural parameters of RF derived carbons	102
Table 5.3	Elemental composition of nanostructured carbons	106
Table 5.4	Deconvolution of C1s photoelectron envelope of RF-derived carbon	110
Table 5.5	Deconvolution of O1s photoelectron envelope of RF-derived carbons	113
Table 5.6	Surface functional groups by Boehm titration method	114
Table 5.7	Kinetic model parameters for CO_2 adsorption on RF-700 at different adsorption temperatures and CO_2 concentrations	124
Table 5.8	Arrhenius equation parameters for CO_2 adsorption on RF-700	126
Table 5.9	Regression results for Langmuir equation for pure CO_2 and N_2 adsorption on RF-700 at different temperatures	129
Table 5.10	Regression results for Sips equation for pure CO_2 and N_2 adsorption on RF-700 at different temperatures	129
Table 5.11	Regression results for dual-site Langmuir equation for pure CO_2 and N_2 adsorption on RF-700 at different temperatures	130
Table 5.12	Physical properties of CO_2 and N_2	131
Table 5.13	Equilibrium selectivity of CO_2 over N_2 for binary system adsorption on RF-700 from breakthrough curve and isotherm models	135

List of Symbols

ΔG	Integral molar Gibbs free energy change, kJ mol^{-1}
ΔH	Integral molar adsorption enthalpy, kJ mol^{-1}
ΔS	Integral molar entropy change, kJ mol^{-1} K^{-1}
ΔT	Temperature difference between adsorption and desorption, K
A	Pre-exponential factor of Arrhenius equation
b	Langmuir and Sips isotherm model parameter
b_o	Langmuir and Sips isotherm model parameter at reference temperature
$b_{o,j}$	Dual-site Langmuir affinity parameter at reference temperature for site j
b_1	Affinity parameter of dual-site Langmuir isotherm for site 1
b_2	Affinity parameter of dual-site Langmuir isotherm for site 2
B	Heat of adsorption from Langmuir equation, J mol^{-1}
c	Sips parameter
C	Effluent CO_2 concentration, volume%
C_o	Inlet CO_2 concentration in simulated feed gas, volume%
C_p	Specific heat capacity of the adsorbent, J g^{-1} K^{-1}
d_{002}	Interlayer d-spacing of (002) diffraction plane, nm
E_a	Activation energy, J mol^{-1}
E_j	Dual-site Langmuir model adsorption energy for site j
Error (%)	Error function
k_1	Pseudo-first order rate constant, min^{-1}
k_2	Pseudo-second order rate constant, g $mmol^{-1}$ min^{-1}
k_n	Fractional order rate constant
m	Fractional order model constant related to adsorption time
M	Mass of the adsorbent, g
n	Fractional order model constant related to driving force

N	Total number of experimental points
N_C	Number of components present in the system
$P_i^0(\pi^*)$	Equilibrium gas phase pressure of pure component i corresponding to spreading pressure π^*, atm
P	Total pressure, atm
$q_{1,m}$	Saturation capacity of dual-site Langmuir isotherm for site 1, mmol g^{-1}
$q_{2,m}$	Saturation capacity of dual-site Langmuir isotherm for site 2, mmol g^{-1}
q_e	Dynamic adsorption capacity at equilibrium, mmol g^{-1}
$q_{e,i}$	Equilibrium adsorption capacity of component i in the mixture, mmol g^{-1}
$q_{e,exp}$	Amount of adsorbate adsorbed at equilibrium determined experimentally, mmol g^{-1}
$q_{e,pred}$	Amount of adsorbate adsorbed at equilibrium as predicted by model, mmol g^{-1}
q_i^*	Pure component adsorption isotherm equation
$q_i^0(P_i^0)$	Adsorbed amount of pure component i at standard state pressure P_i^0
q_i	Adsorbed amount of component i in mixture, mmol g^{-1}
q_m	Maximum monolayer capacity, mmol g^{-1}
q_t	CO_2 adsorption capacity at time t, mmol g^{-1}
q_T	Total adsorbed amount in mixture, mmol g^{-1}
$q_{t,exp}$	Amounts of CO_2 adsorbed at a given time determined experimentally, mmol g^{-1}
$q_{t,pred}$	Amounts of CO_2 adsorbed at a given time predicted by model, mmol g^{-1}
Q	Gas flow rate, cm^3 min^{-1}
Q_{st}	Isosteric heat of adsorption, kJ mol^{-1}
Q_{th}	Thermal energy input, J mol^{-1}
R	Universal gas constant, kJ mol^{-1} K^{-1}
R^2	Regression coefficient
S_{BET}	BET surface area, m^2 g^{-1}
S_{CO_2}	Selectivity of CO_2 over N_2

t	Time, min
t_b	Breakthrough time, min
t_e	Equilibrium time, min
T	Temperature, K
V_{meso}	Mesopore volume, $cm^3\ g^{-1}$
V_{micro}	Micropore volume, $cm^3\ g^{-1}$
V_P	Total pore volume obtained at a relative pressure of 0.99, $cm^3\ g^{-1}$
x_i	Molar fraction of component *i* in the adsorbed phase
y_i	Molar fraction of component *i* in the gas phase

Greek Letters

π_i^*	Reduced spreading pressure of component *i* in the mixture, mmol g^{-1}
π^*	Reduced spreading pressure of the mixture, mmol g^{-1}
π_i	Spreading pressure of component *i* in the mixture, N/m
θ	Bragg's angle
Ω	Surface potential, kJ mol^{-1}

List of Abbreviations

A%	Relative area contribution
APTS	3-aminopropyltriethoxysilane
B. E.	Binding energy
BET	Brunauer–Emmett–Teller
BJH	Barrett–Joyner–Halenda
DEA	Diethanol amine
DSC	Differential scanning calorimetry
DSL	Dual-site Langmuir
ED	Ethylenediamine
FTIR	Fourier transform infrared
FWHM	Full width at half maximum
GHG	Greenhouse gases
$GtCO_2eq$	Gigatonnes CO_2-equivalents
HFC	Hydrofluorocarbons
IAST	Ideal adsorbed solution theory
IPA	Isopropanol amine
IPCC	Intergovernmental panel on climate change
MDEA	Methyldiethanol amine
MEA	Monoethanol amine
MF	Melamine-formaldehyde
MWCNT	Multi-walled carbon nanotubes
PEI	Polyethyleneimine
PFC	Perfluorocarbons
ppm	Parts per million
PN	Perfect negative

PP	Perfect positive
PPy	Polypyrrole
PSA	Pressure swing adsorption
PSD	Pore size distribution
PTSA	Pressure temperature swing adsorption
RF	Resorcinol-formaldehyde
SEM	Scanning electron microscopy
SSE	Sum of the squared relative error
SWCNT	Single-walled carbon nanotubes
TEM	Transmission electron microscopy
TEPA	Tetraethylene penta amine
TEPAN	Tetraethylene penta amine acrylonitrile
TG	Thermogravimetry
TGA	Thermogravimetric analysis
TPD	Temperature programmed desorption
TSA	Temperature swing adsorption
UF	Urea-formaldehyde
VSA	Vacuum swing adsorption
wt%	weight%
XPS	X-ray photoelectron spectroscopy
XRD	X-ray diffraction

Chapter 1 – Introduction

1.1 Greenhouse gases and global warming

Anthropogenic greenhouse gas (GHG) emissions are deemed to be the foremost reason of global climate change. Major greenhouse gases in the atmosphere are carbon dioxide (CO_2), methane (CH_4), nitrous oxide (N_2O), ozone (O_3), perfluorocarbons (PFCs), hydrofluorocarbons (HFCs) and sulphur hexafluoride (SF_6) [1]. In the last decade (2000-2010), anthropogenic GHG emissions have been increasing at a very fast rate with average increase of 1 gigatonnes CO_2-equivalents ($GtCO_2eq$) per year (~2.2% per year) as compared to the previous three decades (1970-2000) with an average increase of 0.4 $GtCO_2eq$ per year (~1.3% per year). In 2010, total GHG emissions have reached the values of 49 ± 4.5 $GtCO_2eq$ with CO_2 being the major contributor, accounting for 38 ± 3.8 $GtCO_2eq$ (~76%), followed by methane (7.8 ± 1.6 $GtCO_2eq$), nitrous oxide (3.1 ± 1.9 $GtCO_2eq$) and fluorinated gases (1 ± 0.2 $GtCO_2eq$). Increase in global emissions of all the major greenhouse gases between 1970 and 2010 is shown in Figure 1.1. Increase in total GHG emissions has mainly come from energy supply, transport and industry sectors. Growth in emissions from buildings (residential and commercial), agriculture and forestry sectors is at a lower rate [2].

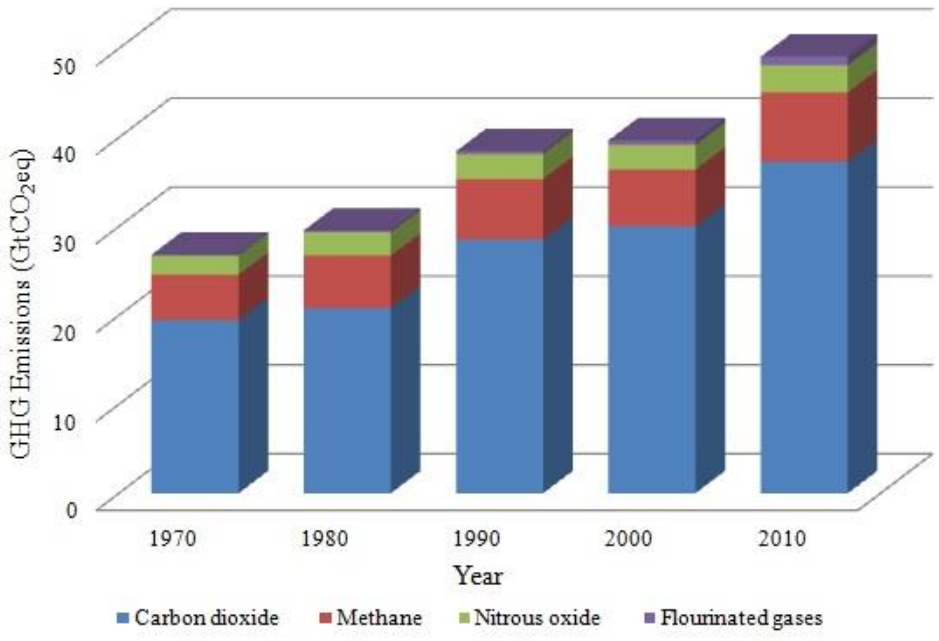

Figure 1.1 Global greenhouse gas emissions during 1970-2010 [2]

Major sources of GHG emissions i.e. energy, transport and industry sectors produce GHGs by the burning of fossil fuels like coal, oil, etc. and at present, more than 80% of the world's energy requirement is furnished by them [3]. Moreover since 1980, the energy demand has almost doubled and is expected to rise to 85% by 2050 [4]. Among all the GHGs, CO_2 is the major contributor to global warming (~76%) on account of its very high emissions in the atmosphere though it has the lowest global warming potential. Fossil fuel combustion contributes to a major part in total anthropogenic CO_2 emissions. Anthropogenic CO_2 emissions from combustion of fossil fuels reached 32 ± 2.7 $GtCO_2eq$ in 2010 and increased additionally by 3% and 1–2% in 2010-2011 and 2011-2012 respectively [2]. Atmospheric CO_2 concentration level has reached a value of ~401.8 ppm in 2014 from a value of ~280 ppm in 1750 i.e. an increase of ca. 45% and is expected to reach up to 570 ppm by 2100. Average annual rate of increase of atmospheric CO_2 concentration has almost doubled from < 1 ppm per year before 1970 to 2.1 ppm per year in the last decade (2005–2014) [5, 6].

This uncontrollable increase in CO_2 levels, due to strong dependence on fossil fuels for energy requirements, has resulted in increase in average global temperature associated with widespread changes in weather patterns. This will also lead to glaciers retreat, increased melting of surface ice and rise in global mean sea level. The linear warming trend over the last 50 years (1956–2005) has almost doubled as compared to that for 100 years (1906–2005) [7]. Arctic ice has been reported to be thinned by 40% in recent decades. A rise in the global sea level by 0.19 m is observed during the period 1901-2010. There is an increase in the frequency of the extreme weather events like large storms, heat waves, droughts, heavy rainfall and wild fires in the recent times. Oceans store large amounts of CO_2 but increased concentration of CO_2 has lead to increase in acidity and hence a drop in pH by 0.1 which has harmful effects on the marine life [8-10]. Current rate of increasing CO_2 levels will lead to rise in average global temperature by 2–6 °C by the end of 21st century. Stabilization of CO_2 concentration at the level of 450 ppm is considered as threshold to avoid the overshoot of average global temperature rise by 2 °C by the year 2100. Global CO_2 emissions need to be reduced by 50% to limit the global warming below 2 °C [11]. Hence, immediate measures need to be taken to address these increasing CO_2 concentrations as this trend will continue for coming decades as fossil fuels will persist to be the foremost energy source.

1.2 Mitigation pathways

To reduce increasing CO_2 concentrations, various approaches can be adopted such as reduction in energy demand by improving the efficiency of energy conversion devices, decreasing carbon intensity by switching to less carbon-intensive fuels or by using renewable energy sources and/or nuclear energy, reduction of non-CO_2 greenhouse gases and carbon dioxide capture and sequestration (CCS) system. Among the mentioned pathways, CCS is considered to be a key technology to drastically reduce increasing CO_2 concentrations in the near term while allowing the usage of fossil fuels for meeting the energy requirements [12, 13]. Alternative sources of energy like renewable sources (wind, solar etc.), nuclear energy sources, hydrogen and biomass appear to hold great potential but they are still under development and are not yet commercially viable to meet the present energy demands. CCS could act as a bridging strategy in providing time for the advancement of fossil fuel alternatives along with decrease in overall CO_2 mitigation cost. According to Intergovernmental Panel on Climate Change (IPCC), a power plant outfitted with CCS technology has the potential to capture around 80–90% of CO_2 emissions to the atmosphere [14].

1.3 Carbon dioxide capture and sequestration

Carbon dioxide capture and sequestration is based on the concept of capturing anthropogenic CO_2 generated from energy sources, without allowing discharge into the atmosphere, followed by transportation to a storage site and sequestering it permanently in the storage site [8, 15]. Various parameters such as fuel cost, capture plant's scale, characteristics of power plant's technology and storage site, distance between capture location and storage site etc. are to be considered while evaluating the cost involved in the application of CCS on fossil fuels. Cost of CO_2 capture and separation is a major part (~70–80%) of the total sequestration cost. Transportation and storage (siting, modeling, drilling, injection, site closure, and monitoring) are usually a marginal portion of the total cost [13]. For the transportation of CO_2, well-known technologies are available which were originally developed for enhanced oil recovery. Potential storage sites include geological formations like oil and gas fields, deep saline formations and unminable coal beds, oceans by direct release into the ocean water column or onto the deep seafloor, and industrial fixation of CO_2 into inorganic carbonates. Large number of geological formations indicates them as promising storage options and it is estimated that around 1120–3400 $GtCO_2$ can be sequestered in the formations recognized until now [16]. But sequestration requires concentrated and high pressure CO_2 stream considering the economics

involved in its transportation and injection into the storage site. Therefore, development of an efficient and cost-effective CO_2 capture technology holds the highest priority in the field of CCS.

1.3.1 CO_2 capture technologies

CO_2 capture is generally applied to large point sources including fossil fuel based energy units, oil refineries, natural gas generation units, major CO_2 liberating industries etc. Capture from small and mobile sources for example transportation sources, commercial and residential building sectors are deemed to include higher costs and difficulty as compared to capture from large point sources. Three approaches are available for CO_2 capture, based on process application, namely post-combustion, pre-combustion and oxy-fuel combustion capture technologies and their schematic diagram is presented in Figure 1.2.

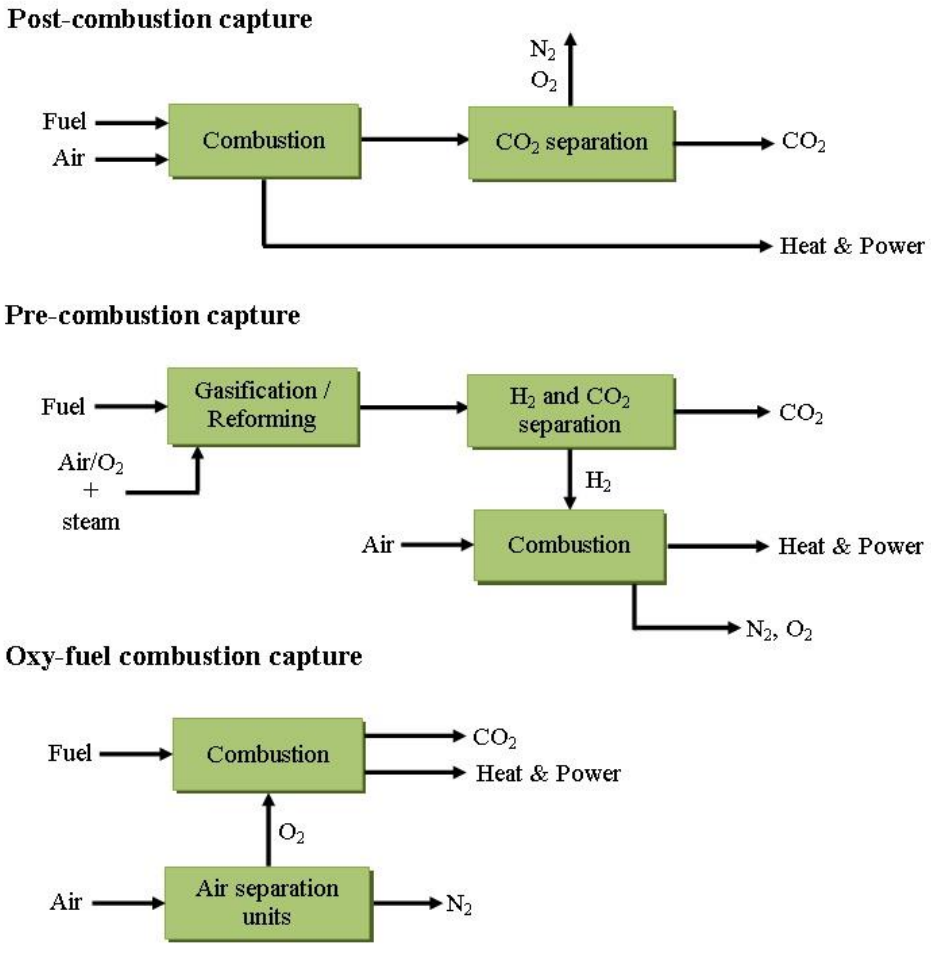

Figure 1.2 Schematic diagram of CO_2 capture processes

Pre-combustion CO_2 capture deals with capturing CO_2 prior to fossil fuel combustion. This is done by either gasification or partial oxidation of fuel to produce synthesis gas (carbon monoxide and hydrogen) followed by water gas shift reaction to produce CO_2 and additional H_2. Produced CO_2 is removed and H_2 is used as fuel in various applications. Fuel conversion is an expensive and complex process but CO_2 pressure and density in the gases leads to its easy removal and small equipment size. This technique is generally used in hydrogen generation and fertilizer industry and can be used in integrated gasification combined cycle (IGCC) plants [17, 18].

Oxy-fuel combustion technology uses high purity oxygen (> 95% purity) instead of air for the combustion of fossil fuel thereby resulting in high concentration of CO_2 (> 80%) in flue gas stream. This helps in easy separation of CO_2 but at the expense of high energy requirements for upstream separation of oxygen from air. It has been estimated that oxygen requirement in an oxy-fuel combustion system is almost three times the requirement in an IGCC plant of comparable size, thereby adding significant cost due to air separation units [19, 20]. Moreover, large part of the flue gas needs to be recycled back to maintain temperature in the boiler because of higher combustion temperatures with pure oxygen than with air [21].

Post-combustion capture technology is a downstream process and is based on the separation of CO_2 in flue gas generated from fossil fuel combustion. It imposes remarkable design challenge because of high temperature of flue gas and low CO_2 partial pressure in flue gas [22]. Selection of capture technology depends on the type of fuel used, pressure of gas stream and CO_2 concentration in flue gas stream. Pre-combustion capture technique is applicable to gasification units while oxy-fuel combustion can be applied to new plants or retrofitted to existing plants. Post-combustion capture is generally applicable to coal-fuelled power plants which are air fired. Moreover, it has the utmost potential in mitigating CO_2 emissions in the near term as it can be retrofitted to existing power plants which contribute to two-thirds of CO_2 generation [16, 23].

1.4 Post-combustion capture technologies

Major challenge for post combustion CO_2 capture is the handling of large volumetric flow rates of flue gas at almost atmospheric pressure with low concentrations of CO_2, typically <15% in temperature range of 100–150 °C [24, 25]. Coal fired plants produce flue gas with CO_2

concentration in the range of 7–14% while only 4% CO_2 is present in gas-fired combustion flue gas [26]. The available post-combustion capture technologies include absorption, membrane separation, cryogenic distillation and adsorption.

CO_2 capture by absorption is the widely established technology in chemical and petroleum industries and is based on the separation by the use of chemical solvents such as aqueous amine solutions of alkanolamines e.g. monoethanol amine (MEA), diethanol amine (DEA), methyldiethanol amine (MDEA) etc., ammonia solution, rectisol (chilled methanol), poly(ethylene glycol) dimethyl ether, fluorinated solvents etc. Despite being a mature technology, it has various disadvantages like equipment corrosion, solvent degradation and toxicity and high energy requirement for regeneration which impede its implementation [27, 28].

Membrane separation is based on the difference between the physical or chemical interactions between various gas components and membranes and hence allows the preferential permeability to some components of gas. Various organic and inorganic membranes have been employed for the separation. This technique is associated with small equipment size, low energy requirement and easy addition to existing power plants without any complicated integration. But they are highly efficient under high concentrations of gas streams only and low concentration of CO_2 in post-combustion capture, high flue gas temperatures and membranes fouling make them an inappropriate approach for CO_2 capture. Moreover, it is relatively a new technique and there is a trade-off between its permeability and selectivity [29-31].

Cryogenic distillation is based on the assumption that all the components of flue gas other than N_2 and CO_2 have been removed. Temperature and pressure conditions in the cryogenic chamber are manipulated such that CO_2 is liquefied while keeping N_2 in the gas form. Highly pure liquid CO_2 is obtained from this distillation process which is ready for transportation. But this process is highly energy extensive process and is viable only for very high CO_2 concentrations thereby making this technique unsuitable for practical applications [32, 33].

Post-combustion CO_2 capture by adsorption process has gained great attention as a viable alternative to the currently used, high energy-demanding aqueous amine absorption technologies because of ease of application, low energy requirements and low equipment cost. This technology uses a porous solid adsorbent to selectively remove CO_2 gas based on gas-

solid interactions. A wide variety of solid adsorbents like zeolites, activated carbons, silica, amine modified adsorbents etc. have been reported for capture of CO_2 from flue gases. But these conventional adsorbents suffer from large pressure and/or temperature gradient between adsorption and desorption steps and low selectivity towards CO_2. Thus, development of an effective and selective adsorbent for CO_2 capture will make adsorption the most promising technology.

1.5 The scope and objectives of thesis

It has been found that conventional adsorbents exhibit low selectivity and poor performance under humid conditions. Extensive work has been carried out on amine modified adsorbents for CO_2 capture. But impregnation of amines or high thermal treatments with various chemical agents is sometimes considered less favorable because this leads to blocking of pores of the adsorbent. Hence, many efforts have been made to fabricate materials with well-developed pore structure and enhanced selectivity towards CO_2. Among the available adsorbents, carbon based adsorbents have been selected for the present study as they can be prepared from a wide range of starting materials and their porous structure can be tailored based on the application. Most of the carbon adsorbent development has been conducted by direct carbonization and/or activation (physical or chemical) of various starting materials. The objective of this work is to develop carbon adsorbents with specific pore structure; hence we have selected the development of carbons by nanocasting technique. Very few research groups have developed carbon adsorbents from nanocasting technique for CO_2 capture from flue gas. Moreover, most of the adsorbents developed for CO_2 capture have been evaluated under static flow conditions generally at room temperature or 0 °C which is not pertinent to flue gas application. Hence, we aim to develop carbon adsorbents from nanocasting technique followed by their evaluation for CO_2 capture under dynamic flow conditions.

The overall objective of the research is to develop effective adsorption process for the continuous removal of CO_2. The specific objectives are:

- Synthesis of adsorbents with specific pore structures and surface areas using nanocasting technique using various polymers and inorganic template materials.
- Characterization of the synthesized adsorbents for their relevant properties.
- Performance evaluation of the adsorbents with simulated post-combustion CO_2 capture conditions.

- To fit the equilibrium and kinetic models for the experimental data.
- Regeneration study of the adsorbents.

1.6 Thesis overview

This thesis has been divided into six chapters. Two different polymeric precursors were used to develop carbon adsorbents by nanocasting technique. Thorough characterization of the prepared carbons was carried out to investigate their textural, surface and chemical properties. Techniques used for the characterization include nitrogen sorption isotherms, X-ray diffraction (XRD), transmission electron microscopy (TEM), scanning electron microscopy (SEM), thermogravimetric analysis (TGA), elemental analysis (CHNS), Fourier transform infrared (FTIR) spectroscopy, X-ray photoelectron spectroscopy (XPS), and surface functional groups by Boehm titration method. Dynamic adsorption-desorption experiments were conducted in the fixed-bed system to evaluate their CO_2 adsorption capacities, selectivity and regeneration under simulated flue gas conditions. Equilibrium uptake of pure CO_2 and N_2 was also investigated at different adsorption tempertaures. Adsorption of CO_2 on these adsorbents was also evaluated from kinetics, isotherm and thermodynamics point of view.

Chapter 1 is introduction which covers the background and the problem statement. It covers the various greenhouse gases especially CO_2 and its impact on global climate. Various approaches for mitigating CO_2 emissions have been introduced in this chapter.

Chapter 2 discusses the literature review on the adsorption technology followed by detailed study on various adsorbents for CO_2 capture. More emphasis has been given to carbon based adsorbents as the current work focuses on them.

Chapter 3 covers the materials used in the work and the experimental methods used for the characterization and performance evaluation of the prepared adsorbents. The experimental setup (for fixed-bed adsorption study) used for carrying out the adsorption-desorption experiments is also presented in this chapter. Theories of various adsorption kinetic and isotherm models (both pure and binary component) and thermodynamic parameters are also discussed.

Chapter 4 discusses the synthesis of carbon adsorbents from melamine-formaldehyde resin via nanocasting technique followed by thorough characterization. CO_2 adsorption performance of the prepared carbons has been evaluated and the results are related with their physico-chemical properties. The optimized sample of this series was further studied under simulated flue gas conditions at varying adsorption temperatures. This chapter also includes the complete kinetic, isothermal and thermodynamic study of CO_2 adsorption on the optimized sample along with energy calculation required for desorption. Equilibrium adsorption-desorption of the optimized sample was also carried out under pure CO_2 and N_2 atmospheres at four different temperatures. Mixed-gas adsorption equilibria and selectivity of the prepared carbons were predicted by binary component isotherm models along with application of ideal adsorbed solution theory to these models and was then compared with the experimental data.

Chapter 5 covers the development and characterization of nanostructured carbons from resorcinol-formaldehyde resin and mesoporous silica as polymeric precursor and hard template respectively. CO_2 adsorption-desorption studies on these carbons were carried out under dynamic conditions and again the optimized sample was investigated comprehensively. Static adsorption capacities of the optimized sample were evaluated at varying temperatures under 100% CO_2 and N_2 conditions. Kinetic models were fitted to the experimental data and thermodynamic parameters were also calculated. Pure component and binary component equilibria were fitted by using the single component and binary system isotherm models. Finally, energy duty required for desorption of adsorbed CO_2 was investigated.

Chapter 6 presents the conclusions and the recommendations for the future work.

Chapter 2 – Literature Review

Increasing atmospheric CO_2 concentrations and its detrimental effect on the global climate has triggered an urgent need to develop CO_2 reduction technologies. Carbon dioxide capture and sequestration is a bridging technology to reduce increasing CO_2 emissions from large point sources along with allowing the use of fossil fuels for meeting the energy demands. Choice of suitable CO_2 capture technology depends on the characteristics of the flue gas i.e. concentration, pressure and temperature which further depends on the power plant technology. Various capture methods including absorption, membrane separation and cryogenic distillation are energy-intensive and expensive. CO_2 capture from flue gas by the use of porous materials appears to be a promising technology but effective adsorbents need to be developed.

2.1 Adsorption technology

Adsorption is the process where a molecule becomes selectively attached (adsorbed) onto a surface of another phase. Thus, by using special solids called adsorbents, substances from gaseous (or liquid) mixtures can be selectively removed. The separation of a substance, the adsorbate, is achieved by its accumulation at the surface of the adsorbent. Depending on the nature of interaction between the adsorbent and adsorbate molecules, adsorption can be classified as physical adsorption and chemical adsorption (chemisorption). Physical adsorption is based on weak Van der Waal forces while chemisorption involves the chemical bond between adsorbent and adsorbate molecules.

A critical step in the adsorption process is the removal of the captured CO_2 from the adsorbent, a process called regeneration or desorption. Adsorbents need to be regenerated periodically so that they can be used in cyclic adsorption processes. There are a variety of methods to force an adsorbent to release the adsorbed components and these depend on the properties of the adsorbents. On this basis, adsorption process can be carried out by means of (i) isothermal regeneration means, like pressure swing adsorption (PSA), including vacuum (VSA) or (ii) non-isothermal regeneration means, like temperature swing adsorption (TSA) or a combination of pressure and temperature gradients (PTSA) [34-36]. In case of TSA, adsorbed gas molecules are desorbed by raising the temperature of the system while in case of PSA, depressurization is carried out for desorption to take place. For a PTSA system, desorption takes place under

low pressure and high temperature conditions. In TSA, adsorption is favored at low temperatures whereas high temperature leads to desorption of adsorbed molecules [37, 38]. Electric swing adsorption (ESA) is an alternative non-isothermal regeneration technique which uses the electricity through the conductor (Joule effect) to increase the temperature thereby facilitating desorption of adsorbate molecules [39]. PSA processes are based on adsorption of the adsorbate molecules (e.g., CO_2) on solid adsorbent under high pressure conditions with recovery of the adsorbed gas at low pressures [40, 41]. For CO_2 capture from power plants, PSA is a commercially available technology with efficiency of > 85% [42]. TSA includes longer regeneration times than PSA but high purity CO_2 (> 95%) can be achieved with more than 80% recovery [43].

2.2 Types of adsorbents

Commercially available adsorbents include zeolites, activated alumina, silica, activated carbons and polymeric adsorbents [44, 45]. For an economical technology in CO_2 separation process, the ideal set of requirements for an adsorbent include high adsorption capacity, selectivity towards CO_2 over other gases present in the stream, fast adsorption kinetics, easy regenerability, stability and low cost. But it is difficult to develop an adsorbent that meets all these requirements. For effective capture of CO_2 by adsorption process, strengths and limitations of each adsorbent should be considered. Eventually, adsorbents that can work effectively within the practical CO_2 capture process will be the winners.

Research has demonstrated that only activated carbon and zeolites can find applications in CO_2 separation. Silica materials have been extensively modified with various amines prior to their application in CO_2 capture. Following sections discuss the research carried out on various adsorbents. Carbon based adsorbents will be discussed more in this review as they are the focus of the present work.

2.2.1 Zeolites

Zeolites are highly ordered crystalline microporous aluminosilicates with large internal specific surface areas and volumes. They are used in separation applications and most widely as mainly adsorbents for CO_2 capture processes because of their unique ability of molecular sieving [46-48]. They are generally used at high pressures (> 2 bar) and their adsorption capacity is reported to reduce drastically in the presence of moisture in gas stream. Polar water molecules get

preferentially adsorbed on zeolite surface because of its hydrophilic nature and block the access for CO_2 thereby reducing CO_2 adsorption capacity. This leads to regeneration of zeolites at very high temperatures (> 300 °C) thereby imposing large energy for their regeneration [49-51]. Many research groups have reported the CO_2 uptake on commercially available zeolites of various types (X, Y, A etc.) and synthesized zeolites mainly zeolites 13X and 5A. Zeolite 13X adsorbent showed CO_2 adsorption capacity of 6.5 mmol g^{-1} at 25 °C and 10 bar [52] while synthesized zeolite 5A showed equilibrium CO_2 uptake of ~4.7 mmol g^{-1} at 25 °C and 1 bar with single component CO_2/N_2 selectivity = 8.45 [53]. Siriwardane et al. [54] reported static equilibrium CO_2 adsorption capacity of 3.64 mmol g^{-1} and 3.07 mmol g^{-1} at 25 °C and 1 bar for commercial zeolites 13X and 4A respectively.

Some research groups have modified the conventional zeolites with various amines in order to improve their CO_2 adsorption capacities at high temperatures. For example, Jadhav et al. [55] modified zeolite 13X with different loadings of monoethanol amine (MEA) via impregnation method. The amine modified samples showed lower dynamic CO_2 adsorption capacity as compared to unmodified zeolite for adsorption at 30 °C and 50 °C while the trend was opposite for adsorption at 75 °C and 120 °C. At 75 °C and 120 °C, amine modified samples showed CO_2 adsorption capacity of 0.35 and 0.49 mmol g^{-1} respectively against 0.28 and 0.14 mmol g^{-1} of unmodified zeolite under same conditions. Despite the reduction in surface area and pore volume of zeolite 13X due to impregnation, higher CO_2 capacities at these temperatures are because of chemical interactions between amine groups on zeolite and CO_2 molecules. In another work, zeolite 13X was modified with various amines namely MEA, ethylenediamine (ED) and isopropanol amine (IPA) and the effect of various parameters such as kind of solvent used, time for shaking, temperature etc. on amine loading was studied. At 75 °C, dynamic CO_2 uptakes were in the order of IPA modified zeolite (0.52 mmol g^{-1}) > MEA modified zeolite (0.45 mmol g^{-1}) > bare zeolite (0.36 mmol g^{-1}) under 15% CO_2 balance in He flow. Equilibrium adsorption capacity of MEA modified zeolite and bare zeolite at 75 °C under 100% CO_2 was found to be 1.1 and 0.85 mmol g^{-1} respectively [56].

Xu et al. [57] reported the incorporation of MEA on β-zeolite and determined the uptake of various gases (CO_2, CH_4 and N_2) by volumetric method at 30 °C. Static equilibrium adsorption capacities of CO_2, CH_4 and N_2 by MEA modified (40 weight%) β-zeolite were found to be ca. 0.80, 0.17 and 0.03 mmol g^{-1} respectively at 30 °C and 1 bar thereby showing very high selectivity of CO_2/N_2 = 25.67. While parent β-zeolite showed CO_2/N_2 selectivity of 12.19 under

same adsorption conditions. Fisher et al. [58] reported CO_2 adsorption capacity up to 2.08 mmol g^{-1} at 30 °C in 10% CO_2 balance argon flow by β-zeolite impregnated with tetraethylenepentamine (TEPA).

2.2.2 Silica based adsorbents

Mesoporous silica materials have received great attention in the field of CO_2 capture despite their very low CO_2 adsorption capacities. This is because they exhibit high surface area, tunable porous structure; facilitate faster diffusion of gas and abundant hydroxyl groups present on their surface allow grafting of amine groups thereby enhancing their affinity for CO_2 molecules.

CO_2 adsorption in amine-impregnated mesoporous silica was first reported by Xu et al. [59]. They impregnated polyethyleneimine (PEI) on MCM-41 silica by wet impregnation method and termed the adsorbent as "molecular basket" [60-63]. Adsorption capacity of PEI-impregnated MCM-41 improved with increase in PEI loading and maximum CO_2 adsorption (determined by thermogravimetric analysis) of 3.02 mmol g^{-1} was achieved for sample with 75 wt% PEI loading under 100% CO_2 atmosphere at 75 °C. But sample with 50 wt% PEI loading showed the maximum efficiency i.e. CO_2/PEI molar ratio and it showed CO_2 uptake of ~2.1 mmol g^{-1} at 75 °C under 10% CO_2 in N_2 [59]. Also adsorbents obtained from one-step wet impregnation method were found to be better than those obtained from two-step impregnation and mechanical mixing method [63]. The adsorption capacity of PEI-impregnated MCM-41 adsorbents improved as temperature increased from 25 °C to 75 °C [60, 62, 63]. Effect of moisture on PEI-impregnated MCM-41 for CO_2 adsorption was studied in simulated flue gas and flue gas from a natural-gas-fired boiler [61]. Increase in adsorption capacity was noted for moisture concentration in the feed equal to or lower than CO_2 concentration. CO_2 adsorption capacity increased to 2.84 mmol g^{-1} in stream having 10% moisture and 13% CO_2 in air from 2.01 mmol g^{-1} in simulated dry flue gas having 15% CO_2. But for higher moisture content in the feed stream, no further rise in adsorption capacity was observed.

Franchi et al. [64] impregnated diethanolamine (DEA) on a pore-expanded MCM-41 (PE-MCM-41) and compared its CO_2 adsorption capacity (obtained gravimetrically) with zeolite 13X. Larger pore size and pore volume of PE-MCM-41 allowed for greater loading level of amine agents, thereby having higher CO_2 adsorption capacity of 2.93 mmol g^{-1} at 25 °C in 5%

CO_2 atmosphere. Moisture had insignificant effect on CO_2 uptake of DEA-loaded PE-MCM-41.

Belmabkhout et al. [65] prepared MCM-41 type mesoporous silicas and evaluated them for CO_2 capture at different temperatures from 60 °C to 120 °C. Mesoporous silica prepared at 100 °C i.e. MCM-41-100 showed CO_2 adsorption capacity of 0.66 and 14.7 mmol g^{-1} at 1 bar and 45 bar respectively at 25 °C. Pore-expanded mesoporous silica (PE-MCM-41), obtained by hydrothermal treatment of prepared MCM-41-100, was grafted with a triamine and was studied for CO_2 adsorption by gravimetric method from very low pressure up to 1 bar at four different temperatures. This grafted silica (TRI-PE-MCM-41) exhibited high CO_2 adsorption capacities of ca. 2.8 mmol g^{-1} at 25 °C and 1 bar and very small uptakes of N_2, CH_4 and H_2 showing high selectivity towards CO_2. CO_2 adsorption capacity of TRI-PE-MCM-41 was found to improve in the presence of moisture due to partial formation of bicarbonate in presence of moisture [66, 67].

Various mesoporous silica materials like MCM-41, MCM-48, SBA-15, SBA-16, and KIT-6 were impregnated with 50 wt% PEI followed by evaluation for CO_2 adsorption by thermogravimetric analyser. CO_2 adsorption performance of these impregnated silicas was strongly dependent on the pore size of mesoporous silica. KIT-6 having largest pores in 3D arrangement exhibited CO_2 uptake of 3.07 mmol g^{-1} and 1.95 mmol g^{-1} under pure CO_2 atmosphere and 5% CO_2 respectively at 75 °C whereas MCM-41 showed the lowest CO_2 uptake of 2.52 mmol g^{-1} under similar experimental conditions [68].

Chen et al. [69] reported CO_2 adsorption on PEI and tetraethylene penta amine (TEPA) impregnated monolithic silica. For 5% CO_2 feed stream, 65% PEI loaded monolith silica exhibited a maximum gravimetric adsorption capacity of 3.75 mmol g^{-1} at 75 °C outperforming PEI modified KIT-6 [68] under same conditions. TEPA modified monolith silica exhibited CO_2 adsorption capacity of 5.91 mmol g^{-1} at 75 °C under 100% CO_2 flow but it showed a steady decrease in adsorption capacity during a 5 run adsorption–desorption cycle.

Ma et al. [70] impregnated 50 wt% PEI on SBA-15 adsorbent and reported its CO_2 adsorption capacity of 3.18 mmol g^{-1} at 75 °C in 15% CO_2 atmosphere. Because of the larger pore diameter and pore volume of SBA-15 than MCM-41, PEI modified SBA-15 adsorbent used the amine groups more efficiently under the same loading of 50 wt% PEI and hence had much higher

CO_2 adsorption capacity than PEI modified MCM-41 adsorbent. Sanz et al. [71] studied CO_2 adsorption at 45 °C on branched PEI impregnated on SBA-15 silica by single component adsorption isotherms. CO_2 adsorption capacity increased with amine content but specific efficiency per unit PEI content decreased. Maximum static CO_2 adsorption capacity of ~2 mmol g^{-1} was shown by 70 wt% PEI impregnated SBA-15 at 45 °C and 1 bar.

2.2.3 Carbon based adsorbents

Carbon based adsorbents have been considered as potential CO_2 adsorbents because of their well-developed porous structures, high adsorption capacities, fast kinetics, easy regeneration and high thermal and chemical stability. Furthermore, they can be obtained from large variety of widely available low cost sources [72-74]. Various carbon based adsorbents are activated carbons, carbon molecular sieves [75-77] and carbon nanotubes (CNT) [78]. Large variety of activated carbons have been synthesized from a variety of materials like coal, industrial byproducts, wood or biomass sources etc. and have been evaluated for CO_2 adsorption [79, 80].

2.2.3.1 Commercial activated carbons

Various commercial activated carbons available have been evaluated for CO_2 capture by various research groups under different evaluation conditions. Na et al. [81] evaluated commercial activated carbon for CO_2 capture under pressure swing adsorption process and reported equilibrium adsorption capacity of 3.2 and 1.6 mmol g^{-1} at 15 °C and 55 °C respectively at 1 bar under pure CO_2 flow. MAXSORB activated carbon showed static equilibrium CO_2 adsorption capacity of 25.7 mmol g^{-1} at 30 bar and 25 °C [82]. In another work, CO_2 adsorption isotherms on Ajax activated carbon were carried out at three different temperatures at a pressure up to 0.2 bar. As adsorption temperature increased from 25 °C to 100 °C, volumetric CO_2 adsorption capacity was found to decrease significantly from around 0.75 to 0.11 mmol g^{-1} [83].

2.2.3.2 Carbon adsorbents from renewable resources

In the recent time, porous carbons have been produced by direct carbonization and/or activation of various waste materials and biomass residue like fly ash, rice husk, carpet waste, coconut shell, cellulose etc. because of their easy availability and evaluated for CO_2 capture. Highly porous carbons were obtained from carbonization and subsequent chemical activation with

potassium hydroxide (KOH) of waste celtuce leaves. They exhibited surface area of 3404 m^2 g^{-1} and equilibrium CO_2 uptake of 4.36 mmol g^{-1} at 1 bar pressure and 25 °C [84].

Fly ash derived carbons were impregnated with organic bases like polyethyleneimine (PEI) aided by polyethylene glycol, tetraethylene-pentaamineacrylonitrile (TEPAN) and diethanolamine (DEA). These materials exhibited CO_2 uptake of 0.91–1.3 mmol g^{-1} at 75 °C in pure CO_2 flow [85]. In another work, fly ash carbons were steam activated prior to amine impregnation to improve the textural properties. Activated fly ash samples were impregnated with 3 different amine solutions i.e. MEA, DEA, and MDEA followed by CO_2 capture performance evaluation at various temperatures. Impregnation lead to decrease in the specific surface area of the carbons by blocking of the pores. At 30 °C, MEA impregnated carbon showed the highest CO_2 uptake of 1.56 mmol g^{-1} as compared to parent activated fly ash carbon (0.95 mmol g^{-1}). At higher adsorption temperatures, all the impregnated samples demonstrated higher CO_2 uptakes than parent activated carbon due to chemical adsorption of CO_2 on carbon materials [86].

Plaza et al. [87] developed activated carbons from biomass residue i.e. olive stones by CO_2 activation and treatment with ammonia (NH_3). CO_2 activated carbons showed CO_2 uptake of 2.4 mmol g^{-1} and 0.7 mmol g^{-1} under 100% CO_2 atmosphere at 25 °C and 100 °C respectively. On the other hand, NH_3 treated carbons exhibited CO_2 capacities of 1.9 mmol g^{-1} and 0.6 mmol g^{-1} at 25 °C and 100 °C respectively. Later on, they reported almond shell based activated carbons obtained from activation with CO_2 having CO_2 adsorption capacity of 1.2 mmol g^{-1} in binary mixture of 15% CO_2 in N_2 and 2.6 mmol g^{-1} under 100% CO_2 atmosphere at 25 °C. Aminated almond shells based carbons, having maximum 4.5% nitrogen content, showed CO_2 uptake of 1.1 and 2.2 mmol g^{-1} under 15% and 100% CO_2 flow respectively at 25 °C [88].

Thote et al. [89] synthesized nitrogen enriched carbons from soybean by chemical activation with zinc chloride followed by physical activation with CO_2. Specific surface area of the prepared carbon was comparable to that of commercial activated carbon but it exhibited better dynamic CO_2 adsorption capacity (0.51 mmol g^{-1}) than that of the commercial carbon (0.36 mmol g^{-1}) at 75 °C under 15.4% CO_2 concentration. This is attributed to the basic character of the adsorbent because of presence of nitrogen functionality in the carbon matrix. This adsorbent showed stable cyclic capacity for adsorption at 30 °C but could not be regenerated completely in the second cycle for adsorption at 75 °C thereby showing zero adsorption in the next cycle.

Carbon adsorbents were obtained from carbonization and activation with KOH of waste carpet materials. Type of precursor used and activation conditions have a strong effect on the porous properties and CO_2 uptake of the carbons. Maximum CO_2 uptake of 3.13 mmol g^{-1} at 30 °C under 100% CO_2 flow was achieved but it reduced drastically to 0.7 mmol g^{-1} with rise in adsorption temperature to 100 °C. CO_2 uptake achieved, under 15% CO_2 concentration, was 0.89 mmol g^{-1} and 0.16 mmol g^{-1} at 25 °C and 100 °C respectively [90].

In another work, porous carbons were produced from hydrothermal carbonization and chemical activation with KOH of polysaccharides (starch and cellulose) and biomass (sawdust). These carbons showed static CO_2 adsorption capacity of 4.8 mmol g^{-1} at 25 °C and 3.6 mmol g^{-1} at 50 °C at 1 bar pressure. A very fast adsorption kinetics, with 95% uptake in around 2 minutes, and selectivity of CO_2/N_2 = 9 (from single component isotherms) were observed for these carbons [91].

2.2.3.3 Carbon adsorbents from synthetic polymers

In addition to the conventionally available activated carbons and waste material or biomass derived carbons, synthetic polymers have been used extensively these days as polymeric precursor for producing porous carbon materials as they help in tuning their pore structure, morphology and allows better control over their chemical properties and hence surface chemistry. Various methods used for synthesizing porous carbons include carbonization of carbon-containing precursor, sol-gel process, chemical vapor deposition and nanocasting or templating method. Generally expensive reagents, large amount of organic solvents and complex synthesis steps are involved in these techniques. Moreover obtaining carbon materials with controlled pore structures, from conventional activation techniques, becomes a big challenge because of complexity of carbon structure evolution. However, use of nanocasting technique can help in overcoming these drawbacks [92, 93]. In this part, literature study on porous carbons has been divided into two groups based on synthesis process (a) template free synthesis i.e. by carbonization and/or activation of carbon-containing polymer, and (b) templating method i.e. by nanocasting technique.

2.2.3.3.1 Template free synthesis

Drage et al. [94] prepared nitrogen containing carbons from urea-formaldehyde (UF) and melamine-formaldehyde (MF) resins by chemical activation with potassium carbonate. CO_2

uptake on these carbons was studied by thermogravimetry and was found to depend on both their textural properties and surface chemistry. UF and MF based carbons showed CO_2 uptake of 1.86 and 1.03 mmol g^{-1} at 25 °C under pure CO_2 respectively.

Hao et al. [95] synthesized nitrogen doped carbons from direct pyrolysis of resorcinol and formaldehyde in the presence of amino acid L-lysine as catalyst. CO_2 uptake of these carbons, determined volumetrically, was found to be 3.13 mmol g^{-1} at 25 °C and 0.62 mmol g^{-1} at 120 °C under 100% CO_2 flow at 1 bar.

Sevilla et al. [96] prepared N-doped carbons from chemical activation of polypyrrole (PPy) and investigated the effect of activation conditions on the CO_2 uptake. Mildly activated carbon (KOH/PPy = 2) obtained at 600 °C showed high static CO_2 uptake of 6.2 mmol g^{-1} at 0 °C but its capacity decreased drastically to 3.9 mmol g^{-1} and 2.1 mmol g^{-1} with increase in temperature to 25 °C and 50 °C respectively. Whereas severely activated carbons (KOH/PPy = 4) exhibited the equilibrium CO_2 capacity up to 2.1–2.6 mmol g^{-1} at 25 °C and 1 bar. Large number of nitrogen functional groups (pyridonic-N and pyridinic-N) and narrower microporosity in mildly activated carbons than severely activated carbons caused higher CO_2 uptake by former.

In another study, nitrogen containing nanoporous carbon was prepared from polypyrrole by chemical activation with sodium hydroxide. It demonstrated narrow microporosity and high nitrogen content up to 7 wt% along with high surface area of 2169 m^2 g^{-1}. CO_2 uptake was determined volumetrically and maximum static CO_2 equilibrium capacity of ca. 4 mmol g^{-1} at 25 °C and 1 bar was achieved [97].

Liu et al. [98] synthesized nitrogen enriched carbons from by carbonization and chemical activation with KOH of urea-formaldehyde resin. Highest equilibrium CO_2 capacity was found to be 3.21 mmol g^{-1} at 25 °C and 1.27 mmol g^{-1} at 75 °C. It was found that microporosity of the material is not the only factor affecting the CO_2 adsorption performance but the presence of the heteroatoms also play an important role. In another work, they used urea and furfural as precursors to develop N-doped carbons by carbonization and subsequent chemical activation with KOH. These materials also demonstrated high nitrogen content and microporosity thereby having equilibrium CO_2 uptake of 4.6 mmol g^{-1} at 25 °C and 1 bar [99].

Synthetic activation carbon (F50) was prepared by carbonization followed by steam activation of mixture of coal tar pitch and furfural. It exhibited microporous structure and basic character due to presence of various oxygen functionalities on the surface. Dynamic CO_2 adsorption capacity of F50 was investigated by breakthrough column study and capacity was found to be 0.61 mmol g^{-1} at 30 °C under 15% CO_2 concentration. Its capacity decreased to ca. 0.30 mmol g^{-1} and 0.15 mmol g^{-1} on increasing the adsorption temperature to 50 °C and 75 °C respectively [100].

Tseng et al. [101] prepared highly porous carbons from steam activation of melamine modified phenol-formaldehyde resin for CO_2 capture. Very high equilibrium CO_2 uptake of 6.71 mmol g^{-1} was achieved at 0 °C and 1 bar but it decreased drastically to 2.2 mmol g^{-1} and 0.4 mmol g^{-1} with increase in adsorption temperature to 25 °C and 50 °C respectively.

2.2.3.3.2 Carbons from nanocasting technique

Nanocasting is a powerful technique for the fabrication of hierarchical mesoporous carbon materials whose synthesis by conventional processes is challenging. It involves three steps: (i) infiltration of suitable carbon precursor into the template pores, (ii) heat treatment under controlled atmosphere and (iii) removal of template by selective dissolution [92, 102]. Hence, the space formerly occupied by template is consequently transferred into the pores in the resulting carbon materials, and the carbon precursor in the pores of the template becomes the continuous carbon framework [103, 104]. Fabrication by this technique takes place in the confined nanospaces, provided by the template pores, hence sintering of the particles is restricted and formation of nanostructures is accomplished. Although high temperatures are involved in this technique, porous structure of the prepared carbons can be tailored depending on the template's pore characteristics. Choice of suitable precursor is also important for carbon material synthesis as it governs their surface chemistry. Various thermally stable carbon sources that have been used include sucrose, phenolic resins, furfuryl alcohol etc. Using carbon precursors, having high nitrogen content, such as urea-formaldehyde resin, melamine-formaldehyde resin, acrylonitrile, acetonitrile etc. for nanocasting technique will incorporate nitrogen functionalities in the carbon matrix thereby enhancing basic character of the carbons and interaction between carbon surface and acidic CO_2 molecules. Xu et al. reported [105] the synthesis of mesoporous carbons by nanocasting technique with sucrose as the carbon source and nano-$CaCO_3$ as hard template. They studied the effect of template to precursor ratio on the textural properties and capacitance of the prepared materials.

Pevida et al. [106] developed nitrogen enriched carbons from melamine-formaldehyde resin and fumed silica by nanocasting technique. Porous carbon obtained at 600 °C showed highest CO_2 uptake of 1.41 mmol g^{-1} and 2.25 mmol g^{-1} under 15% and 100% CO_2 flow respectively at 25 °C. These values were higher than capacities of commercial activated carbon. Carbonization above 600 °C affected the chemistry of the materials and a decrease in the basic character of the carbon was observed. This lead to the reduction in CO_2 uptake of MF derived carbons obtained at 700 °C despite their best textural properties. Hence, both textural parameters and surface chemistry have an effect on the CO_2 capture performance of the adsorbents.

Sevilla et al. [107] prepared mesoporous carbons by nanocasting technique followed by chemical activation with KOH. Furfural alcohol was used as the carbon source and two different types of mesostructured silica (hexagonally ordered SBA-15 and cubic ordered KIT-6) were used as hard templates. Activated carbons obtained from both the silicas exhibited similar static CO_2 capacity of ca. 3.2 mmol g^{-1} and 2.0 mmol g^{-1} at 25 °C and 50 °C respectively at 1 bar.

In another work, nitrogen-doped carbons were obtained by using IBN-9 mesoporous silica template by nanocasting technique with subsequent chemical activation with KOH at 600 °C. Two different precursors were used in this work (i) p-diaminobenzene, and (ii) combination of p-diaminobenzene and furfural alcohol. Chemical activation improved the textural properties of both the prepared carbons with maximum micropore area reaching a value of 890 m^2 g^{-1}. Equilibrium CO_2 uptake achieved was ca. 4.5 mmol g^{-1} at 25 °C and 1 bar attributing to microporous structure and high nitrogen doping levels [108].

Li et al. [109] synthesized carbon nitride spheres by using ethylenediamine and carbon tetrachloride as precursors and spherical mesoporous cellular silica foams as hard template via nanocasting technique. Highly mesoporous structure with specific surface area of 550 m^2 g^{-1} and high nitrogen content of 17.8 wt% was obtained by this approach. The prepared carbon materials showed CO_2 uptake of 2.9 mmol g^{-1} and 0.97 mmol g^{-1} at 25 °C and 75 °C respectively under pure CO_2 flow.

In another study, mesoporous carbon nitride materials were obtained by polymerization of ethylenediamine and carbon tetrachloride in the pores of mesoporous silica FDU-12 followed by carbonization at 600 °C for 5 h. At 25 °C, these materials showed static equilibrium adsorption capacity of 1.4 mmol g^{-1} and 5.9 mmol CO_2 per g of adsorbent at 1 bar and 30 bar pressure respectively [110].

2.2.3.4 Carbon nanotubes

Carbon nanotubes are a new class of materials having well defined pore structure along with thermal and chemical stability. A wide range of surface functional groups can be achieved by thermal or chemical treatments thereby making them potential candidates for CO_2 capture [111, 112]. These include single-walled carbon nanotubes (SWCNTs) and multi-walled carbon nanotubes (MWCNTs) modified with amine solutions. CO_2 adsorption was carried out on purified SWCNTs in the temperature range of 0-200 °C [78]. SWCNTs had a high surface area of 1587 m^2 g^{-1} and a total pore volume of 1.55 cm^3 g^{-1}. The CO_2 adsorption capacity of SWCNTs was ~4.1 mmol g^{-1} against ~2.2 mmol g^{-1} of activated carbon at 35 °C and 1 bar.

Multi-walled carbon nanotubes (MWCNTs) impregnated with 3-aminopropyltriethoxysilane (APTS) showed dynamic CO_2 adsorption capacity of 0.93 and 2.2 mmol g^{-1} at 25 °C under 10% and 50% CO_2 flow respectively [113]. Su et al. [114] also impregnated MWCNTs with APTS and reported CO_2 adsorption capacity of 2.25 and 3.0 mmol g^{-1} under 15% and 50% CO_2 flow respectively at 25 °C.

Ye et al. [115] impregnated TEPA onto commercially available MWCNTs and evaluated them for CO_2 adsorption by fixed-bed experiments. 30 wt% TEPA modified CNTs exhibited CO_2 adsorption capacity of 2.97 and 3.56 mmol g^{-1} at 25 °C and 40 °C respectively under 2% CO_2 flow.

It can be concluded from the literature review that most of the carbon development in the field of CO_2 capture has been carried out by direct carbonization and/or activation of either waste materials or synthetic polymers followed by CO_2 adsorption study under static conditions leading to no control on surface chemistry and pore structure respectively. For the control of these two parameters, development of carbon adsorbents by nanocasting technique have been used by very few research groups and among them also majority of them evaluated these materials at room temperature under static flow conditions which does not present the real

picture in flue gas application. For practical adsorption systems, dynamic CO_2 adsorption performance of the carbon adsorbents needs to be evaluated and further work is required to address several important characteristics like adsorption kinetics, prediction of mixed-gas adsorption equilibria, selectivity, and long-term stability of adsorbents under simulated flue gas conditions.

Chapter 3 – Experimental Methods, Kinetics and Isotherm Models

3.1 Materials

Mesoporous silica (MCM-41 type) having trade name of CTF-04S was procured from M/s Tianjin Chemist Scientific Ltd., Tianjin, China. It had specific surface area of 450 m^2 g^{-1} and average pore diameter of 3.5 nm. In the present work, it was used as hard template to obtain porous carbon materials by nanocasting technique.

Melamine, formaldehyde solution (37% w/v), resorcinol, sodium hydroxide pellets, concentrated sulphuric acid, hydrochloric acid (35% concentration), di-sodium tetra borate (borax), potassium carbonate, methanol and acetone were purchased from M/s S. D. Fine Chemicals India Ltd. All the reagents and chemicals were of analytical grade and were used without any further purification.

Grade-1 (99.999% pure) dry helium, dry nitrogen and dry carbon dioxide gases were purchased from M/s Sigma Gases and Services, India.

3.2 Characterization techniques

3.2.1 Surface area and pore size distribution

The surface area and pore volume of the carbon adsorbents were determined by using a static volumetric analyzer (Model ASAP 2010, Micromeritics, USA) with N_2 adsorption isotherms at -196 °C. The samples were degassed at 220 °C under vacuum for 6 h before any adsorption measurements. Multipoint adsorption method was employed to obtain the results of Brunauer–Emmett–Teller (BET) surface area. Total pore volume (V_P) of the prepared carbons was assessed from the amount of N_2 adsorbed at a relative pressure of 0.99 and micropore volume was estimated from t-plot method. The mesopore volume and pore size distribution were derived from the adsorption branch of isotherm by using the Barrett–Joyner–Halenda (BJH) model.

3.2.2 X-ray diffraction analysis

Structural characterization of the samples was carried out by recording their powder X-ray diffraction patterns using X'Pert Pro diffractometer (Model X'Pert Pro, PANalytical, Almelo, Netherlands), operated at 45 kV and 40 mA with monochromatic Cu–Kα radiation (λ = 1.5406 Å), in the 2θ range of 10–80°.

3.2.3 Transmission electron microscopy

Transmission electron micrographs of prepared carbons were recorded on a transmission electron microscope (Model CM200, Philips, Netherlands) operated at an accelerating voltage of 200 kV. Samples for TEM measurements were prepared by placing a drop of the dispersion of carbon adsorbent in toluene on carbon-coated copper grid. The toluene was allowed to evaporate slowly at room temperature.

3.2.4 Scanning electron microscopy

The surface morphology of the synthesized carbon adsorbents was observed on a scanning electron microscope (Model JSM-6510 LV, JEOL, Japan) at an accelerating voltage of 10.0 kV. In order to avoid charging of samples under electron beam, samples were coated with gold film (of 50 µm thickness) in an automatic sputter coater (Polaron) prior to SEM studies.

3.2.5 Thermal analysis

3.2.5.1 Thermogravimetric analysis (TGA)

Thermal stability of the synthesized adsorbents was evaluated by using a thermogravimetric analyzer (TA Q500, TA Instrument, USA). In a typical experiment, about 10 mg of sample was heated from 30 °C to 900 °C at a heating rate of 10 °C min^{-1} under dry nitrogen at a flow rate of 50 cm^3 min^{-1}.

3.2.5.2 Differential scanning calorimetry (DSC)

A differential scanning calorimeter (NETZSCH DSC 200F3, Netzsch-Geratebau GmbH, Germany) was used to measure the specific heat capacity of the prepared carbons. Around 10 mg of the sample was heated at 10 °C min^{-1} under N_2 flow from room temperature to 300 °C.

3.2.6 Elemental composition

The elemental composition of the carbon adsorbents was determined using a Flash EA 1112 Series elemental analyzer (Thermo Finnigan, Italy). Oxygen content of the samples was

obtained by difference. The nitrogen content of the materials was also estimated by Kjeldahl method [89].

3.2.7 Fourier transform infrared (FTIR) spectroscopy

Fourier transform infrared (FTIR) spectra of mesoporous carbons were recorded on a Perkin Elmer Spectrum 100 FTIR spectrometer (Perkin Elmer, USA) fitted with universal ATR sampling accessories. The spectra were recorded in the range of 4000–650 cm^{-1} with a resolution of 4 cm^{-1}.

3.2.8 X-ray photoelectron spectroscopy

X-ray photoelectron spectroscopy (XPS) analysis of porous carbons was performed on a SPECS system equipped with a hemispherical electron analyzer with an Mg Kα X-ray source to analyze the surface chemistry of the prepared carbons. The survey spectra were recorded with a pass energy of 50 eV while the high resolution spectra with a pass energy of 20 eV at operating at an anode potential of 15 kV and emission current of 10 mA. The pressure in the analysis chamber was less than 2×10^{-9} torr. The data processing was carried out with XPS peak 4.1 software and the core level spectra were fitted with mixed Gaussian-Lorentzian convoluted function (80/20) and Shirley function was used for background subtraction

3.2.9 Surface basicity by Boehm titration

Surface functional groups of the carbon adsorbents were determined by Boehm titration [116, 117]. 200 mg of each adsorbent was placed in 20 ml of 0.1 N solutions of sodium hydroxide (NaOH) and hydrochloric acid (HCl). The flasks were sealed and shaken for 24 h and then filtered. The excess base or acid of the filtrate was titrated with HCl or NaOH, respectively. The number of basic sites was estimated from the amount of HCl that reacted with the adsorbent and the number of acidic sites was calculated from the amount of sodium hydroxide that reacted with the adsorbent.

3.2.10 Temperature programmed desorption

Carbon dioxide temperature programmed desorption (CO_2-TPD) study of prepared carbons was carried out on a Micromeritics AutoChem II 2920 chemisorption analyzer equipped with a thermal conductivity detector. Around 100 mg of the carbon sample was placed in a quartz reactor and pretreated under flow of pure helium gas at 200 °C. Hereafter the temperature was decreased to 30 °C and CO_2 adsorption was carried out by switching to pure CO_2 gas for 30

minutes. Desorption experiment was performed by switching back to He gas at a flow rate of 20 cm^3 min^{-1} and increasing the temperature from 45 °C to 250 °C at a heating rate of 10 °C min^{-1}.

3.3 Performance evaluation of adsorbents

3.3.1 Fixed-bed adsorption study setup

A fixed-bed adsorption study set up was used to evaluate the dynamic CO_2 adsorption-desorption performance of the prepared carbon adsorbents. Figure 3.1 shows the schematic representation of the experimental setup used in the present study and Figure 3.2 shows the actual adsorption study set up coupled with gas chromatograph. The experimental setup consists of gas mixing section, adsorption column, and an online gas chromatograph. Gas mixing section consists of mass flow controllers, pre-mixer and non-return valves. Two mass flow controllers (Bronkhorst, Netherlands), each for CO_2 and N_2, are used to regulate the feed CO_2 concentration by controlling the flow rates of pure nitrogen and carbon dioxide gases entering the mixing chamber (100 mm length and 9.39 mm internal diameter) made up of stainless steel. Then the gas mixture (simulated flue gas) is passed through the adsorption bed. The gas mixture can also be directly bypassed to the gas chromatograph for the inlet concentration measurement of the gas mixture entering the adsorption column.

Adsorption column is a fixed-bed reactor (length = 300 mm and internal diameter = 9.39 mm) made up of stainless steel and is enclosed in a temperature-controlled oven. Adsorbent bed temperature is monitored by a K type thermocouple placed in the middle of the bed. Temperature controller is used to control the bed temperature for adsorption and desorption.

At the end of the adsorption column, a gas chromatograph (GC 7890A, Agilent Technologies, US) is used to periodically monitor the CO_2 and N_2 concentrations. Fused silica capillary column of 30 m length having inner diameter of 0.32 mm and 20 μm film thickness of polystyrene divinylbenzene (HP Plot Q, Agilent Technologies, USA) is used for the analysis. The gas chromatograph is operated at an injection temperature of 180 °C, oven temperature of 60 °C and detector temperature of 200 °C with helium as the carrier gas.

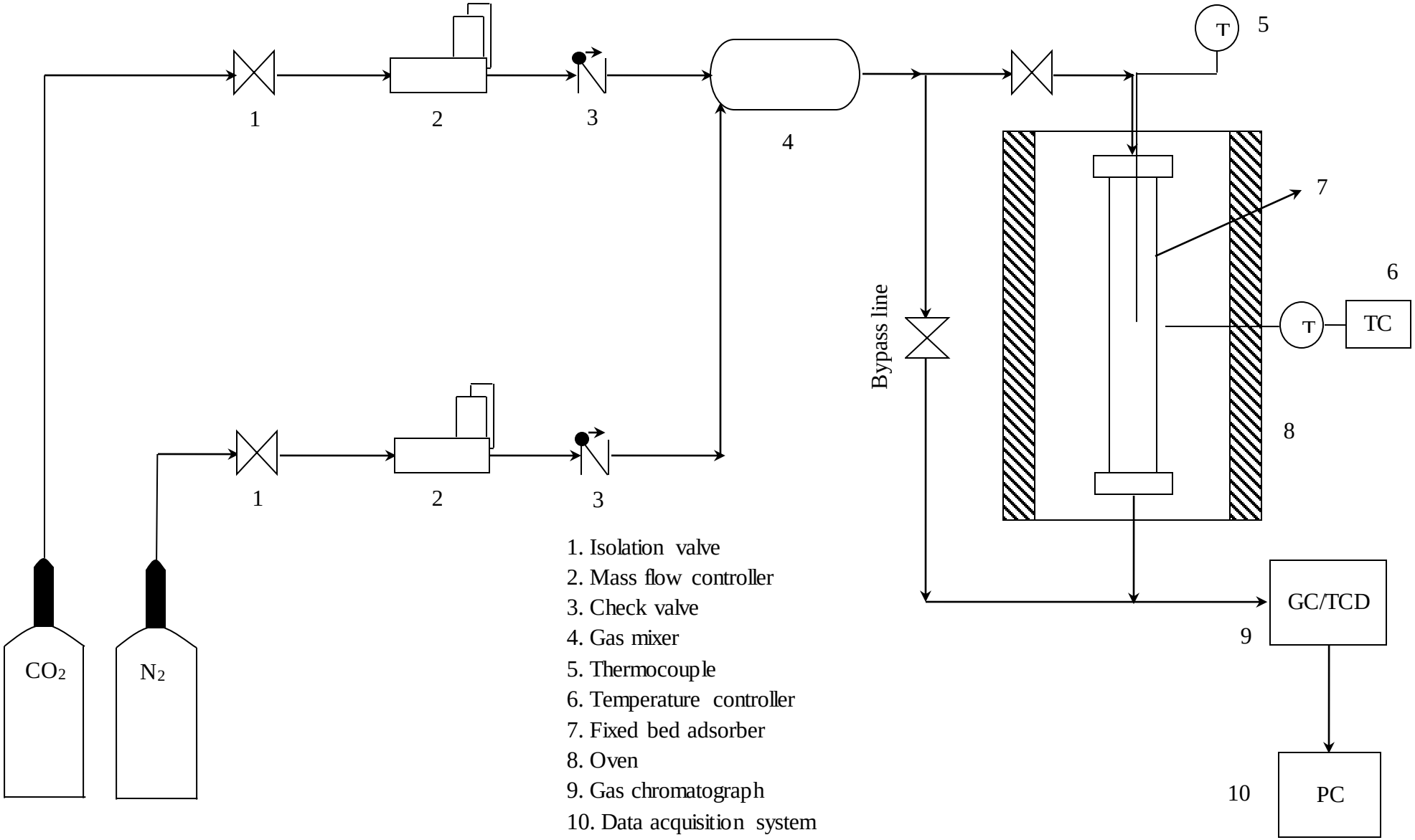

Figure 3.1 Schematic diagram of the experimental setup

Figure 3.2 Adsorption study set up coupled with gas chromatograph

3.3.2 Dynamic CO_2 adsorption measurements

Adsorbent evaluation in fixed-bed system included both CO_2 adsorption and desorption experiments. In a typical experiment, about 2 g of dry adsorbent, mixed with dry inert glass beads, is packed into the adsorption bed. A layer of glass wool is used at the bottom to support the adsorbent bed. Before CO_2 adsorption study, the adsorbent is pretreated at 200 °C in N_2 atmosphere for 2 h to remove moisture or any other adsorbed gases. Hereafter adsorbent column is cooled down to the desired adsorption temperature (30, 50, 75 and 100 °C). Adsorption runs are carried out by feeding the reactor bed with a gas stream, consisting of N_2 and CO_2, at 80 cm^3 min^{-1} (evaluated at temperature (T) = 20 °C and pressure (P) = 1 atm), with varying CO_2 volumetric concentrations ranging from 5% to 12.5%. The CO_2 concentration at the bed exit is monitored as a function of time until the outlet CO_2 concentration approached the inlet CO_2 concentration i.e., until the saturation is reached. The adsorbed CO_2 is completely desorbed by switching the gas to pure N_2 and raising the bed temperature to 200 °C. The adsorbent is subjected to four consecutive adsorption-desorption cycles.

The CO_2 adsorption capacity (q_t) in milli moles per gram (mmol g^{-1}) of the adsorbent at a certain time, t (min) is estimated as follows:

$$q_t = \frac{1}{M}\int_0^t Q(C_o - C)dt \quad (3.1)$$

where Q (cm^3 min^{-1}) is the volumetric gas flow rate, M (g) is the mass of the adsorbent, and C_o and C are the inlet and effluent CO_2 concentrations (percent in volume) respectively. Equilibrium adsorption capacity of adsorbents is obtained by integrating equation (1) from time t = 0 to equilibrium time t_e when C reaches C_o. Response time of this fixed-bed adsorption study set up was estimated to be ca. 15.6 seconds.

3.3.3 Equilibrium sorption measurements

Equilibrium adsorption-desorption experiments of pure CO_2 and N_2 were carried out on a volumetric analyzer (ASAP 2010, Micromeritics, USA) at four different adsorption temperatures ranging from 30–100 °C and pressure varying from 0 to 1 atm. Temperature for adsorption was achieved by using a Dewar, having a circulating jacket and is connected to a thermostatic bath. Before each adsorption experiment, carbon samples were outgassed at 200 °C for 12 h under vacuum.

3.4 Kinetic study

Adsorption kinetics of the prepared carbons need to be studied in order to evaluate their separation efficiency and ability to endure high flow of adsorbate. It is also required for the rational design and simulation of gas-treating systems. Three kinetic models namely pseudo-first order, pseudo-second order and fractional order kinetic models have been employed in this work to investigate the kinetics of CO_2 adsorption onto prepared carbon adsorbents.

3.4.1 Pseudo-first order model

The pseudo-first order adsorption model of Lagergren is one of the most commonly used kinetic model illustrating kinetics on the basis of adsorption capacity. Lagergren's first order kinetic model can be expressed as [118]:

$$\frac{dq_t}{dt} = k_1(q_e - q_t) \quad (3.2)$$

where q_t (mmol g^{-1}) is amount adsorbed at time t (minutes), q_e (mmol g^{-1}) is the amount adsorbed at equilibrium and k_1 (min^{-1}) is the pseudo-first order model rate constant. The integration of Eq. (3.2) with initial conditions ($q_t = 0$ at $t = 0$ and $q_t = q_t$ at $t = t$) gives the following form:

$$log\frac{q_e}{q_e - q_t} = \frac{k_1}{2.303}t \tag{3.3}$$

which can be rearranged to:

$$q_t = q_e(1 - e^{-k_1 t}) \tag{3.4}$$

3.4.2 Pseudo-second order model

Pseudo-second order model was given by Ho et al. [119] and is based on the assumption of proportionality of adsorption capacity to the number of occupied sites on the adsorbent surface. It can be written as:

$$\frac{dq_t}{dt} = k_2(q_e - q_t)^2 \tag{3.5}$$

where k_2 (g $mmol^{-1}$ min^{-1}) is the rate constant of pseudo-second order kinetic model. Integrating Eq. (3.5) for above stated boundary conditions leads to the following equation:

$$\frac{1}{q_e - q_t} = \frac{1}{q_e} + k_2 t \tag{3.6}$$

which can be rearranged to

$$q_t = \frac{k_2 q_e^2 t}{1 + k_2 q_e t} \tag{3.7}$$

3.4.3 Fractional order model

The fractional order kinetic model is based on the assumption that adsorption rate is influenced by n^{th} power of driving force and m^{th} power of the adsorption time [120, 121] and is given by Eq. (3.8):

$$\frac{dq_t}{dt} = k_n(q_e - q_t)^n t^{m-1} \tag{3.8}$$

where k_n is the rate constant of fractional order kinetic model with model parameters *m* and *n*. Eq. (3.8) reduces to pseudo-first order or pseudo-second order kinetic models for *m = 1* and *n = 1 or 2*, respectively. Its integrated form under the given boundary condition is:

$$q_t = q_e - \frac{1}{\left[\left((n-1)\,k_n/m\right)t^m + \left(1/q_e^{n-1}\right)\right]^{1/n-1}} \tag{3.9}$$

Generally, pseudo-first order and pseudo-second order kinetic models have been solved by linear regression method in order to identify the best fitted kinetic model. It is found that pseudo-second order kinetic equation has four different linear forms with each form leading to different values of the model parameters. When non-linear form of the model is linearized, there is a change in the error structure which results in different parameter values. Therefore, suitable way of solving these kinetic models is to use non-linear regression method [122-124]. OriginPro 8 software was used to obtain kinetic model parameters by nonlinear regression on experimental data.

3.4.4 Error calculation

Additionally, an error function (*Error %*) on the basis of normal standard deviation was evaluated to find the appropriateness of each kinetic model. This error function provides the constancy between the experimental data and values predicted by kinetic models.

$$Error\,(\%) = \sqrt{\frac{\sum\left[\left(q_{t,exp} - q_{t,pred}\right)/q_{t,exp}\right]^2}{N-1}} \times 100 \tag{3.10}$$

where $q_{t,exp}$ and $q_{t,pred}$ are the amounts of CO_2 adsorbed at a given time *t* determined experimentally and model predicted respectively and *N* is the total number of experimental points.

3.4.5 Activation energy

Dependence of kinetic rate constants (*k*) with adsorption temperature can be explained by Arrhenius equation:

$$k = Ae^{-(E_a/RT)} \tag{3.11}$$

where A is the pre-exponential factor of Arrhenius equation and E_a (J mol^{-1}) is the activation energy. The plot between *ln (k)* and *1/T* is a straight line with slope $-E_a/R$ and hence the activation energy for CO_2 adsorption can be calculated from the slope of Arrhenius plot.

3.5 Isotherm study

One of the important parameters for designing an adsorption system is the equilibrium data. Equilibrium is achieved when adsorbate-containing phase is allowed to come in contact with the adsorbent for sufficient period of time and the bulk adsorbate concentration is in dynamic balance with the interface adsorbate concentration. This data is explained by an isotherm model having certain parameters that describe the adsorbent's affinity towards the adsorbate and the surface properties. Many well established adsorption isotherm models are used to fit the equilibrium data at a specific temperature over a wide range of adsorbate concentration. For designing practical adsorption systems, data of both pure and multicomponent adsorption equilibria are required over a varied temperature and pressure range.

3.5.1 Pure component isotherm

In the present study, equilibrium adsorption data of pure components on prepared carbons were correlated with three isotherm models, namely Langmuir, Sips and dual-site Langmuir adsorption isotherm models.

3.5.1.1 Langmuir isotherm model

Langmuir isotherm is the most widely used adsorption isotherm model. It describes monolayer adsorption on finite number of localized adsorption sites, with each site being identical and energetically equivalent and holding only one adsorbate molecule. It also assumes no interaction between the adsorbed molecules [125]. The Langmuir isotherm model can be expressed as:

$$q_e = \frac{q_m b P}{1 + bP} \tag{3.12}$$

where q_e (mmol g^{-1}) is the equilibrium adsorption capacity, q_m (mmol g^{-1}) is the maximum monolayer capacity, b (atm^{-1}) is the Langmuir parameter related to free energy of adsorption and P (atm) is the pressure. Parameter b is the measure of the affinity of the adsorbed molecules

to the solid adsorbent surface and its temperature dependence is explained by following Arrhenius type equation:

$$b = b_o e^{-(B/RT)} \tag{3.13}$$

where b_o is the adsorption affinity at reference temperature and B (J mol^{-1}) is the heat of adsorption.

3.5.1.2 Sips isotherm model

However, complex pure and surface structures of the adsorbent causes the heterogeneity of the adsorption process thereby hardly satisfying the assumptions of Langmuir isotherm model. Heterogeneity of adsorption process is an attribute of both the adsorbent and the adsorbate materials instead of adsorbent material only. Hence, some other empirical formulas like Sips or dual-site Langmuir (DSL) equations have been developed to explain the adsorption equilibria. Sips isotherm model is a three parameter adsorption isotherm model with parameters q_m, b and c and can be written as:

$$q_e = \frac{q_m b P^{1/c}}{1 + bP^{1/c}} \tag{3.14}$$

As compared to Langmuir isotherm model, it contains an additional parameter c which describes the system heterogeneity and could be caused by adsorbent, adsorbate or their combination. Value of c equal to 1 reduces Sips equation to Langmuir equation [44]. Parameter b is given same temperature dependence as that for Langmuir constant.

3.5.1.3 Dual-site Langmuir model

Another model for fitting pure component adsorption data is dual-site Langmuir isotherm model which describes the adsorption of pure component on an energetically heterogeneous adsorbent comprising of two homogeneous but energetically heterogeneous sites or patches. All the assumptions of the Langmuir isotherm model are applicable to each site with no interaction between the two sites [126]. Amount adsorbed by a component can be described by the following equation:

$$q_e = \frac{q_{1,m} b_1 P}{1 + b_1 P} + \frac{q_{2,m} b_2 P}{1 + b_2 P} \tag{3.15}$$

where $q_{1,m}$ and $q_{2,m}$ are the saturation capacities of the adsorbate at sites 1 and 2 respectively while b_1 and b_2 are the affinity parameters on sites 1 and 2 respectively and P is the total pressure. Hence, the total adsorbed amount is the sum of capacities at each site $(q_{1,m} + q_{2,m})$. Moreover, in the present study, saturation capacity for each component on each site is allowed to be different. Affinity parameters of DSL isotherm are also considered to be temperature dependent as shown in Eq. (3.16).

$$b_j = b_{o,j} e^{E_j/RT} \qquad j = 1, 2 \tag{3.16}$$

where subscript j refers to the energy level of site 1 or 2, $b_{o,j}$ is the adsorption affinity at reference temperature and E_j is the corresponding adsorption energy. In the above equation, $j = 1$ always denotes higher energy level while $j = 2$ always indicates lower adsorbent-adsorbate energy level. For pure component adsorption, site 1 is always considered as higher energy site as compared to site 2 [127].

3.5.1.4 Error calculation

Pure component adsorption equilibria for both CO_2 and N_2 were fitted by above mentioned three isotherm models by minimizing the sum of the squared relative errors (SSE) by using OriginPro 8 software. SSE is the relative difference between the adsorbed amounts determined experimentally and model predicted at all adsorption temperatures for a particular adsorbent-adsorbate pair and it can be expressed as:

$$SSE\ (\%) = \sqrt{\frac{\sum\left[\left(q_{e,exp} - q_{e,pred}\right)/q_{e,exp}\right]^2}{N-1}} \times 100 \tag{3.17}$$

where $q_{e,exp}$ and $q_{e,pred}$ are the experimental and model predicted amounts of adsorbate adsorbed respectively and N is the total number of data points.

3.5.2 Binary component isotherm

Prediction of multicomponent adsorption equilibria counts completely on the accuracy of pure component adsorption measurement and its reliable correlation with adsorption isotherm model. Adsorption equilibria of binary system (CO_2 and N_2) has been predicted from pure component adsorption isotherm parameters by using two approaches. In the first approach, pure component adsorption isotherm equations have been extended empirically to binary isotherms while the second approach includes usage of ideal adsorbed solution theory (IAST) to derive

binary system isotherms from pure component adsorption isotherms. Then these predicted isotherms are compared with the measured binary system isotherms.

3.5.2.1 Extended Sips isotherm model

The extended form of Sips isotherm model for N_C number of components is:

$$q_{e,i} = \frac{q_{m,i}\, b_i P_i^{1/c_i}}{1 + \sum_{j=1}^{N_C} b_j P_j^{1/c_i}} \tag{3.18}$$

where subscript i indicates the component for which isotherm is evaluated and $q_{e,i}$ is the equilibrium adsorption capacity of component i in the mixture.

3.5.2.2 Extended dual-site Langmuir isotherm model

Dual-site Langmuir equation for single component can be extended for multicomponent system as follows:

$$q_{e,i} = \frac{q_{1,m,i} b_{1,i} P_i}{1 + \sum_{j=1}^{N_C} b_{1,j} P_j} + \frac{q_{2,m,i} b_{2,i} P_i}{1 + \sum_{j=1}^{N_C} b_{2,j} P_j} \tag{3.19}$$

To correctly apply DSL isotherm to a multicomponent system, energetic site-matching issue needs to be addressed which mentions the fact that all the adsorbates present in a multicomponent system may not see sites 1 and 2 as high and low energy sites respectively. For a binary system, there is possibility of existence of four different adsorbate-adsorbent free energies corresponding to two free energies for component A (i.e. one on each adsorption site) and two free energies for component B. When sites 1 and 2 are considered as high and low energy sites by both the adsorbates, then their adsorbate-adsorbent free energies correlate in a perfect positive (PP) fashion. But for the case, when site 1 is considered as high free energy site by one component while low free energy site by second component and vice-versa for site 2, then adsorbate-adsorbent free energies correlate in a perfect negative (PN) fashion [126, 127]. For PP correlation for energetic site-matching in a binary system, amount adsorbed by each component (A and B) is given by:

$$q_{e,A} = \left(\frac{q_{1,m,A} b_{1,A} P_A}{1 + b_{1,A} P_A + b_{1,B} P_B}\right)_{site\ 1} + \left(\frac{q_{2,m,A} b_{2,A} P_A}{1 + b_{2,A} P_A + b_{2,B} P_B}\right)_{site\ 2} \tag{3.20}$$

$$q_{e,B} = \left(\frac{q_{1,m,B} b_{1,B} P_B}{1 + b_{1,B} P_B + b_{1,A} P_A}\right)_{site\ 1} + \left(\frac{q_{2,m,B} b_{2,B} P_B}{1 + b_{2,B} P_B + b_{2,A} P_A}\right)_{site\ 2} \tag{3.21}$$

In case of PN correlation for energetic site-matching, amounts adsorbed by component A and B are obtained by following expressions:

$$q_{e,A} = \left(\frac{q_{1,m,A} b_{1,A} P_A}{1 + b_{1,A} P_A + b_{2,B} P_B}\right)_{site\ 1} + \left(\frac{q_{2,m,A} b_{2,A} P_A}{1 + b_{2,A} P_A + b_{1,B} P_B}\right)_{site\ 2} \quad (3.22)$$

$$q_{e,B} = \left(\frac{q_{1,m,B} b_{1,B} P_B}{1 + b_{1,B} P_B + b_{2,A} P_A}\right)_{site\ 1} + \left(\frac{q_{2,m,B} b_{2,B} P_B}{1 + b_{2,B} P_B + b_{1,A} P_A}\right)_{site\ 2} \quad (3.23)$$

where $q_{e,A}$ and $q_{e,B}$ are the amounts adsorbed by components A and B in mixture. Only difference in Eqs. (3.20) and (3.22) and in Eqs. (3.21) and (3.23) is the ordering of the affinity parameter on each site.

3.5.2.3 Ideal adsorbed solution theory (IAST)

To predict binary system equilibria from pure component isotherm, another approach used in the present study is application of ideal adsorbed solution theory (IAST) to pure component adsorption isotherms. IAST is a well renowned technique, given by Myers and Prausnitz, for prediction of adsorption equilibria of a multi-component system using only pure component adsorption isotherms at the same temperature. IAST is a thermodynamic approach and is based on analogy of adsorption equilibria to Raoult's law for vapor-liquid equilibrium. It assumes the formation of an ideal solution by the adsorbed phase and the equilibrium between the ideal gas and adsorbed phase can be stated as [128-130]:

$$P y_i = P_i^0(\pi^*) x_i \quad (3.24)$$

where y_i and x_i are the molar fractions of component i in the gas phase and adsorbed phase respectively. P is the total pressure of the mixture and $P_i^0(\pi^*)$ is the equilibrium gas phase pressure of pure component i corresponding to solution temperature and solution spreading pressure, π^*. As compared to vapor-liquid equilibrium, presence of solid adsorbent in the adsorption system imposes an additional degree of freedom for equilibrium between the adsorbed phase and the gaseous phase which is denoted by spreading pressure [131]. Spreading pressure is an intensive variable and can be defined as the reduction in surface tension of the solid surface because of adsorbate spreading over the adsorbent surface [132]. Moreover, for an ideal solution no interactions should be present between the adsorbed molecules in the adsorbed phase with equal spreading pressure of each component at a given temperature.

Reduced spreading pressure (π_i^*) of component i in the standard state can be obtained from integration of Gibbs adsorption isotherm as follows:

$$\pi_i^* = \frac{\pi_i A}{RT} = \int_0^{P_i^0} \frac{q_i^*}{P_i} dP_i \tag{3.25}$$

where π_i^* and π_i are reduced spreading pressure and spreading pressure of component i in the adsorbed phase respectively, A is the specific surface area of the adsorbent, q_i^* is pure component adsorption isotherm equation and P_i^0 is the standard state pressure of pure component i corresponding to spreading pressure of the mixture. Standard state is defined as state at which reduced spreading pressure of the mixture (π^*) is the same as reduced spreading pressure for each component, i.e.

$$\pi_i^* = \pi^* \qquad i = 1, 2, 3 \ldots N_C \tag{3.26}$$

As there is no change in area on mixing for an ideal adsorbed mixture, total amount adsorbed (q_T) can be calculated from pure component loadings at standard state by using following equation:

$$\frac{1}{q_T} = \sum_{i=1}^{N_C} \frac{x_i}{q_i^0(P_i^0)} \tag{3.27}$$

where N_C is the number of species, $q_i^0(P_i^0)$ is the amount of pure component i adsorbed at standard state pressure P_i^0. Adsorbed amount of each component in the mixture can be calculated using the following expression:

$$q_i = x_i q_T \tag{3.28}$$

Following constraints of the mole fractions in the gas phase and adsorbed phase have to be considered while solving IAST equations:

$$\sum_{i=1}^{N_C} x_i = \sum_{i=1}^{N_C} y_i = 1 \tag{3.29}$$

Spreading pressure for each component has to be evaluated precisely for accurate predictions of the multicomponent system. For each component, equation (3.25) can be evaluated by specifying the pure component isotherm equation by fitting a continuous function to a discrete set of adsorption data obtained over a finite range of pressures.

3.5.2.4 IAST based Sips and dual-site Langmuir models

In the present work, IAST was used in conjunction with Sips and dual-site Langmuir isotherm equations. Equations for reduced spreading pressure of the adsorbed mixture (π^*), for IAST-Sips and IAST-DSL models, were obtained by substituting pure component Sips and DSL isotherm equations respectively in Eq. (3.25) followed by its integration. Eqs. (3.30) and (3.31) give the reduced spreading pressure for Sips and DSL models respectively.

$$\pi_i^* = q_{m,i} c_i \, ln\left(1 + b_i (P_i^0)^{1/c_i}\right) \tag{3.30}$$

$$\pi_i^* = q_{1,m,i} \, ln\left(1 + b_{1,i} P_i^0\right) + q_{2,m,i} \, ln\left(1 + b_{2,i} P_i^0\right) \tag{3.31}$$

The equations for reduced spreading pressure were then equated for each component and the expressions for Sips and DSL models are given by Eqs. (3.32) and (3.33) respectively.

$$q_{m,1} c_1 \ln\left(1 + b_1 \left(\frac{P_1}{x_1}\right)^{1/c_1}\right) = q_{m,2} c_2 \ln\left(1 + b_2 \left(\frac{P_2}{1 - x_1}\right)^{1/c_2}\right) \tag{3.32}$$

$$q_{1,m,1} \ln\left(1 + b_{1,1} \frac{P_1}{x_1}\right) + q_{2,m,1} \ln\left(1 + b_{2,1} \frac{P_1}{x_1}\right) = q_{1,m,2} \ln\left(1 + b_{1,2} \frac{P_2}{1 - x_1}\right) + q_{2,m,2} \ln\left(1 + b_{2,2} \frac{P_2}{1 - x_1}\right) \tag{3.33}$$

Above mentioned equations were then solved implicitly, by using MATLAB program, to calculate x_i and were used further to evaluate amount adsorbed by each component by using Eqs. (3.32) and (3.33).

3.5.2.5 Selectivity

In addition to prediction of equilibrium uptakes by these isotherm models, selectivity of CO_2 over N_2 $\left(S_{CO_2}\right)$ in the binary mixture was also predicted by using the following expression [133] and was compared with the experimental values obtained from breakthrough curves.

$$S_{CO_2} = \frac{x_{CO_2}/x_{N_2}}{y_{CO_2}/y_{N_2}} \tag{3.34}$$

where x_{CO_2} and x_{N_2} are the molar fractions of CO_2 and N_2 in the adsorbed phase respectively and y_{CO_2} and y_{N_2} are the molar ratios of CO_2 and N_2 in the gas phase respectively.

3.6 Thermodynamic study

3.6.1 Thermodynamic parameters

Thermodynamics of adsorption generally concentrates on three parameters i.e. Gibbs free energy, enthalpy and entropy. Analysis of these thermodynamic parameters explicates the behavior of adsorption process. The integral molar Gibbs free energy change for the adsorption process (ΔG) is the minimum amount of work required to load adsorbent to a certain level under an isothermal condition and can be obtained by using the following equation [134, 135]:

$$\Delta G = \frac{\Omega}{q} = -\frac{RT \int_0^P q \, d(\ln P)}{q} \tag{3.35}$$

where Ω is the surface potential (kJ mol^{-1}), R is the universal gas constant (kJ mol^{-1} K^{-1}), q is the amount of adsorbate adsorbed (mmol g^{-1}) and T is the temperature (K).

The integral molar enthalpy, ΔH (kJ mol^{-1}) indicates the heat effects associated with adsorption process and can be obtained from the fundamental thermodynamic relationships:

$$\Delta H = \frac{\left[\frac{\partial(\Omega/T)}{\partial(1/T)}\right]_P}{q} \tag{3.36}$$

The integral molar entropy change, ΔS (kJ mol^{-1} K^{-1}), is the measure of the ways in which a thermodynamic system may be rearranged and is taken as a measure of disorder. It also helps in comprehending the packing manner of the adsorbed molecules on the adsorbent surface. It can be calculated from the following expression:

$$\Delta S = \frac{-\left(\frac{\partial \Omega}{\partial T}\right)_P}{q} \tag{3.37}$$

These thermodynamic parameters are obtained by numerical analysis based on isotherm model for pure component adsorption on prepared carbons.

3.6.2 Energy duty for desorption

Another important aspect of thermodynamic study is energy requirement for regeneration process. From application point of view, energy penalty for desorption of CO_2 should be

calculated for binary system under dynamic conditions. Therefore, energy requirement for pure component adsorption has not been evaluated.

The thermal energy input (Q_{th}) required to regenerate the adsorbent is the sum of heat of desorption (Q_{st}) and the sensible heat required to heat the adsorbent from the adsorption temperature up to temperature for desorption.

$$Q_{th} = Q_{st} + Sensible\ heat \tag{3.37}$$

Sensible heat requirement is a function of adsorbent's heat capacity, difference between adsorption and desorption temperatures and the adsorption capacity of the adsorbent material [136, 137].

$$Sensible\ heat = \frac{C_p \Delta T}{adsorption\ capacity} \tag{3.38}$$

where C_p (J g^{-1} K^{-1}) is the specific heat capacity of the adsorbent material and ΔT is the difference between adsorption and desorption temperatures. Specific heat capacity of the prepared carbon was measured from a differential scanning calorimeter (as discussed in section 3.2.5.2)

Heat of desorption is assumed to be equal to heat of adsorption i.e. isosteric heat of adsorption [43]. It can be defined as the difference between the activation energy required for adsorption and desorption process and is obtained by using Clausius–Clapeyron equation [138]:

$$Q_{st} = -R \left[\frac{\partial\, ln\ P}{\partial \left(\frac{1}{T}\right)} \right]_{q_e} \tag{3.39}$$

where Q_{st} (kJ mol^{-1}) is the isosteric heat of adsorption at a given q_e. It can be calculated from the slope of the plot between *ln (P)* and *1/T* for constant adsorbate coverage (i.e. isosteres).

3.7 Software used

OriginPro 8 software was used for fitting various kinetic and pure component adsorption isotherm models to the experimental data by nonlinear regression. MATLAB R2015b software

was used for calculation of reduced spreading pressure for various IAST based isotherm models by applying Newton-Raphson formula to spreading pressure equations.

Chapter 4 - Nitrogen Doped Mesoporous Carbons for Carbon Dioxide Capture

4.1 Introduction

This chapter consists of mainly three parts including synthesis, characterization and CO_2 performance evaluation of nitrogen doped mesoporous carbon adsorbents from melamine-formaldehyde resin and silica template by nanocasting technique. A series of adsorbents have been prepared by varying the carbonization temperature and one sample has been prepared without nanocasting technique for comparison purpose. This is followed by characterization of adsorbents for their textural, elemental and surface properties. The effectiveness of these synthesized materials as CO_2 adsorbents has been evaluated by fixed-bed column adsorption experiments using simulated flue gas. Effect of temperature and CO_2 feed concentration has been investigated on the dynamic adsorption capacity and breakthrough time. Suitability of these adsorbents in cyclic process application has also been studied by temperature swing adsorption with nitrogen as the purge gas. Static adsorption-desorption study under pure CO_2 and N_2 flow is also discussed at four different temperatures. Kinetic adsorption data has been illustrated by suitable adsorption kinetic models. Equilibrium adsorption uptakes of CO_2 and N_2 have been correlated with their breakthrough capacities obtained from fixed bed experiments by using pure and binary component isotherm models. Finally thermodynamic parameters for CO_2 adsorption and energy required for desorption of CO_2 are calculated.

4.2 Adsorbent synthesis

Nitrogen doped mesoporous carbon adsorbents were synthesized via nanocasting technique by using melamine-formaldehyde resin and mesoporous silica as polymeric precursor and template respectively Three steps were involved in the synthesis: (i) templated resin synthesis, (ii) carbonization of the templated resin and (iii) removal of template.

4.2.1 Templated resin synthesis

Figure 4.1 presents the block diagram for the process of templated resin synthesis. In a typical experiment, 46.6 g of melamine was added to 200 ml of 5 wt% methanol solution under continuous stirring and heated to 70 °C. To this reaction mixture, 200 ml of 37% w/v

formaldehyde solution was added slowly over the duration of 3 h to form hexamethylomelamine while maintaining pH in the range of 8–9 by adding potassium carbonate. Reaction temperature was raised to 75 °C, under continuous stirring, in order to carry out advanced polymerization. Solution pH was maintained in the range of 7–8 by adding 0.1 N sodium hydroxide solution and 0.4 g of di-sodium tetra borate (borax) for further 2 h. Hereafter, reaction mixture was cooled down to room temperature and 6 ml of H_2SO_4 solution (48%) was added to it. Hard template i.e. mesoporous silica (15.0 g) was added to this reaction mixture and mixed thoroughly to obtain the templated resin followed by curing at 60 °C for 2 h. It was then left at room temperature until complete solidification has occurred. The setup for the synthesis of melamine-formaldehyde resin is shown in Figure 4.2.

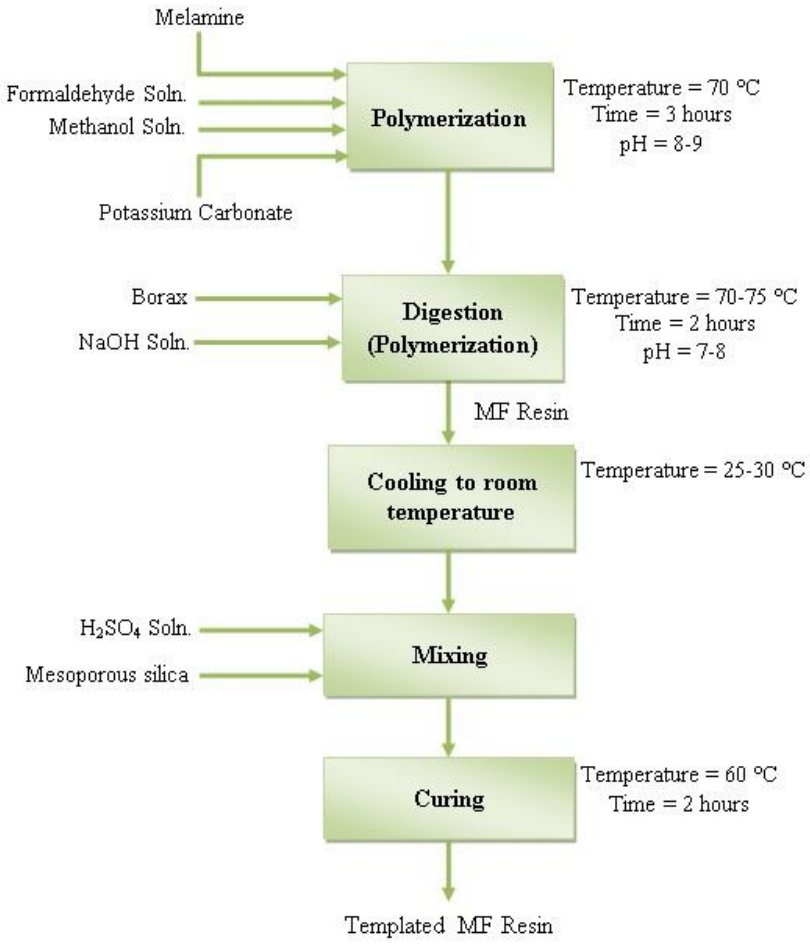

Figure 4.1 Block diagram of templated resin synthesis process

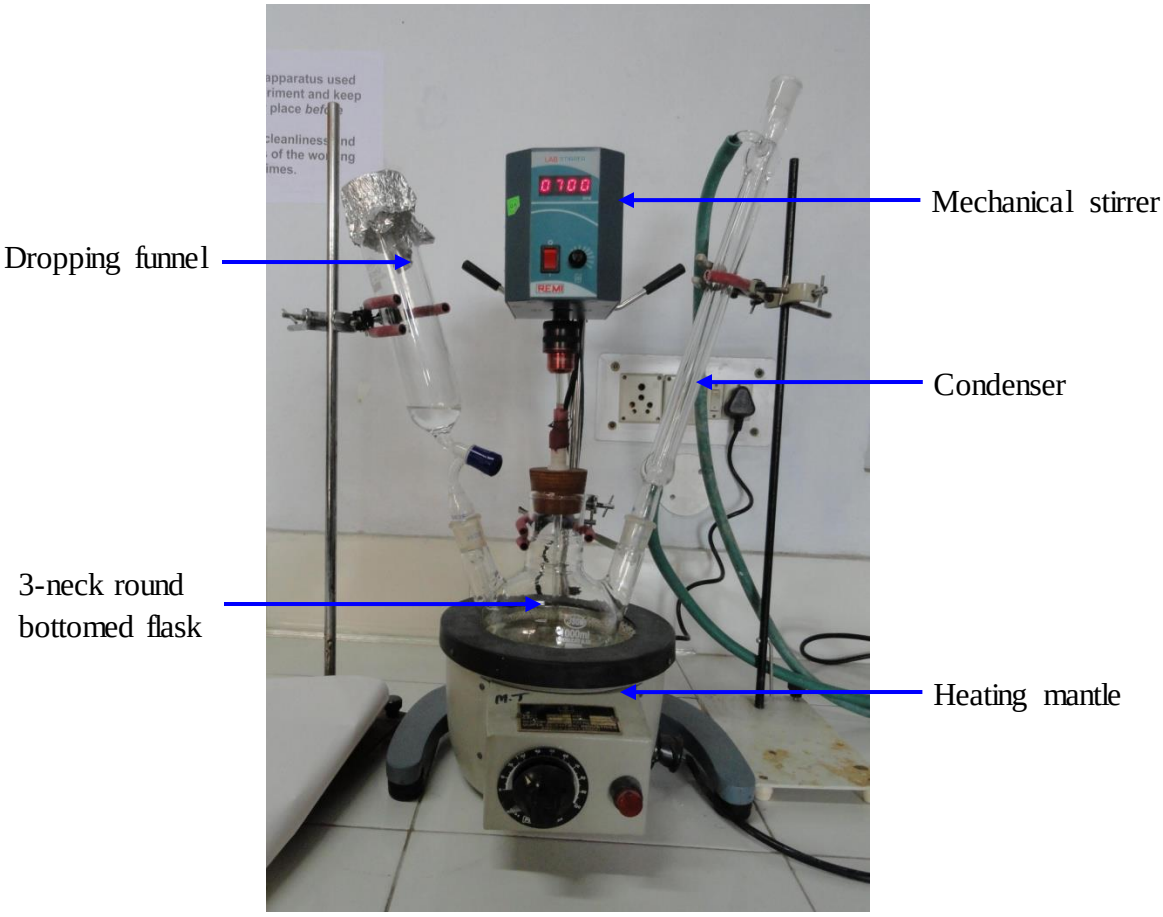

Figure 4.2 MF resin synthesis setup

4.2.2 Carbonization of templated resin

Carbonization is the process for producing carbon materials from carbon containing organic compounds by heat treatment under inert atmosphere. It is a complex process involving various types of reactions such as dehydrogenation, condensation etc. resulting in thermal decomposition of the precursor and hence release of the volatile matter.

Carbonization of templated MF resin samples was carried out in ceramic boats loaded into a quartz tubular furnace under pure nitrogen atmosphere. Templated samples were heated from room temperature to the desired carbonization temperature (400–800 °C) at a heating rate of 10 °C min^{-1} and were held at final temperature for 1 h followed by cooling to room temperature under inert atmosphere.

4.2.3 Removal of template

Last step in the synthesis involves the removal of silica template from carbonized samples. This was achieved by dissolution of carbonized samples in 40 wt% sodium hydroxide (NaOH)

solution for at least 24 h. This was followed by washing with copious amounts of water and drying in oven at 100 °C for 2 h. Synthesized adsorbents were labeled as MF-*x*, where *x* refers to the carbonization temperature (400–800 °C).

For comparison purpose, one sample was prepared without nanocasting technique. The process for its synthesis was same as above mentioned except template addition and its subsequent removal. This sample was labeled as 'MF-C'.

4.3 Adsorbent characterization

4.3.1 Surface area and pore size distribution

Figure 4.3a presents the N_2 sorption isotherms of MF-*x* carbons prepared at different carbonization temperatures along with mesoporous silica template. Based on the IUPAC classification, adsorption isotherms of all the prepared carbons except MF-700 and MF-800 can be classified as type IV which is typical of mesoporous materials whereas MF-700, MF-800 and silica exhibit a combination of type I and type IV isotherms indicating the presence of both micropores and mesopores in these materials. The presence of a hysteresis loop in all the samples, at relative pressure (P/P_o) around 0.8, is usually associated with the filling and emptying of the mesopores by the phenomena of capillary condensation. Volume of nitrogen adsorbed increases as carbonization temperature increased up to 700 °C followed by decrease in the amount of N_2 adsorbed on further increase in carbonization temperature to 800 °C (Table 4.1). Very high carbonization temperature of 800 °C leads to the partial collapse of pore structure thereby decreasing the surface area and total pore volume of MF-800. Samples obtained at carbonization temperature up to 600 °C demonstrate very less amount of N_2 adsorbed, thereby indicating this temperature to be insufficient for the porosity development. For carbonization temperature $\geq$ 700 °C, a steep rise in N_2 adsorption is also observed at low relative pressure ($P/P_o < 0.1$) which corresponds to the micropore filling and the increase in nitrogen uptake is sustained throughout the entire pressure range. This indicates the development of micro and meso-porosity in MF-700 and MF-800 samples. Dissolution of template i.e. silica from the carbon framework results in the mesoporosity in the prepared carbons. However, small microporosity in MF-700 and MF-800 is created in the course of the carbonization of precursor of its own accord. MF-700 exhibits the highest BET surface area of 266 $m^2\ g^{-1}$ and total pore volume of 0.309 $cm^3\ g^{-1}$ with very low micropore volume of 0.033

$cm^3\ g^{-1}$. Sample obtained by direct carbonization of MF resin (MF-C) exhibits very small amount of N_2 adsorbed indicating almost no porosity development in this sample.

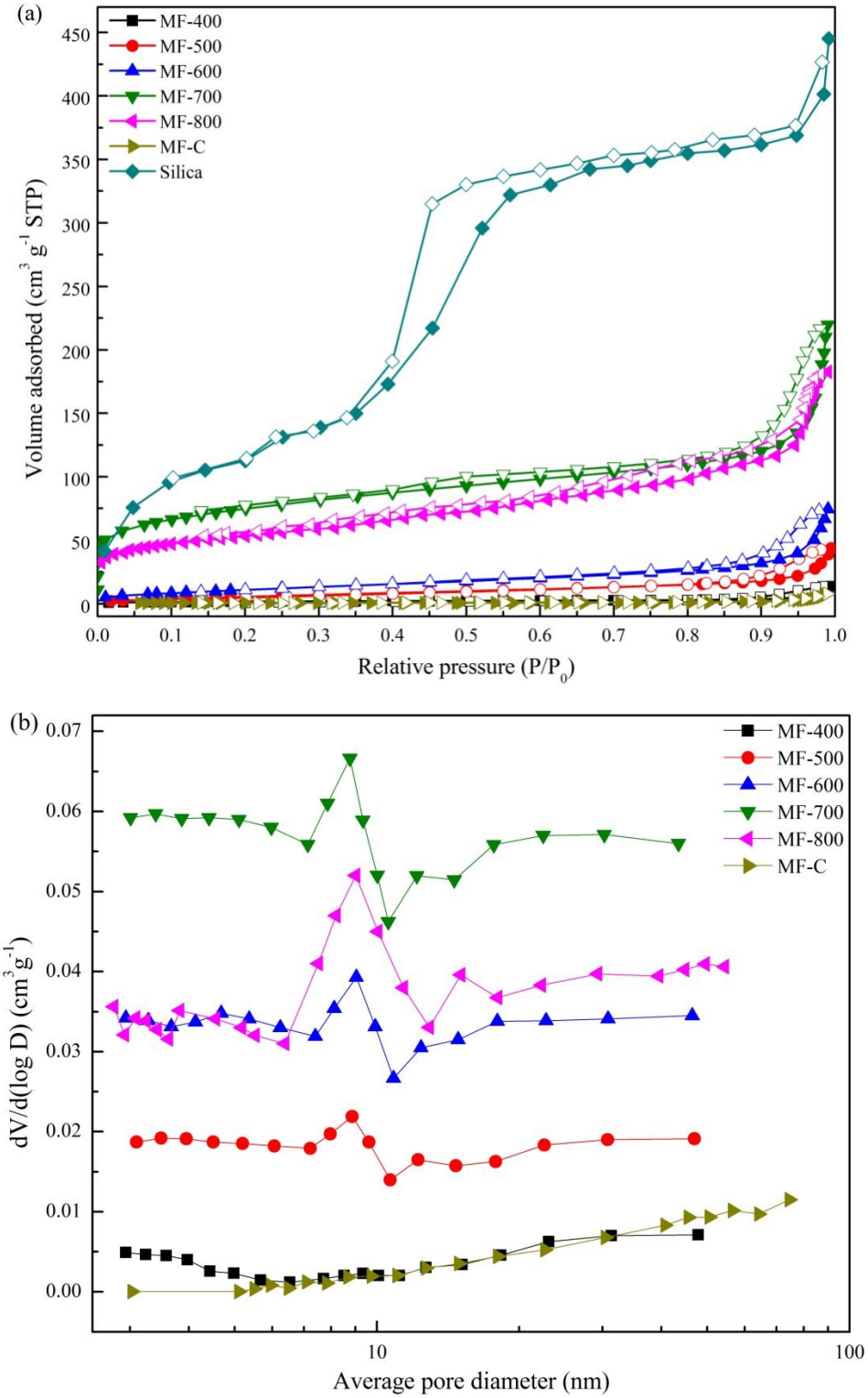

Figure 4.3 (a) N_2 adsorption (closed symbols) - desorption (open symbols) isotherms at -196 °C of prepared carbons and mesoporous silica, **(b)** pore size distribution of nitrogen doped mesoporous carbon adsorbents

Pore size distribution (PSD) of prepared carbon adsorbents are obtained from adsorption branch of BJH method and the results are presented in Figure 4.3b. Average pore diameter of all the samples lie in the mesopore region i.e. 2 to 50 nm. PSD of all of the samples except MF-400 are centered around 9-10 nm and the peak mainly comes from the mesopores formed after dissolution of the silica. For MF-400, most of the pore volume lies in the pores with size > 10 nm. On the other hand, average pore size of the silica template is found to be 3.5 nm. There is large difference in average pore diameters of porous carbons and parent silica template. Furthermore, width of the hysteresis loop for silica template is relatively more noticeable than prepared carbons. This is because hysteresis loop of silica template occurred at lower relative pressure than that of prepared mesoporous carbons. Textural properties of silica template and replicated carbons are in good accord with literature reported properties [110, 139, 140]. Thus, fabrication of porous carbons by nanocasting technique helps in tailoring their pore structure by using a template with suitable pore size.

Table 4.1 Textural properties of nitrogen doped mesoporous carbon adsorbents

Sample	BET Surface Area, S_{BET} (m^2 g^{-1})	Total pore volume, V_P (cm^3 g^{-1})	Pore volume obtained from BJH method, V_{BJH} (cm^3 g^{-1})	t-plot micropore volume, V_{micro} (cm^3 g^{-1})
MF-400	6	0.023	0.022	-
MF-500	23	0.067	0.067	-
MF-600	42	0.117	0.117	-
MF-700	266	0.309	0.249	-
MF-800	191	0.225	0.198	0.033
MF-C	2	0.12	0.011	0.022
Silica	450	0.721	0.697	-

The development of the pore structure of a material depends on many factors namely nature of starting material, carbonization conditions (heating rate, gas atmosphere, final temperature and time) and post-synthesis processing. It is found that the surface area of MF-700 carbon is

comparatively lower than other carbon adsorbents reported in literature. This difference is mainly due to nature of the material to be carbonized which is templated melamine-formaldehyde resin in this case. Carbons from various raw materials under same synthesis conditions are reported to exhibit different pore structure. Moreover, carbonization conditions have a strong influence on the textural properties. Low heating rate results in material having micropores and mesopores while high heating rate produces mainly macroporous materials with some amount of mesopores. Additionally, most of the literature reported carbons have been prepared by activation after carbonization in order to improve the textural properties. But, activation has not been carried out in the present work. Thus, all these factors contribute to lower surface area of MF-700 carbon as compared to literature values.

4.3.2 X-ray diffraction analysis

The wide angle X-ray diffraction patterns of the prepared carbons as a function of Bragg's angle (2θ) are displayed in Figure 4.4. All the samples demonstrated a broad diffraction peak at 2θ = 26–27° which corresponds to the (002) diffraction planes of hexagonal graphitic carbon as per JCPDS X-ray Powder Diffraction Database No. 75-1621.

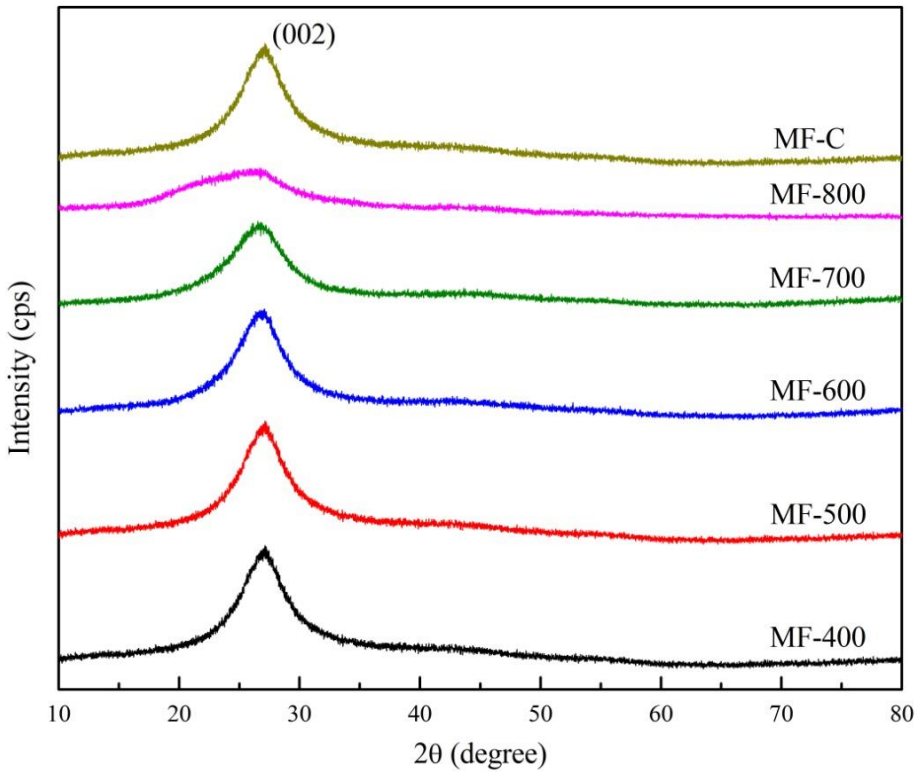

Figure 4.4 XRD patterns of nitrogen doped carbon adsorbents

The interlayer spacing between the graphite layers corresponding to the (002) diffraction plane, d_{002}, is found to be 0.334 nm which is very close to that of the ideal graphite (with d_{002} = 0.335 nm) (Table 4.2) [141]. With increase in carbonization temperature, a decrease in the intensities at (002) diffraction plane is observed that indicate an increase in the irregularity of the layer structures. Also widening of the peak range for MF-800 causes the cracking or collapse of the layer structure, thereby affecting the textural properties [142] and the same is supported by the nitrogen sorption isotherms at -196 °C. Furthermore, absence of sharp diffraction patterns implies that the prepared mesoporous carbons do not exhibit completely crystalline character.

Table 4.2 Structural parameters of nitrogen doped carbons

Sample	Diffraction angle, 2θ (°)	Interlayer spacing of (002) diffraction plane, d_{002} (nm)
MF-400	26.53	0.336
MF-500	26.65	0.334
MF-600	26.65	0.334
MF-700	26.67	0.334
MF-800	26.06	0.341
MF-C	26.64	0.334

Also, the line broadening of the most intense peak in XRD patterns is observed which is mainly due to the very small crystallite size. This is an apparent property of the nano-materials and causes broadening of diffraction peak [143]. Thus, the synthesized material is nanostructured carbon.

4.3.3 Transmission electron microscopy

Figure 4.5 displays the TEM images of the synthesized adsorbents and nanostructures can be clearly seen. Nanostructures in these prepared materials are in the size range of 30–50 nm. XRD pattern also indicates that the synthesized adsorbents are nanostructured carbon, which is in agreement with that obtained from TEM images. Sample obtained by direct carbonization of MF resin i.e. MF-C exhibited very big structures (>120 nm) and are not in the range of nano-materials.

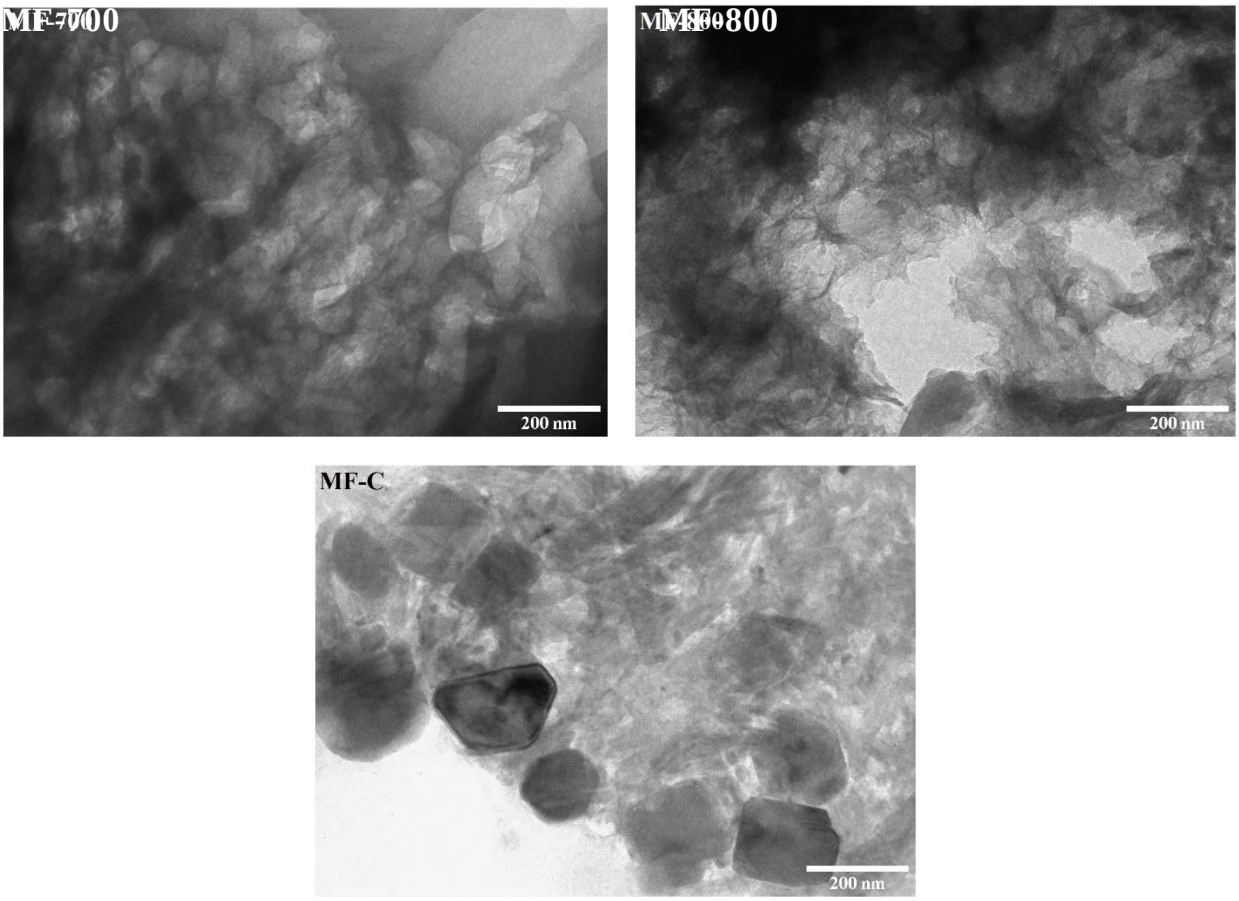

Figure 4.5 TEM images of prepared nitrogen doped carbons

4.3.4 Scanning electron microscopy

Figure 4.6 shows the SEM images of the synthesized adsorbents, clearly indicating the development of irregular and heterogeneous pores. Many large stacking (external) pores between the particles can be seen, which expedites the gas diffusion from the bulk gas phase to the surface of the adsorbent. Surface of MF-800 seems to be compact as compared to the other carbons which could be attributed to collapse of the pore structure as also observed from N_2 sorption isotherms and XRD. On the other hand, the surface of MF-C sample has very less number of pores indicating very low porosity development.

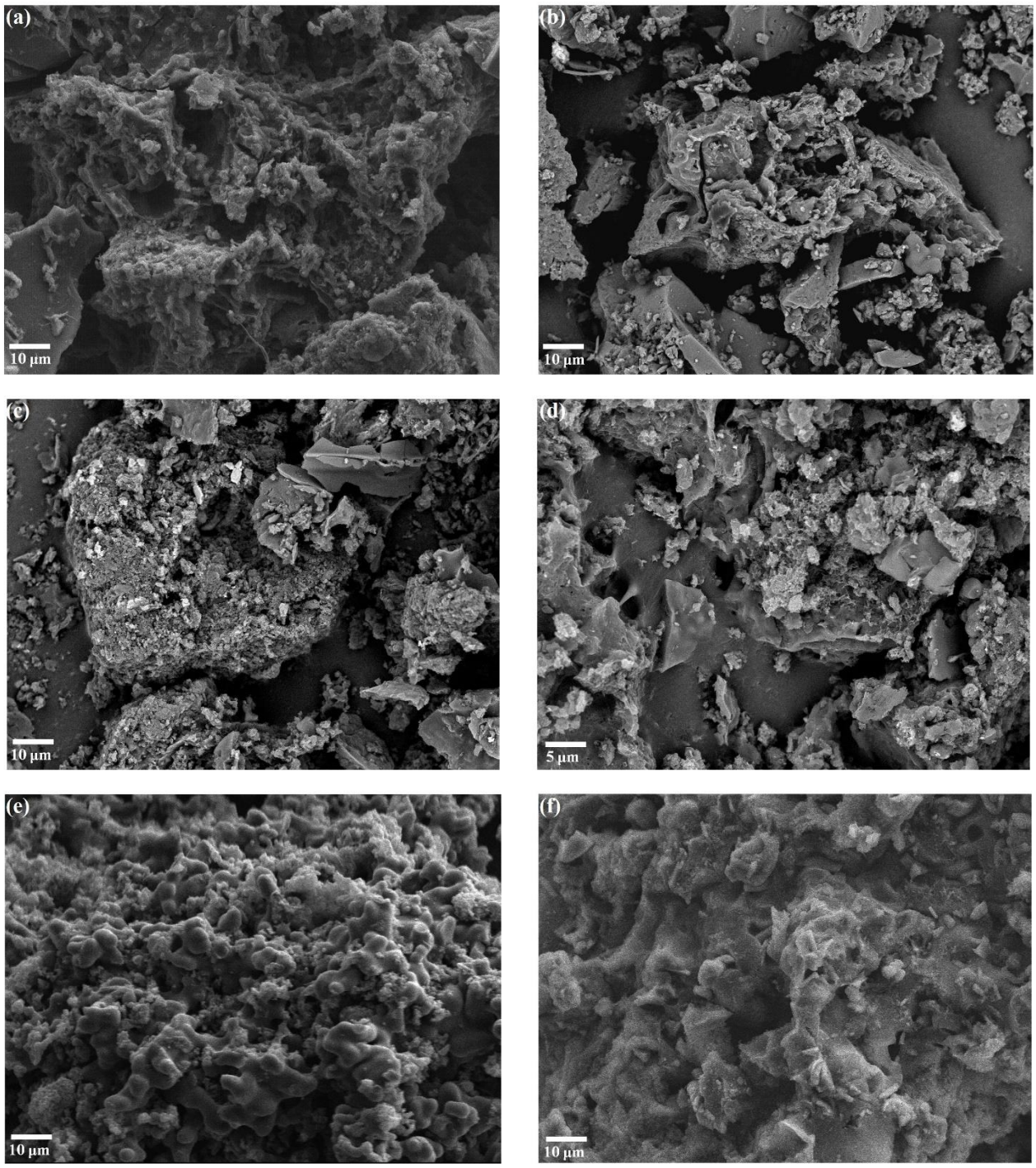

Figure 4.6 SEM images of nitrogen doped carbons **(a)** MF-500, **(b)** MF-600, **(c, d)** MF-700, **(e)** MF-800, and **(f)** MF-C

4.3.5 Thermogravimetric analysis

Thermogravimetric (TG) profiles of synthesized carbons in the inert atmosphere are depicted in Figure 4.7. The weight loss profile of all the samples is similar with all of them showing ca. 8% weight loss up to temperature of 100 °C, owing to desorption of CO_2, moisture and some other adsorbed gases, followed by their degradation in single step. Thermal stability of the synthesized adsorbents increases with increase in carbonization temperature. MF-400 and MF-500 are stable up to 350 °C. MF-600, MF-700 and MF-800 are stable up to 400 °C, 450 °C and 500 °C respectively. After these temperatures, there is a gradual decrease in the weight of the adsorbents owing to their decomposition at higher temperatures. MF-700 and MF-C materials have the similar thermal stability under inert atmosphere thus indicating no significant effect of the development method on the thermal stability of the materials.

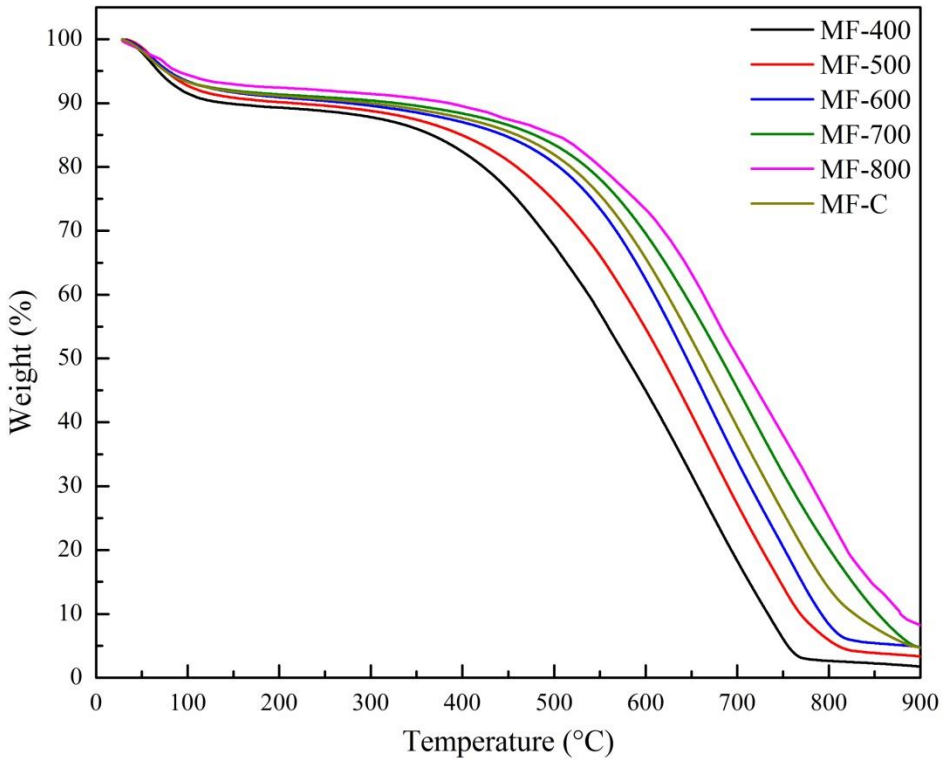

Figure 4.7 Thermogravimetric profiles of nitrogen doped mesoporous carbon adsorbents

4.3.6 Elemental composition

Elemental composition and Kjeldahl nitrogen of synthesized carbon adsorbents are presented in Table 4.3. Nitrogen content of the prepared carbons is found to decrease from 35 wt% to 21 wt% with increase in temperature of carbonization from 400 °C to 700 °C and similar trend is

observed for Kjeldahl nitrogen of the adsorbents. At higher carbonization temperatures, decline in nitrogen amount of carbons causes an increase in their carbon amount from 41wt% to 52 wt%. However, further increase in carbonization temperature to 800 °C resulted in drastic decrease in nitrogen and carbon content to 10.46% and 35.60% respectively. As expected, the N/C molar ratio decreased with increase in carbonization temperature from 0.363 to 0.126.

Table 4.3 Chemical properties of mesoporous carbon adsorbents

Sample	Kjeldahl Nitrogen (%)	Elemental analysis				
		Carbon (%)	Nitrogen (%)	Hydrogen (%)	Oxygen (%)	N/C molar ratio
MF-400	38.3	41.35	35.07	3.27	20.31	0.363
MF-500	34.9	42.61	33.12	2.19	22.08	0.333
MF-600	27.9	48.11	26.13	2.29	23.46	0.233
MF-700	22.5	52.53	21.11	2.20	24.17	0.172
MF-800	9.88	35.60	10.46	0.72	53.22	0.126
MF-C	19.6	35.02	20.04	0.70	44.25	0.245

Carbons obtained with and without nanocasting technique i.e. MF-700 and MF-C respectively exhibited similar nitrogen content but the carbon content in MF-C was ca. 17.5% lower than MF-700. This indicates that decomposition of the precursor and hence release of volatile matter during carbonization process is affected by the presence of silica template thereby helping in controlling the chemical properties of the obtained carbons.

4.3.7 Fourier transform infrared (FTIR) spectroscopy

To understand adsorption of MF derived carbons, it is important to identify the functional groups developed in these materials but exact chemical structure of MF resin is difficult to be determined on account of complexity in its structure. Furthermore, it is challenging to establish the exact structure of carbon adsorbent obtained from carbonization of MF resin as there is development of very broad range of chemical functional groups during pyrolysis. Qualitative analysis of the functional groups present in the synthesized carbons was carried out by FTIR

spectroscopy. FTIR spectra of nitrogen doped mesoporous carbons demonstrate the presence of similar functional groups as shown in Figure 4.8. Peaks at 1059 cm^{-1} and 1246 cm^{-1} can be assigned to C–O bond's stretching vibrations in ester, ether or alcohol group and aromatic C–N stretching vibration respectively. A band is observed ca. 1604 cm^{-1} attributing to N-H bond's in-plane deformation vibrations and/or aromatic C=C stretching vibration thereby showing the presence of aromatic ring structures. The peak at 1770 cm^{-1} is assigned to the stretching vibration of C=O bonds of carbonyls, esters or anhydrides. A small peak is also observed ca. 3000 cm^{-1} which can be ascribed to stretching vibration of C–H bond of $–CH_2–NH–CH_2–$ or $–CH_2–NH–CH_3$ while the weak bands at 3400 cm^{-1} indicate the presence of N–H symmetric stretching vibration [95, 144, 145]. Elemental analysis and FTIR confirmed the existence of nitrogen functional groups on the carbon surface that act as Lewis base active sites for adsorption of acidic CO_2.

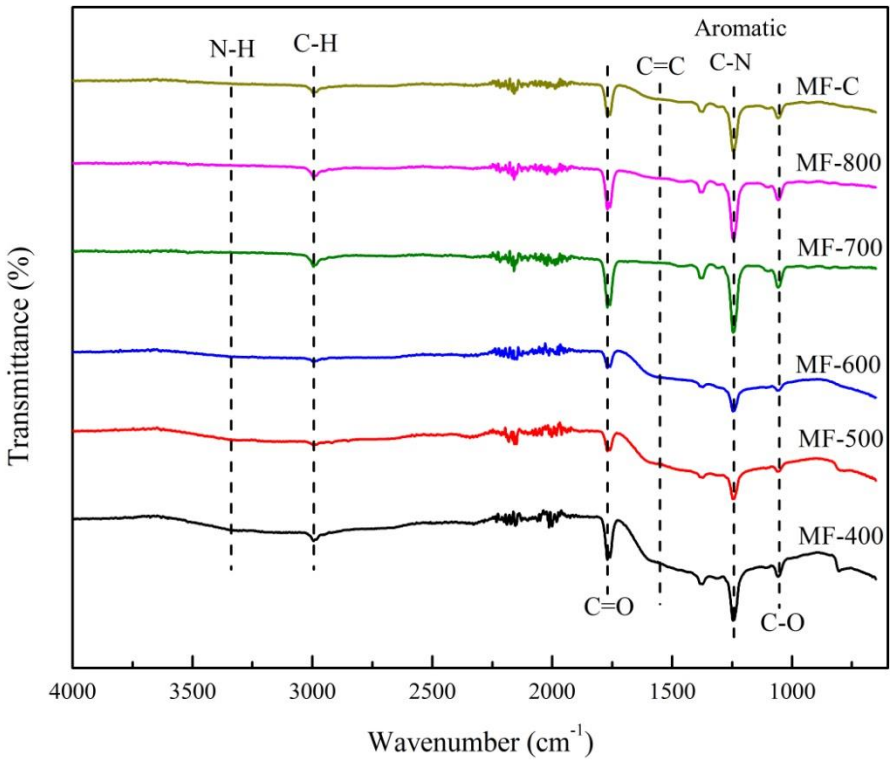

Figure 4.8 FTIR spectra of nitrogen doped mesoporous carbons

4.3.8 X-ray photoelectron spectroscopy

X-ray photoelectron spectroscopy (XPS) was employed to identify the chemical functional groups developed on the prepared carbons during carbonization of MF resin. Figure 4.9 demonstrates the survey spectra of nitrogen doped carbons and only three different peaks were observed ca. 285, 400, 532 eV corresponding to carbon (C1s), nitrogen (N1s) and oxygen (O1s)

respectively. Absence of silica template in the obtained carbons was confirmed by absence of peak in survey spectra for Si (2s or 2p). Further, high resolution spectra of the obtained carbons were also investigated to find the chemical binding states of C, N and O in the prepared carbon materials.

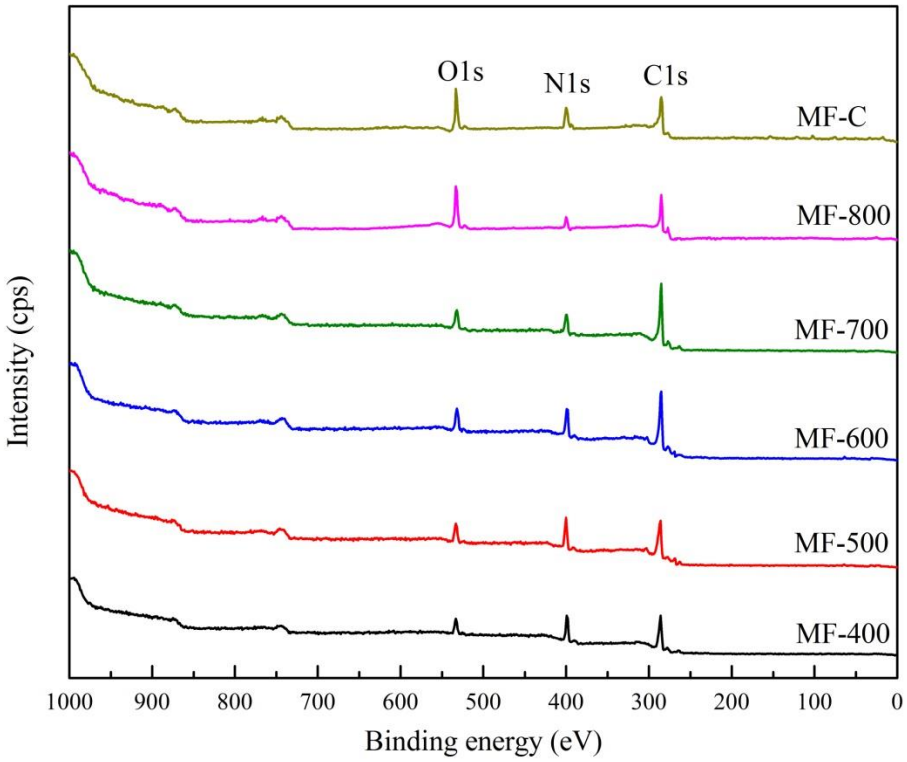

Figure 4.9 XPS survey scan spectra of MF-based carbons

Figure 4.10 illustrates the XPS spectra of the C1s core level region of MF derived carbons. The C1s spectra of these carbons were deconvoluted into five different peaks with binding energies ca. 284.8, 285.7, 286.8, 288.6 and 290.0 eV marked as C1, C2, C3, C4 and C5 respectively. Peak C1 is attributed to sp^2 (C=C) and sp^3 (C-C) hybridized graphitic carbon whereas peak C2 attributes to C-O bond of alcohol, phenol or ether and/or C=N bond. Peak C3 is ascribed for quinone or carbonyl groups and/or C-N linkage while peak C4 for ester or carboxyl bonds, and peak C5 corresponds to shake up satellite peaks due to π-π^* transitions in aromatic rings [146]. Table 4.4 reports the corresponding binding energy (B. E.), full width at half maximum (FWHM) and relative area contribution (A%) of each deconvoluted peak.

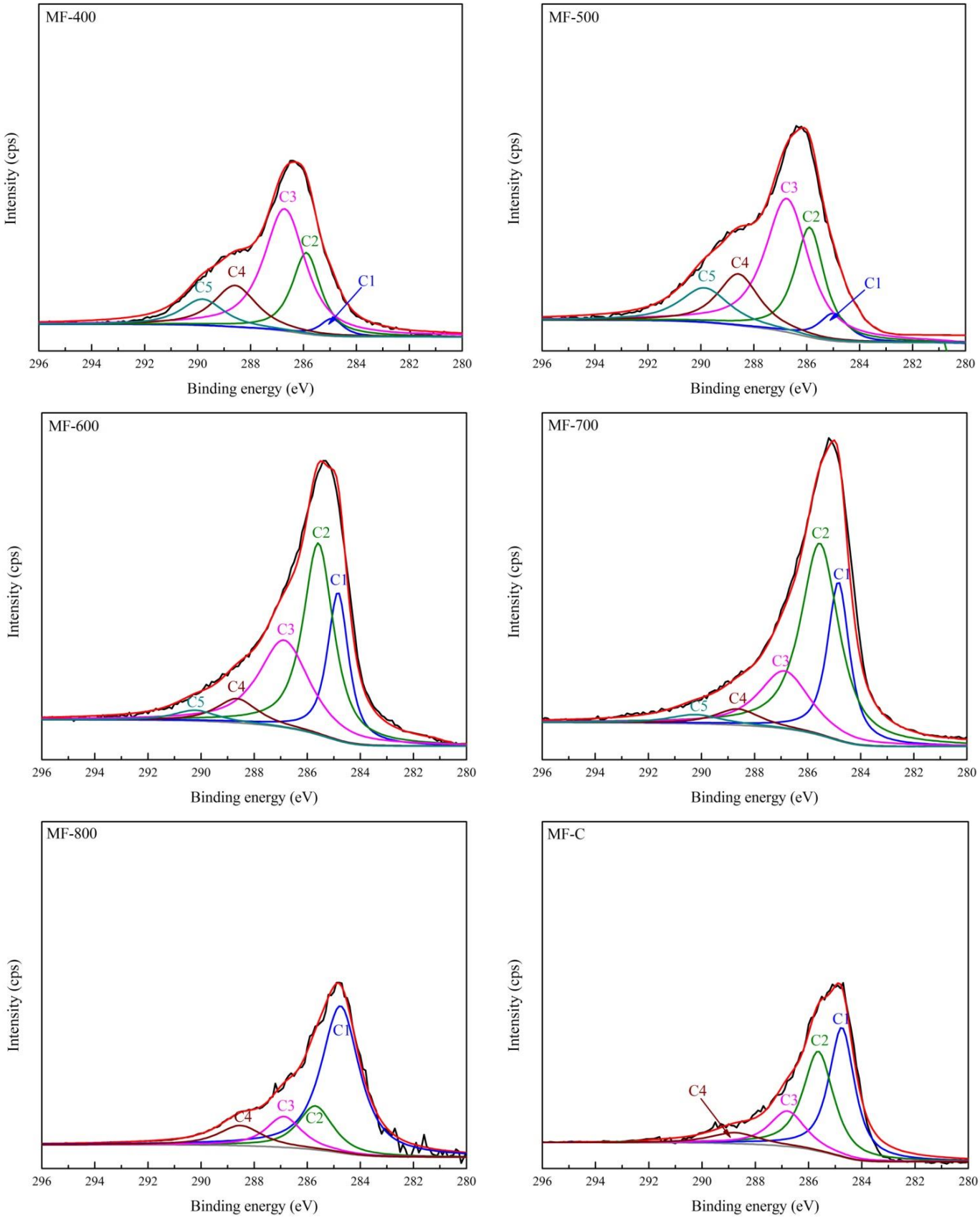

Figure 4.10 Deconvoluted XPS spectra of C1s region of nitrogen doped carbons

Table 4.4 Deconvolution of XPS spectra of C1s region of nitrogen doped carbons

Sample		C1	C2	C3	C4	C5
MF-400	BE	284.93	285.89	286.71	288.58	289.81
	FWHM	1.02	1.29	1.87	1.92	1.91
	A%	3.72	21.76	47.50	16.59	10.43
MF-500	BE	284.98	285.89	286.75	288.58	289.86
	FWHM	1.29	1.33	1.96	1.86	2.23
	A%	5.80	23.68	42.46	15.54	12.52
MF-600	BE	284.84	285.58	286.87	288.65	290.22
	FWHM	0.95	1.36	2.27	1.83	1.93
	A%	21.233	39.23	29.80	6.65	3.09
MF-700	BE	284.84	285.54	286.87	288.63	290.22
	FWHM	0.99	1.71	2.29	1.98	2.37
	A%	23.42	48.93	19.70	4.75	3.20
MF-800	BE	284.75	285.69	286.88	288.52	-
	FWHM	1.71	1.56	1.58	1.94	-
	A%	61.69	16.75	11.96	9.60	-
MF-C	BE	284.75	285.63	286.79	288.76	-
	FWHM	1.15	1.36	1.60	2.11	-
	A%	40.86	37.23	15.53	6.37	-

With increasing temperature of carbonization from 400 °C to 800 °C, relative area percentage of peak C1 increased from ca. 3.7% to 61.69% with a substantial increase at 800 °C demonstrating enhanced graphitization character at higher temperatures. C1s core level region of MF-400 and MF-500 carbons was found to be similar with dominant components being quinone or carbonyl and/or C-N bonds. Significant change was observed in the chemical functional groups for carbonization $\geq$ 600 °C. As compared to MF-400 and MF-500 carbons, a substantial increase in ether, phenol, alcohol and/or C=N bonds was observed for MF-600 and MF-700 as indicated by increase in A% of C2 peak. On increasing carbonization

temperature from 700 °C to 800 °C, relative area percentage of C2 peak has decreased significantly which could be attributed to drastic decrease in nitrogen content and hence C=N bonds. In contrast, MF-C sample exhibited much higher content of graphitic carbon while ca. 12% lower phenol, alcohol, ether and/or C=N bonds as compared to MF-700 sample. Therefore, there is an appreciable variation in the A% of graphitic carbon, C-N structures and C-O structures with rise in carbonization temperature indicating the cleavage of C=O, C-O and C-N structures and the formation of more stabilized structures.

Next, N1s core level region spectra of MF based carbons (Figure 4.11) was deconvoluted into four well resolved peaks with B. E. ca. 398.8, 400.0, 401.1, and 403.0 eV labeled as N1, N2, N3, and N4 respectively. Table 4.5 reports the corresponding B. E., FWHM and A% of the deconvoluted peaks for all the prepared carbons. Peak N1 ca. 398.8 eV is attributed to the pyridinic nitrogen while peak N2 is assigned for pyrrolic and/or pyridonic nitrogen. Pyridinic nitrogen has been described to be highly stable, up to 1000 °C. Although pyridonic and pyridinic forms of nitrogen have a six membered ring structure, they are not found at same B. E. Pyridonic nitrogen has similar chemical environment as that of pyrrolic nitrogen due to tautomeric equilibrium in pyridonic nitrogen and both of them contribute two p-electrons to the aromatic π-system. However, only one p-electron is contributed by pyridinic nitrogen to the π-system. Hence, it is not possible to differentiate pyrrolic nitrogen and pyridonic N within the precision of XPS measurements. Peak N3 is assigned to quaternary nitrogen while peak N4 corresponds to pyridinic nitrogen oxides. Quaternary nitrogen can have several structures but only structures in which nitrogen substitutes carbon in aromatic graphene structure at center or valley positions are stable during pyrolysis [146-149]. B. E. of peak N2 was found to increase from 399.84 to 400.15 eV with increase in carbonization temperature signifying the presence of other nitrogen structures such as amide, amine or imide along with pyrrolic and pyridonic forms of nitrogen. Usually, amide groups are found at B. E. of ca. 399.6–399.9 eV whereas imides are found ca. 399.7 eV and therefore, it is difficult to separate these peaks [150].

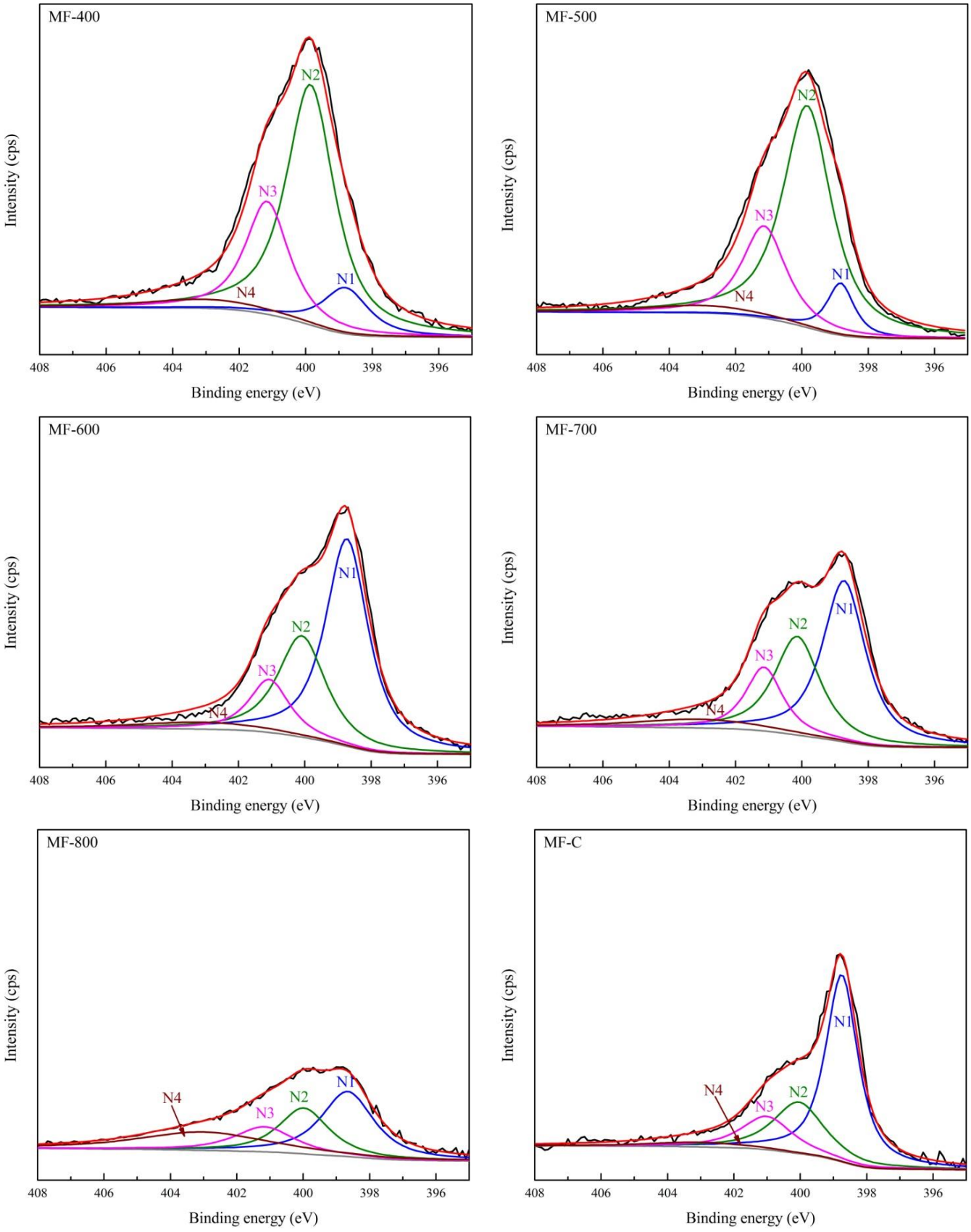

Figure 4.11 Deconvoluted XPS spectra of N1s region of nitrogen doped carbons

Table 4.5 Deconvolution of XPS spectra of N1s region of nitrogen doped carbons

Sample		N1	N2	N3	N4
MF-400	BE	398.80	399.86	401.16	403.05
	FWHM	1.65	1.73	1.56	4.45
	A%	10.76	58.70	24.89	5.66
MF-500	BE	398.83	399.84	401.14	403.04
	FWHM	0.98	1.76	1.57	4.41
	A%	8.25	63.04	23.38	5.33
MF-600	BE	398.73	400.09	401.07	403.13
	FWHM	1.54	1.71	1.44	4.52
	A%	53.22	28.85	12.70	5.23
MF-700	BE	398.73	400.14	401.14	403.12
	FWHM	1.55	1.64	1.33	4.48
	A%	46.66	30.19	15.84	7.31
MF-800	BE	398.66	400.15	401.17	403.01
	FWHM	1.89	1.79	2.15	4.66
	A%	35.72	23.83	15.62	24.83
MF-C	BE	398.75	400.04	401.01	403.04
	FWHM	1.16	1.81	1.83	3.49
	A%	56.07	24.06	15.72	4.15

Carbonization $\leq$ 500 °C resulted in carbons having majorly pyrrolic and/or pyridonic form of nitrogen along with amides, amines and/or imides. However, increasing carbonization temperature to 600 °C lead to a significant increase in A% of peak N1 and decrease in A% of N2 peak. Conversion of pyrrolic nitrogen to pyridinic nitrogen could be the reason for this change in A% of these two peaks. Also primary amines present may be lost at this carbonization temperature as they have been reported to decompose at 600 °C. A% of peak N4 attributing to pyridinic nitrogen oxides was minimum for all N-doped carbons except MF-800. During the carbonization, pyridinic nitrogen and quaternary nitrogen are reported to be the most stable

forms of nitrogen. Contribution of these two forms of nitrogen were found to increase from ca. 35.6% to 62.5% with increase in carbonization temperature from 400 °C to 700 °C. But further rise in carbonization temperature to 800 °C resulted in decrease in their content. Increased oxygen content and drastically decreased nitrogen content in MF-800 may lead to formation of pyridinic nitrogen oxides and hence higher A% of N4 peak for this sample. Additionally, N-doped carbons have most of the nitrogen functionality as pyridinic and pyrrolic and/or pyridonic nitrogen and these forms of nitrogen have electron donating capability thereby exhibiting Lewis basicity and serving as active sites for adsorption of CO_2. Relative area percentage of pyridinic nitrogen is more for MF-C sample as compared to MF-700 sample but rest of the nitrogen functionalities have similar relative contributions. As the overall nitrogen content of MF-C is much lower than MF-700, the former sample will be exhibiting lower basicity than the later.

High resolution spectra O1s region of N-doped carbons (Figure 4.12) was deconvoluted into four different peaks with B.E. around 531.3, 532.4, 533.6, and 535.0 eV referred as O1, O2, O3 and O4 respectively (Table 4.6). O1 peak is assigned to C=O bond of ketone, carbonyl lactone linkages whereas peak O2 corresponds to carbonyl oxygen of anhydrides, esters, amides, and oxygen atom of alcohol, phenol or ether groups. Peak O3 and O4 are attributed to oxygen of carboxylic groups and oxygen in water respectively [146]. MF-400 carbon has oxygen mainly as carboxylic linkages as suggested by highest relative area contribution of peak O3. While A% of peaks O1 and O2 was found to increase appreciably with rise in temperature from 400 °C to 700 °C and is at the cost of carboxylic groups. Further increase in carbonization temperature to 800 °C leads to drastic decrease in O1 peak while a substantial increase in O2 peak. O1s envelope of MF-C sample is substantially different from rest of the carbon samples. The dominant component in MF-C sample is anhydrides, esters, amides, and/or alcohol, phenol or ether groups followed by almost equal contribution of carbonyl/ketone and carboxylic groups. Oxygen functional groups as predicted by high resolution O1s spectra, developed during different carbonization conditions, are in good accord with that obtained from high resolution C1s spectra of the prepared carbons.

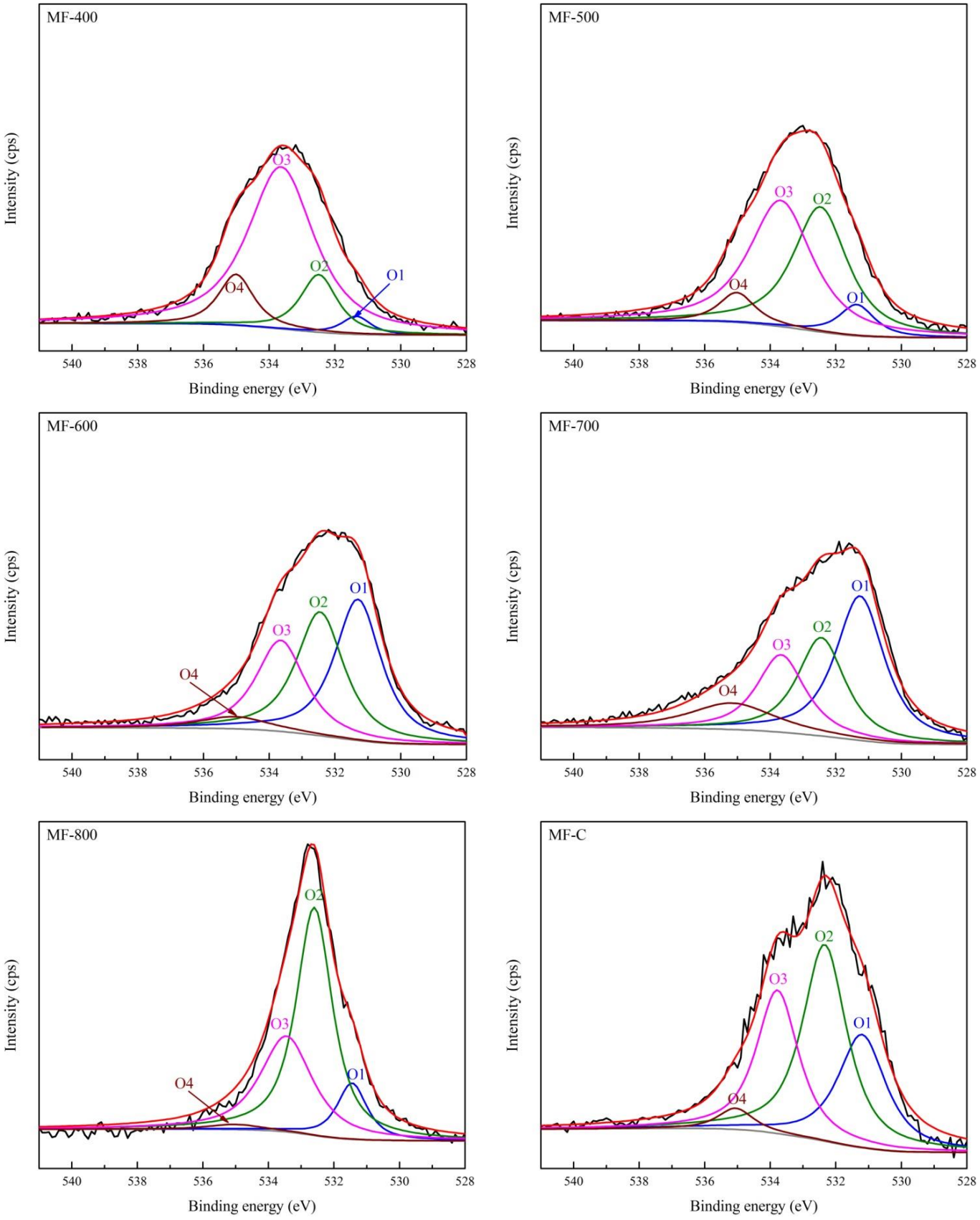

Figure 4.12 Deconvoluted XPS spectra of O1s region of nitrogen doped carbons

Table 4.6 Deconvolution of XPS spectra of O1s region of nitrogen doped carbons

Sample		O1	O2	O3	O4
MF-400	BE	531.35	532.49	533.64	535.01
	FWHM	1.05	1.33	2.41	1.27
	A%	3.46	13.92	70.85	11.77
MF-500	BE	531.36	532.47	533.68	535.02
	FWHM	1.30	1.98	2.29	1.30
	A%	6.62	40.18	46.90	6.31
MF-600	BE	531.30	532.45	533.65	535.06
	FWHM	1.69	1.73	1.77	2.59
	A%	36.98	33.18	25.00	4.85
MF-700	BE	531.26	532.44	533.67	535.16
	FWHM	1.78	1.73	1.75	3.11
	A%	39.84	26.40	21.03	12.73
MF-800	BE	531.45	532.60	533.45	535.01
	FWHM	1.08	1.31	1.89	1.90
	A%	11.06	54.30	32.85	1.79
MF-C	BE	531.20	532.34	533.78	535.06
	FWHM	1.75	1.61	1.52	1.26
	A%	26.08	41.69	28.70	3.53

4.3.9 Surface basicity by Boehm titration

Carbon materials exhibit acidic surface properties because of the existence of phenols, carboxyl, lactones or lactols, groups. On the other hand, functionalities like pyrones, chromenes, ethers and carbonyls are account for basic properties of the carbon surfaces. Surface acidity of the synthesized adsorbents decreases with the increase in the carbonization temperature from 400 °C to 700 °C. Alternatively surface basicity increases from 2.98 to 4.07 milli equivalents per gram (meq g^{-1}) (Table 4.7) with increase in carbonization temperature

from 400 °C to 600 °C but after further increase in temperature, there is no change in the basicity.

Table 4.7 Surface acidity and basicity by Boehm titration of the carbon adsorbents

Sample	Acidity (meq g^{-1})	Basicity (meq g^{-1})
MF-400	2.12	2.98
MF-500	1.69	3.35
MF-600	1.15	4.07
MF-700	0.86	4.05
MF-800	1.05	1.70
MF-C	2.67	0.54

On increasing the carbonization temperature to 800 °C, surface basicity of the obtained carbon decreased drastically to 1.7 meq g^{-1} with a small increase in surface acidity. On the other hand, carbon obtained without nanocasting technique displayed very low basic character and a very high surface acidity of 2.67 meq g^{-1}. Generally acidic and basic surface sites coexist usually but the concentration of basic sites increases with decreasing acidic character of the surface. For all the samples except MF-C, the amount of basic groups is significantly higher than total amount of acidic groups. These results suggest that all the synthesized carbon adsorbents from nanocasting technique have mainly basic character.

4.4 CO_2 adsorption performance

4.4.1 Effect of carbonization temperature

Prepared nitrogen doped carbon adsorbents were evaluated for CO_2 adsorption capacity at 30 °C under 10% CO_2 concentration in N_2 and results are illustrated in Figure 4.13. The breakthrough curve for CO_2 adsorption is obtained by monitoring the CO_2 concentration at the exit of the adsorption bed as a function of time. At the outset of adsorption process, for the most part mass transfer takes place near the adsorption bed inlet when the adsorbate comes in contact with the adsorbent. At that time, the adsorbate concentration at the bed exit becomes zero. With time, adsorbate near the inlet becomes saturated and the mass transfer zone moves

further in the direction of adsorbate flow. This continues till the complete bed is saturated with the adsorbate. Adsorbate concentration at the outlet gradually increases and finally becomes equal to the inlet concentration when the adsorbent bed is completely saturated.

Two parameters namely equilibrium CO_2 adsorption capacity (q_e) and breakthrough time (t_b) are calculated. Breakthrough time is the time when effluent CO_2 concentration reaches 10% of inlet CO_2 concentration and typically the gas mixture is diverted to a fresh adsorbent bed on reaching this limit. CO_2 breakthrough curves of the prepared carbons tend to shift towards higher times as the carbonization temperature increased from 400 °C to 700 °C signifying higher CO_2 adsorption capacities at higher carbonization temperatures while increase in carbonization temperature to 800 °C resulted in shifting of the breakthrough curve to lower times indicating decline in adsorption capacity of MF-800 sample (Figure 4.13a). MF-700 carbon exhibited the highest t_b of ca. 3.5 minutes followed by MF-800 (1.9 minutes) and then MF-600 (0.24 minutes). MF-C carbon exhibited a very small t_b of ca. 0.15 minutes demonstrating very low CO_2 adsorption capacity.

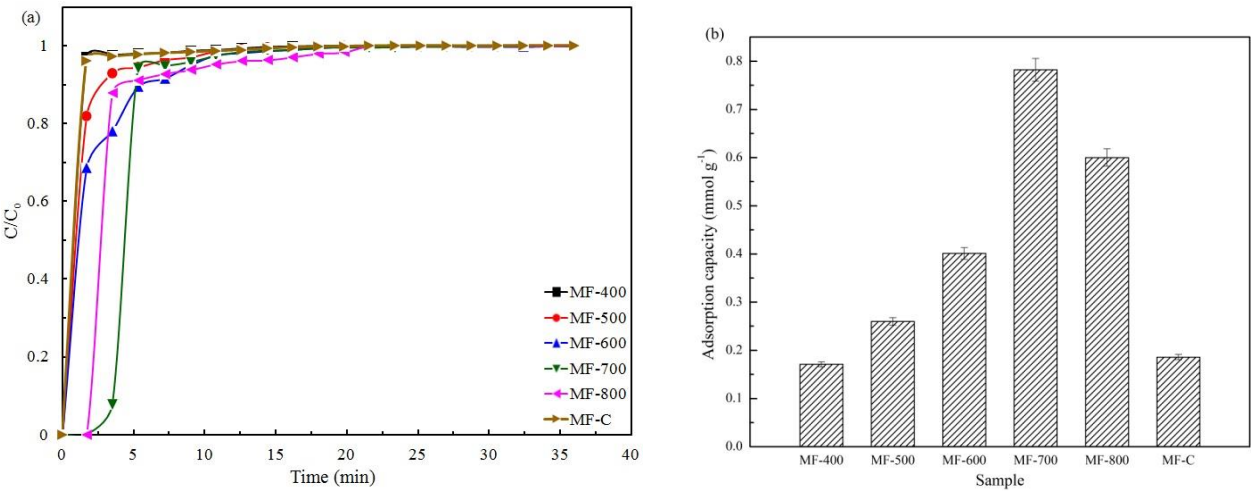

Figure 4.13 (a) Breakthrough profiles of CO_2 adsorption, and **(b)** CO_2 adsorption capacity of nitrogen doped carbon adsorbents at 30 °C and 10% CO_2 inlet concentration

As the carbonization temperature was increased from 400 °C to 700 °C, the dynamic adsorption capacity (q_e) is found to increase significantly reaching a maximum value of 0.782 mmol g^{-1} for MF-700 (Figure 4.13b). Adsorbents synthesized up to carbonization temperature of 600 °C have small CO_2 adsorption capacities due to relatively lower surface area and pore volume. On the other hand, carbonization at 700 °C introduced the microporosity in the adsorbent thereby significantly enhancing the textural properties like BET surface area and pore volume as well

as CO_2 adsorption capacity. Further increase in carbonization temperature to 800 °C resulted in decrease in value of q_e to 0.62 mmol g^{-1} at 30 °C and 10% CO_2 feed concentration which could be ascribed to decreased textural properties and surface basicity due to partial collapse of pore structure. On the other hand MF-C sample showed very small CO_2 uptake of 0.186 mmol g^{-1} under similar conditions due to very less development of pore structure.

On account of improved textural properties and enhanced basic character, MF-700 sample exhibited the best dynamic CO_2 adsorption capacity. N_2 sorption isotherms indicated the considerable enhancement in textural properties of MF-700 i.e. development of microporosity along with high mesopore volume. Presence of heteroatoms such as nitrogen and oxygen imparted high basic character to MF derived carbon. Carbonization up to 500 °C produced carbons having nitrogen functionalities majorly as pyrrolic and/or pyridonic nitrogen followed by quaternary nitrogen with very small amount of pyridinic nitrogen. In contrast, carbons obtained at carbonization temperature of equal or more than 600 °C have nitrogen moieties in the form of pyridinic nitrogen followed by pyrrolic and/or pyridonic nitrogen with low amount of quaternary nitrogen. Both pyridinic and pyrrolic and/or pyridonic form of nitrogen have been reported to have lone pair of electrons thereby exhibiting Lewis basicity, thus providing active sites for adsorption of acidic CO_2 gas. Pyridinic nitrogen has been reported to be more basic in nature than pyrrolic nitrogen and hence having higher affinity for CO_2 [144, 151]. On the other hand, quaternary nitrogen exhibits Lewis acidic character [96, 152]. Therefore, carbons obtained at or above 600 °C i.e. MF-600 to MF-800 have more basicity than rest of the two samples (MF-400 and MF-500). It should also be noted that adsorption capacity depends on the nature of nitrogen functionalities present on the surface and not on the total nitrogen content. Thus, CO_2 adsorption capacity of MF-600, MF-700 and MF-800 was found to be higher than that of MF-400 and MF-500 though total nitrogen content had decreased with carbonization temperature.

Surface chemistry of the prepared carbons is also affected by the nature of oxygen moieties present. Basic character to the carbon is imparted by carbonyls, ether and pyrone groups whereas phenols, carboxyls, lactols or lactones are responsible for acidic character of the carbon materials. Relative area contribution of carbonyl and pyrone groups was found to increase while A% of carboxyl and lactone/lactol groups decreased with rise in carbonization temperature as indicated by high resolution O1s spectra. However, it is not possible to distinguish ether and phenol functionality by XPS as both of them are found ca. 532.4 eV.

From Boehm titration method, surface basicity was found to increase with increase in carbonization temperature which may further enhance the adsorbent's affinity towards CO_2. As a result, it can be said that CO_2 adsorption capacity of the prepared carbons is dependent on both textural parameters and surface chemistry of the carbon materials. MF-700 has been selected for further adsorption studies on account of its best textural properties, high basicity along with highest dynamic CO_2 adsorption capacity among the prepared N-doped carbons.

4.4.2 Effect of adsorption temperature and CO_2 feed concentration

To investigate the effect of temperature and CO_2 feed concentration on CO_2 adsorption performance of synthesized carbon adsorbent, breakthrough adsorption experiments were carried out at four different temperatures ranging from 30 °C to 100 °C with four different feed CO_2 concentrations (5–12.5% by volume) and the breakthrough curves obtained for MF-700 as a function of adsorption temperature are depicted in Figure 4.14.

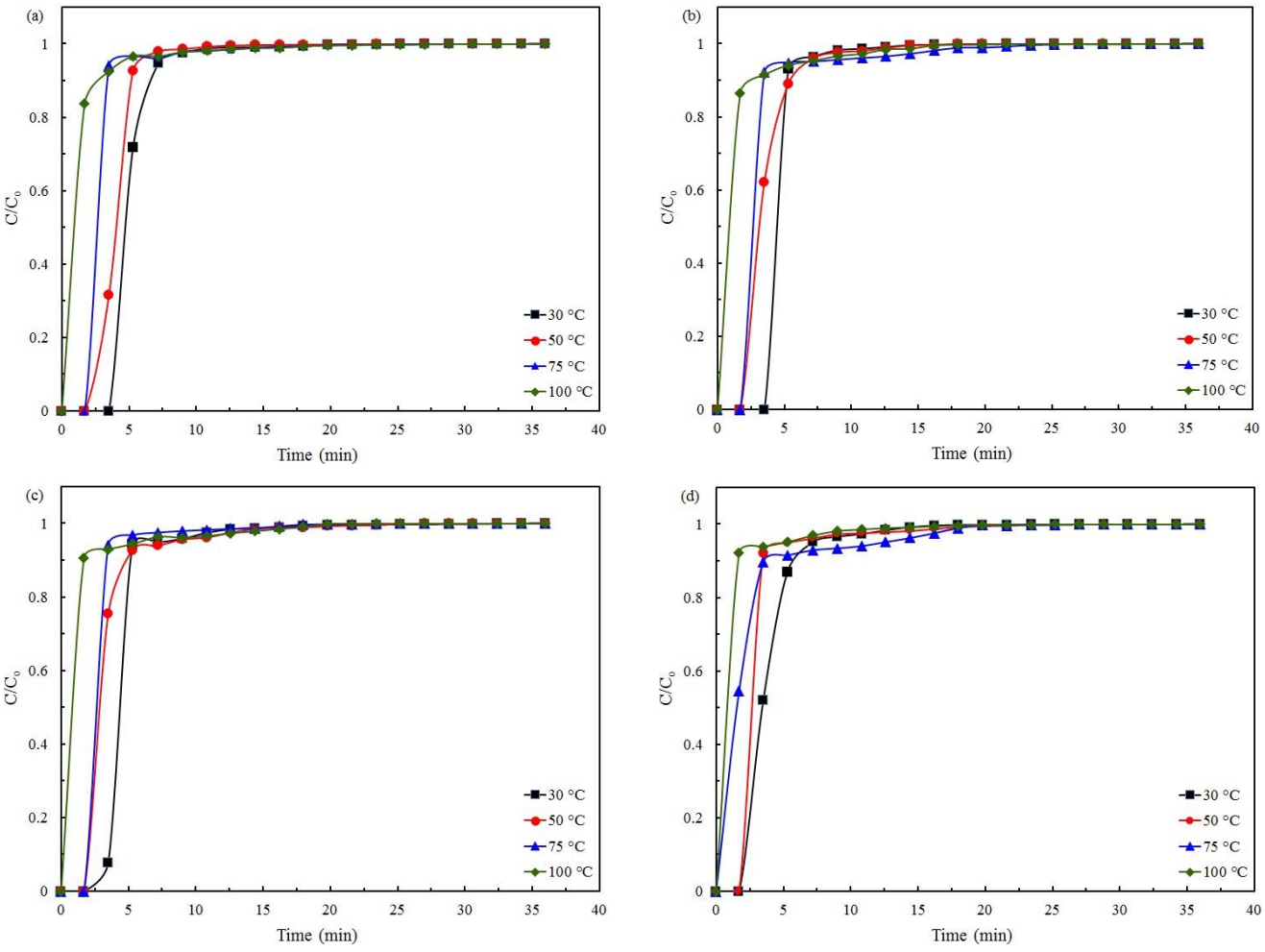

Figure 4.14 Breakthrough curves of MF-700 as a function of adsorption temperature at **(a)** 5%, **(b)** 7.5%, **(c)** 10%, and **(d)** 12.5 % feed CO_2 concentration in N_2

During the initial phase of the process, no CO_2 was detected in the outlet stream because of the complete adsorption. The ratio of C/C_o shows the gradual increase in outlet CO_2 concentration, where C and C_o refer to the outlet and inlet CO_2 concentrations respectively. For a fixed inlet CO_2 concentration, the breakthrough curve is found to shift towards lower times with increase in adsorption temperature. For 5% CO_2 concentration, t_b decreased from 3.84 min to 0.16 min as temperature increased from 30 °C to 100 °C. This elucidates the fall in CO_2 adsorption capacity with temperature. Besides, breakthrough time is observed to decrease with increase in inlet CO_2 concentration, for each temperature, though this change in t_b becomes smaller at higher temperature. For 100 °C, t_b is almost constant at 0.16 min for all CO_2 concentrations. Time required for outlet CO_2 concentration to become equal to inlet concentration i.e. equilibrium time also decreased with temperature due to more rapid movement of CO_2 in the carbon pores and hence faster adsorption kinetics.

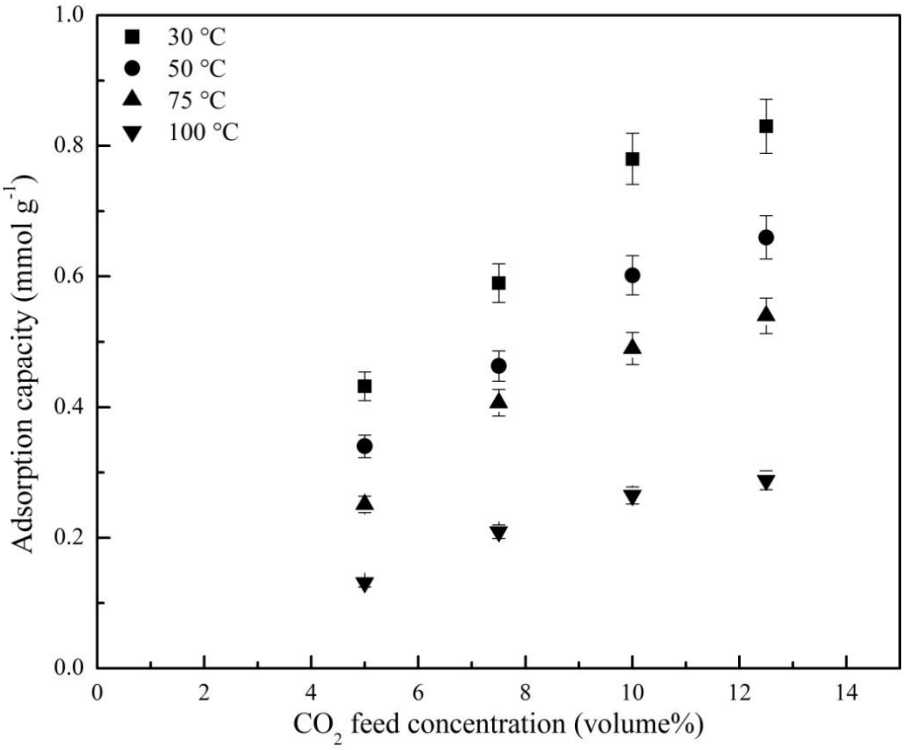

Figure 4.15 Adsorption capacity of MF-700 as a function of CO_2 feed concentration at different temperatures

Figure 4.15 presents the dynamic CO_2 adsorption capacity of MF-700 carbon as a function of CO_2 inlet concentration for all adsorption temperatures. Dynamic adsorption capacity tend to decrease with rise in adsorption temperature for all CO_2 inlet concentrations (Table 4.8), indicating exothermic nature of adsorption process. With increase in temperature, both surface

adsorption energy and rate of diffusion of adsorbate molecules increase thereby leading to instability of adsorbate molecules on adsorbent surface and hence leads to desorption. CO_2 adsorption capacity declined from 0.83 mmol g^{-1} to 0.29 mmol g^{-1} with increase in temperature from 30 °C to 100 °C under 12.5% CO_2 concentration This drop in adsorption capacity is more significant at higher CO_2 feed composition. For low CO_2 concentration, there is limited availability of CO_2 per site of adsorbent, thereby having less impact on decrease in CO_2 uptake with temperature.

Table 4.8 CO_2 adsorption capacity of MF-700 at different adsorption temperatures

CO_2 feed concentration (%)	CO_2 adsorption capacity (mmol g^{-1})			
	30 °C	50 °C	75 °C	100 °C
5	0.43	0.34	0.25	0.13
7.5	0.59	0.46	0.41	0.21
10	0.78	0.60	0.49	0.27
12.5	0.83	0.66	0.54	0.29

On the contrary at a given temperature, dynamic adsorption capacity was found to increase with increase in CO_2 gas concentration due to increased driving force and therefore, increased CO_2 mass transfer rate across the boundary and within the carbon pores at high CO_2 concentration. But the increment in CO_2 uptake decreases with increasing concentration and would reach saturation at a certain CO_2 partial pressure. With increase in concentration from 10% to 12.5% at 30 °C, there was only ~6% increase in CO_2 adsorption capacity whereas increase in CO_2 concentration from 7.5% to 10% lead to ~32% increment in CO_2 uptake. Dynamic adsorption capacities observed for MF-700 are in conformity with literature reported values for carbons under similar operating conditions [153]. Synthetic activated carbons, produced by carbonization and steam activation of coal tar pitch and furfural, exhibited dynamic CO_2 adsorption capacity of 0.61 mmol g^{-1} and 0.30 mmol g^{-1} under 15% CO_2 rest N_2 flow at 30 °C and 50 °C respectively [100]. MF-700 carbon exhibited adsorption capacity ~2 times than this synthetic carbon at 50 °C. Chemical ($ZnCl_2$) and physical (CO_2) activation of soybean produced carbons having dynamic adsorption capacity of 0.93 mmol g^{-1} and 0.51 mmol g^{-1} at 30 °C and 75 °C respectively under 15.4% CO_2 atmosphere. However, this carbon

was not regenerated completely during second cycle for adsorption at 75 °C thereby showing zero adsorption capacity in the next cycle [89]. Maroto-Valer et al. [86] reported CO_2 uptake of 0.93 mmol g^{-1} and 0.42 mmol g^{-1} at 30 °C and 75 °C respectively by fly ash derived activated carbons. Dynamic capacities of MF-700 are comparable with these activated carbons at higher adsorption temperatures suggesting them as potential candidates for adsorption of CO_2 under real flue gas conditions.

4.4.3 CO_2 selectivity

CO_2 adsorption selectivity is another important parameter along with the adsorption capacity of the adsorbent for an efficient adsorption process. Figure 4.16 shows the breakthrough curves for CO_2 and N_2 for adsorption on MF-700 in 12.5% CO_2 rest N_2 atmosphere at two adsorption temperatures i.e. 30 °C and 50 °C. It can be seen that N_2 is observed immediately at the exit of the adsorption column showing very small adsorption capacity for N_2. On the other hand, no CO_2 was detected for around 2 minutes, showing higher affinity towards CO_2.

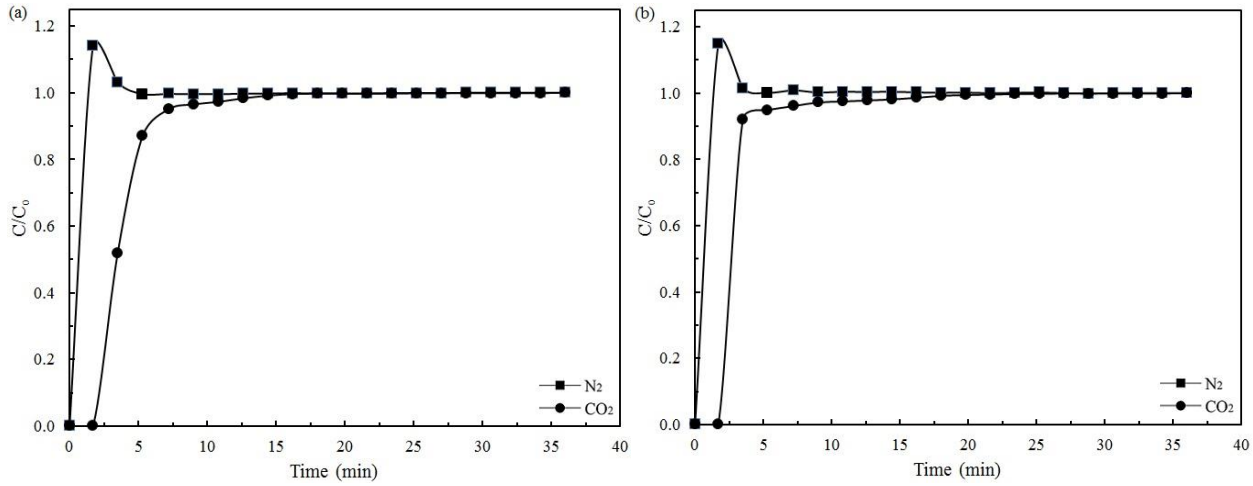

Figure 4.16 Breakthrough curves of CO_2 and N_2 for 12.5% CO_2 rest N_2 on MF-700 at **(a)** 30 °C, and **(b)** 50 °C

A hump ($C/C_o > 1$) is observed in breakthrough curve for N_2 which represents the competitive nature of the adsorption process. As the concentration of N_2 is higher than CO_2 in the feed gas, it occupies more sites on the adsorbent surface initially but with time adsorbed N_2 is displaced by CO_2 due to selectivity of adsorbent towards CO_2. Hence, concentration of N_2 at the exit shows a hump of concentration over that in the inlet gas. Presence of nitrogen on the carbon matrix results in basic carbon adsorbents with increased delocalized electrons, thereby enhancing their selectivity towards CO_2 over N_2.

4.4.4 Cyclic adsorption-desorption study

For long-term use of an adsorbent, another key factor is its reusability. Hence, multi-cycle adsorption-desorption experiments were conducted to assess the regenerability and cyclic stability of the prepared carbons. After the saturation of adsorbent with CO_2, gas flow was switched from simulated flue gas to pure N_2 with increase in bed temperature to 200 °C to carry out desorption. Figure 4.17a demonstrates the multi-cycle CO_2 adsorption-desorption profile of MF-700 for adsorption at 30 °C and 12.5% CO_2 concentration. It can be seen that complete saturation is achieved within 10 minutes. Adsorbed CO_2 was easily removed from the adsorbent surface as indicated by the sudden drop in CO_2 concentration profile.

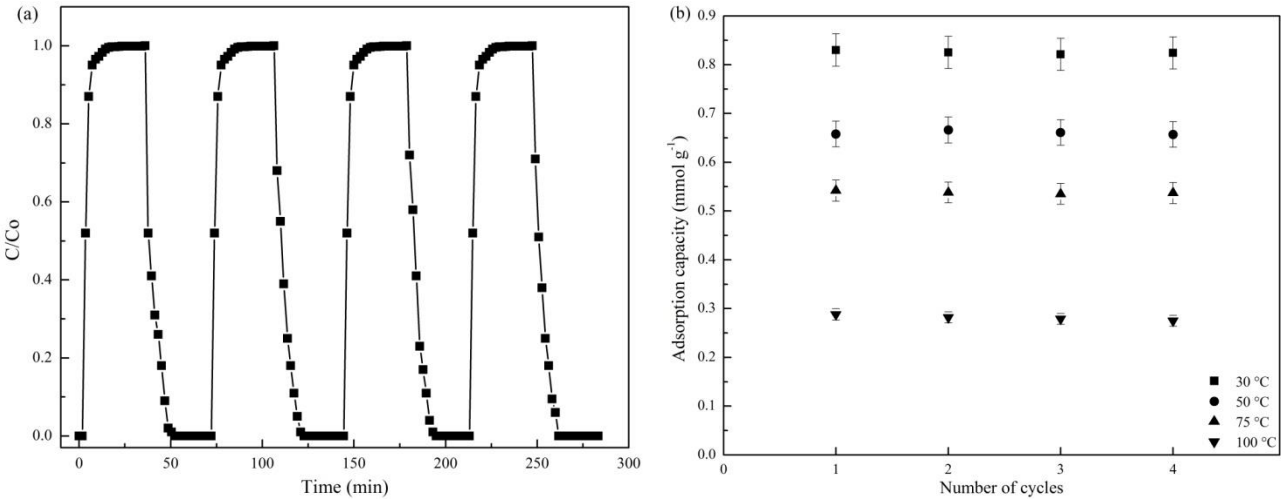

Figure 4.17 (a) Multi-cycle adsorption-desorption concentration profile for adsorption at 30 °C & 12.5% CO_2, and **(b)** Adsorption capacity over 4 consecutive adsorption-desorption cycles as a function of temperature at 12.5% CO_2 concentration

Figure 4.17b depicts the cyclic dynamic CO_2 adsorption capacity of MF-700 carbon at different adsorption temperatures under 12.5% CO_2 flow. CO_2 adsorption capacities for four runs were nearly identical showing complete regeneration and stability of MF-700 for long-term cyclic operations. Thus, temperature swing adsorption of CO_2 on prepared carbons is completely reversible. Sudden drop in CO_2 concentration profile could be due to removal of some physically adsorbed molecule but high temperature is required for the complete removal of adsorbed CO_2 as most of the CO_2 is strongly adsorbed on the carbon surface due to bonding with basic sites present on the material. This has been confirmed from the temperature programmed desorption (TPD) study of CO_2 on MF-700. It was carried out to identify the nature of adsorption process and the result is presented in Figure 4.18. Two desorption peaks

were observed in the temperature range of 65–85 °C and 200–225 °C. First desorption peak ca. 65–85 °C could be mainly due to removal of physically adsorbed CO_2 molecules while the second desorption peak ca. 200–225 °C indicates strong bonding, due to covalent bond formation, between MF based carbon and CO_2 molecules [154]. The second peak of MF-700 is centred at 210 °C at which CO_2 desorption is very high. This is possibly due to very high basic character of carbon surface imparted by basic nitrogen functionalities (pyridinic and pyridonic/pyrrolic nitrogen) and the same has been confirmed by XPS results. Moreover, desorption temperature also indicates the strength of the basic sites present on the material [155] and desorption of CO_2 at such high temperature of ca. 200 °C suggests existence of highly basic sites on the carbon surface thereby indicating chemisorption of CO_2 on nitrogen doped mesoporous carbon materials.

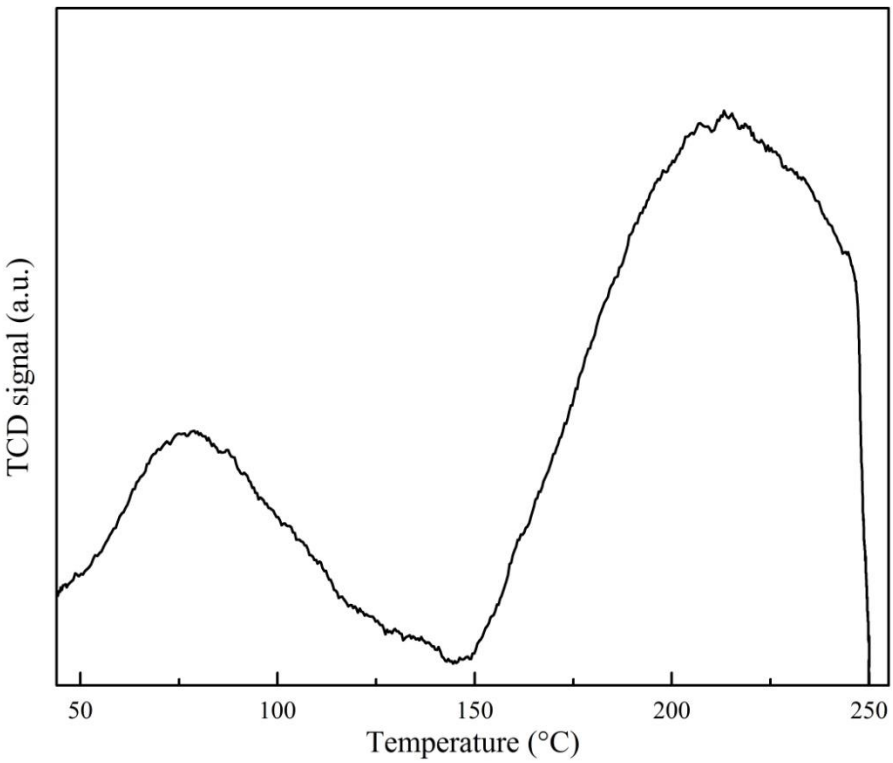

Figure 4.18 CO_2-Temperature programmed desorption profile of MF-700

4.5 Equilibrium sorption measurements

Among the prepared carbons as nitrogen doped mesoporous carbon obtained at 700 °C i.e. MF-700 exhibited the best textural and surface properties, equilibrium CO_2 and N_2 uptake of only this adsorbent was investigated at four different temperatures (30–100 °C). Figure 4.19 shows the adsorption-desorption isotherms of pure CO_2 and N_2 on MF-700 carbon as a function of

pressure at different temperatures. CO_2 was found to adsorb more strongly than N_2 on MF-700 at all adsorption temperatures. The amounts of CO_2 and N_2 adsorbed decreased with rise in adsorption temperature while they increased with increase in pressure. With increase in adsorption temperature from 30 °C to 100 °C, equilibrium CO_2 adsorption capacity decreased from 1.15 mmol g^{-1} to 0.52 mmol g^{-1} respectively at 1 atm. Adsorption-desorption isotherms of CO_2 and N_2 exhibited a hysteresis loop for all adsorption temperatures indicating requirement of small energy for adsorbent reuse. This energy requirement is because of strong binding between acidic CO_2 molecules with basic nitrogen functional groups present in the carbon matrix. N_2 uptake of MF-700 was very small with a maximum of ca. 0.08 mmol g^{-1} at 30 °C indicating higher selectivity of MF-700 towards CO_2 over N_2.

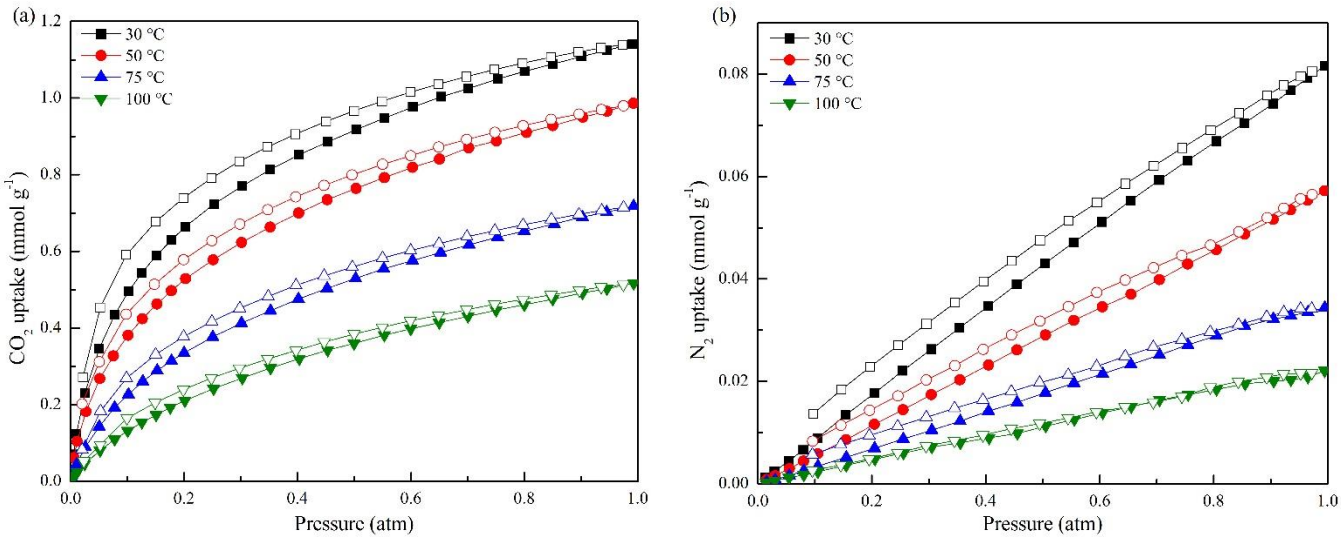

Figure 4.19 Adsorption (closed symbols) - desorption (open symbols) isotherms of **(a)** CO_2, and **(b)** N_2 on MF-700 at different adsorption temperatures (30–100 °C) as function of pressure

Carbon nitride materials prepared from polymerization of ethylenediamine and carbon tetrachloride in pores of mesoporous silica (FDU-12) followed by carbonization at 600 °C for 5 h exhibited CO_2 adsorption capacity of 1.4 mmol g^{-1} at 25 °C and 1 bar [110]. Direct pyrolysis of resorcinol, formaldehyde and lysine at 500 °C (RFL-500) produced carbon that exhibited very high CO_2 uptake of 3.13 mmol g^{-1} at 25 °C as compared to our material [95]. However, uptake of CO_2 at higher adsorption temperatures (100–120 °C) are comparable with MF-700 carbon. Also CO_2 adsorption capacity at higher temperatures has more relevance pertaining to CO_2 capture from flue gas.

4.6 Kinetic study

CO_2 adsorption kinetics on MF derived carbon was studied by isothermal adsorption at four different temperatures (30–100 °C) under varying CO_2 concentrations using three kinetic models i.e. pseudo-first order, pseudo-second order and fractional order kinetic models. Figure 4.20 shows the CO_2 adsorption capacity of MF-700 as a function of time at various adsorption temperatures and CO_2 feed concentrations and the corresponding adsorption profiles as predicted by different kinetic models. Most of the adsorption occurred within few minutes of contact with CO_2. Later on adsorption rate became slower until equilibrium condition was attained. During the adsorption process, there is an increase in diffusion resistance and reduction in the unoccupied active sites which leads to a decrease in the adsorption rate. Kinetic model parameters along with correlation coefficients (R^2) and associated errors (as calculated by Eq. (3.10)) are reported in Table 4.9.

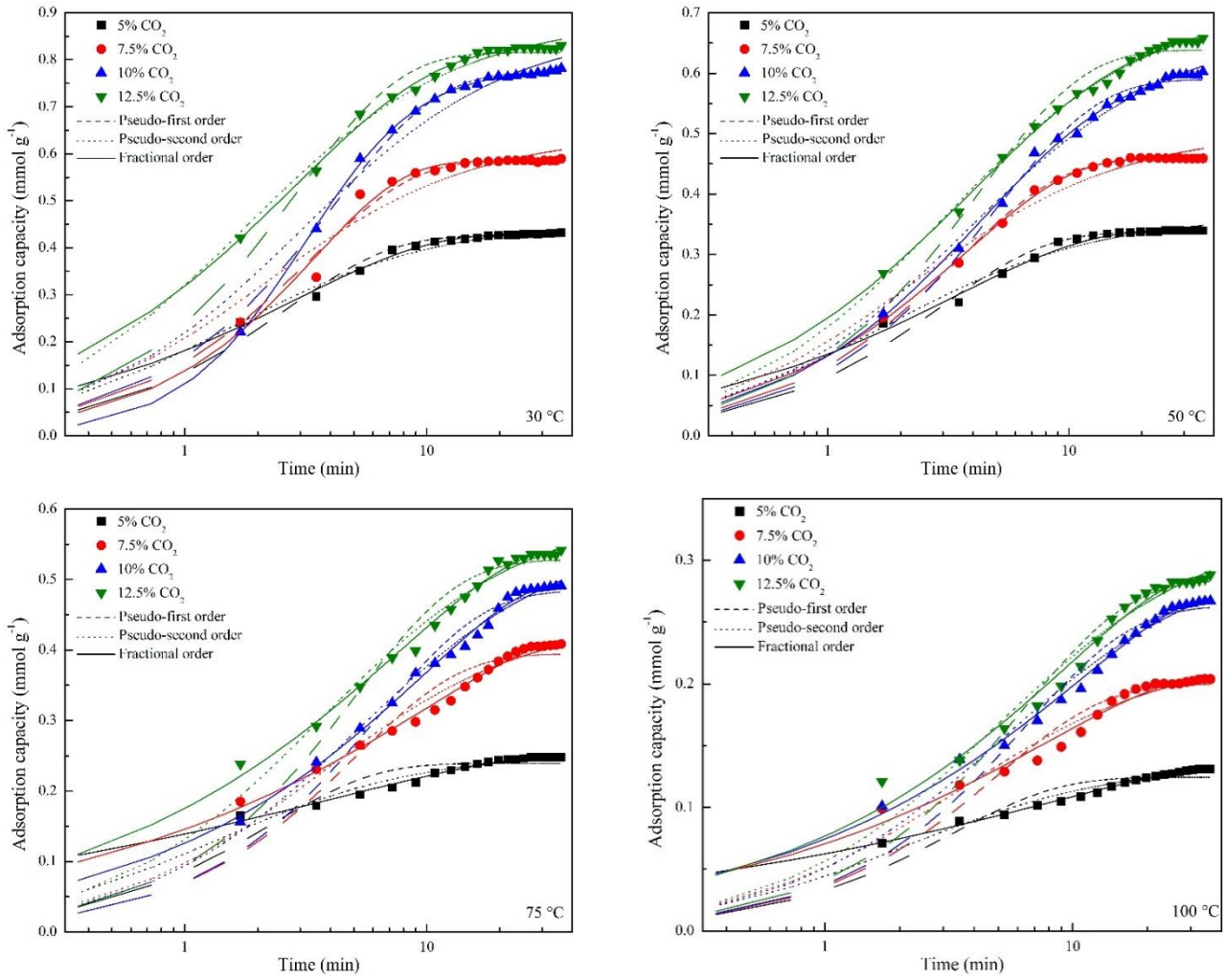

Figure 4.20 Experimental uptake of CO_2 on MF-700 carbon along with corresponding fit to adsorption kinetic models at different adsorption temperatures and CO_2 inlet concentrations

Pseudo-first order and pseudo-second order kinetic models showed some limitations with regard to prediction of CO_2 adsorption on MF-700 while fractional order kinetic model is observed to provide the best explanation of CO_2 adsorption process on mesoporous carbon adsorbent in the fixed bed. Pseudo-first order kinetic model underestimated the uptake of CO_2 up to 3–4 minutes at all adsorption temperatures and CO_2 concentrations. After this, it closely followed the adsorption process for adsorption at 30 °C and 50 °C while continuously overestimating the CO_2 uptake till equilibrium for adsorption at 75 °C and 100 °C under 5% and 7.5% CO_2 concentrations. In contrast for adsorption under 10% and 12.5% CO_2 concentrations, pseudo-first order kinetic model overestimated CO_2 uptake at all adsorption temperatures after ca. 3–4 minutes. Pseudo-second order kinetic model overestimated CO_2 uptake for adsorption at 30 °C and 50 °C while underestimated the same for adsorption at higher temperatures up to 3 minutes. Hereafter it closely followed the experimental data while predicting very high equilibrium capacities. On the other hand, pseudo-first order model was found to be in good accord with the experimental equilibrium capacities. Moreover, higher values of error %, based on normal standard deviation, for these two kinetic models suggest that these models are not strictly followed by the experimental CO_2 uptake for mesoporous carbon.

On the other hand, adsorption behavior as predicted by fractional order model was in good agreement with the experimental data over the entire adsorption region with maximum error of ca. 4.2%. Also predicted equilibrium adsorption capacity was also found to be in good concord with the experimental value. Lower values of error % from fractional order model compared to pseudo-first and pseudo-second order models, within the range of adsorption temperature and CO_2 feed concentration, recommend its applicability for mesoporous carbon adsorbent.

Table 4.9 Kinetic model parameters for adsorption of CO_2 on MF-700 at different CO feed concentrations and adsorption temperatures

Adsorption temp. (°C)	CO_2 concn. (volume %)	Pseudo-first order model				Pseudo-second order model				Fractional order model					
		k_1 (min^{-1})	q_e (mmol g^{-1})	R^2	Error %	k_2 (g $mmol^{-1}$ min^{-1})	q_e (mmol g^{-1})	R^2	Error %	k_n ($mmol^{1-m}$ g^{m-1} min^{-n})	q_e (mmol g^{-1})	n	m	R^2	Error %
30	5	0.381	0.425	0.987	4.177	1.434	0.457	0.992	1.746	0.268	0.429	0.796	0.627	0.997	1.678
	7.5	0.308	0.587	0.989	4.012	0.737	0.644	0.962	7.486	0.295	0.584	0.921	1.081	0.989	4.017
	10	0.244	0.773	0.996	4.480	0.383	0.871	0.976	10.414	0.307	0.783	1.755	1.614	0.999	0.749
	12.5	0.347	0.815	0.989	3.828	0.639	0.885	0.996	1.864	0.334	0.829	1.954	1.703	0.998	1.097
50	5	0.341	0.337	0.983	5.163	1.576	0.365	0.988	3.232	0.168	0.340	0.760	0.606	0.995	2.360
	7.5	0.290	0.459	0.998	2.213	0.883	0.505	0.985	4.150	0.192	0.459	0.850	0.837	0.999	1.067
	10	0.203	0.589	0.993	4.026	0.398	0.675	0.996	2.480	0.272	0.615	1.302	0.943	0.998	1.579
	12.5	0.235	0.638	0.982	5.807	0.465	0.718	0.998	1.559	0.268	0.677	1.364	0.960	0.998	1.279
75	5	0.446	0.239	0.933	7.556	2.979	0.256	0.984	3.810	0.085	0.249	0.466	0.290	0.997	1.627
	7.5	0.196	0.394	0.938	10.959	0.622	0.448	0.980	6.137	0.091	0.412	0.490	0.405	0.996	1.928
	10	0.158	0.484	0.979	7.791	0.344	0.569	0.995	2.997	0.111	0.493	0.521	0.565	0.996	2.223

	12.5	0.198	0.528	0.961	9.418	0.465	0.599	0.987	5.046	0.156	0.541	0.532	0.599	0.996	2.294
100	5	0.307	0.124	0.928	8.891	3.505	0.137	0.983	4.306	0.042	0.132	0.347	0.298	0.998	1.149
	7.5	0.201	0.200	0.939	11.142	1.307	0.225	0.972	7.015	0.057	0.205	0.403	0.465	0.987	4.101
	10	0.155	0.263	0.961	10.919	0.640	0.308	0.985	6.571	0.072	0.269	0.445	0.503	0.996	2.594
	12.5	0.159	0.284	0.960	11.153	0.619	0.331	0.977	7.705	0.088	0.288	0.523	0.554	0.991	4.161

As CO_2 adsorption is an exothermic process and is favored at lower temperatures, there was a decrease in adsorption rate constant k_n with increase in adsorption temperature. Parameters n and m of fractional order model indicate the effect of the driving force and diffusion resistance respectively. It has been reported that effect of driving force is also related to adsorption apparatus and mode of filling of adsorbent [121]. But in the present study as the adsorption apparatus and filling method have been same thus the effect of these two parameters on parameter n may not be significant. With increase in CO_2 inlet concentration, n is found to increase which could be ascribed to the increased driving force at higher CO_2 concentrations that helps in diffusion of CO_2 into the carbon adsorbent. Pseudo-order with respect to driving force i.e. n had the maximum value at 30 °C and decreased with increase in adsorption temperature thereby indicating the large driving force at 30 °C. Parameter m indicates the fastness of the adsorption process and its value increased with increasing CO_2 concentrations thus showing faster adsorption at higher CO_2 concentrations.

Temperature dependence of fractional order kinetic constants was described by Arrhenius equation. The plot of $ln\ (k_n)$ vs. $1/T$ for adsorption of CO_2 on MF-700 is depicted in Figure 4.21 and the parameters of Arrhenius equation, obtained by nonlinear regression, are listed in Table 4.10. Value of activation energy (E_a) was found to be negative (deactivation) which was due to declining rate constant values with increasing temperatures. Negative activation energies have been reported by few research groups and such reactions have been considered as typically barrierless ones in which reaction is dependent on capture of molecules in the potential well [156, 157]. Moreover, absolute value of E_a decreased with increase in CO_2 concentration which is indicative of facilitated CO_2 adsorption at high partial pressure of CO_2.

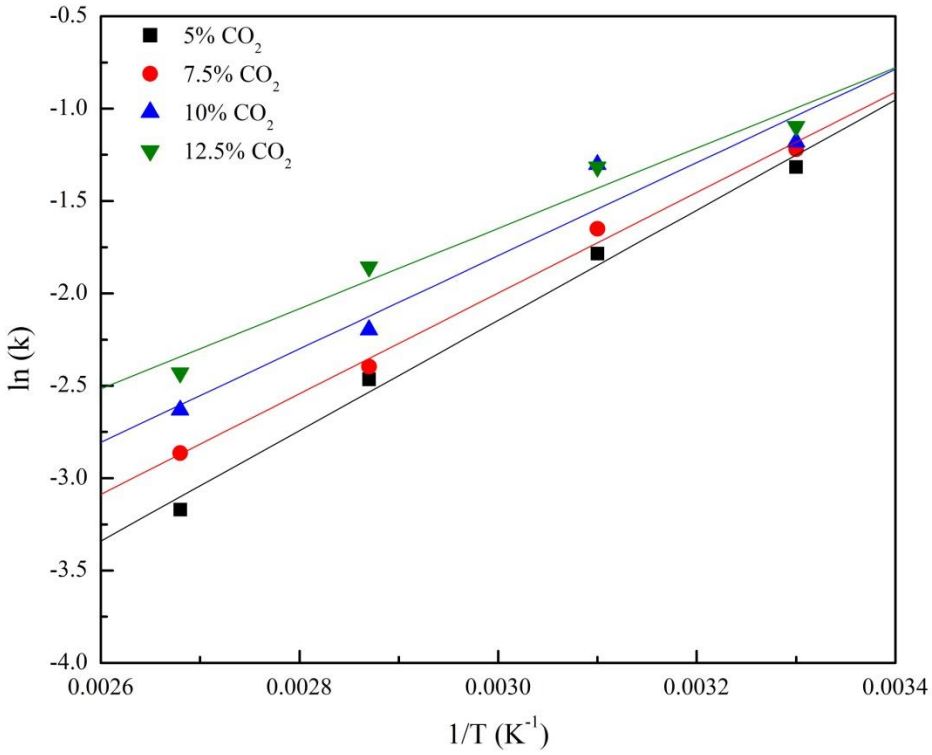

Figure 4.21 Arrhenius plot for fractional order kinetic rate constant of CO_2 adsorption on MF-700

Table 4.10 Parameters of Arrhenius equation for adsorption of CO_2 on MF-700

CO_2 concentration (volume %)	A	E_a (kJ mol^{-1})	R^2
5	1.46×10^{-5}	-24.914	0.990
7.5	3.72×10^{-5}	-22.726	0.992
10	8.39×10^{-5}	-21.031	0.941
12.5	2.78×10^{-4}	-18.127	0.965

4.7 Isotherm study

4.7.1 Pure component isotherm

Experimental data of pure component adsorption of CO_2 and N_2 on MF-700 were fitted by using three pure component isotherm models i.e. Langmuir, Sips and dual-site Langmuir isotherm models at different adsorption temperatures. The experimental data and the model predicted isotherms for both the adsorbates are presented in Figure 4.22 and the obtained model parameters along with sum of the squared relative errors (SSE) are reported in Tables 4.11–4.13.

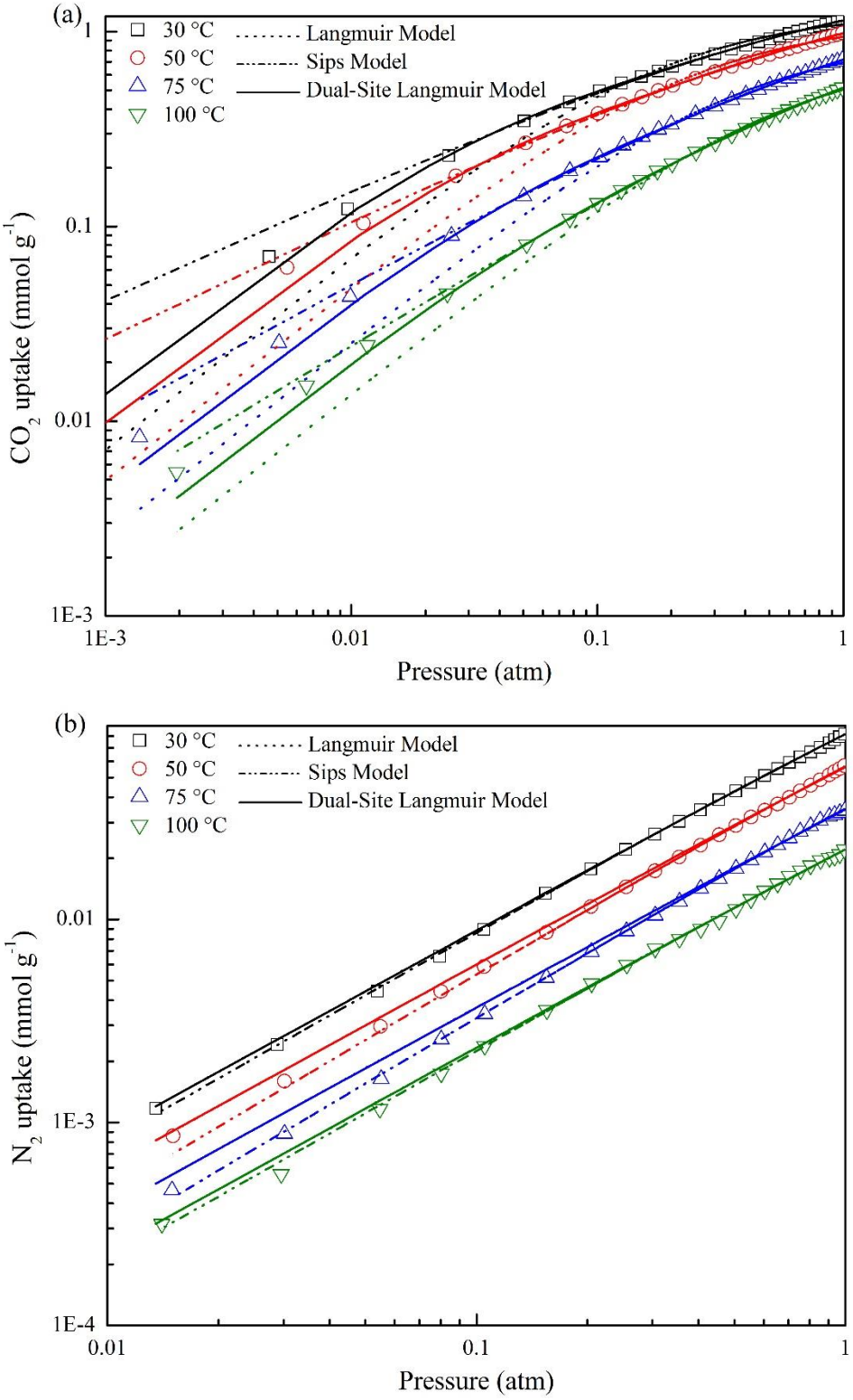

Figure 4.22 Experimental adsorption isotherms of **(a)** CO_2, and **(b)** N_2 on MF-700 at different temperatures and their corresponding isotherm model fits

Langmuir adsorption isotherm model is thermodynamically sound and exhibits correct asymptotic behavior as it approaches Henry's law in the low pressure range. But this model

could not explain well adsorption of CO_2 on MF-700 at all adsorption temperatures. It continuously deviated from the experimental data at all pressures, with SSE in the range of 16–22%, though it has been reported to be suitable for adsorption in low pressure regions. On the other hand, experimental data of CO_2 adsorption was fitted considerably better by both Sips and DSL isotherm models as compared to Langmuir isotherm model and the same is indicated by lower values of SSE for Sips (< 4.5%) and DSL (< 3.8%) models than Langmuir model. Heterogeneity of the adsorbent surface is signified from these results. Several research groups have also shown the conformity of Sips and DSL equation with CO_2 adsorption on carbon materials [127, 158]. Adsorption of N_2 was explained well by all the three isotherm models and a small difference is found between them. This could be due to linear shape of N_2 isotherm which can be fitted reasonably well with all these isotherm models [158].

Table 4.11 Langmuir isotherm model parameters for pure component adsorption on MF-700 at different temperatures

Component	Parameter	Temperature (°C)			
		30	50	75	100
CO_2	q_m (mmol g^{-1})	1.29	1.16	0.95	0.78
	b (atm^{-1})	5.63	4.34	2.73	1.79
	SSE (%)	20.37	22.08	18.93	16.23
	b_o (atm^{-1})	0.0122			
	B (kJ mol^{-1})	-15.586			
N_2	q_m (mmol g^{-1})	1.03	0.85	0.58	0.39
	b (atm^{-1})	0.086	0.071	0.064	0.060
	SSE (%)	2.56	5.12	6.03	7.34
	b_o (atm^{-1})	0.0130			
	B (kJ mol^{-1})	-4.675			

Table 4.12 Sips isotherm model parameters for pure component adsorption on MF-700 at different temperatures

Component	Parameter	Temperature (°C)			
		30	50	75	100
CO_2	q_m (mmol g^{-1})	2.26	2.02	1.62	1.30
	b (atm^{-c})	1.028	0.937	0.793	0.655
	c	1.728	1.621	1.434	1.302
	SSE (%)	4.40	1.78	3.17	2.47
	b_o (atm^{-c})	0.0953			
	B (kJ mol^{-1})	-6.058			
N_2	q_m (mmol g^{-1})	0.661	0.495	0.326	0.223
	b (atm^{-c})	0.141	0.130	0.121	0.110
	c	0.971	0.930	0.928	0.969
	SSE (%)	1.59	7.70	6.46	5.91
	b_o (atm^{-c})	0.0392			
	B (kJ mol^{-1})	-3.227			

Table 4.13 Dual-site Langmuir isotherm model parameters for pure component adsorption on MF-700 at different temperatures

Component	Parameter	Temperature (°C)			
		30	50	75	100
CO_2	$q_{1,m}$ (mmol g^{-1})	0.508	0.404	0.253	0.142
	$q_{2,m}$ (mmol g^{-1})	1.195	1.254	1.128	0.973
	b_1 (atm^{-1})	25.765	22.235	14.238	10.329
	b_2 (atm^{-1})	1.200	0.909	0.746	0.657

	SSE (%)	3.04	2.79	3.70	3.09
	$b_{o,1}$ (atm^{-1})	0.174		$b_{o,2}$ (atm^{-1})	0.048
	E_1 (kJ mol^{-1})	-12.749		E_2 (kJ mol^{-1})	-8.029
	$q_{1,m}$ (mmol g^{-1})	0.406	0.326	0.204	0.195
	$q_{2,m}$ (mmol g^{-1})	0.627	0.502	0.385	0.195
	b_1 (atm^{-1})	0.0863	0.0730	0.0629	0.0604
N_2	b_2 (atm^{-1})	0.0859	0.0729	0.0628	0.0604
	SSE (%)	2.55	2.69	5.65	7.27
	$b_{o,1}$ (atm^{-1})	0.0120		$b_{o,2}$ (atm^{-1})	0.0123
	E_1 (kJ mol^{-1})	-4.905		E_2 (kJ mol^{-1})	-4.838

Parameter *b* of these isotherm models indicates the affinity of adsorbate towards the adsorbent surface and significantly higher values of *b* were obtained for CO_2 as compared to N_2. Moreover, higher values of q_m were obtained for CO_2 adsorption than N_2 in all the three isotherm models. For adsorption of N_2 on MF-700, values of parameters b_1 and b_2 in DSL isotherm are almost equal thereby indicating that component 2 i.e. N_2 in the binary system considers both the adsorption sites as equal free-energy sites. Hence, there will be no energetic site-matching issue and component 1 i.e. CO_2 will see site 1 as high free energy site and site 2 as low free energy site. So, there will be only one value of adsorbed amount for an adsorbate at a given temperature and gas composition conditions. Decrease in value of parameter *b* (Langmuir and Sips model), b_1 and b_2 with temperature indicates exothermic nature of adsorption process. Heterogeneity of the adsorbent surface is indicated by parameter *c* of Sips isotherm model and deviation in value of *c* from unity in case of CO_2 indicates heterogeneity of the adsorption process.

4.7.2 Binary component isotherm

As pure component adsorption data of CO_2 and N_2 on MF-700 was explained suitably by Sips and DSL isotherm models, only these models were extended for binary component adsorption. Also, ideal adsorbed solution theory was applied to isotherms of these two pure component

models. Total and partial adsorbed amounts of CO_2 and N_2, in binary system, on MF-700 at different adsorption temperatures are depicted in Figure 4.23. Comparison between predicted adsorbed amounts of CO_2 from Sips, DSL, IAST-Sips and IAST-DSL isotherm models and experimental values of CO_2 adsorbed is presented in Table 4.14.

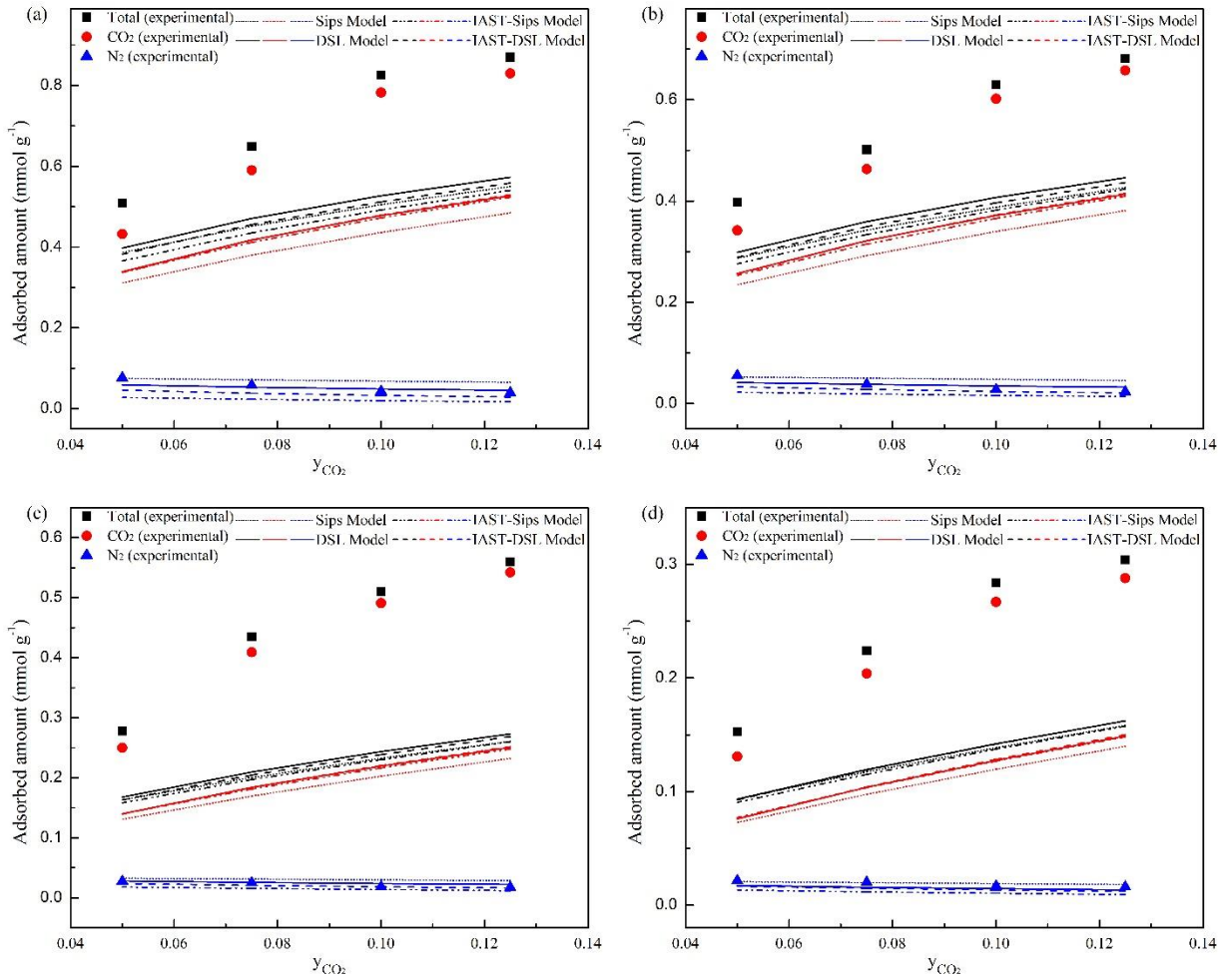

Figure 4.23 Binary adsorption isotherms for CO_2-N_2 mixture on MF-700 at **(a)** 30 °C, **(b)** 50 °C, **(c)** 75 °C, and **(d)** 100 °C (symbols represent experimental data and lines represent model predicted data)

It can be seen that both Sips and DSL equations varied wildly in their prediction of CO_2 adsorbed amounts. Binary system DSL equation predicted higher CO_2 adsorption capacity than binary component Sips equation while lower capacity for N_2 adsorption. But both the isotherm models predicted significantly lower CO_2 adsorption capacities compared to breakthrough capacities. IAST forms of these two isotherm models predicted almost similar capacities for CO_2 although these values were considerably lower than the experimental values. Uptake of N_2 was also under predicted by IAST forms of both Sips and DSL models. Therefore, it can be

concluded that all the models used in the present study to predict binary system adsorption equilibria (from pure component adsorption isotherms) deviated greatly from the experimental data (obtained from binary breakthrough curves). Total and partial adsorbed amounts were highly under predicted by all these models with maximum under estimation by Sips and IAST based Sips isotherm models for CO_2 and N_2 adsorption respectively.

Table 4.14 Comparison of experimental and predicted binary system CO_2 adsorption capacities on MF-700 based on binary component adsorption isotherms

Temperature	CO_2 mole fraction in feed	CO_2 adsorption capacity (mmol g^{-1})				
		Experimental	Sips model	DSL model	IAST-Sips model	IAST-DSL model
30 °C	0.050	0.432	0.311	0.339	0.337	0.337
	0.075	0.590	0.380	0.418	0.412	0.417
	0.100	0.782	0.436	0.478	0.472	0.479
	0.125	0.830	0.484	0.527	0.523	0.529
50 °C	0.050	0.342	0.235	0.257	0.253	0.256
	0.075	0.463	0.292	0.322	0.315	0.321
	0.100	0.602	0.340	0.372	0.366	0.373
	0.125	0.658	0.381	0.413	0.409	0.415
75 °C	0.050	0.250	0.131	0.140	0.140	0.140
	0.075	0.409	0.169	0.184	0.181	0.184
	0.100	0.491	0.203	0.220	0.216	0.220
	0.125	0.542	0.232	0.251	0.248	0.252
100 °C	0.050	0.131	0.073	0.076	0.077	0.076
	0.075	0.204	0.098	0.104	0.103	0.104
	0.100	0.267	0.120	0.128	0.127	0.128
	0.125	0.288	0.140	0.149	0.148	0.150

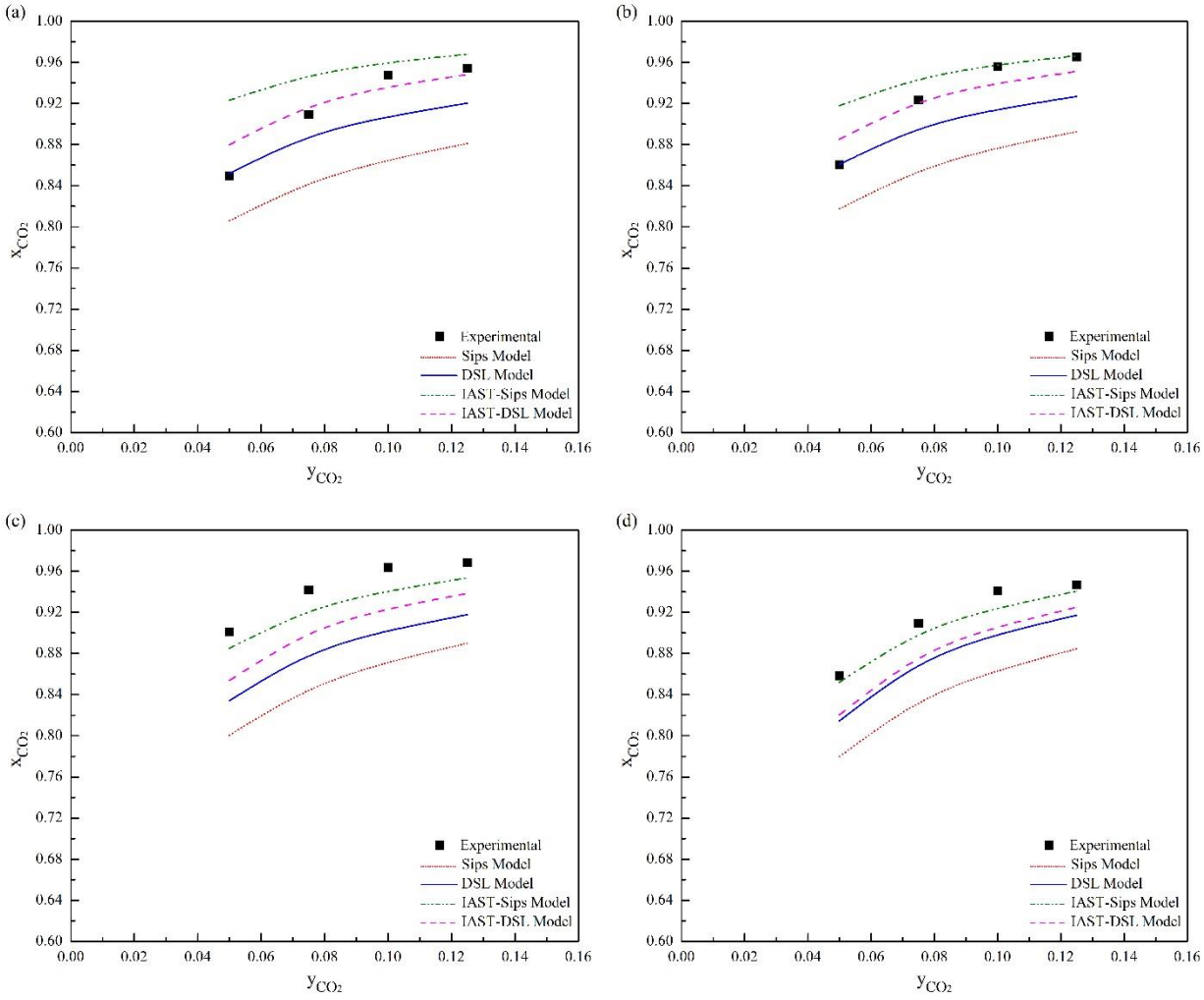

Figure 4.24 *x-y* diagram for binary adsorption of CO_2 and N_2 on MF-700 at **(a)** 30 °C, **(b)** 50 °C, **(c)** 75 °C, and **(d)** 100 °C

Figure 4.24 presents the molar fraction of CO_2 in adsorbed phase vs. that in gas phase for CO_2-N_2 binary system determined experimentally and model predicted for different adsorption temperatures. Maximum deviation in predicting x for a given y was observed for Sips model followed by DSL model. This is in accord with trend of the partial adsorbed amounts by these models. However, IAST based models closely followed the experimental curves data for CO_2 mole fraction in adsorbed phase at 30 °C and 50 °C while at higher temperatures IAST models under predicted x_{CO_2}. In contrast to vapor-liquid equilibrium, the *x-y* diagram for a gas-solid equilibrium is a function of both temperature and pressure on account of extra degrees of freedom in this system. Also, symmetric *x-y* diagrams along with rising total adsorbed amount with molar fraction in gas phase are exhibited by gas mixtures showing ideal behavior at equilibrium [159]. Adsorption of CO_2-N_2 gas mixture on MF-700 does not show symmetric *x-*

y diagram though total adsorbed amount increased with gas phase molar fraction. This suggests that carbon dioxide and nitrogen do not form ideal adsorptive mixtures on mesoporous carbon MF-700.

Adsorption selectivity of CO_2 over N_2 was also calculated from breakthrough curves under dynamic conditions and was then compared with adsorption selectivity estimated from various isotherm models along with from application of IAST to isotherm models. The results are presented in Table 4.15 and an appreciable difference in the experimental and predicted values was observed. This is on account of inability of multicomponent adsorption isotherm models in predicting mixed gas adsorption equilibria. It can be seen that binary component Sips and DSL equations under predicted selectivity of CO_2 over N_2. While IAST based Sips equation over estimated adsorption selectivity to a great extent for adsorption at 30 °C and 50 °C and under estimated for adsorption at higher temperatures. Selectivity of CO_2 over N_2 obtained from breakthrough curves tend to increase with increase in CO_2 feed fraction while Sips and DSL equations predicted a decrease in this value and IAST based these models predicted almost constant selectivity over complete range of CO_2 feed fraction.

Table 4.15 Experimental and isotherm model predicted selectivities for CO_2-N_2 binary system on MF-700

Temp.	CO_2 mole fraction in feed	Experimental	Sips model	DSL model	IAST-Sips model	IAST-DSL model
30 °C	0.050	107.5	78.9	109.4	228.7	139.4
	0.075	123.9	65.5	96.6	217.5	134.4
	0.100	163.2	57.4	87.6	213.3	130.8
	0.125	145.7	51.9	80.9	212.6	128.2
50 °C	0.050	117.2	85.1	117.6	212.4	146.8
	0.075	148.4	71.9	104.8	203.9	142.3
	0.100	196.4	63.8	95.7	201.8	139.1
	0.125	196.4	58.2	88.7	202.9	136.9

75 °C	0.050	172.6	76.3	95.6	146.4	111.0
	0.075	199.9	66.8	88.3	142.1	109.0
	0.100	238.5	60.8	82.7	141.7	107.7
	0.125	215.7	56.6	78.3	143.2	106.7
100 °C	0.050	114.9	67.3	83.5	109.5	86.8
	0.075	124.0	60.9	81.1	108.2	86.4
	0.100	143.6	56.7	79.2	109.0	86.2
	0.125	125.0	53.6	77.6	110.9	86.3

It is important to note that Sips and DSL isotherm models for a multicomponent system are reported to predict equilibrium capacities accurately when saturation adsorption capacity of each component in the system are comparable. Whereas in case of large difference between the saturation capacities of the adsorbates, these isotherm models result in significant error in the prediction of equilibrium loadings [160].

Prediction of adsorption equilibria of a multicomponent system by IAST necessitates pure component adsorption isotherms to be extrapolated beyond the pressure range over which pure component adsorption data was collected and isotherm was fitted. This is on account of adsorbate's spreading pressure equality at equilibrium. Generally, isotherm of weakly adsorbed component is extrapolated to a larger degree as spreading pressure is associated with adsorbed amount and hence may lead to uncertainty in multicomponent predictions by IAST. Furthermore, ideal adsorbed solution theory bestows good predictions of adsorption capacities and selectivites in multicomponent systems which are usually ideal in nature with all the components, present in the system, having similar adsorption levels. But IAST is not able to predict the adsorption performance of multicomponent systems having species that vary in size, polarity considerably and/or components not having comparable adsorption capacities. Also, IAST leads to inadequate predictions of adsorption capacity in case of heterogeneous adsorbents. It provides relatively accurate multi-component behavior of systems such as CH_4-CO_2, CH_4-N_2, noble gases etc. [161]. In the present study, IAST based models under predicted the adsorption behavior of CO_2-N_2 system which is due to difference in their adsorption levels.

CO_2 was found to adsorb strongly as compared to N_2 leading to different adsorption strengths thereby resulting in deviation in behavior of an ideal mixture and incorrect behavior prediction of binary system by IAST.

Despite these limitations, IAST has been used extensively and is considered a standard for predicting mixed-gas adsorption equilibria. Most of the work for predicting mixed-gas adsorption equilibria has been studied for CO_2 adsorption in high pressure regions generally pertaining to pre-combustion capture application. Separation of CO_2 from CO_2/N_2 mixture by NaX zeolite in a PSA system was well predicted by IAST while extended Langmuir isotherm could not capture the proper behavior of CO_2 and N_2 adsorption [162]. Caldwell et al. [158] related equilibrium adsorption capacities of CO_2 and N_2 with breakthrough capacities obtained from fixed-bed experiments for high pressure CO_2 capture application. Multicomponent adsorption equilibria was well explained by dual-site Langmuir isotherm model for CO_2-N_2 system on activated carbons while Sips and IAST based DSL models under predicted CO_2 uptake.

4.8 Thermodynamic study

4.8.1 Thermodynamic parameters

All the thermodynamic parameters for adsorption of CO_2 and N_2 on MF-700 were calculated by numerical analysis using Eqs. (3.35) – (3.37) based on Sips isotherm model. For the given adsorption system, similar adsorption behavior was observed at different adsorption temperatures hence thermodynamic parameters for adsorption at 30 °C only are presented in Figure 4.25. The integral molar Gibbs free energy change of adsorption process was found to be negative at all temperatures suggesting the feasibility and spontaneity of the process. Moreover, it was found to fall off monotonically on MF-700 with increase in pressure for both CO_2 and N_2. This indicates that higher isothermal work is needed as compared to the initial adsorption process for packing more number of adsorbate molecules into the adsorbent's cavity space because of screened sites in the later stage. At the same coverage of 0.08 mmol g^{-1}, ΔG on MF-700 for CO_2 and N_2 were -2.13 and -2.57 kJ mol^{-1} respectively implying less work requirement for loading of CO_2 on MF-700 than N_2 [163].

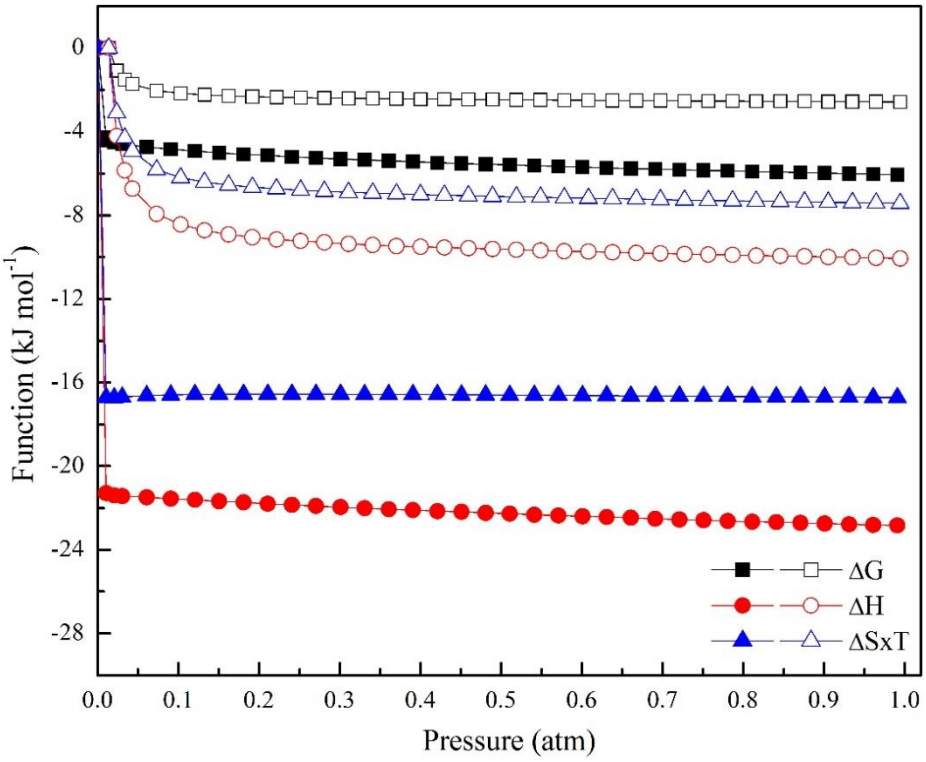

Figure 4.25 Thermodynamic functions *(ΔG, ΔH* and ΔS×T*)* for CO_2 (closed symbols) and N_2 (open symbols) on MF-700 at 30 °C

Value of ΔS×T was also found to be negative for both the adsorbates at 30 °C over the complete pressure range demonstrating that adsorption of CO_2 and N_2 was from a random to an ordered stage on adsorbent surface. As the loading in adsorption proceeds, degrees of freedom associated with adsorbed molecules decreases and leads to the formation of more ordered arrangement in carbon adsorbent cavities. For N_2, ΔS×T tend to decrease gradually while almost constant entropy was observed for CO_2. With increase in loading, cavity's free space becomes minimal with adsorbate molecules' freedom becoming extremely limited. This elucidates decrease in entropy for N_2 adsorption and cavity filling by N_2 adsorption is considered to be homogenous. On the other hand, slight increase in entropy of CO_2 over low pressure region signifies that CO_2 adsorption on MF-700 is a heterogeneous process [134, 164]. At the same coverage of 0.08 mmol g^{-1}, ΔS×T values for CO_2 and N_2 adsorption on MF-700 at 30 °C are -10.31 and -7.41 kJ mol^{-1} respectively. More negative value of entropy for CO_2 adsorption than N_2 adsorption indicates lower degree of disorder for CO_2 while higher degree of disorder for N_2, as entropy is also taken as measure of disorder. This also indicates formation of more ordered configuration by CO_2 on carbon surface i.e. lesser degree of freedom of constrained CO_2 after it adsorbed onto carbon adsorbent. Higher ordered configuration or efficient packing of CO_2 on the adsorbent cavity is because of localized adsorption which is

due to its higher quadrupole moment than N_2. These quadrupole moments of both CO_2 and N_2 interact with electrostatic-field gradients thereby causing increased rotation and hence orientation of these molecules producing more efficient packing and this is more evident for CO_2 than N_2 due to its about three fold quadrupole moment than N_2 [135].

Adsorption of CO_2 and N_2 on MF-700 at 30 °C are exothermic in nature as illustrated by negative values of integral molar enthalpy change. ΔH followed the similar trend as that of $\Delta S \times T$. Integral molar enthalpy change of CO_2 on MF-700 ranged from -21.29 to -22.84 kJ mol^{-1} as the pressure increased from 0.01 to 1 atm while that of N_2 varied from -4.21 to -10.06 kJ mol^{-1}. Higher release of heat during adsorption process is associated with more effective molecule packing. Value of ΔH for adsorption of CO_2 on prepared carbon is in good accord with other activated carbons like Maxsorb III (-20.37 kJ mol^{-1}) [165], coal based activated carbon (21.89 kJ mol^{-1}) [166], activated carbon beads (-23.17 kJ mol^{-1}) [167] etc.

As these parameters are calculated using the isotherm equation for each component, hence it is not possible to calculate them for binary system adsorption because there is no isotherm available to accurately predict the binary system equilibria.

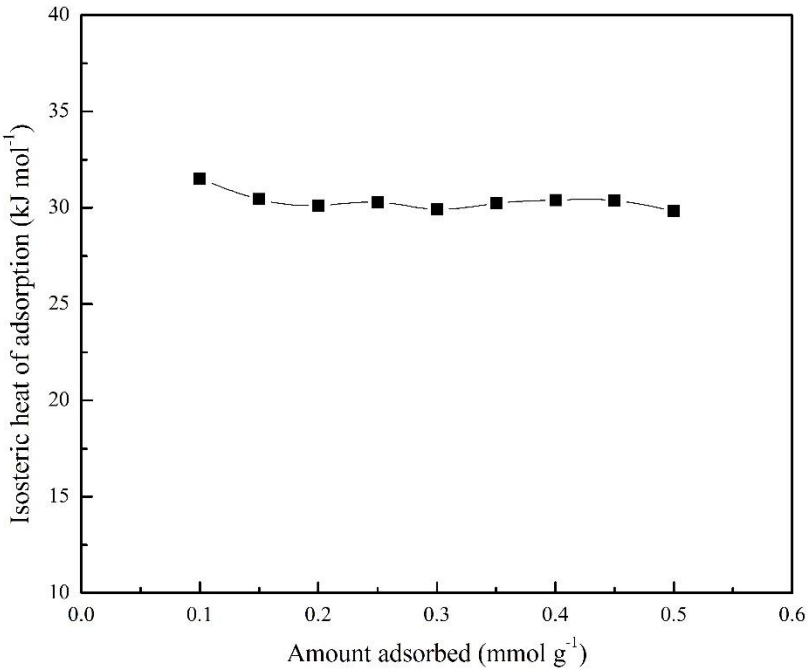

Figure 4.26 Isosteric heat of adsorption of pure CO_2 from equilibrium isotherms on MF-700

Hereafter, isosteric heat of adsorption for adsorption of pure CO_2 from equilibrium isotherms is calculated using Clausius-Clapeyron equation (Eq. 3.39) and the result is presented in Figure 4.26. Isosteric heat of adsorption is the measure of interaction between adsorbate molecules and adsorbent surface. Average isosteric heat of adsorption for CO_2 was calculated to be ca. 30.4 kJ mol^{-1}. It can be seen that the value of isosteric heat of adsorption was almost constant at different surface loadings. This is in line with the assumption of dual-site Langmuir adsorption model wherein isosteric heat of adsorption is independent of adsorbate loading on the adsorbent surface. Also, this supports the accurate prediction of CO_2 adsorption on MF-700 by dual-site Langmuir isotherm model.

4.8.2 Energy duty for desorption of CO_2

Energy requirement for desorption of adsorbed CO_2 on MF-700 was calculated using Eq. (3.37). Thermal energy input for regeneration depends on both heat of desorption and sensible heat. Firstly, specific heat capacity of MF-700 carbon adsorbent was measured by DSC and then sensible heat required to raise the bed temperature for desorption was calculated.

Specific heat capacity of the prepared carbon MF-700, C_p = 1.2 J g^{-1} K^{-1}

Adsorption was carried out at 30 °C under 12.5% CO_2 in N_2 while desorption was carried out at 200 °C under pure N_2 flow.

Temperature difference, $\Delta T = (200 - 30)\ ℃ = 170\ ℃ = 170\ K$

$$\mathrm{CO_2\ adsorption\ capacity\ of\ MF-700} = 0.83\ \mathrm{mmol\ CO_2/g\ adsorbent}$$

$$= 0.83 \times 10^{-3} \mathrm{mol\ CO_2/g\ adsorbent} = 0.03652\ \mathrm{kg\ CO_2/kg\ adsorbent}$$

$$\mathrm{Hence, sensible\ heat} = \frac{1.2\ \times\ 170}{0.83\ \times 10^{-3}}\ \mathrm{J\ per\ mole\ CO_2} = 245.783\ \mathrm{kJ\ per\ mole\ CO_2}$$

It is assumed that around 75% of the sensible heat required for heating the adsorbent can be recovered by direct or indirect heat exchanger [136].

Therefore, net sensible heat required in the process $= (25\%\ \mathrm{of}\ 245.783)\ \mathrm{kJ\ per\ mole\ CO_2}$

$$\mathrm{Sensible\ heat} = 61.45\ \mathrm{kJ\ per\ mole\ CO_2}$$

Now, heat of desorption is equivalent to isosteric heat of adsorption and it is obtained from the slope of the isosteres (logarithmic pressure of CO_2 vs. inverse of adsorption temperature at constant surface coverage). Figure 4.27 shows the isosteric heat of adsorption as a function of

amount of CO_2 adsorbed on MF-700. During the gradual covering of thermodynamically favorable adsorption sites, most favorable sites are filled first followed by filling of rest of the sites. This leads to decrease in isosteric heat of adsorption with increase in surface coverage, which further suggests the adsorbent surface to be energetically heterogeneous. Average heat of adsorption is estimated to be 17.01 kJ mol^{-1} and values between 16–30 kJ mol^{-1} have been reported for adsorption on various carbon based adsorbents [82, 168, 169]. However, this trend of isosteric heat of adsorption differs from isosteric heat of adsorption obtained from pure adsorption isotherms. Heterogeneity of adsorption process, due to adsorbates, adsorbent or their combination, could be the reason behind this difference.

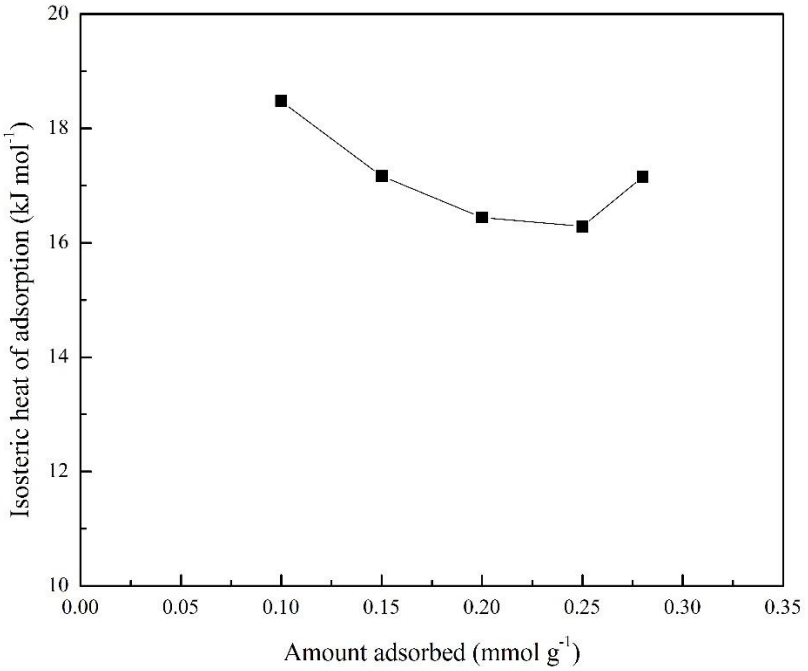

Figure 4.27 Isosteric heat of adsorption of CO_2 on MF-700

Isosteric heat of adsorption, $Q_{st} = 17.01$ kJ per mole CO_2

Thermal energy input $= (17.01 + 61.45)$ kJ per mole $CO_2 = 78.46$ kJ per mole CO_2

$= 1.78$ MJ per kg CO_2

Hence, desorption of 1 kg CO_2 requires energy equal to 1.78 MJ which is obtained from the burning of fossil fuels. For desorption of 0.83 mmol g^{-1} of CO_2 (0.03652 kg kg^{-1}), energy required is 0.0651 MJ.

Assuming that bituminous coal is used as fossil fuel for energy production, amount of CO_2 generated is 0.0884 kg per MJ of energy [170].
Thus, CO_2 generated to produce 0.0651 MJ of energy for desorption = 0.00576 kg CO_2

It can be concluded (on 1 kg adsorbent basis) that energy duty for desorption of 0.03652 kg CO_2 requires 0.0651 MJ of energy which leads to generation of 0.00576 kg CO_2 from combustion of fossil fuel (bituminous coal).

4.9 Conclusions

A range of nitrogen enriched mesoporous carbon adsorbents have been developed by templating melamine formaldehyde resin in the pores of mesoporous silica and varying the carbonization temperature. Carbonization temperature regulated the textural and surface properties of the synthesized adsorbents. Among the synthesized adsorbents, carbonization at 700 °C resulted in adsorbent with surface area of 266 m^2 g^{-1}, surface basicity of 4.05 meq g^{-1} and nitrogen content up to 21 wt%. These materials were found to be the promising adsorbents for CO_2 capture. CO_2 uptake of MF-700 was evaluated by fixed-bed adsorption studies at four different temperatures ranging from 30–100 °C and for four different CO_2 concentrations (5–12.5% by volume). It achieved the highest CO_2 adsorption capacity of 0.83 mmol g^{-1} at 30 °C in 12.5% CO_2 rest N_2 atmosphere. CO_2 adsorption on synthesized carbons is an exothermic process with decrease in adsorption capacity as adsorption temperature increases. In contrast, equilibrium CO_2 uptake tends to rise with CO_2 concentration due to increase in the concentration gradient. After consecutive adsorption-desorption cycles, no significant detoriation in CO_2 adsorption capacity was observed suggesting the reusability of the material. Different adsorption kinetic models were fitted to experimental data of CO_2 adsorption and fractional order kinetic model was found to describe the CO_2 adsorption on prepared carbons over the entire adsorption region.

Pure CO_2 and N_2 adsorption-desorption isotherms were also obtained on MF-700 carbon through a static volumetric analyzer at four different adsorption temperatures ranging from 30 °C to 100 °C up to 1 atm pressure. Sips and dual-site Langmuir isotherm models well predicted the adsorption equilibria of pure CO_2 and N_2 over the entire pressure range. The applicability of binary system models i.e. extended Sips, extended dual-site Langmuir, IAST based Sips and IAST based DSL equations have been studied for prediction of binary adsorption equilibria.

Preferential adsorption of CO_2 over N_2 by MF derived carbons resulted in unacceptable prediction errors by these models. Neither the total amount adsorbed nor the selectivity with adsorbate's molar concentration could be predicted by these isotherm equations as a result of unaccountability of interaction adsorbates with heterogeneous adsorbent surface and strong adsorption of one component than second component.

Thermodynamic functions such as molar Gibbs free energy change, entropy change, and enthalpy change for pure component adsorption suggest spontaneous, exothermic adsorption process with efficient packing of CO_2 molecules in the cavities of carbon adsorbent. As compared to CO_2, N_2 required higher pressure and hence higher chemical potential to load on the carbon surface. Average isosteric heat of adsorption for binary adsorption of CO_2 was estimated to be 17 kJ mol^{-1} while energy duty required for desorption of CO_2 found to be 1.78 MJ per kg CO_2 captured which resulted in generation of 0.00576 kg of CO_2 per kg adsorbent from combustion of bituminous coal.

Chapter 5 – Resorcinol-Formaldehyde Based Nanostructured Carbons for Carbon Dioxide Capture

5.1 Introduction

In this chapter, nanostructured carbons have been prepared via nanocasting technique by using resorcinol-formaldehyde resin as polymeric precursor and mesoporous silica as template. Obtained carbons are characterized thoroughly followed by CO_2 adsorption study by dynamic and static methods under four different adsorption temperatures. Three kinetic models have been used to describe adsorption of CO_2 on prepared nanostructured carbons. Equilibrium adsorption data was explained by using three pure component isotherm models followed by prediction of adsorption data of a binary system by extending pure component isotherms and by applying IAST to these models. Thermodynamic study was also carried out for CO_2 adsorption followed by energy penalty calculation for desorption of adsorbed CO_2.

5.2 Synthesis of porous carbons

Nanostructured carbon materials were synthesized by templating resorcinol-formaldehyde (RF) resin as polymeric precursor in the pores of mesoporous silica template by using nanocasting technique, followed by carbonization under inert atmosphere and template removal in the last.

5.2.1 Templated RF resin synthesis

About 100 g of resorcinol was added to 50 ml of water and was mixed for 20 minutes. To this mixture, 50 ml of 37% w/v formaldehyde solution was added and stirred for 30 minutes. Then 0.2 ml of 5N NaOH solution was added under continued mixing for another 20 minutes to achieve the pH in the range of 4.4–5.4. Digestion was carried out, by increasing the temperature to 70–75 °C, for next 3 h to achieve refractive index in the range of 1.48 ± 0.1. Atmospheric distillation was carried out at 100 °C to remove water till the Norton flow followed by cooling to room temperature. RF resin thus obtained was dissolved in ca. 200 ml of acetone and 15 g of silica template was added to it under continuous stirring at room temperature. Excess acetone was removed from templated resin by evaporating in oven at 60 °C. Figure 5.1 presents the block diagram for the synthesis of templated RF resin.

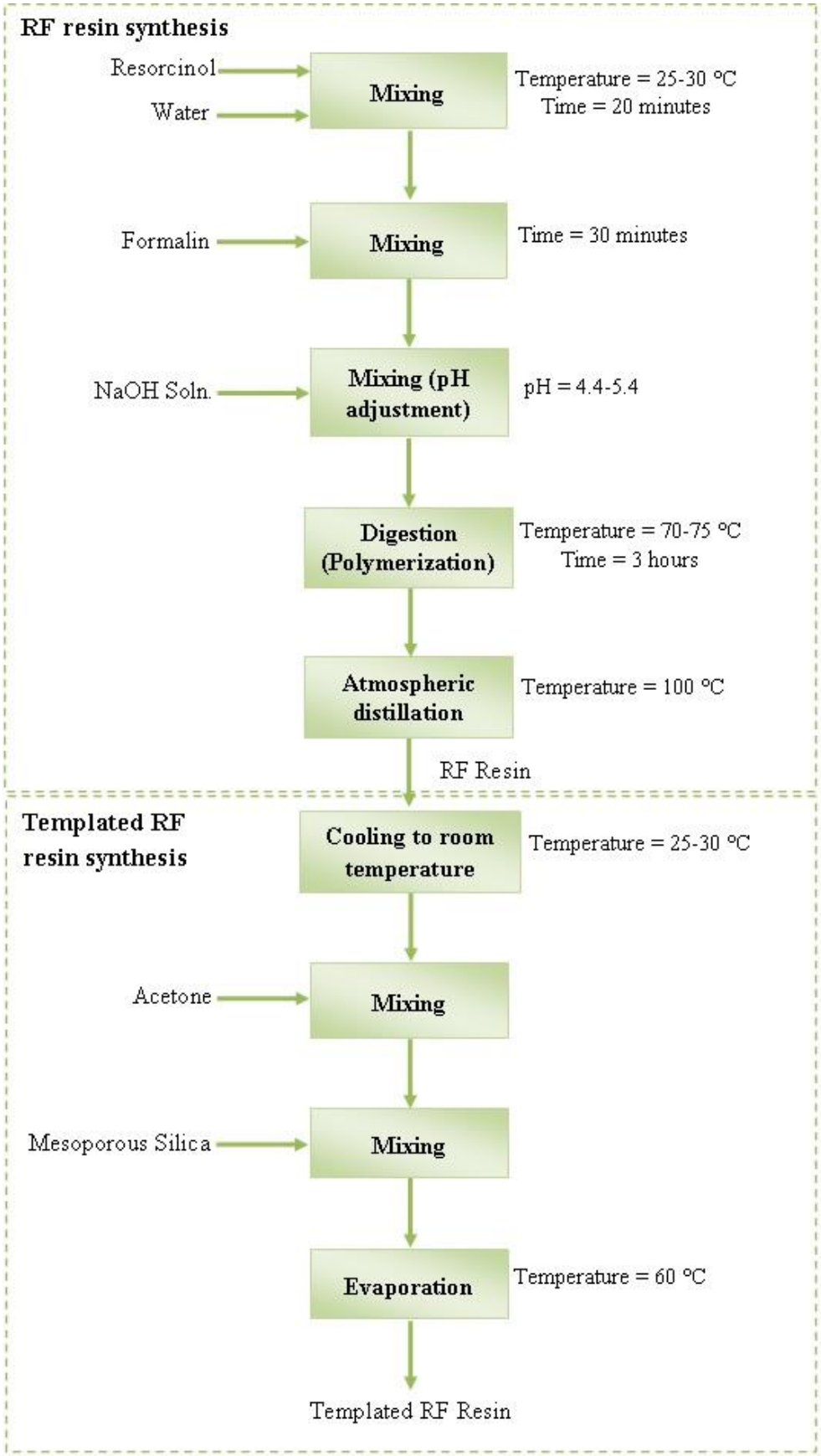

Figure 5.1 Templated RF resin synthesis process diagram

5.2.2 Carbonization of templated RF resin

A series of adsorbents were prepared by carbonizing the templated RF resin samples, placed in quartz tubular furnace, at varying carbonization temperatures ranging from 400 °C to 800 °C for 1 h in N_2 flow with a heating rate of 10 °C min^{-1}.

5.2.3 Template removal

Silica template from the obtained materials was removed by dissolution in NaOH solution for at least 24 h followed by washing with deionized water and drying at 100 °C for 2 h. Synthesized carbon materials were marked as RF-x, where *x* stands for temperature of carbonization (400–800 °C). One more carbon sample was synthesized by direct carbonization of RF resin at 700 °C (based on optimized conditions for RF based carbons) in order to investigate the effect of synthesis process on its physico-chemical properties. This prepared carbon was denoted as 'RF-C'.

5.3 Characterization of porous carbons

5.3.1 Surface area and pore size distribution

Textural properties of synthesized carbon materials were evaluated by N_2 adsorption-desorption isotherms at liquid N_2 temperature (-196 °C). N_2 sorption isotherms of all the samples can be classified as a combination of type I and type IV isotherm, indicating the presence of both micropores and mesopores, with a hysteresis loop of type H4 (Figure 5.2a). Pore size distributions (PSDs) of the prepared carbons were obtained from BJH method using the adsorption branch of the isotherm and the results are presented in Figure 5.2b. Carbonization at 400 °C and 500 °C resulted in carbons showing very small amount of N_2 adsorption attributing to less developed pore structure while carbonization at or above 600 °C produced carbons with well-developed porosity. Small adsorption by RF-400 and RF-500 at low relative pressure P/P_o of 0.05 indicated less microporosity in these samples. On the other hand, carbons obtained at carbonization temperature $\geq$ 600 °C exhibited significant adsorption at low relative pressure P/P_o of 0.05 indicating presence of large number of micropores, in addition to mesopores as suggested by the hysteresis loop. As seen in Table 5.1, BET surface area, total pore volume, micropore volume and mesopore volume tend to increase with increase in carbonization temperature from 400 °C to 700 °C but further increase in carbonization temperature to 800 °C lead to decrease in these textural properties.

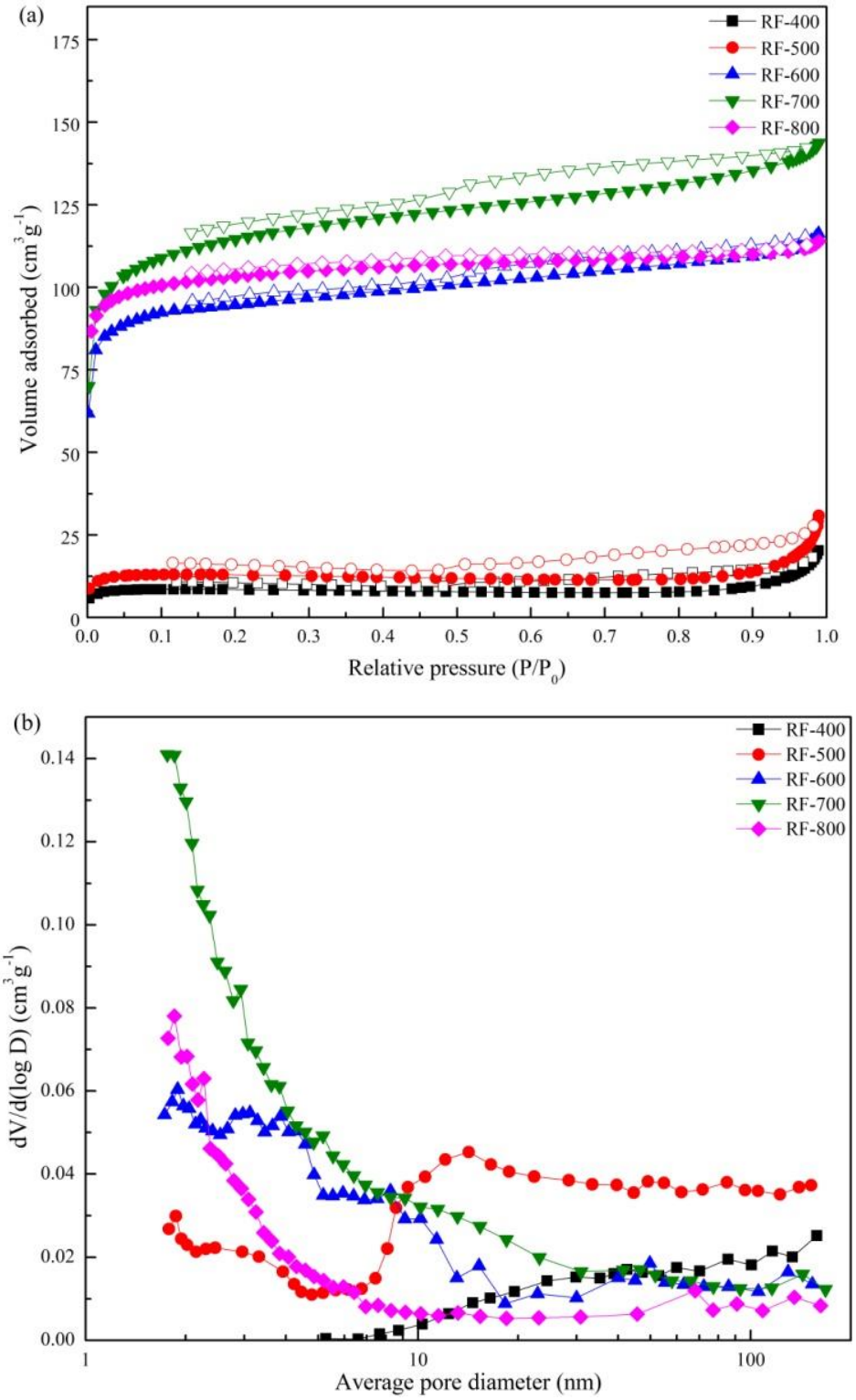

Figure 5.2 (a) N_2 adsorption (closed symbols) and desorption (open symbols) isotherms, and **(b)** pore size distribution of nanostructured carbons

Table 5.1 Textural parameters of RF derived nanostructured carbons

Sample	BET Surface Area, S_{BET} (m^2 g^{-1})	Total pore volume, V_P (cm^3 g^{-1})	Pore volume obtained from BJH method, V_{BJH} (cm^3 g^{-1})	t-plot micropore volume, V_{micro} (cm^3 g^{-1})
RF-400	27	0.031	0.019	0.014
RF-500	58	0.085	0.065	0.028
RF-600	369	0.180	0.052	0.124
RF-700	435	0.222	0.074	0.126
RF-800	407	0.176	0.030	0.134
RF-C	-	-	-	-

Micropores contributed largely towards the total pore volume for samples obtained at carbonization temperature $\geq$ 600 °C. BET surface area and total pore volume of RF-700 were found to be 435 m^2 g^{-1} and 0.22 cm^3 g^{-1} with ca. 57% contribution from micropores (V_{micro} = 0.126 cm^3 g^{-1}) respectively. RF-800 sample demonstrated a very small hysteresis loop indicating mainly the presence of micropores in this material and the same can be inferred from very small amount of mesopore volume as compared to micropore volume. RF-400 and RF-500 consisted mainly of mesopores having majority of the pore volume in pores of diameter above 10 nm while rest of the samples showed a well-developed PSD (< 10 nm). On the other hand, for the carbon derived from RF resin without nanocasting technique, almost no adsorption of N_2 was observed at liquid N_2 temperature indicating this carbon to be completely non-porous material. This signifies that the carbons obtained from the same starting material under same conditions can range from completely non-porous material to highly porous material depending on the method employed for their synthesis.

5.3.2 X-ray diffraction analysis

Figure 5.3 represents the powder XRD patterns of the synthesized carbon materials. All the samples show similar diffraction patterns with two broad peaks at ca. 23° and 43° corresponding to (002) and (100) diffraction planes respectively of graphitic carbon. Table 5.2 presents the 2θ values for (002) diffraction plane along with interlayer spacing (d_{002}) values.

Observed interlayer d-spacing values are larger than value for ideal graphite (d_{002} = 0.335 nm) [141] indicating the presence of turbostratic structures in the carbon i.e. formation of fully disordered structures [171]. Increase in d-spacing values leads to shifting of XRD peaks to lower angles. Carbonization up to 500 °C resulted in decrease in 2θ value and an increase in the d-spacing while further increase in carbonization temperature reduced the d_{002} values suggesting the formation of short ordered structures and more graphitic character at higher temperatures. The irregularity of the layer structures also increased as indicated by a decrease in the intensity of (002) diffraction plane. RF-C carbon sample exhibited very broad diffraction peak suggesting this carbon to be an amorphous material.

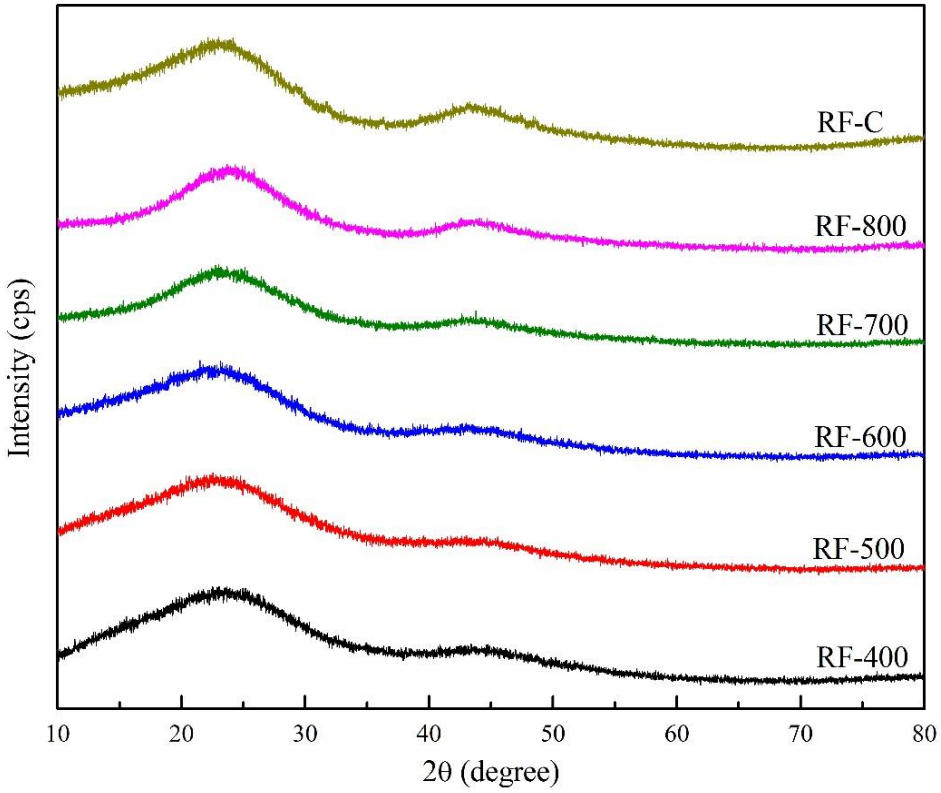

Figure 5.3 Powder XRD patterns of synthesized carbons

Table 5.2 Structural parameters of RF derived carbons

Sample	Diffraction angle, 2θ (°)	Interlayer spacing of (002) diffraction plane, d_{002} (nm)
RF-400	23.04	0.385
RF-500	22.55	0.394
RF-600	22.77	0.390
RF-700	23.03	0.386
RF-800	23.70	0.375
RF-C	24.12	0.368

The synthesized carbons are nano-materials as suggested by the line broadening of diffraction peak ca. 23° which is due to very small crystallite size. Moreover, broadened peaks suggest the poor crystallinity of the materials and hence presence of short range structural order. These results are in good agreement with TEM results.

5.3.3 Transmission electron microscopy

Transmission electron micrographs of prepared carbons can be seen in Figure 5.4. Development of nanostructures can be clearly observed from the TEM images of RF-600, RF-700 and RF-800 samples along with amorphous porous structure and these observations are in accord with XRD results. But there is no such development of nanostructures in the carbon sample prepared without nanocasting technique thereby signifying the role of silica template in the development process of carbon materials.

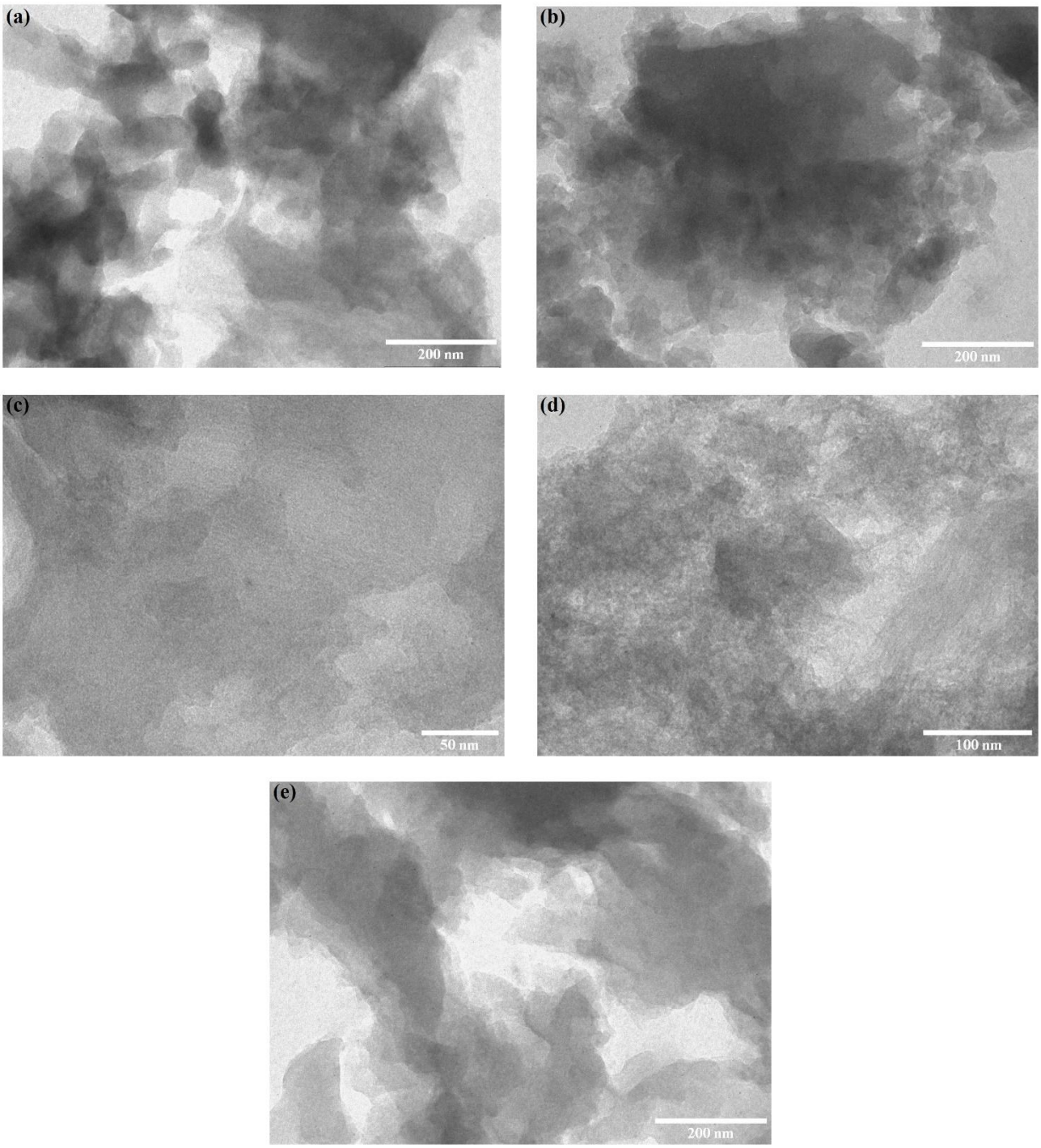

Figure 5.4 TEM images of nanostructured carbons **(a)** RF-600, **(b, c)** RF-700, **(d)** RF-800, and **(e)** RF-C

5.3.4 Scanning electron microscopy

SEM micrographs (Figure 5.5) of carbons obtained from RF resin show the development of irregular pores on the carbon surface that assist the adsorbate diffusion from bulk phase to the surface. Fine needle like structures are observed for carbons obtained from carbonization at or

above 700 °C. However, RF-C sample is found to have very compact surface with very less porous structure.

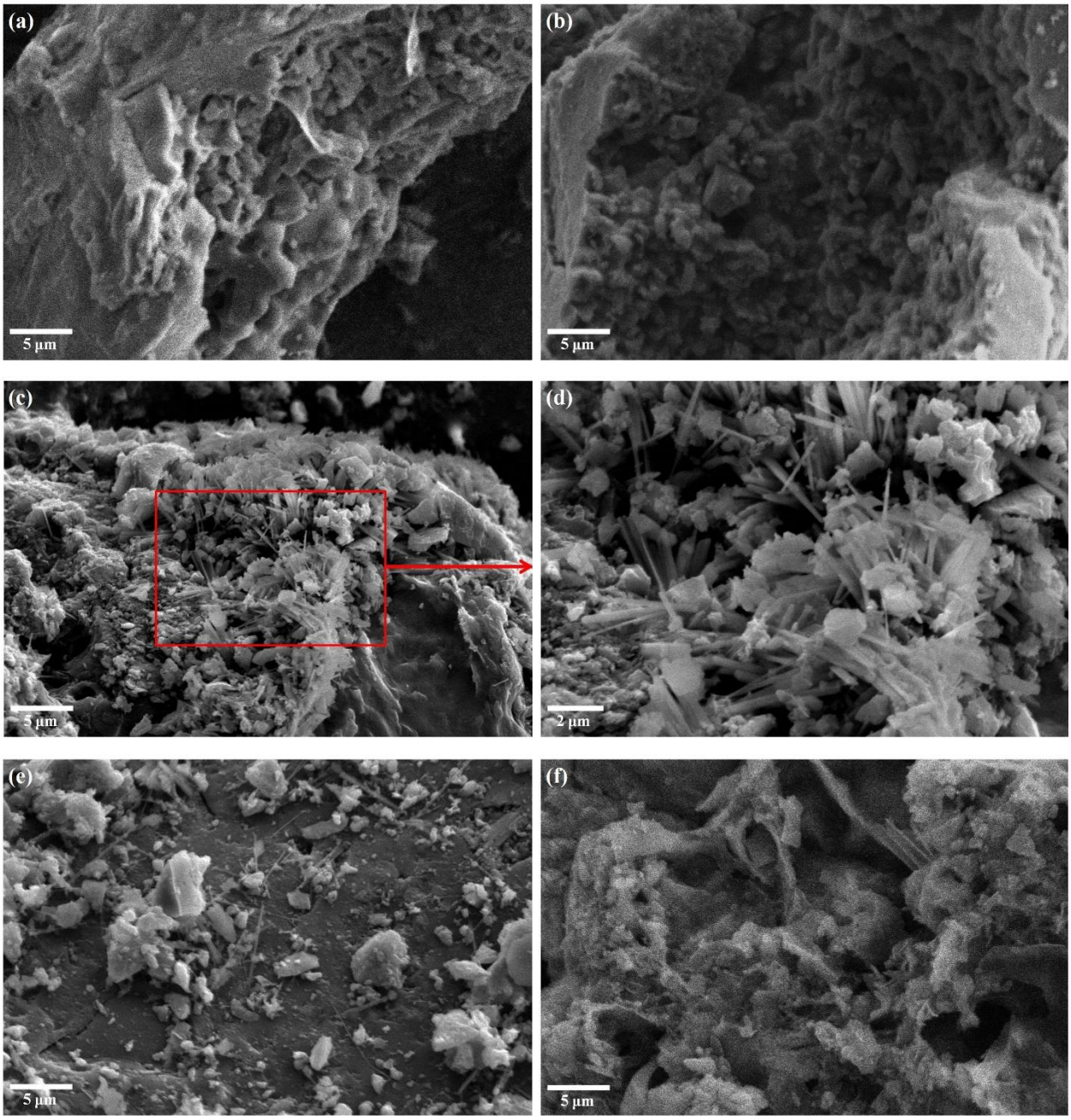

Figure 5.5 SEM images of nanostructured carbons **(a)** RF-500, **(b)** RF-600, **(c, d)** RF-700, **(e)** RF-800, and **(f)** RF-C

5.3.5 Thermogravimetric analysis

All the prepared carbon samples show a weight loss of ca. 6–8% (Figure 5.6) up to temperature of 100 °C due to desorption of moisture and other adsorbed gases. There is an increase in the thermal stability of the materials with increase in the carbonization temperature with maximum

stability being exhibited by RF-800 carbon (up to 500 °C). On the other hand, among the prepared carbons RF-400 and RF-500 are the least thermally stable materials and show a maximum weight loss of ca. 50%. RF-700 and RF-800 exhibit maximum weight loss of 25% and 15% respectively even up to temperature of 900 °C. Carbon material obtained by direct carbonization of RF resin showed ca. 2 wt% loss up to 100 °C but exhibited similar thermal stability as that of RF-700 carbon.

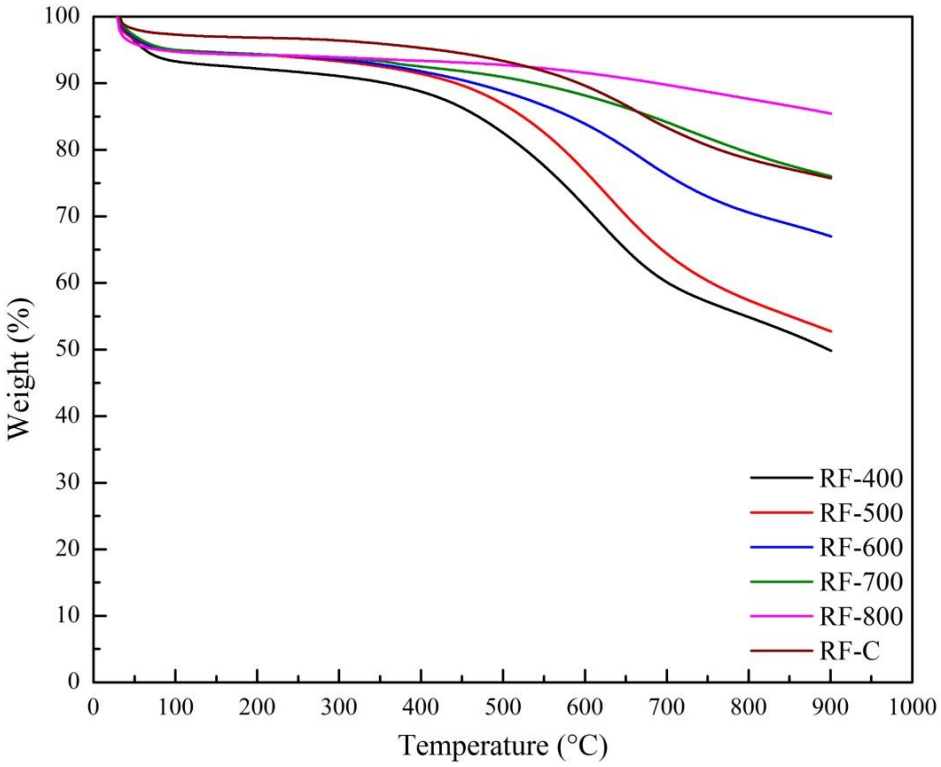

Figure 5.6 Thermogravimetric profiles of RF-derived carbons

5.3.6 Elemental composition

Table 5.3 presents the elemental composition of RF derived nanostructured carbons. There is a decrease in carbon content and an increase in oxygen content of the prepared carbons with increase in temperature of carbonization up to 600 °C. This could be due to cleavage of more carbon-carbon bonds than oxygen functionalities. On the other hand, further increase in carbonization temperature resulted in the opposite trend which is attributed to decomposition of oxygen containing groups at higher temperatures of pyrolysis. RF-C carbon sample had very high carbon content and low oxygen content as compared to that of RF-700 indicating that presence of silica template effected the chemical composition of the obtained materials.

Table 5.3 Elemental composition of nanostructured carbons

Sample	Elemental analysis		
	Carbon (%)	Hydrogen (%)	Oxygen (%)
RF-400	68.28	3.57	28.13
RF-500	65.11	3.01	31.87
RF-600	62.02	2.11	35.87
RF-700	66.25	1.49	32.23
RF-800	70.02	0.97	28.99
RF-C	83.66	1.49	14.83

5.3.7 Fourier transform infrared (FTIR) spectroscopy

Figure 5.7 depicts the FTIR spectra of the porous carbons derived from RF resin at various carbonization temperatures. Small peak at 1056 cm^{-1} can be assigned to stretching vibration of alkoxy C-O bond while a peak at 1250 cm^{-1} corresponds to acyl or phenyl C-O bond. A band around 1540 cm^{-1} is observed attributing to stretching vibrations of C=C bond of aromatic rings of quinone group. Peaks at 1770 cm^{-1} and 3000 cm^{-1} correspond to C=O stretching vibration in carboxylic groups, anhydrides, lactones, etc. and C-H stretching vibration respectively [172, 173]. With increase in carbonization temperature, there is a decrease in the intensity of the band around 1540 cm^{-1} suggesting loss of C=C bonds present in the samples. This may lead to a decrease in the carbon content of the prepared carbons with increase in carbonization temperature and similar results are obtained for carbon content from the elemental analysis. In case of RF-C carbon, peaks for C-O and C=O bond are very small as compared to other samples, demonstrating lesser oxygen functionalities which is in good accord with the elemental analysis. Majorly a broad band ca. 1540 cm^{-1} for stretching vibrations of C=C bond is observed.

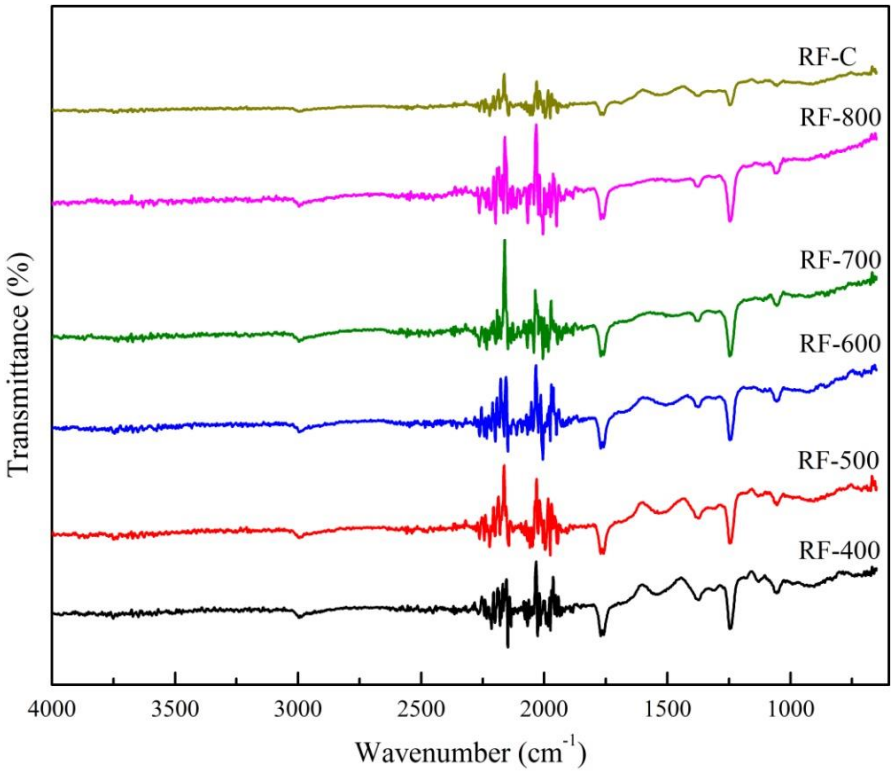

Figure 5.7 FTIR spectra of porous carbons obtained from RF resin

5.3.8 X-ray photoelectron spectroscopy

X-ray photoelectron spectroscopy (XPS) analysis was carried out for all the synthesized carbons to study the evolution of oxygen functional groups during the carbonization process. Two typical peaks for carbon (C1s) and oxygen (O1s) are observed, around 285 and 532 eV respectively, in the survey spectra of the synthesized carbons (Figure 5.8). The absence of peak for Si suggests removal of silica via dissolution in NaOH solution.

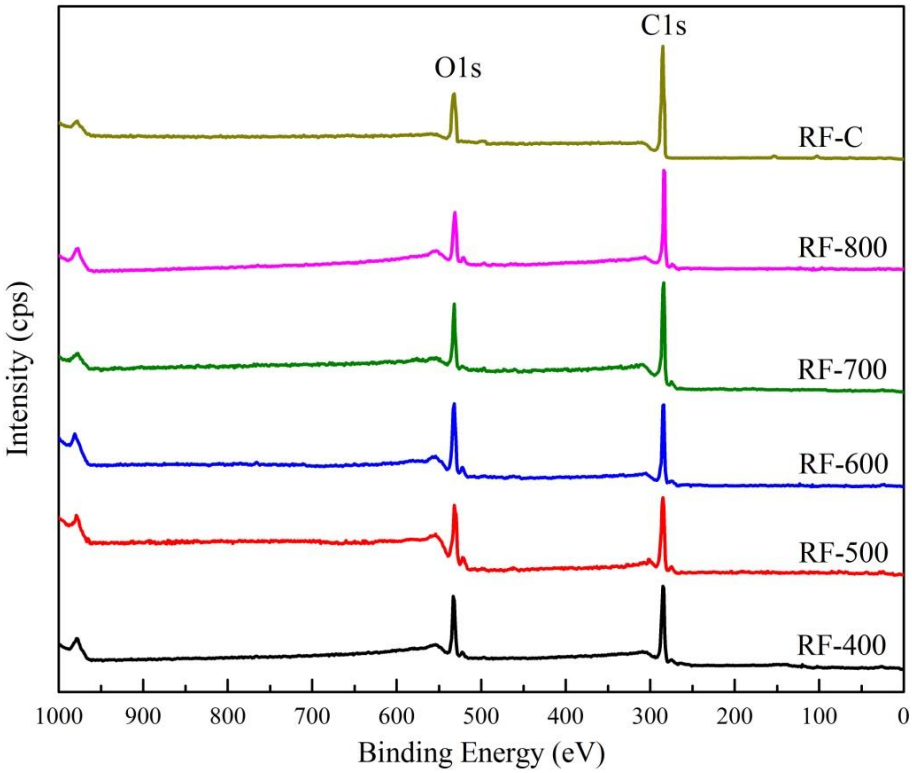

Figure 5.8 Survey scan spectra of RF derived carbons

Figure 5.9 shows the C1s XPS spectra of nanostructured carbons and RF-C carbon. The C1s spectra of all the samples were deconvoluted into four well resolved peaks and their corresponding binding energy (B.E.), full width at half maximum (FWHM) and relative area contribution (A%) are reported in Table 5.4. Peaks C1 and C2 are assigned for graphitic carbon and carbon in alcohol, phenol or ether groups respectively. Peak C3 corresponds to carbonyl or quinone groups and C4 corresponds to carboxyl, ester and/or lactone linkages [146]. With increase in carbonization temperature from 400 °C to 500 °C, there is a drastic decrease in relative area percentage of peak C1 from ca. 60% to 35.7% indicating decreased graphitic character, which has also been indicated by XRD results. Further increase in carbonization temperature resulted in increase in the relative area percentage of C1 peak and hence improvement in the graphitic character of the porous carbons. For RF-800, C1 peak has small area percentage of ca. 17.7% with the development of a new peak at ca. 283.4 eV for carbidic carbon. After C1 peak, relative area percentage is the maximum for peak C2 for all the prepared carbons suggesting that most of the carbon is linked to one oxygen atom by single bond. For carbons obtained at carbonization temperature $\geq$ 700 °C, no peak is observed at ca. 286.3 eV indicating the absence of carbonyl and/or quinone groups in these samples.

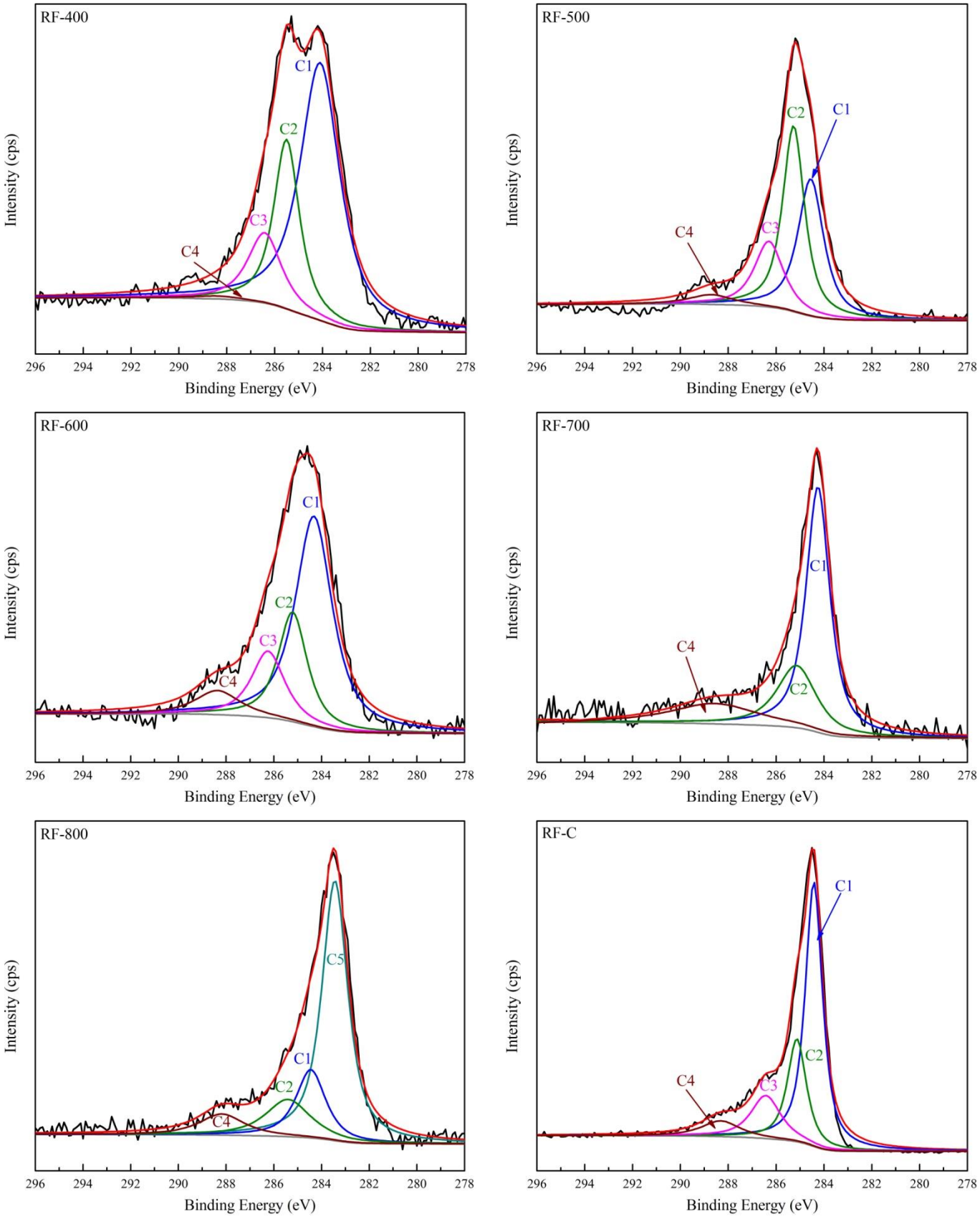

Figure 5.9 Deconvoluted C1s spectra of RF based carbons

Table 5.4 Deconvolution of C1s photoelectron envelope of RF-derived carbons

Sample		C1	C2	C3	C4	C5
RF-400	BE	284.10	285.50	286.42	288.40	-
	FWHM	1.99	1.27	1.68	2.53	-
	A%	60.08	25.22	13.83	0.88	0.00
RF-500	BE	284.55	285.27	286.30	288.70	-
	FWHM	1.29	1.09	1.45	2.11	-
	A%	35.72	40.87	19.24	4.17	0.00
RF-600	BE	284.32	285.21	286.24	288.36	-
	FWHM	1.85	1.45	1.65	2.23	-
	A%	54.69	22.32	15.44	7.55	0.00
RF-700	BE	284.25	285.14	-	288.56	-
	FWHM	1.18	1.96	-	4.3	-
	A%	58.02	24.44	0.00	17.54	0.00
RF-800	BE	284.45	285.41	-	288.18	283.44
	FWHM	1.47	2.24	-	2.24	1.29
	A%	17.71	14.67	0.00	8.35	59.27
RF-C	BE	284.42	285.13	286.43	288.31	-
	FWHM	0.86	0.94	1.48	1.90	-
	A%	54.43	23.17	15.27	7.13	0.00

In case of RF-C carbon, C1 and C2 peaks have similar relative percentage area as that of RF-700. But it contained carbon double bonded to oxygen in form of both carbonyl/quinone (ca. 15.3%) and carboxyl/ester (ca. 7.13%) unlike from RF-700. A considerable change is observed in C1s core level spectra of synthesized samples with carbonization temperature which indicates that condensation and cyclization of the aromatic ring structures take place during the carbonization process leading to the development of carbidic and graphitic carbon structures.

High resolution XPS spectra of O1s region of RF derived carbon adsorbents are shown in Figure 5.10. The O1s spectra were deconvoluted into three different peaks and their corresponding binding energy (B.E.), full width at half maximum (FWHM) and relative area contribution (A%) are listed in Table 5.5. Peak O1 corresponds to carbonyl, ketone or lactone groups, peak O2 corresponds to oxygen of ether, phenol, alcohol and/or carboxyl oxygen of esters and/or anhydrides and peak O3 is attributed to oxygen in carboxyl groups [146]. As seen in Figure 5.10, there is an appreciable change in the nature of oxygen functionalities present on the carbon surface with increase in carbonization temperature. Increase in carbonization temperature from 400 °C to 500 °C lead to decrease in carboxylic content of the carbons as suggested by decrease in relative area percentage of O3 peak from ca. 28% to 16.9% with an increase in carbonyl, ketone or lactone group as indicated by increase in O1 peak. But further increase in temperature of carbonization up to 700 °C lead to increase in carboxylic content at the expense of mainly O1 peak. No peak for carboxylic is observed for RF-800 sample indicating the conversion of carboxylic groups to lactone groups as shown by large increase in relative area percentage of O1 peak. Peak O1 for RF-800 is only due to lactone group because other functional groups (i.e. carbonyl and quinone) attributed to O1 peak are already found to be absent for this carbon sample. As compared to RF-700 carbon, RF-C contained higher carbonyl or lactonic content and lower carboxylic content. Difference in these oxygen functionalities will affect the surface basicity of these carbons.

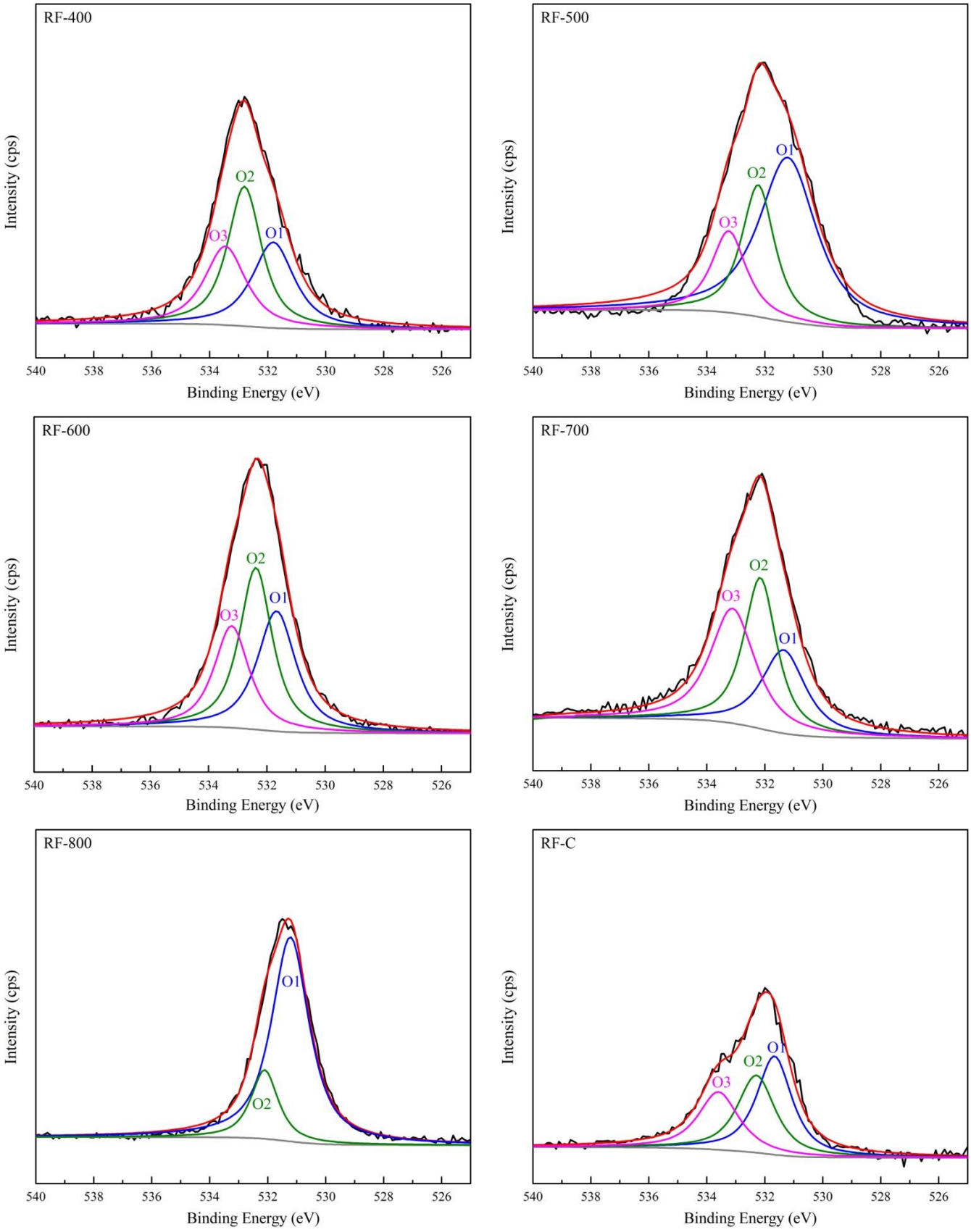

Figure 5.10 Deconvoluted O1s spectra of RF derived carbons

Table 5.5 Deconvolution of O1s photoelectron envelope of RF-derived carbons

Sample		O1	O2	O3
RF-400	BE	531.81	532.80	533.46
	FWHM	1.73	1.38	1.69
	A%	31.25	40.68	28.07
RF-500	BE	531.21	532.23	533.24
	FWHM	2.36	1.34	1.41
	A%	57.06	26.02	16.92
RF-600	BE	531.67	532.38	533.21
	FWHM	1.57	1.33	1.43
	A%	34.34	39.15	26.51
RF-700	BE	531.35	532.16	533.11
	FWHM	1.80	1.35	1.84
	A%	26.58	36.10	37.32
RF-800	BE	531.22	532.11	-
	FWHM	1.54	1.10	-
	A%	80.55	19.45	0.00
RF-C	BE	531.67	532.29	533.60
	FWHM	1.45	1.54	1.66
	A%	39.93	33.29	26.79

5.3.9 Surface functional groups by Boehm titration

Table 5.6 reports the quantitative distribution of surface acidic and basic groups based on Boehm titration method. With increase in carbonization temperature from 400 °C to 700 °C, surface acidity is found to decrease from 1.67 to 0.78 milli equivalents per gram (meq g^{-1}). But further increase in temperature to 800 °C resulted in increase in surface acidity to 1.09 meq g^{-1} and this could be attributed to increase in lactone groups in RF-800. Carboxyl, lactone or lactols and phenol groups are responsible for surface acidity of carbon materials while functional groups like carbonyls, ethers, pyrones and chromenes contribute towards the surface

basicity. Surface basicity of the prepared carbons tends to increase from 0.54 to 1.93 meq g^{-1} with increase in carbonization temperature from 400 °C to 700 °C and finally decreases considerably to 0.78 meq g^{-1} for carbonization at 800 °C. In contrast, carbon obtained from direct carbonization of RF resin exhibited similar surface acidity as that of RF-700 but exhibited very low surface basicity of 0.88 meq g^{-1}. For RF-600 and RF-700, amount of basic functional groups is higher than amount of acidic functional groups thereby indicating primarily basic nature of the carbon materials whereas rest of the samples have mainly acidic character.

Table 5.6 Surface functional groups by Boehm titration method

Sample	Acidity (meq g^{-1})	Basicity (meq g^{-1})
RF-400	1.67	0.54
RF-500	1.48	0.81
RF-600	1.24	1.75
RF-700	0.78	1.93
RF-800	1.09	0.78
RF-C	0.85	0.88

5.4 CO_2 capture performance

5.4.1 Adsorption capacity with carbonization temperature

Dynamic CO_2 adsorption capacity of the synthesized nanostructured carbon adsorbents was investigated by fixed-bed adsorption experiments at 30 °C under 10% (by volume) CO_2 inlet concentration. Figure 5.11a depicts the CO_2 breakthrough curves of the prepared carbons. With increase in carbonization temperature from 400 °C to 700 °C, the breakthrough curves shift towards the higher times indicating an increase in adsorption capacity whereas it shifts to lower time with further increase in carbonization temperature to 800 °C, demonstrating decrease in CO_2 adsorption capacity of RF-800. The breakthrough time (t_b) follows the order of RF-700 > RF-600 > RF-800 > RF-500 > RF-400 > RF-C. Dynamic CO_2 adsorption capacity (q_e) of the prepared carbons, at 30 °C under 10% CO_2 flow, increased from 0.217 to 0.704 mmol g^{-1} with increase in carbonization temperature from 400 °C to 700 °C and then it decreased to 0.606

mmol g^{-1} for sample carbonized at 800 °C (Figure 5.11b). RF-400 and RF-500 showed small adsorption capacities owing to their poor textural properties and high surface acidity. Alternatively, RF-600 and RF-700 samples exhibited improved textural properties and high surface basicity thereby resulting in improved CO_2 capacities. Increasing the carbonization temperature to 800 °C leads to some deterioration in the textural properties with large decrease in basic functional groups thus reducing its affinity for acidic CO_2 gas and hence showing drop in adsorption capacity. Therefore, CO_2 adsorption capacity of the prepared materials depends on their textural properties as well as their surface chemistry. Moreover, under similar experimental conditions, RF-C carbon exhibited very low dynamic CO_2 adsorption capacity of 0.152 mmol g^{-1}. This could be attributed to almost non-porous carbon sample and this small uptake could be due to some macropores, mainly voids between the particles, present on the surface.

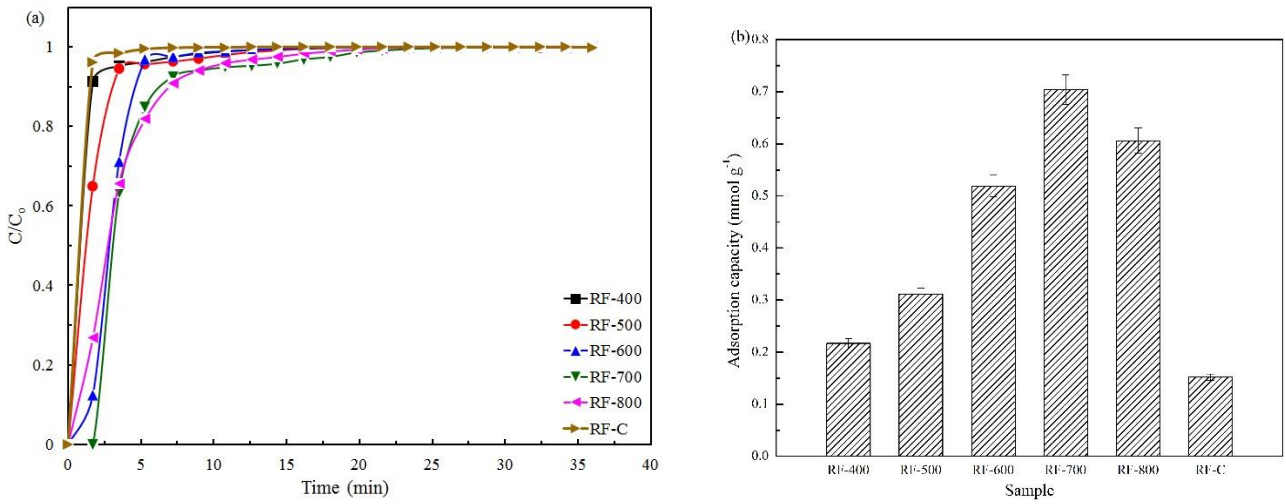

Figure 5.11 (a) CO_2 breakthrough profiles, and **(b)** CO_2 adsorption capacity of RF-derived carbons at 30 °C and 10% CO_2 feed concentration

Additionally, it is interesting to note that adsorption capacity of RF-700 is lower than MF-700 under same conditions, though RF-700 exhibits almost double the surface area of MF-700. Textural and chemical properties are the controlling parameters for the adsorption potential of a material. Absence of nitrogen functional groups in RF-700 adsorbent along with decreased surface basicity (as determined by Boehm titration method) lead to its lower CO_2 adsorption capacity, despite of better textural properties. Moreover, this has been reported in literature that high surface area of a material cannot be directly linked to its high adsorption capacity and its elemental composition and surface chemistry have strong influence on adsorption capacity. In the present work, similar argument has been observed. Furthermore, total pore volume is

important along with BET surface area with respect to adsorption capacity of a material. RF-700 exhibited lower pore volume than MF-700 and also accounts for lower adsorption performance of RF-700. Finally, it can be concluded that BET surface area solitary does not present the real scenario of adsorption capacity of an adsorbent. Other parameters such as pore volume, nitrogen content, kind of nitrogen functionality and surface basicity have a strong influence on the adsorption performance of the material.

5.4.2 Adsorption capacity with adsorption temperature and CO_2 feed concentration

Effect of adsorption temperature and CO_2 feed concentration on the adsorption performance of the prepared carbons was evaluated for RF-700 carbon only as it exhibited the highest dynamic CO_2 capacity. CO_2 adsorption breakthrough curves for RF-700 as a function of adsorption temperature for varying CO_2 feed concentrations ranging from 5% to 12.5% by volume are presented in Figure 5.12.

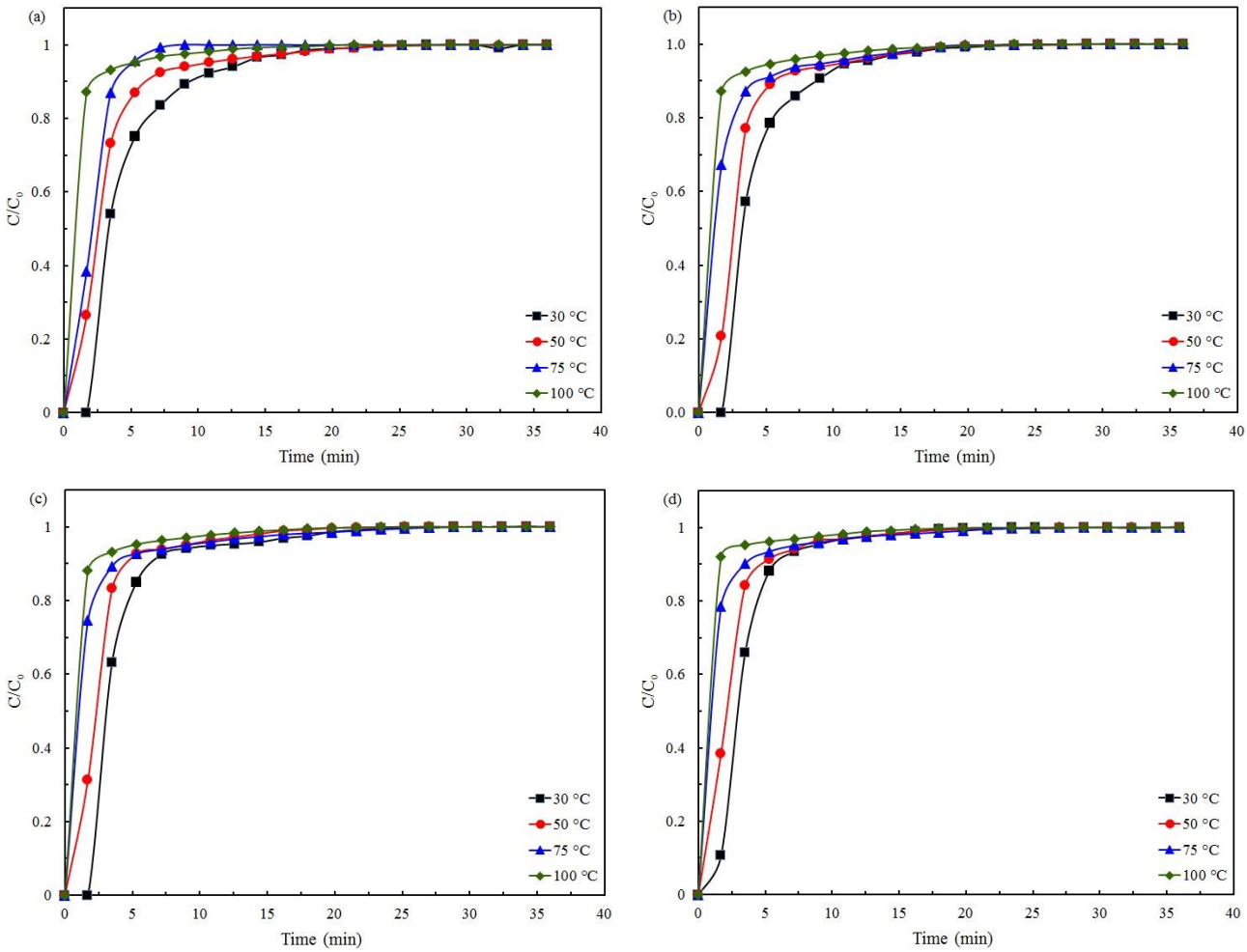

Figure 5.12 Breakthrough profiles for CO_2 adsorption on RF-700 under **(a)** 5%, **(b)** 7.5%, **(c)** 10%, and **(d)** 12.5 % CO_2 concentration at different adsorption temperatures

Longer breakthrough time appears at lower temperatures for a fixed feed concentration indicating drop in adsorption capacity with temperature. With increase in adsorption temperature from 30 °C to 100 °C, t_b decreased from 2.12 minutes to 0.22 minutes for 5% feed concentration and for 12.5% feed concentration, t_b decreased from 1.67 minutes to 0.21 minutes. Moreover, increase in feed concentration also lead to decrease in breakthrough time at a fixed temperature. It decreased from 2.12 minutes to 1.67 minutes with increase in feed concentration from 5% to 12.5%. But this decrease in t_b is almost negligible at higher adsorption temperatures like at 100 °C the value is ca. 0.22 minutes at all inlet concentrations.

Dynamic adsorption capacity of RF-700 is also calculated from the breakthrough curves at all adsorption temperatures and inlet CO_2 concentrations. It is observed that q_e tends to increase with increase in feed CO_2 concentration but decreases with increase in adsorption temperature (Figure 5.13). Value of q_e increased from 0.405 mmol g^{-1} to 0.761 mmol g^{-1} with increase in CO_2 concentration from 5% to 12.5% at 30 °C adsorption temperature. This can be explained by increased driving force for the adsorption process i.e. the concentration gradient which leads to increased CO_2 mass transfer rate across the boundary layer and within the adsorbent pores. On the other hand, decrease in q_e with temperature at a fixed inlet concentration is due to exothermic nature of the adsorption process and it is favored at lower temperatures. Furthermore with increase in adsorption temperature, both surface energy and CO_2 diffusion rate increases thus decreasing the stability of CO_2 on adsorbent surface and hence causing CO_2 desorption. For 12.5% feed concentration, value of q_e decreased from 0.761 mmol g^{-1} to 0.281 mmol g^{-1} on increasing temperature from 30 °C to 100 °C.

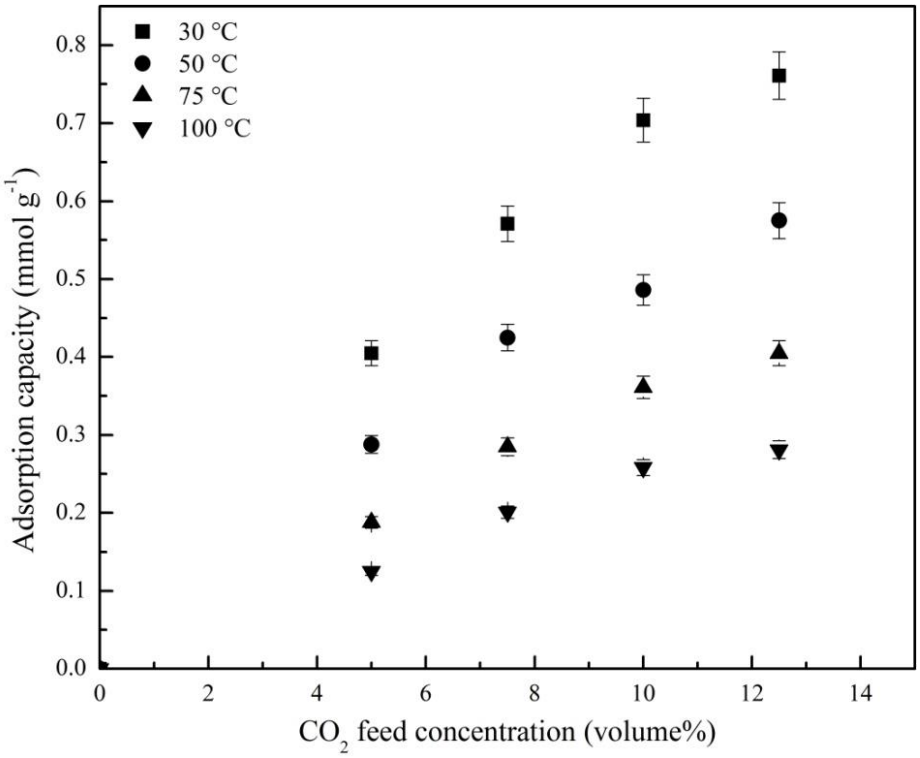

Figure 5.13 CO_2 adsorption capacity of RF-700 at different adsorption temperatures as a function of inlet CO_2 concentration

Activated carbons obtained from steam activation of fly ash have been reported to exhibit gravimetric CO_2 adsorption capacity of 0.93 mmol g^{-1} and 0.42 mmol g^{-1} at 30 °C and 75 °C respectively under 100% CO_2 flow [86]. RF-700 showed comparable dynamic adsorption capacity of 0.405 mmol g^{-1} at 75 °C and 12.5% feed concentration. This value was ~1.8 times higher than adsorption capacity of commercial activated carbon (0.225 mmol g^{-1}) at 75 °C under pure CO_2 flow [94]. For CO_2 capture application from flue gas, dynamic capacities of the adsorbent materials are more pertinent at higher temperatures. Dynamic adsorption capacity of RF-700 at all temperatures is higher than dynamic capacities of synthetic carbon obtained from carbonization and steam activation of coal tar pitch and furfural [100]. This synthetic carbon exhibited dynamic CO_2 adsorption capacity of 0.61 mmol g^{-1} at 30 °C and 0.30 mmol g^{-1} 50 °C under 15% CO_2 concentration.

5.4.3 Adsorbent selectivity and regenerability

For an efficient adsorption process, selectivity of adsorbent towards CO_2 over N_2 is another significant factor besides adsorption capacity. Breakthrough profiles for adsorption of CO_2 and N_2 on RF-700 at 30 °C and 50 °C under 12.5% feed CO_2 concentration are depicted in Figure 5.14a. N_2 appeared instantly in the exit gas stream after the onset of adsorption process. This

indicates very low N_2 adsorption capacity of the adsorbent material. In contrast for adsorption at 30 °C, concentration of CO_2 in exit gas stream was zero for ca. 2 minutes and increased gradually with time indicating adsorbent's affinity towards CO_2. Moreover, concentration of N_2 in the exit gas stream surpassed the N_2 feed gas concentration. This is attributed to slower movement of CO_2 adsorption front as compared to N_2 adsorption front followed by replacement of adsorbed N_2 molecules by CO_2 gas molecules which increases N_2 outlet concentration as compared to its inlet concentration.

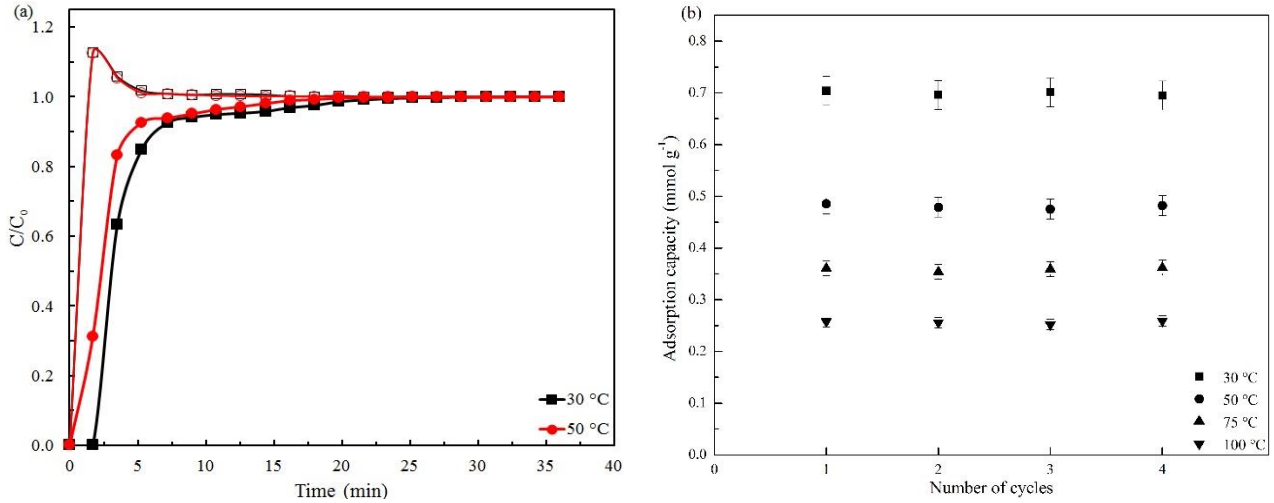

Figure 5.14 (a) Breakthrough curves of N_2 (open symbols) and CO_2 (closed symbols) on RF-700 at 30 °C and 50 °C for 12.5% CO_2 feed concentration, and **(b)** CO_2 adsorption capacity of RF-700 over multiple cycles of adsorption-desorption at 10% CO_2 feed concentration as a function of temperature

It is important for an adsorbent material to maintain CO_2 adsorption capacities in multiple adsorption-desorption cycles from practical application point of view. Figure 5.14b demonstrates the CO_2 adsorption capacity of RF-700 during multiple adsorption-desorption cycles at different adsorption temperatures and 10% feed concentration. Desorption was carried out at 200 °C under pure N_2 gas. CO_2 adsorption performance of RF-700 is almost unaltered for four cycles for all adsorption temperatures suggesting completely reversible adsorption process thereby indicating the reusability of these carbons in long-term operations. Desorption temperature of 200 °C was found to be sufficient enough for complete removal of adsorbed CO_2. This can be seen in the CO_2-TPD plot of RF-700 sample (Figure 5.15). One broad desorption peak in the temperature range of 75–175 °C is observed which indicates chemisorption of CO_2 on carbon materials [154] and is attributed to covalent bond formation between the surface basic functionalities of carbon and CO_2 gas molecules. Desorption peak is

centered around 120 °C suggesting maximum CO_2 desorption occurring at this temperature. XPS and Boehm titration results also confirm the presence of basic functional groups on the carbon surface which leads to chemical adsorption of CO_2 on these carbon adsorbents.

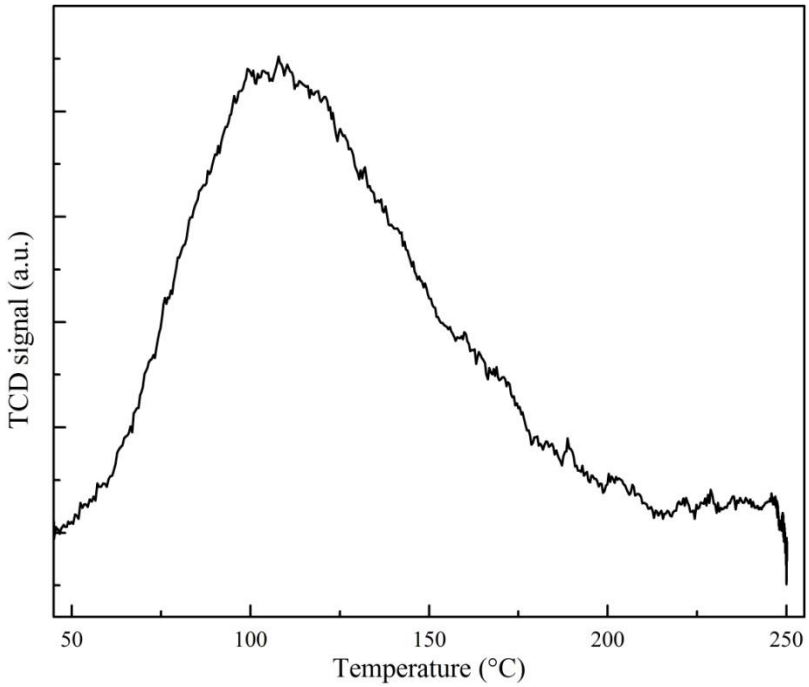

Figure 5.15 Temperature programmed desorption profile of CO_2 from RF-700

5.5 Equilibrium sorption measurements

Pure component adsorption of CO_2 and N_2 was carried out on RF-700 at different temperatures by using a volumetric analyzer and their adsorption-desorption isotherms are depicted in Figure 5.16. For all temperatures, the amount of CO_2 adsorbed on RF-700 was remarkably larger than that of N_2 within the experimental temperature and pressure range. Amount of CO_2 and N_2 adsorbed are 1.72 and 0.18 mmol g^{-1} at 30 °C and 1 atm respectively. Almost linear curve was obtained for N_2 adsorption isotherm, at all adsorption temperatures, indicating weak dispersion forces between adsorbent surface and nitrogen molecule. Very small hysteresis loop was observed for adsorption of CO_2 and N_2 which indicates that low energy is required in order to reuse the carbon. For all adsorption temperatures, CO_2 was found to be strongly adsorbed than N_2.

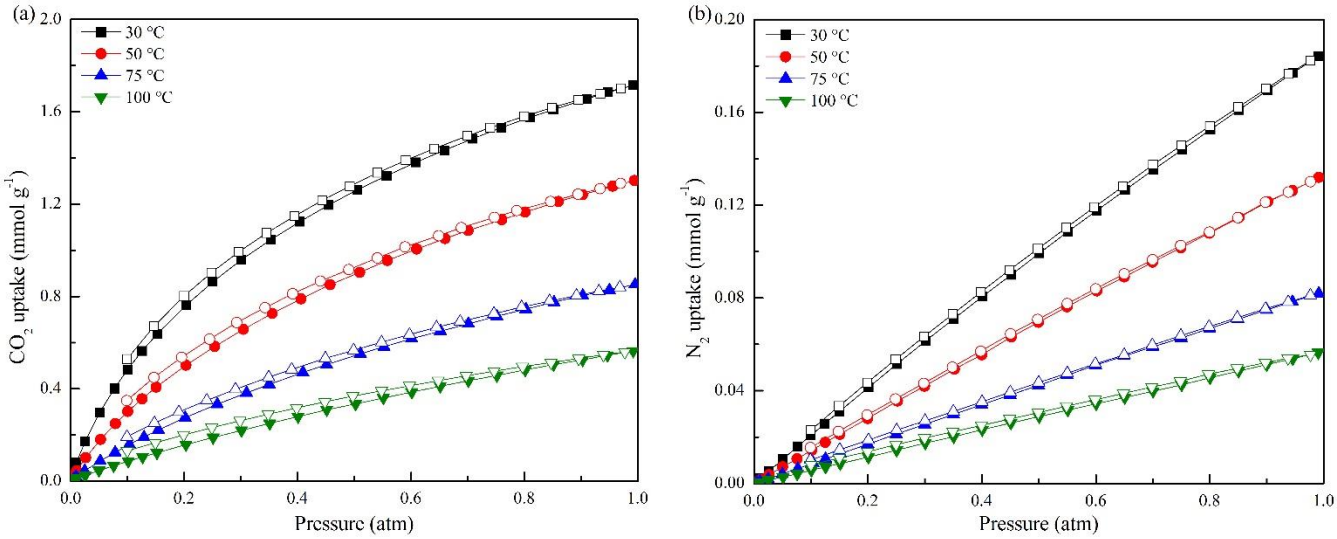

Figure 5.16 Pure component adsorption (closed symbols) - desorption (open symbols) isotherms of (a) CO_2, and (b) N_2 on RF-700 at different adsorption temperatures

Amount of CO_2 and N_2 adsorbed on RF-700 tend to increase with increase in pressure while increase in adsorption temperature lead to decrease in their uptakes. As pressure increased from 0.01 atm to 1 atm, CO_2 uptake increased from 0.079 mmol g^{-1} to 1.72 mmol g^{-1} at 30 °C and N_2 uptake increased from 0.002 mmol g^{-1} to 0.18 mmol g^{-1}. However, rise in adsorption temperature from 30 °C to 100 °C lead to decrease in CO_2 uptake from 1.72 mmol g^{-1} to 0.564 mmol g^{-1} and that of N_2 from 0.18 mmol g^{-1} to 0.056 mmol g^{-1}. Uptake of CO_2 and N_2 by RF-700 are comparable with activated carbon beads obtained from carbonization and activation of coal tar pitch though they exhibited better textural properties than RF-700. These activated carbon beads exhibited CO_2 and N_2 uptake of 1.918 mmol g^{-1} and 0.27 mmol g^{-1} at 30 °C and 1 atm respectively [174]. Hao et al. [95] prepared carbon monoliths from carbonization of resorcinol-formaldehyde resin with lysine as nitrogen source. These monoliths were reported to show CO_2 adsorption capacity of 3.13 mmol g^{-1} at 25 °C while at higher temperature of 120 °C it decreased drastically to 0.62 mmol g^{-1} and was comparable with CO_2 uptake of RF-700 at 100 °C (0.56 mmol g^{-1}).

5.6 Kinetic study

Kinetics of CO_2 adsorption on RF-700 has been investigated by using three kinetic models. Figure 5.17 presents the experimental CO_2 adsorption capacity with time at different adsorption temperatures and feed concentrations along with fitted curves obtained from all the three kinetic models. The values of kinetic model parameters, correlation coefficients (R^2) and

associated errors (error %) are listed in Table 5.7. Results indicate that fractional order kinetic model presents the best explanation for adsorption of CO_2 on nanostructured carbons in fixed-bed system. As seen in Figure 5.17, for adsorption temperature of 30 °C and 50 °C pseudo-first order kinetic model overestimated the uptake of CO_2 up to 5–6 minutes of adsorption process but it underestimated the CO_2 uptake at 75 °C and 100 °C in the initial phase of adsorption process. During the final stage of adsorption, pseudo-first order kinetic model closely followed the experimental data at all adsorption temperatures and the equilibrium CO_2 adsorption capacities were in close agreement with the experimental values. On the other hand, pseudo-second order kinetic model always overestimated the CO_2 uptake on RF-700 and predicted very high capacities at equilibrium as compared to the experimental values. Higher values of error % of both pseudo-first order and pseudo-second order kinetic models indicate that these models were not able to describe the adsorption process of CO_2 on nanostructured carbons.

For fractional order kinetic model, small value of error % and high R^2 values indicated good conformity between experimental data and model predicted values. For all CO_2 concentrations, adsorption rate constant k_n was found to decrease with increase in adsorption temperature because of exothermic nature of adsorption process. At higher temperatures, adsorption rate may become faster but CO_2 adsorbed is lesser due to faster desorption of CO_2 from carbon surface. On the other hand, k_n tends to increase with increase in CO_2 concentrations due to enhanced concentration gradient leading to faster diffusion of CO_2 molecules into the adsorbent surface. Kinetic model parameters n and m demonstrate the effect of driving force and diffusion resistance respectively [121]. Parameter n decreased with increase in adsorption temperature and was maximum at 30 °C suggesting maximum driving force at this temperature while it increased with increase in CO_2 concentration. This could be attributed to increase in concentration gradient at high CO_2 concentrations thereby leading to faster diffusion of CO_2. Value of m indicates the fastness of adsorption process. With increase in CO_2 concentrations, m tends to increase suggesting the faster adsorption of CO_2 on RF-700 at high CO_2 concentrations. Dynamic CO_2 adsorption capacities at saturation as predicted by fractional order model were also in good accord with the experimental values.

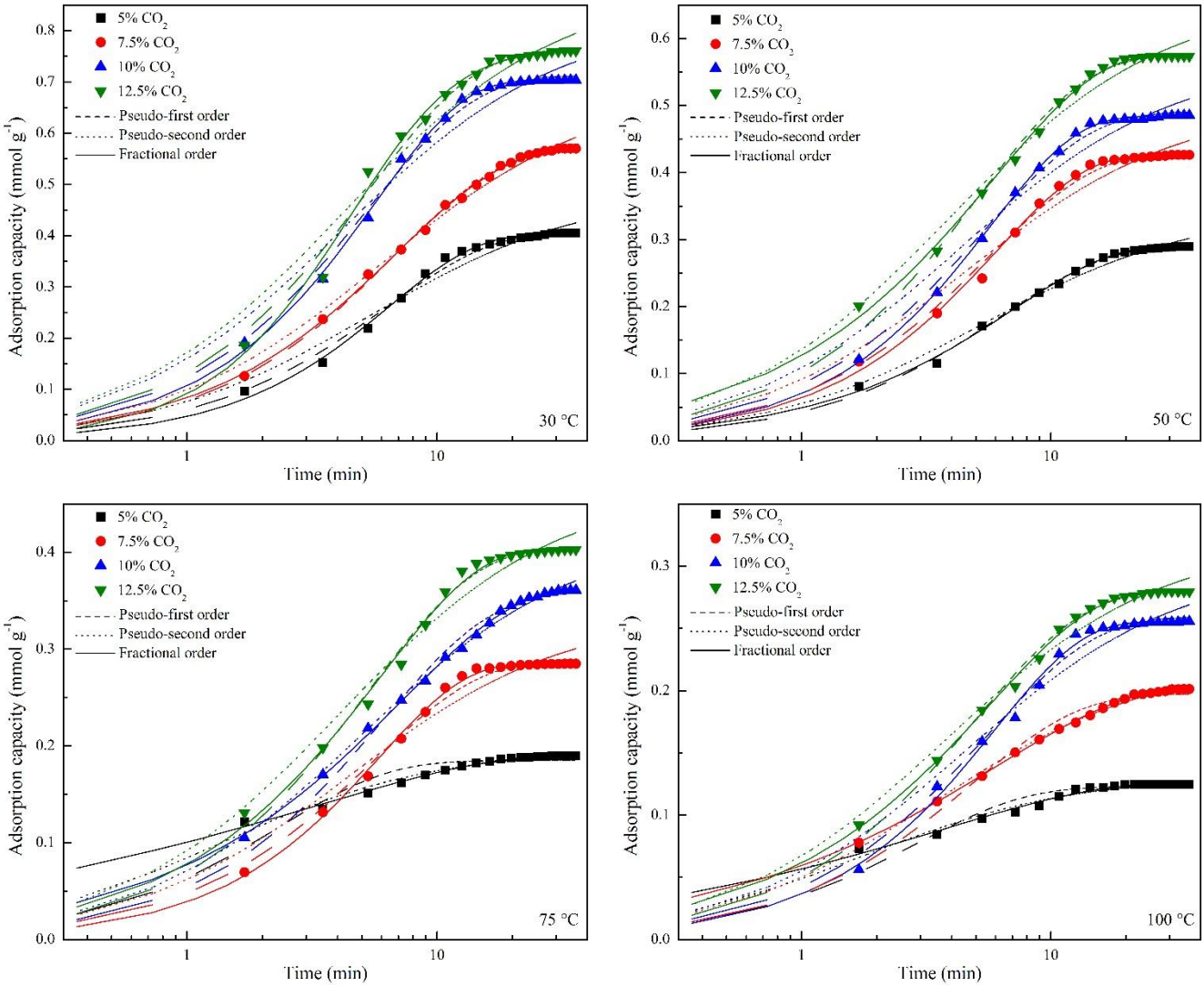

Figure 5.17 Comparison of kinetic models for CO_2 uptake on RF-700 at different adsorption temperatures as a function of feed concentration

Table 5.7 Kinetic model parameters for CO_2 adsorption on RF-700 at different adsorption temperatures and CO_2 concentrations

Adsorption temp. (°C)	CO_2 concn. (volume %)	Pseudo-first order model				Pseudo-second order model				Fractional order model					
		k_1 (min^{-1})	q_e (mmol g^{-1})	R^2	Error %	k_2 (g $mmol^{-1}$ min^{-1})	q_e (mmol g^{-1})	R^2	Error %	k_n ($mmol^{1-m}$ g^{m-1} min^{-n})	q_e (mmol g^{-1})	n	m	R^2	Error %
30	5	0.160	0.410	0.993	4.458	0.378	0.489	0.974	9.014	0.126	0.402	0.898	1.020	0.997	4.207
	7.5	0.147	0.574	0.998	1.991	0.242	0.690	0.993	5.569	0.152	0.578	1.009	1.036	0.999	1.682
	10	0.190	0.712	0.996	2.854	0.289	0.826	0.974	8.303	0.162	0.703	1.106	1.048	0.999	2.200
	12.5	0.192	0.764	0.993	5.435	0.269	0.887	0.973	11.128	0.190	0.763	1.326	1.353	0.996	3.710
50	5	0.160	0.292	0.997	3.960	0.549	0.346	0.987	5.430	0.123	0.289	0.754	0.871	0.998	3.140
	7.5	0.179	0.432	0.995	3.649	0.437	0.504	0.975	7.082	0.141	0.426	0.838	1.020	0.997	3.268
	10	0.189	0.491	0.996	3.435	0.411	0.570	0.973	9.654	0.150	0.484	0.863	1.076	0.999	0.951
	12.5	0.195	0.577	0.995	4.585	0.389	0.662	0.987	3.835	0.169	0.576	0.862	1.097	0.998	2.272
75	5	0.424	0.185	0.955	6.551	3.761	0.198	0.992	2.923	0.121	0.190	0.590	0.370	0.998	1.450
	7.5	0.183	0.290	0.994	3.694	0.665	0.338	0.969	9.741	0.133	0.285	0.762	0.693	0.998	1.931

	10	0.164	0.359	0.994	4.719	0.478	0.422	0.997	1.620	0.136	0.363	0.770	0.739	0.999	1.297
	12.5	0.188	0.406	0.994	4.132	0.519	0.468	0.981	4.654	0.152	0.403	0.793	0.875	0.996	3.013
100	5	0.342	0.123	0.960	6.981	4.377	0.133	0.989	3.350	0.119	0.125	0.655	0.467	0.995	2.124
	7.5	0.208	0.197	0.984	6.393	1.277	0.224	0.995	1.752	0.125	0.202	0.703	0.607	0.999	0.546
	10	0.180	0.259	0.993	5.583	0.729	0.303	0.971	11.862	0.130	0.255	0.748	1.052	0.996	3.107
	12.5	0.200	0.280	0.997	3.222	0.822	0.321	0.989	3.773	0.147	0.280	0.775	1.114	0.999	1.262

Figure 5.18 presents the Arrhenius plot for kinetic rate constants for CO_2 adsorption on RF-700 obtained from fractional order kinetic model at all CO_2 feed concentrations. The values of Arrhenius pre-exponential factor and activation energy are reported in Table 5.8. For adsorption at all CO_2 concentrations, negative values of E_a (deactivation) are obtained because of the decreasing rate constant values with adsorption temperature and this trend is in agreement with literature. Reactions having negative activation energies are usually regarded as without barriers wherein reaction takes place depending on capture of molecules in the potential well [156, 157].

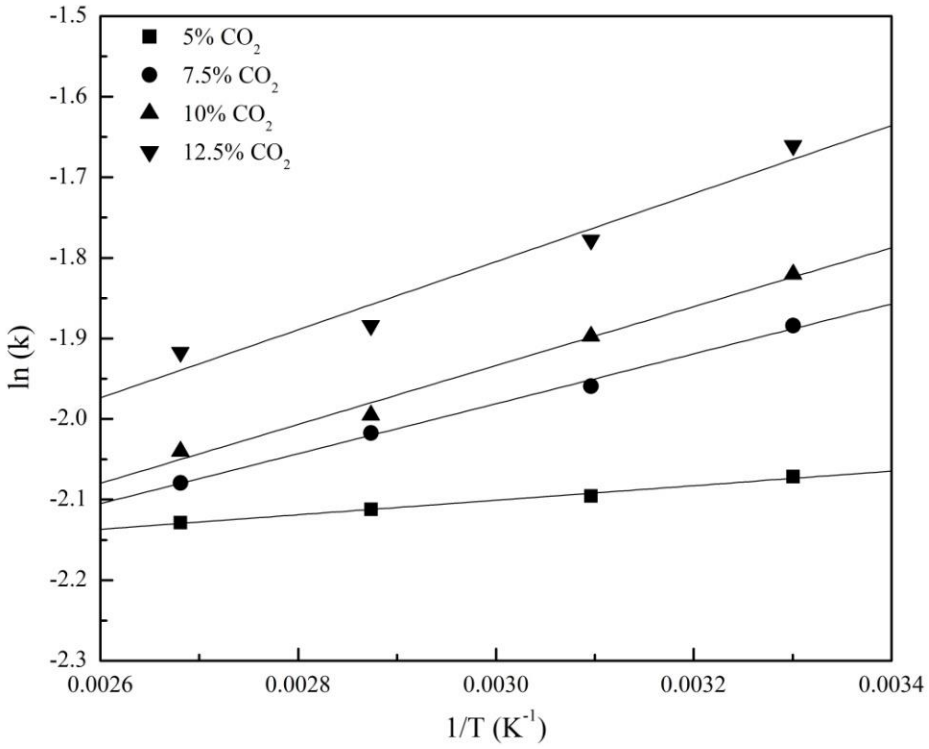

Figure 5.18 Arrhenius plot for kinetic rate constants obtained from fractional order kinetic model

Table 5.8 Arrhenius equation parameters for CO_2 adsorption on RF-700

CO_2 concentration (volume %)	A	E_a (kJ mol^{-1})	R^2
5	0.0933	-0.750	0.990
7.5	0.0545	-2.576	0.996
10	0.0483	-3.038	0.988
12.5	0.0463	-3.512	0.960

5.7 Isotherm study

5.7.1 Pure component isotherm

Pure CO_2 and N_2 adsorption isotherms on RF-700 at different adsorption temperatures have been analyzed according to the nonlinear form of the isotherm models. Figure 5.19a and 5.19b display the model fitted data of CO_2 and N_2 adsorption along with their experimental data respectively. Experimental data is represented by symbols while various isotherm models are represented by lines with Langmuir model by dotted lines, Sips model by dashed and dotted lines and DSL equation by solid lines. Tables 5.9–5.11 report the regressed parameters of the adsorption isotherm models for describing pure adsorption isotherms of CO_2 and N_2 along with their corresponding errors. Sips and DSL equations were able to capture CO_2 adsorption behavior properly at all adsorption temperatures and showed maximum SSE% of 4.4% and 5.2% respectively. However, Langmuir equation under predicted CO_2 uptake during initial adsorption phase and hence resulted in higher SSE%. In case of pure N_2 adsorption on RF-700, all the models used in this study can illustrate the experimental data with small errors (< 5%). Accurate predictions of pure component adsorption by Sips and DSL equations indicated energetically heterogeneous adsorbent surface.

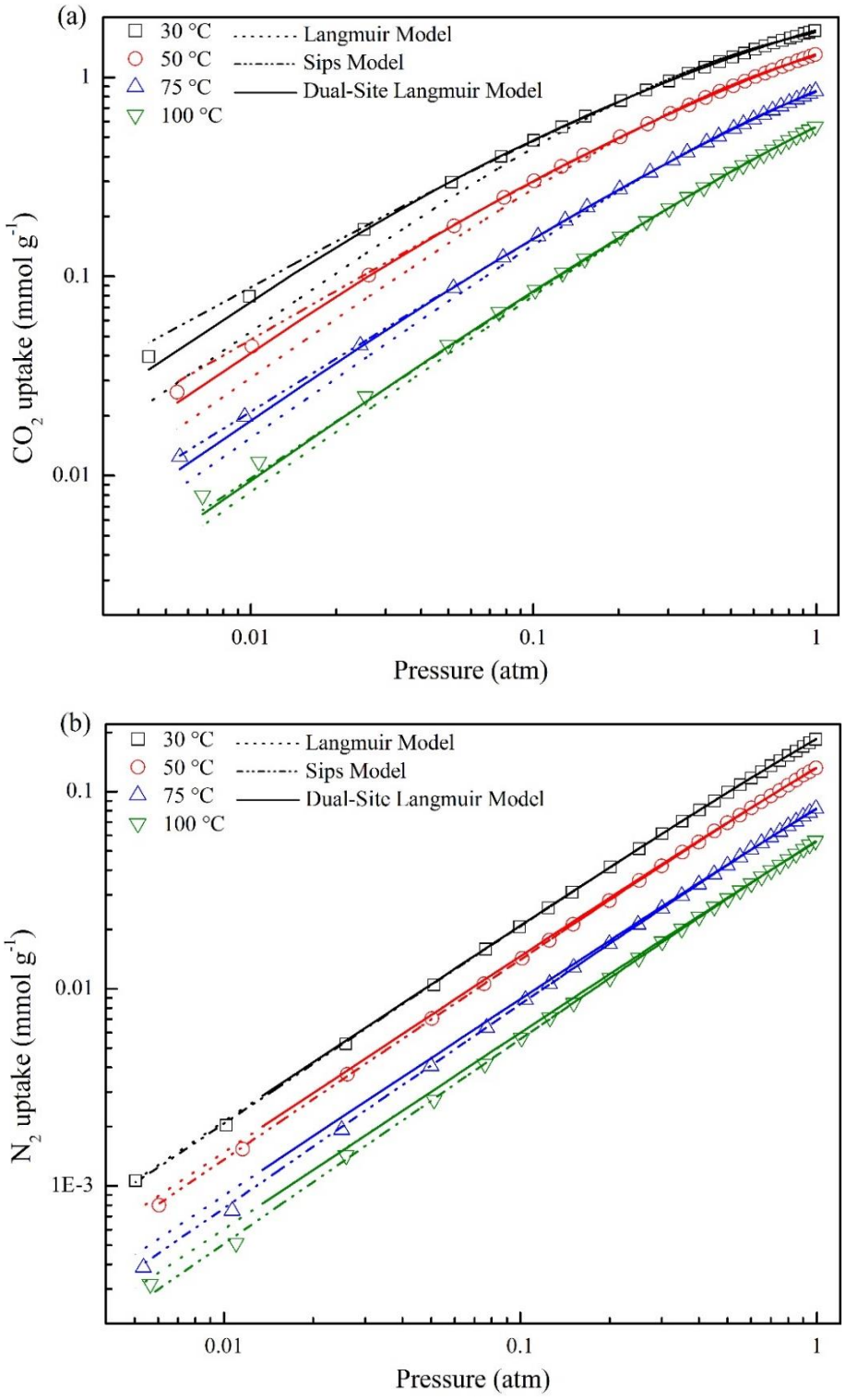

Figure 5.19 Measured and correlated adsorption isotherms of pure **(a)** CO_2, and **(b)** N_2 on RF-700 at different adsorption temperatures

Table 5.9 Regression results for Langmuir equation for pure CO_2 and N_2 adsorption on RF-700 at different temperatures

Component	Parameter	Temperature (°C)			
		30	50	75	100
CO_2	q_m (mmol g^{-1})	2.442	2.163	1.839	1.709
	b (atm^{-1})	2.22	1.46	0.85	0.49
	SSE (%)	13.01	11.30	9.45	9.02
	b_o (atm^{-1})	0.00075			
	B (kJ mol^{-1})	-20.231			
N_2	q_m (mmol g^{-1})	1.492	1.232	0.982	0.785
	b (atm^{-1})	0.142	0.120	0.091	0.077
	SSE (%)	1.63	4.11	3.71	3.48
	b_o (atm^{-1})	0.0049			
	B (kJ mol^{-1})	-8.523			

Table 5.10 Regression results for Sips equation for pure CO_2 and N_2 adsorption on RF-700 at different temperatures

Component	Parameter	Temperature (°C)			
		30	50	75	100
CO_2	q_m (mmol g^{-1})	3.47	3.15	2.61	2.13
	b (atm^{-c})	0.982	0.707	0.487	0.361
	c	1.271	1.207	1.125	1.056
	SSE (%)	4.11	3.18	0.56	4.39
	b_o (atm^{-c})	0.0047			
	B (kJ mol^{-1})	-13.474			
N_2	q_m (mmol g^{-1})	1.370	1.241	0.820	0.685

	b (atm^{-c})	0.157	0.120	0.112	0.090
	c	0.993	0.981	0.964	0.960
	SSE (%)	1.08	0.89	2.49	4.54
	b_o (atm^{-c})	0.0098			
	B (kJ mol^{-1})	-6.909			

Table 5.11 Regression results for dual-site Langmuir equation for pure CO_2 and N_2 adsorption on RF-700 at different temperatures

Component	Parameter	Temperature (°C)			
		30	50	75	100
CO_2	$q_{1,m}$ (mmol g^{-1})	2.616	2.501	2.186	2.052
	$q_{2,m}$ (mmol g^{-1})	0.448	0.257	0.091	0.041
	b_1 (atm^{-1})	0.997	0.751	0.546	0.348
	b_2 (atm^{-1})	12.362	9.771	8.452	6.030
	SSE (%)	3.22	2.70	3.36	5.15
	$b_{o,1}$ (atm^{-1})	0.004		$b_{o,2}$ (atm^{-1})	0.332
	E_1 (kJ mol^{-1})	-13.856		E_2 (kJ mol^{-1})	-9.142
N_2	$q_{1,m}$ (mmol g^{-1})	0.746	0.616	0.491	0.393
	$q_{2,m}$ (mmol g^{-1})	0.746	0.616	0.489	0.393
	b_1 (atm^{-1})	0.142	0.120	0.091	0.077
	b_2 (atm^{-1})	0.142	0.120	0.091	0.077
	SSE (%)	1.63	4.11	4.71	3.48
	$b_{o,1}$ (atm^{-1})	0.0049		$b_{o,2}$ (atm^{-1})	0.0049
	E_1 (kJ mol^{-1})	-8.510		E_2 (kJ mol^{-1})	-8.511

At all adsorption temperatures, strong adsorption of CO_2 as compared to N_2 on RF-700 carbon was indicated by higher values of parameters q_m and b of all the three isotherm models. Exothermic nature of the adsorption process was signified by decrease in affinity parameter (b) of these isotherm models with increase in adsorption temperature. Adsorption process takes place when interaction potential energy becomes equal to work done in bringing adsorbate molecule from gas to adsorbed phase. This interaction potential energy is dependent primarily on dispersion forces and permanent dipole. For carbon adsorbents, dispersion forces dominate and also for nonpolar molecules i.e. CO_2 and N_2, in this study, there is no permanent dipole. Hence, interaction of CO_2 and N_2 on prepared carbons relies on dispersion forces and it is determined by their polarizability [44, 174]. Table 5.12 reports the physical properties of CO_2 and N_2. Since CO_2 molecule has higher polarizability than N_2 molecules, adsorption of CO_2 is associated with higher heat of adsorption than N_2 and hence stronger affinity of CO_2 towards carbon surface than N_2. This is corroborated by higher values of heats of adsorption, obtained from isotherm equations, for CO_2 adsorption than N_2 adsorption.

Table 5.12 Physical properties of CO_2 and N_2 [174]

Properties	CO_2	N_2
Diameter (nm)	0.330	0.364
Polarizability ($\times 10^{-25}$ cm^3)	29.1	17.4
Quadrupole moment ($\times 10^{-40}$ cm^2)	-13.7	-4.9
Dipole moment (Debye)	0	0

DSL equation parameters b_1 and b_2 are also equal for N_2 adsorption on this carbon. Therefore, amount of adsorbate adsorbed calculated from Eqs. (3.20) and (3.22) for PP and PN correlation respectively will be same indicating no energetic site-matching issue.

5.7.2 Binary component isotherm

To predict binary system adsorption equilibria of CO_2 and N_2 on RF-700, Sips and DSL equations were extended empirically, leaving Langmuir equation, since these models were able to predict pure component equilibria accurately for both adsorbates. For carbon dioxide-nitrogen separation using RF-700, partial and total adsorbed amounts and x-y diagrams were

obtained experimentally at different adsorption temperatures and gas phase concentrations. Pure component adsorption isotherms of CO_2 and N_2 were employed to predict binary system adsorption equilibria by using two different adsorption models along with application of IAST thermodynamic model in conjunction with those models. These predicted results are then compared with experimentally obtained data and are presented in Figures 5.20 and 5.21.

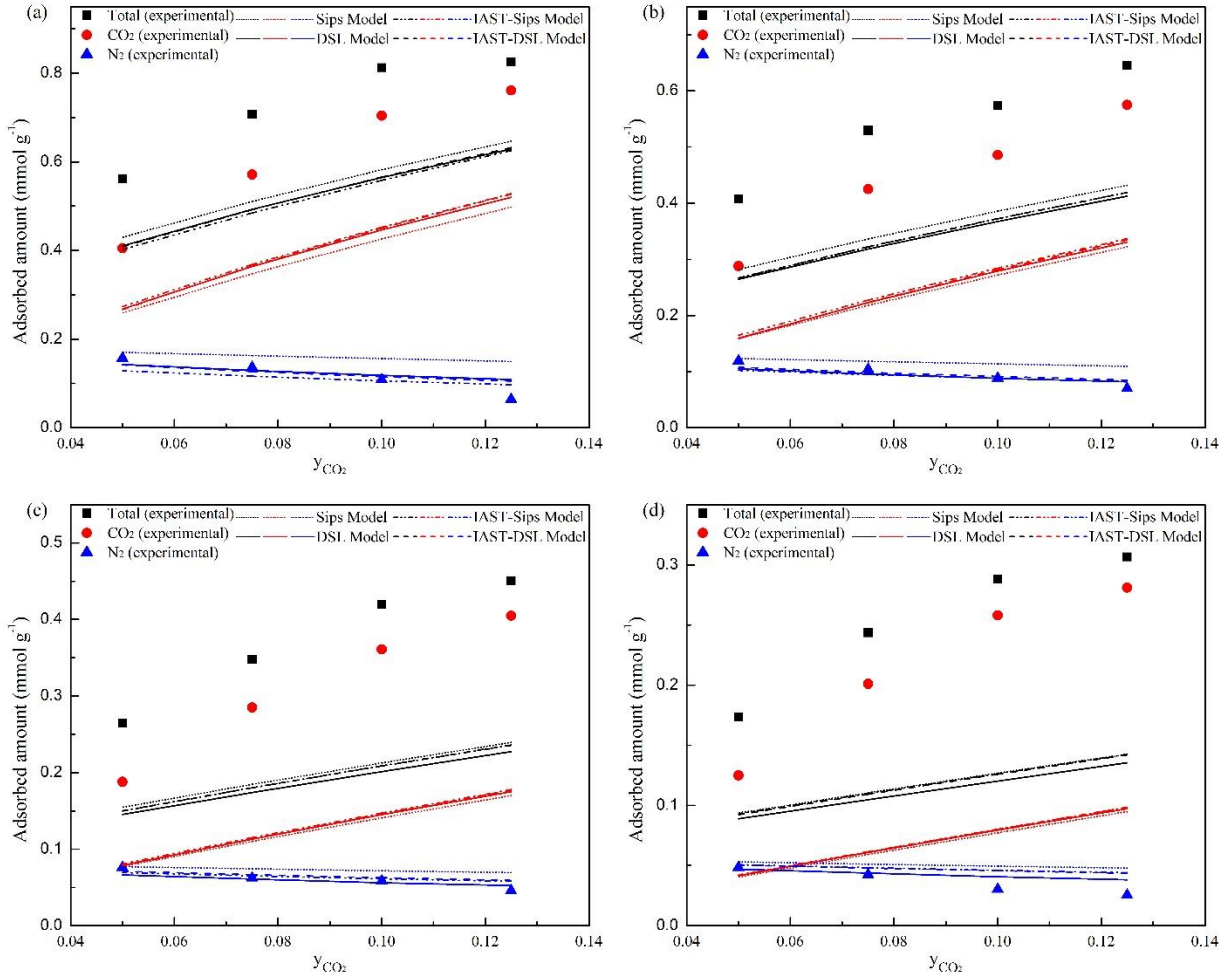

Figure 5.20 Total and partial adsorbed amounts of CO_2 and N_2 binary adsorption on RF-700 at **(a)** 30 °C, **(b)** 50 °C, **(c)** 75 °C, and **(d)** 100 °C (symbols represent experimental data and lines represent model predicted data)

None of the employed models were able to predict CO_2 adsorption isotherm in binary system accurately. DSL isotherm model predicted higher CO_2 uptake than Sips equation at 30 °C while adsorption equilibria at rest of the adsorption temperatures was almost equally predicted by all the isotherm models along with their IAST forms. However, all the equations highly under predicted the uptake of CO_2 on RF-700. Prediction of N_2 uptake and hence total adsorbed amount also deviated considerably from experimental values at all adsorption temperatures.

This can be attributed to difference in the adsorptive properties of adsorbates which is not being accounted by these isotherm equations.

Total adsorbed amount along with CO_2 adsorbed amount increased with increase in CO_2 composition in the binary mixture whereas amount of N_2 continuously decreased, demonstrating competition for adsorption sites and preferential adsorption of CO_2 over N_2. Higher critical temperature of CO_2 (31 °C) as compared to that of N_2 (-147 °C) is the main reason for this behavior. CO_2 is expected to behave as a condensable vapor rather than a supercritical gas thereby becoming less volatile and getting adsorbed easily. Additionally, carbon dioxide exhibits higher polarizability than nitrogen (Table 5.12) that may enhance attractive forces with the adsorbent surface and a permanent quadrupole results in stronger interactions with carbon surface [175, 176].

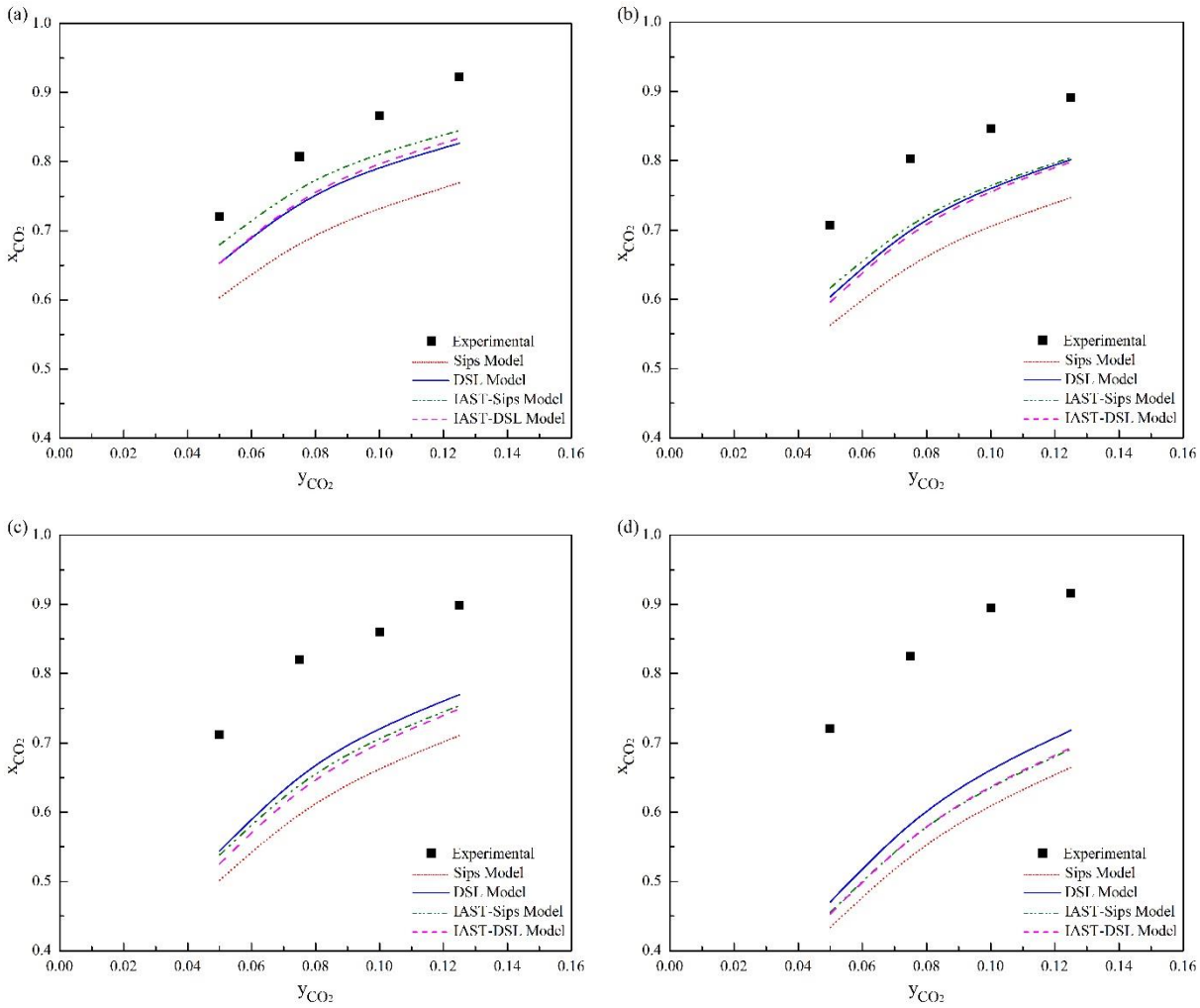

Figure 5.21 *x-y* diagram for CO_2 and N_2 binary adsorption on RF-700 at **(a)** 30 °C, **(b)** 50 °C, **(c)** 75 °C, and **(d)** 100 °C

CO_2 mole fraction in adsorbed phase was found to increase with CO_2 mole fraction in gas phase thereby indicating positive deviation from Raoult's law at all adsorption temperatures. Total amount adsorbed was found to increase with molar fraction of CO_2 in gas phase with non-symmetric *x-y* diagram thereby implying formation of non-ideal adsorptive mixture of CO_2 and N_2 at equilibrium. As the assumptions of IAST are not satisfied in this case, it results in large deviation from the experimental data and same can be observed in Figure 5.21. Moreover, Sips and DSL equations for binary system also deviated greatly from the experimental curves indicating the inability of these models to explain binary system adsorption equilibria of CO_2 and N_2 on nanostructured carbon RF-700.

Table 5.13 reports the comparison between selectivity of CO_2 over N_2 obtained from experimental breakthrough curves and isotherm model predicted values. Experimental selectivity of CO_2 over N_2 was found to increase with gas phase molar fraction at all adsorption temperatures while all the isotherms predicted a decrease in the selectivity. IAST based DSL model predicted a small decrease in selectivity from 35.8 to 35.1 with increase in CO_2 feed fraction from 0.05 to 0.125 at 30 °C whereas experimental values showed an increase from 48.9 to 83.1 under same conditions. Rise in temperature did not have a substantial effect on experimental values of selectivity for a given CO_2 feed fraction but a decrease in the selectivity was predicted by all the isotherm models. Both Sips and DSL isotherm models along with their IAST based equations predicted lower selectivity values as compared to experimental values at all gas phase compositions and adsorption temperatures. This could be mainly due to under prediction of CO_2 equilibria by these models. Therefore, it can be said that prediction of CO_2/N_2 selectivity is highly dependent on the accuracy of isotherm model.

Table 5.13 Equilibrium selectivity of CO_2 over N_2 for binary system adsorption on RF-700 from breakthrough curve and isotherm models

Temp.	CO_2 mole fraction in feed	Experimental	Sips model	DSL model	IAST-Sips model	IAST-DSL model
30 °C	0.050	48.9	28.9	35.7	40.3	35.8
	0.075	51.6	26.3	34.8	39.1	35.4
	0.100	58.5	24.6	34.0	38.5	35.2
	0.125	83.1	23.3	33.4	38.1	35.1
50 °C	0.050	45.8	24.4	28.9	30.5	28.0
	0.075	50.1	22.7	28.7	29.6	27.8
	0.100	49.5	21.5	28.5	29.1	27.7
	0.125	57.3	20.6	28.3	28.8	27.7
75 °C	0.050	46.9	19.1	22.7	22.2	21.0
	0.075	56.2	18.2	22.9	21.8	21.0
	0.100	55.5	17.6	23.2	21.6	20.9
	0.125	61.8	17.2	23.4	21.5	20.9
100 °C	0.050	48.9	14.5	16.9	15.9	15.7
	0.075	58.2	14.2	17.2	15.7	15.7
	0.100	76.6	14.0	17.5	15.7	15.8
	0.125	76.7	13.9	17.8	15.6	15.8

Similar kind of behavior of isotherm models was observed in predicting adsorption equilibria of binary CO_2-N_2 system on both types of carbon materials prepared in the present work. As discussed earlier, this is majorly due to different adsorptive strengths of CO_2 and N_2. These isotherm models are based on the major assumption of equal adsorption capacities of two components which is practically not the case. Hence, it is difficult to predict adsorption equilibria of dissimilar adsorbates by these isotherm equations. Also as prediction by IAST

involves extrapolation of pure component isotherms outside the experimental pressure range, isotherm of less strongly adsorbed component (i.e. N_2 in this case) is extrapolated to a greater extent thereby introducing ambiguity in IAST predictions. Different polarities and quadrupole moment of CO_2 and N_2 results in large difference in interaction strength between different mixture components. Thus, both adsorbent heterogeneity and unlike adsorbates lead to nonconformity between IAST based values and experimental values.

IAST has been found to accurately predict multicomponent adsorption equilibria but majorly at high pressure conditions. For example, Schell et al. [133] reported that IAST using the pure component Sips parameters described competitive behavior of CO_2/N_2 mixtures on commercial activated carbon under high pressure conditions accurately. In another work, adsorption equilibria and selectivity of CO_2 in binary system of CO_2-N_2, on mesoporous activated carbon, at 18 bar was explained accurately by IAST based dual-site Sips isotherm model [177]. It should also be noted that adsorption equilibrium in these systems is typically evaluated by volumetric and gravimetric methods. But in the present work, predicted adsorption capacities do not match with the experimental data mainly due to different method (dynamic method) and adsorption conditions (atmospheric pressure and low CO_2 mole fraction in gas phase) adopted for evaluation of experimental values.

5.8 Thermodynamic study

5.8.1 Thermodynamic parameters

In addition to equilibrium study, thermodynamic study was also carried out to characterize the adsorption behavior. Figure 5.22 displays the calculated thermodynamic parameters i.e. ΔG, ΔH and $\Delta S \times T$ for pure component adsorption of CO_2 and N_2 on RF-700 carbon at 30 °C and 50 °C by using Sips equation. All the thermodynamic parameters showed similar behavior at various adsorption temperatures. Negative values of ΔG for adsorption of CO_2 and N_2 on RF-700 over the complete experimental pressure range indicated the adsorption process to be spontaneous in nature. With rise in pressure, integral molar Gibbs free energy change of adsorption declined for both adsorbates at all temperatures suggesting lower work requirement during initial adsorption phase than later stages for packing of more molecules into cavities of carbon material. Value of ΔG was found to be -2.53 and -2.67 kJ mol^{-1} for CO_2 and N_2 respectively for the same coverage value of 0.18 mmol g^{-1} at 30 °C. This indicates that CO_2 loading on RF-700 carbons has slightly lower work requirement as compared to N_2 and higher

pressure and hence higher chemical potential is required by N_2 than CO_2 to load on the prepared carbons [164, 166].

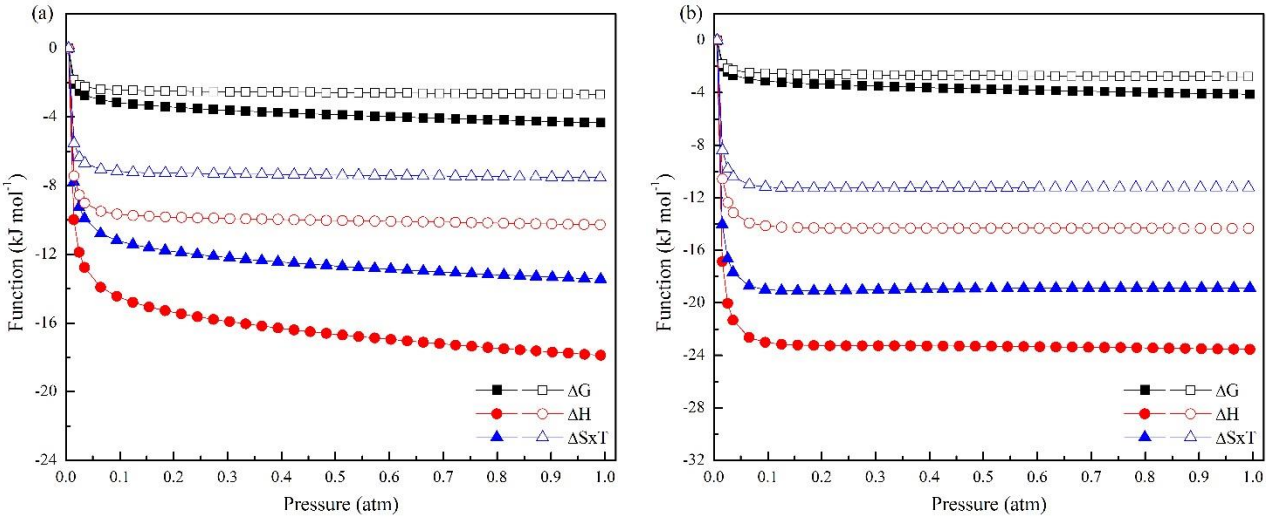

Figure 5.22 Three functions ΔG, ΔH and $\Delta S \times T$ for pure CO_2 (closed symbols) and N_2 (open symbols) adsorption on RF-700 at **(a)** 30 °C, and **(b)** 50 °C

Next, thermodynamic parameter integral molar entropy change was evaluated and the function $\Delta S \times T$ is presented in Figure 5.22. At low pressure of 0.05 atm, $\Delta S \times T$ for CO_2 and N_2 was -10.4 and -6.88 kJ mol^{-1} respectively at 30 °C while at higher pressure value (1 atm) the corresponding values were -13.44 and -7.53 kJ mol^{-1}. Higher magnitude of this function for adsorption of CO_2 than N_2 indicated more ordered arrangement by CO_2 on adsorbent surface. In other words, CO_2 confined in the cavities of the adsorbent has less degree of freedom than N_2 and this is on account of almost three folds quadrupole moment of CO_2 than N_2 and hence localized adsorption of CO_2 [134]. Integral molar entropy change also showed negative values for both CO_2 and N_2 over the complete experimental temperature and pressure range thereby indicating formation of ordered configuration from random stage on adsorption with decrease in degree of freedom of adsorbate. Also, this thermodynamic parameter decreased progressively with increase in pressure for N_2 adsorption. But in case of CO_2 adsorption, there was decrease in entropy at 30 °C while at rest of the adsorption temperatures, it was almost constant over the complete pressure range.

Integral molar enthalpy change and function $\Delta S \times T$ of adsorption of CO_2 and N_2 displayed similar trends and negative values of ΔH demonstrated exothermic nature of adsorption process [178]. For CO_2 adsorption at 30 °C, as pressure changed from 0.01 to 1.0 atm ΔH varied from

-9.97 to -17.88 kJ mol^{-1}. However, for N_2, this value ranged from -7.43 to -10.27 kJ mol^{-1}. There was gradual decrease in enthalpy values (more in case of CO_2) i.e. higher heat release during adsorption process which was due to more effective packing of CO_2 molecules. Same inference was obtained from trend of entropy change for CO_2 adsorption. But at higher adsorption temperatures, ΔH showed almost constant values for pressure > 0.1 atm (ca. -23.5 kJ mol^{-1} for CO_2 adsorption at 50 °C).

Above evaluated parameters explain the pure CO_2 and N_2 adsorption on RF-700. However, assessment of these parameters for binary adsorption is unworkable due to lack of an accurate isotherm equation that could define binary adsorption equilibria. Now, using Clausius-Clapeyron equation, isosteric heat of adsorption was calculated as a function of surface loading from pure component adsorption isotherm. As shown in Figure 5.23, isosteric heat of adsorption for RF-700 carbon did not change significantly, with an average values of 29 kJ mol^{-1}, thereby following the DSL isotherm model's assumption. There was slight variation in the value which can be attributed to energetically heterogeneous adsorbent surface.

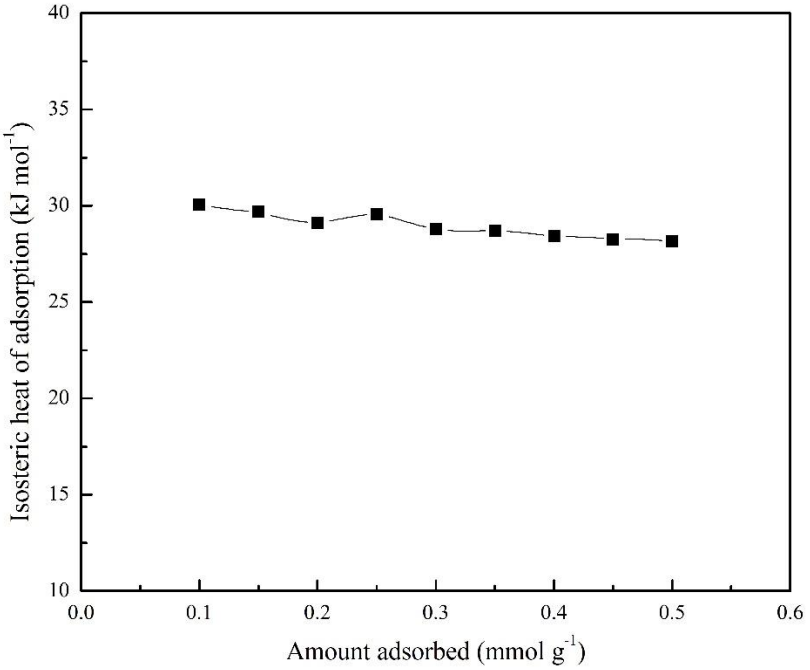

Figure 5.23 Isosteric heat of adsorption of pure CO_2 on RF-700 carbon

5.8.2 Energy duty for desorption of CO_2

For evaluation energy duty for CO_2 desorption, sensible heat was calculated from specific heat capacity, obtained by using DSC.

Specific heat capacity of RF-700 carbon, C_p = 1.215 J g^{-1} K^{-1}

Adsorption conditions:

Adsorption temperature: 30 °C

Feed gas concentration: 12.5% CO_2 in N_2

Pressure: 1 atm

Desorption conditions:

Desorption temperature: 200 °C

Purge gas: 100% N_2

Temperature difference, $\Delta T = (200 - 30)\ ℃ = 170\ ℃ = 170\ K$

CO_2 adsorption capacity of $RF - 700 = 0.76$ mmol CO_2 per g adsorbent

$= 0.76 \times 10^{-3}$ mol CO_2 per g adsorben $= 0.03344$ kg CO_2 per kg adsorbent

Hence, sensible heat $= 271.776$ kJ per mole CO_2

Net sensible heat $=$ 67.94 kJ per mole CO_2 (for 75% recovery of sensible heat [136])

To calculate isosteric heat of adsorption, value of *P* is determined at multiple temperatures from isotherm for CO_2 adsorption on RF-700 for a given q_e and the slope is determined from the plot of *ln P* against *1/T*. The isosteric heat of adsorption for RF-700 is in the range of 15.1–16.8 kJ mol^{-1} with an average value of 15.74 kJ mol^{-1}, demonstrating strong interaction between the carbon surface and CO_2 gas molecules (Figure 5.24). With increase in surface coverage, there is small decrease in isosteric heat of adsorption which indicates energetically heterogeneous adsorbent surface. But at higher surface coverage, an increase in isosteric heat of adsorption is observed which is due to intermolecular interaction between the adsorbed CO_2 molecules. For other carbon materials, value of Q_{st} has been reported to be in the range of 11–30 kJ mol^{-1} [168, 179-181]. However, the trend of isosteric heat of adsorption with surface loading under equilibrium and dynamic conditions does not match. This could be due to heterogeneity of adsorption process on account of adsorption of both CO_2 and N_2 in dynamic system.

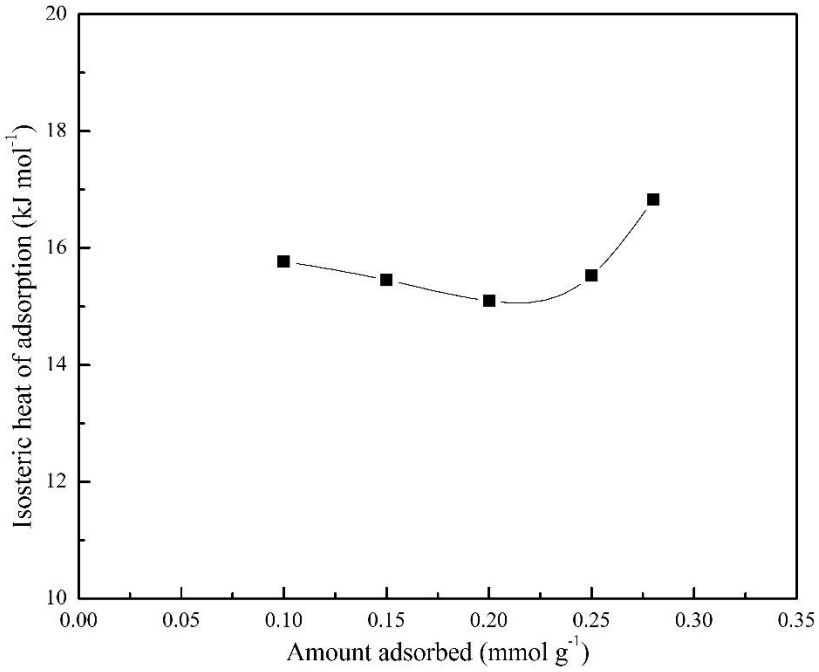

Figure 5.24 Isosteric heat of adsorption with surface coverage on RF-700

Isosteric heat of adsorption, Q_{st} = 15.74 kJ per mole CO_2

Thermal energy input = 83.68 kJ per mole CO_2 = 1.90 MJ per kg CO_2

This indicates that to desorb 1 kg of CO_2, energy required is 1.90 MJ and this energy is supplied by combustion of fossil fuels.

For 1 kg adsorbent basis

Amount of CO_2 adsorbed = 0.76 mmol g^{-1} of CO_2 = 0.03344 kg per kg adsorbent

Hence, energy required to desorb this CO_2 = 0.0636 MJ

Now, amount of CO_2 generated to produce this much energy = 0.00562 kg (source of energy: bituminous coal; CO_2 generated = 0.0884 kg per MJ of energy [170])

It can be said that 0.00562 kg of CO_2 is produced, from burning of bituminous coal, for desorption of 0.03344 kg CO_2 adsorbed on 1 kg RF-700 carbon adsorbent.

5.9 Conclusions

Nanostructured carbon adsorbents were prepared from resorcinol-formaldehyde resin and silica template via nanocasting technique followed by characterization for their textural,

chemical and surface properties. XRD and TEM analysis confirmed the development of nanostructured carbon adsorbents having partial amorphous character whereas the presence of various oxygen functional groups on the carbon surface was proved by XPS analysis, FTIR analysis and surface functionality by Boehm titration. Among the prepared carbons, RF-700 showed maximum BET surface area and total pore volume of 435 m^2 g^{-1} and 0.22 cm^3 g^{-1} respectively. Dynamic CO_2 capture experiments were carried out under simulated flue gas composition at varying temperatures and RF-700 exhibited a dynamic CO_2 adsorption capacity of 0.761 mmol g^{-1} at 30 °C and 0.405 mmol g^{-1} at 75 °C under 12.5% CO_2 concentration. CO_2 adsorption capacities of RF-700 decreased with increase in temperature due to exothermic nature of adsorption process while it increased with increase in CO_2 feed concentrations because of increased driving force. Fast adsorption kinetics with complete and easy regeneration was observed for the prepared carbons making them potential candidates for CO_2 capture from flue gas. Among the studied kinetic models, fractional order adsorption kinetic model explained CO_2 adsorption on prepared carbons over the entire adsorption region.

Pure component CO_2 and N_2 adsorption data on all the four adsorption temperatures was well predicted by both Sips and dual-site Langmuir models with low SSE%. Regressed parameters of these isotherm models were used to predict adsorption equilibria of binary system by extending these equations and by using thermodynamic model i.e. IAST in conjunction with these isotherm models. These theoretical models were unable to predict binary adsorption equilibria on RF-700 carbon across the complete experimental range, as indicated by total and partial adsorbed amounts, molar fraction in adsorbed phase and selectivity, due to heterogeneity of the adsorbent and different saturation capacities of two adsorbates. Negative values of molar enthalpy change and molar Gibbs free energy change, for pure CO_2 and N_2 adsorption, suggested the exothermic nature and feasibility of adsorption process respectively. It was also found that work requirement for CO_2 loading is lesser than that of N_2 with more ordered packing of CO_2 in the sites of carbon adsorbent. This is due to higher polarizability and quadrupole moment of CO_2 than N_2. Energy duty for CO_2 desorption, estimated from the sensible heat requirement and isosteric heat of adsorption, is equal to 1.9 MJ per kg CO_2 captured.

Chapter 6 - Conclusions and Recommendations for Future Work

6.1 Conclusions

Nanostructured carbon adsorbents were prepared by nanocasting technique using two different polymeric precursors namely melamine-formaldehyde and resorcinol-formaldehyde resins and mesoporous silica as template under varying carbonization conditions. Textural, chemical and surface parameters of the prepared carbons were found to be strongly dependent on the temperature of carbonization with 700 °C being the optimum temperature for the carbon synthesis. Carbonization under severe conditions (≥ 800 °C) lead to partial collapse of the pore structure and hence reduction in the textural properties and CO_2 adsorption capacity. Also, there was drastic decrease in basicity imparting surface functional groups, associated with both oxygen and nitrogen heteroatoms, thereby leading to a decrease in the affinity of prepared carbon materials towards slightly acidic CO_2 molecules. For both the series of carbons, development of nanostructures was confirmed by XRD and TEM results.

Dynamic CO_2 adsorption capacity of the prepared carbons, obtained from breakthrough experiments, was found to be dependent on both the textural properties and surface chemistry of the prepared carbons. Carbon obtained at 700 °C exhibited the best properties, in each set, with reference to their textural and surface properties along with their performance for CO_2 capture under dynamic conditions and hence was evaluated further to study the effect of temperature and CO_2 inlet concentration on CO_2 adsorption capacity, kinetics, isotherm and thermodynamic studies. CO_2 adsorption capacity of the prepared carbons decreased with increase in adsorption temperature due to exothermic adsorption process while it increased with CO_2 concentration due to increased driving force. These prepared carbons were suitable to separate CO_2 from dilute simulated flue gas with complete regenerability. CO_2 adsorption kinetics followed fractional order kinetic model with negative temperature dependence of rate constant.

Pure component Sips and dual-site Langmuir models well predicted the adsorption equilibria of pure CO_2 and pure N_2 on the prepared carbons. However, their extended forms highly under predicted the amount of CO_2 adsorbed over the complete temperature and feed concentration

range because of the difference in adsorptive strengths of CO_2 and N_2 molecules. Also, ideal adsorbed solution theory was not able to describe the mixed-gas adsorption equilibria. This was due to dissimilar adsorption levels of the adsorbates and also due to formation of non-ideal adsorptive mixtures on the prepared carbons at equilibria. Total adsorbed amounts were found to increase with CO_2 gas phase molar fraction implying positive deviation from Raoult's law with asymmetric *x-y* diagrams.

Feasibility and spontaneity of the adsorption process was confirmed from the Gibbs free energy change thermodynamic parameter while molar enthalpy change indicated adsorption process to be exothermic in nature. CO_2 was found to be associated with lesser degrees of freedom and showed more ordered configuration on carbon surface than N_2 as it has higher polarizability and quadrupole moment than N_2.

Nature of the starting material i.e. polymeric precursor had a great effect on the kind of surface functional groups present on the carbon surface which further affected their CO_2 adsorption capacity. Presence of nitrogen functionality enhanced the basic character of these carbons thereby leading to higher CO_2 adsorption capacities (of MF-700) than carbons without nitrogen (RF-700) though later showed better textural properties. Moreover, surface basicity imparted by oxygen functional groups was almost two times higher in MF based carbon as compared to RF derived carbons. There was a considerable effect on the adsorbent's selectivity also towards CO_2 over N_2. MF based carbons exhibited very high selectivity (ca. 2–4 times) as compared to RF-700 carbon.

Carbons obtained by direct carbonization of polymeric precursors exhibited poor properties in terms of surface area, pore volume, nitrogen content and surface basicity and hence poor CO_2 adsorption capacity. This indicates the benefit of using nanocasting technique which produced carbon adsorbents having great potential in the field of CO_2 capture.

On the whole, the present work is a comprehensive study of development, characterization and performance evaluation, under dynamic conditions, of nanostructured carbons from nanocasting technique followed by kinetics, isotherm (pure and binary system) and thermodynamic studies of CO_2 adsorption.

6.2 Recommendations for future work

- Further adsorption study of these developed carbons should be undertaken at high pressure conditions depending on their application in various fields.
- Effect of various impurities such as particulate matter, SO_x and NO_x on CO_2 adsorption performance of these carbons can be evaluated in order to have complete overview of the capture process.
- Effect of carbonization conditions, like heating rate and carbonization time, on the properties of the obtained carbons should be investigated that will further affect the CO_2 adsorption capacity.
- Development of mesoporous carbon adsorbents can be carried out by using other template materials like silica (MCM-48 and SBA-15) and zeolites and can be investigated for CO_2 capture.

References

[1] Mondal, M.K., Balsora, H.K., Varshney, P., Progress and trends in CO_2 capture/separation technologies: A review, *Energy*, **2012**, *46*, 431-441.

[2] IPCC, 2014: Climate change 2014: Mitigation of climate change. Contribution of working group III to the fifth assessment report of the Intergovernmental panel on climate change, in: Edenhofer, O., Pichs-Madruga, R., Sokona, Y., Farahani, E., Kadner, S., Seyboth, K., Adler, A., Baum, I., Brunner, S., Eickemeier, P., Kriemann, B., Savolainen, J., Schlömer, S., von Stechow, C., Zwickel, T., Minx, J.C. (Eds.), Cambridge, United Kingdom and New York, NY, USA, **2014**.

[3] Spigarelli, B.P., Kawatra, S.K., Opportunities and challenges in carbon dioxide capture, *Journal of CO_2 Utilization*, **2013**, *1*, 69-87.

[4] Energy technology perspectives 2012: Pathways to a clean energy system, IEA, OECD Publishing, Paris, **2012**.

[5] Sreenivasulu, B., Gayatri, D.V., Sreedhar, I., Raghavan, K.V., A journey into the process and engineering aspects of carbon capture technologies, *Renewable and Sustainable Energy Reviews*, **2015**, *41*, 1324-1350.

[6] Hofmann, D.J., Butler, J.H., Tans, P.P., A new look at atmospheric carbon dioxide, *Atmospheric Environment*, **2009**, *43*, 2084-2086.

[7] Yu, K.M.K., Curcic, I., Gabriel, J., Tsang, S.C.E., Recent advances in CO_2 capture and utilization, *ChemSusChem*, **2008**, *1*, 893-899.

[8] Plasynski, S.I., Litynski, J.T., McIlvried, H.G., Srivastava, R.D., Progress and new developments in carbon capture and storage, *Critical Reviews in Plant Sciences*, **2009**, *28*, 123-138.

[9] Lal, R., Sequestering atmospheric carbon dioxide, *Critical Reviews in Plant Sciences*, **2009**, *28*, 90-96.

[10] Climate change indicators in the United States, 2014, *U.S. Environmental Protection Agency*, **2014**.

[11] Markewitz, P., Kuckshinrichs, W., Leitner, W., Linssen, J., Zapp, P., Bongartz, R., Schreiber, A., Muller, T.E., Worldwide innovations in the development of carbon capture technologies and the utilization of CO_2, *Energy & Environmental Science*, **2012**, *5*, 7281-7305.

[12] Yang, H., Xu, Z., Fan, M., Gupta, R., Slimane, R.B., Bland, A.E., Wright, I., Progress in carbon dioxide separation and capture: A review, *Journal of Environmental Sciences*, **2008**, *20*, 14-27.

[13] Steeneveldt, R., Berger, B., Torp, T.A., CO_2 capture and storage: Closing the knowing–doing gap, *Chemical Engineering Research and Design*, **2006**, *84*, 739-763.

[14] Metz, B., Davidson, O., De Coninck, H., Loos, M., Meyer, L., IPCC special report on carbon dioxide capture and storage. Prepared by working group III of the intergovernmental panel on climate change, in, IPCC, Cambridge University Press: Cambridge, United Kingdom and New York, USA, **2005**.

[15] Sengupta, S., Studies on CO_2 capture using adsorption from simulated refinery flue gas, *Ph. D. Thesis*, Department of Chemical Engineering, Thapar University, Patiala, **2015**.

[16] Figueroa, J.D., Fout, T., Plasynski, S., McIlvried, H., Srivastava, R.D., Advances in CO_2 capture technology—the U.S. Department of energy's carbon sequestration program, *International Journal of Greenhouse Gas Control*, **2008**, *2*, 9-20.

[17] Sánchez, J.M., Maroño, M., Cillero, D., Montenegro, L., Ruiz, E., Laboratory- and bench-scale studies of a sweet water–gas-shift catalyst for H_2 and CO_2 production in pre-combustion CO_2 capture, *Fuel*, **2013**, *114*, 191-198.

[18] Danaei Kenarsari, S., Fan, M., Jiang, G., Shen, X., Lin, Y., Hu, X., Use of a robust and inexpensive nanoporous TiO_2 for pre-combustion CO_2 separation, *Energy & Fuels*, **2013**, *27*, 6938-6947.

[19] Wall, T., Stanger, R., Liu, Y., Gas cleaning challenges for coal-fired oxy-fuel technology with carbon capture and storage, *Fuel*, **2013**, *108*, 85-90.

[20] Buhre, B.J.P., Elliott, L.K., Sheng, C.D., Gupta, R.P., Wall, T.F., Oxy-fuel combustion technology for coal-fired power generation, *Progress in Energy and Combustion Science*, **2005**, *31*, 283-307.

[21] Rubin, E.S., Mantripragada, H., Marks, A., Versteeg, P., Kitchin, J., The outlook for improved carbon capture technology, *Progress in Energy and Combustion Science*, **2012**, *38*, 630-671.

[22] Goto, K., Yogo, K., Higashii, T., A review of efficiency penalty in a coal-fired power plant with post-combustion CO_2 capture, *Applied Energy*, **2013**, *111*, 710-720.

[23] Jones, C.W., CO_2 capture from dilute gases as a component of modern global carbon management, *Annual Review of Chemical and Biomolecular Engineering*, **2011**, *2*, 31-52.

[24] D'Alessandro, D.M., Smit, B., Long, J.R., Carbon dioxide capture: Prospects for new materials, *Angewandte Chemie*, **2010**, *49*, 6058-6082.

[25] Samanta, A., Zhao, A., Shimizu, G.K.H., Sarkar, P., Gupta, R., Post-combustion CO_2 capture using solid sorbents: A review, *Industrial & Engineering Chemistry Research*, **2012**, *51*, 1438-1463.

[26] Leung, D.Y.C., Caramanna, G., Maroto-Valer, M.M., An overview of current status of carbon dioxide capture and storage technologies, *Renewable and Sustainable Energy Reviews*, **2014**, *39*, 426-443.

[27] Muraleedharan, R., Mondal, A., Mandal, B., Absorption of carbon dioxide into aqueous blends of 2-amino-2-hydroxymethyl-1,3-propanediol and monoethanolamine, *Separation and Purification Technology*, **2012**, *94*, 92-96.

[28] Thiruvenkatachari, R., Su, S., An, H., Yu, X.X., Post combustion CO_2 capture by carbon fibre monolithic adsorbents, *Progress in Energy and Combustion Science*, **2009**, *35*, 438-455.

[29] Ho, M.T., Allinson, G.W., Wiley, D.E., Reducing the cost of CO_2 capture from flue gases using membrane technology, *Industrial & Engineering Chemistry Research*, **2008**, *47*, 1562-1568.

[30] Sridhar, S., Smitha, B., Aminabhavi, T.M., Separation of carbon dioxide from natural gas mixtures through polymeric membranes—a review, *Separation & Purification Reviews*, **2007**, *36*, 113-174.

[31] Brunetti, A., Scura, F., Barbieri, G., Drioli, E., Membrane technologies for CO_2 separation, *Journal of Membrane Science*, **2010**, *359*, 115-125.

[32] Aaron, D., Tsouris, C., Separation of CO_2 from flue gas: A review, *Separation Science and Technology*, **2005**, *40*, 321-348.

[33] Goel, C., Preparation of adsorbent(s) using nano-casting technique for carbon dioxide capture from flue gases, *M. Tech. Thesis*, Thapar University, Patiala, **2011**.

[34] Liu, Z., Grande, C.A., Li, P., Yu, J., Rodrigues, A.E., Multi-bed vacuum pressure swing adsorption for carbon dioxide capture from flue gas, *Separation and Purification Technology*, **2011**, *81*, 307-317.

[35] Ribeiro, R.P.P.L., Grande, C.A., Rodrigues, A.E., Adsorption of water vapor on carbon molecular sieve: Thermal and electrothermal regeneration study, *Industrial & Engineering Chemistry Research*, **2011**, *50*, 2144-2156.

[36] Pires, J.C.M., Martins, F.G., Alvim-Ferraz, M.C.M., Simões, M., Recent developments on carbon capture and storage: An overview, *Chemical Engineering Research and Design*, **2011**, *89*, 1446-1460.

[37] Merel, J., Clausse, M., Meunier, F., Experimental investigation on CO_2 post-combustion capture by indirect thermal swing adsorption using 13X and 5A zeolites, *Industrial & Engineering Chemistry Research*, **2008**, *47*, 209-215.

[38] Siriwardane, R.V., Shen, M.-S., Fisher, E.P., Adsorption of CO_2 on zeolites at moderate temperatures, *Energy & Fuels*, **2005**, *19*, 1153-1159.

[39] Grande, C.A., Ribeiro, R.P.L., Oliveira, E.L.G., Rodrigues, A.E., Electric swing adsorption as emerging CO_2 capture technique, *Energy Procedia*, **2009**, *1*, 1219-1225.

[40] Santos, M.P.S., Grande, C.A., Rodrigues, A.E., Pressure swing adsorption for biogas upgrading. Effect of recycling streams in pressure swing adsorption design, *Industrial & Engineering Chemistry Research*, **2011**, *50*, 974-985.

[41] Chou, C.-T., Chen, C.-Y., Carbon dioxide recovery by vacuum swing adsorption, *Separation and Purification Technology*, **2004**, *39*, 51-65.

[42] Takamura, Y., Aoki, J., Uchida, S., Narita, S., Application of high-pressure swing adsorption process for improvement of CO_2 recovery system from flue gas, *The Canadian Journal of Chemical Engineering*, **2001**, *79*, 812-816.

[43] Clausse, M., Merel, J., Meunier, F., Numerical parametric study on CO_2 capture by indirect thermal swing adsorption, *International Journal of Greenhouse Gas Control*, **2011**, *5*, 1206-1213.

[44] Yang, R.T., Adsorbents: Fundamentals and Applications, John Wiley & Sons, Inc., **2003**.

[45] Sharma, M., Vyas, R.K., Singh, K., A review on reactive adsorption for potential environmental applications, *Adsorption*, **2012**, *19*, 161-188.

[46] Choi, S., Drese, J.H., Jones, C.W., Adsorbent materials for carbon dioxide capture from large anthropogenic point sources, *ChemSusChem*, **2009**, *2*, 796-854.

[47] Hu, X., Mangano, E., Friedrich, D., Ahn, H., Brandani, S., Diffusion mechanism of CO_2 in 13X zeolite beads, *Adsorption*, **2014**, *20*, 121-135.

[48] Hedin, N., Andersson, L., Bergström, L., Yan, J., Adsorbents for the post-combustion capture of CO_2 using rapid temperature swing or vacuum swing adsorption, *Applied Energy*, **2013**, *104*, 418-433.

[49] Li, G., Xiao, P., Webley, P., Zhang, J., Singh, R., Marshall, M., Capture of CO_2 from high humidity flue gas by vacuum swing adsorption with zeolite 13X, *Adsorption*, **2008**, *14*, 415-422.

[50] Rege, S.U., Yang, R.T., A novel FTIR method for studying mixed gas adsorption at low concentrations: H_2O and CO_2 on NaX zeolite and γ-alumina, *Chemical Engineering Science*, **2001**, *56*, 3781-3796.

[51] Brandani, F., Ruthven, D.M., The effect of water on the adsorption of CO_2 and C_3H_8 on type X zeolites, *Industrial & Engineering Chemistry Research*, **2004**, *43*, 8339-8344.

[52] Cavenati, S., Grande, C.A., Rodrigues, A.E., Adsorption equilibrium of methane, carbon dioxide, and nitrogen on zeolite 13X at high pressures, *Journal of Chemical & Engineering Data*, **2004**, *49*, 1095-1101.

[53] Saha, D., Bao, Z., Jia, F., Deng, S., Adsorption of CO_2, CH_4, N_2O, and N_2 on MOF-5, MOF-177, and zeolite 5A, *Environmental Science & Technology*, **2010**, *44*, 1820-1826.

[54] Siriwardane, R.V., Shen, M.-S., Fisher, E.P., Poston, J.A., Adsorption of CO_2 on molecular sieves and activated carbon, *Energy & Fuels*, **2001**, *15*, 279-284.

[55] Jadhav, P.D., Chatti, R.V., Biniwale, R.B., Labhsetwar, N.K., Devotta, S., Rayalu, S.S., Monoethanol amine modified zeolite 13X for CO_2 adsorption at different temperatures, *Energy & Fuels*, **2007**, *21*, 3555-3559.

[56] Chatti, R., Bansiwal, A.K., Thote, J.A., Kumar, V., Jadhav, P., Lokhande, S.K., Biniwale, R.B., Labhsetwar, N.K., Rayalu, S.S., Amine loaded zeolites for carbon dioxide capture: Amine loading and adsorption studies, *Microporous and Mesoporous Materials*, **2009**, *121*, 84-89.

[57] Xu, X., Zhao, X., Sun, L., Liu, X., Adsorption separation of carbon dioxide, methane and nitrogen on monoethanol amine modified β-zeolite, *Journal of Natural Gas Chemistry*, **2009**, *18*, 167-172.

[58] Fisher, J.C., Tanthana, J., Chuang, S.S.C., Oxide-supported tetraethylenepentamine for CO_2 capture, *Environmental Progress & Sustainable Energy*, **2009**, *28*, 589-598.

[59] Xu, X., Song, C., Andresen, J.M., Miller, B.G., Scaroni, A.W., Novel polyethylenimine-modified mesoporous molecular sieve of MCM-41 type as high-capacity adsorbent for CO_2 capture, *Energy & Fuels*, **2002**, *16*, 1463-1469.

[60] Xu, X., Song, C., Miller, B.G., Scaroni, A.W., Adsorption separation of carbon dioxide from flue gas of natural gas-fired boiler by a novel nanoporous "molecular basket" adsorbent, *Fuel Processing Technology*, **2005**, *86*, 1457-1472.

[61] Xu, X., Song, C., Miller, B.G., Scaroni, A.W., Influence of moisture on CO_2 separation from gas mixture by a nanoporous adsorbent based on polyethylenimine-modified molecular sieve MCM-41, *Industrial & Engineering Chemistry Research*, **2005**, *44*, 8113-8119.

[62] Xu, X., Song, C., Andresen, J.M., Miller, B.G., Scaroni, A.W., Adsorption separation of CO_2 from simulated flue gas mixtures by novel CO_2 "molecular basket" adsorbents, *International Journal of Environmental Technology and Management*, **2004**, *4*, 32-52.

[63] Xu, X., Song, C., Andrésen, J.M., Miller, B.G., Scaroni, A.W., Preparation and characterization of novel CO_2 "molecular basket" adsorbents based on polymer-modified mesoporous molecular sieve MCM-41, *Microporous and Mesoporous Materials*, **2003**, *62*, 29-45.

[64] Franchi, R.S., Harlick, P.J.E., Sayari, A., Applications of pore-expanded mesoporous silica. 2. Development of a high-capacity, water-tolerant adsorbent for CO_2, *Industrial & Engineering Chemistry Research*, **2005**, *44*, 8007-8013.

[65] Belmabkhout, Y., Serna-Guerrero, R., Sayari, A., Adsorption of CO_2 from dry gases on MCM-41 silica at ambient temperature and high pressure. 1: Pure adsorption, *Chemical Engineering Science*, **2009**, *64*, 3721-3728.

[66] Belmabkhout, Y., Serna-Guerrero, R., Sayari, A., Adsorption of CO_2-containing gas mixtures over amine-bearing pore-expanded MCM-41 silica: Application for gas purification, *Industrial & Engineering Chemistry Research*, **2010**, *49*, 359-365.

[67] Serna-Guerrero, R., Belmabkhout, Y., Sayari, A., Triamine-grafted pore-expanded mesoporous silica for CO_2 capture: Effect of moisture and adsorbent regeneration strategies, *Adsorption*, **2010**, *16*, 567-575.

[68] Son, W.-J., Choi, J.-S., Ahn, W.-S., Adsorptive removal of carbon dioxide using polyethyleneimine-loaded mesoporous silica materials, *Microporous and Mesoporous Materials*, **2008**, *113*, 31-40.

[69] Chen, C., Yang, S.T., Ahn, W.S., Ryoo, R., Amine-impregnated silica monolith with a hierarchical pore structure: Enhancement of CO_2 capture capacity, *Chemical Communications*, **2009**, 3627-3629.

[70] Ma, X., Wang, X., Song, C., "Molecular basket" sorbents for separation of CO_2 and H_2S from various gas streams, *Journal of the American Chemical Society*, **2009**, *131*, 5777-5783.

[71] Sanz, R., Calleja, G., Arencibia, A., Sanz-Pérez, E.S., CO_2 adsorption on branched polyethyleneimine-impregnated mesoporous silica SBA-15, *Applied Surface Science*, **2010**, *256*, 5323-5328.

[72] Jimenez, V., Ramirez-Lucas, A., Diaz, J.A., Sanchez, P., Romero, A., CO_2 capture in different carbon materials, *Environmental Science & Technology*, **2012**, *46*, 7407-7414.

[73] Stein, A., Wang, Z., Fierke, M.A., Functionalization of porous carbon materials with designed pore architecture, *Advanced Materials*, **2009**, *21*, 265-293.

[74] Pietrzak, R., Nowicki, P., Kaźmierczak, J., Kuszyńska, I., Goscianska, J., Przepiórski, J., Comparison of the effects of different chemical activation methods on properties of carbonaceous adsorbents obtained from cherry stones, *Chemical Engineering Research and Design*, **2014**, *92*, 1187-1191.

[75] Wahby, A., Ramos-Fernández, J.M., Martínez-Escandell, M., Sepúlveda-Escribano, A., Silvestre-Albero, J., Rodríguez-Reinoso, F., High-surface-area carbon molecular sieves for selective CO_2 adsorption, *ChemSusChem*, **2010**, *3*, 974-981.

[76] Zhou, L., Liu, X., Li, J., Wang, N., Wang, Z., Zhou, Y., Synthesis of ordered mesoporous carbon molecular sieve and its adsorption capacity for H_2, N_2, O_2, CH_4 and CO_2, *Chemical Physics Letters*, **2005**, *413*, 6-9.

[77] Bikshapathi, M., Sharma, A., Sharma, A., Verma, N., Preparation of carbon molecular sieves from carbon micro and nanofibers for sequestration of CO_2, *Chemical Engineering Research and Design*, **2011**, *89*, 1737-1746.

[78] Cinke, M., Li, J., Bauschlicher, C.W., Ricca, A., Meyyappan, M., CO_2 adsorption in single-walled carbon nanotubes, *Chemical Physics Letters*, **2003**, *376*, 761-766.

[79] Sircar, S., Golden, T.C., Rao, M.B., Activated carbon for gas separation and storage, *Carbon*, **1996**, *34*, 1-12.

[80] Davini, P., Flue gas treatment by activated carbon obtained from oil-fired fly ash, *Carbon*, **2002**, *40*, 1973-1979.

[81] Na, B.-K., Koo, K.-K., Eum, H.-M., Lee, H., Song, H., CO_2 recovery from flue gas by PSA process using activated carbon, *Korean J. Chem. Eng.*, **2001**, *18*, 220-227.

[82] Himeno, S., Komatsu, T., Fujita, S., High-pressure adsorption equilibria of methane and carbon dioxide on several activated carbons, *Journal of Chemical & Engineering Data*, **2005**, *50*, 369-376.

[83] Do, D.D., Wang, K., A new model for the description of adsorption kinetics in heterogeneous activated carbon, *Carbon*, **1998**, *36*, 1539-1554.

[84] Wang, R., Wang, P., Yan, X., Lang, J., Peng, C., Xue, Q., Promising porous carbon derived from celtuce leaves with outstanding supercapacitance and CO_2 capture performance, *ACS Applied Materials & Interfaces*, **2012**, *4*, 5800-5806.

[85] Arenillas, A., Smith, K.M., Drage, T.C., Snape, C.E., CO_2 capture using some fly ash-derived carbon materials, *Fuel*, **2005**, *84*, 2204-2210.

[86] Maroto-Valer, M.M., Lu, Z., Zhang, Y., Tang, Z., Sorbents for CO_2 capture from high carbon fly ashes, *Waste Management*, **2008**, *28*, 2320-2328.

[87] Plaza, M.G., Pevida, C., Arias, B., Fermoso, J., Casal, M.D., Martín, C.F., Rubiera, F., Pis, J.J., Development of low-cost biomass-based adsorbents for postcombustion CO_2 capture, *Fuel*, **2009**, *88*, 2442-2447.

[88] Plaza, M.G., Pevida, C., Martín, C.F., Fermoso, J., Pis, J.J., Rubiera, F., Developing almond shell-derived activated carbons as CO_2 adsorbents, *Separation and Purification Technology*, **2010**, *71*, 102-106.

[89] Thote, J.A., Iyer, K.S., Chatti, R., Labhsetwar, N.K., Biniwale, R.B., Rayalu, S.S., In situ nitrogen enriched carbon for carbon dioxide capture, *Carbon*, **2010**, *48*, 396-402.

[90] Olivares-Marín, M., García, S., Pevida, C., Wong, M.S., Maroto-Valer, M., The influence of the precursor and synthesis method on the CO_2 capture capacity of carpet waste-based sorbents, *Journal of Environmental Management*, **2011**, *92*, 2810-2817.

[91] Sevilla, M., Fuertes, A.B., Sustainable porous carbons with a superior performance for CO_2 capture, *Energy & Environmental Science*, **2011**, *4*, 1765-1771.

[92] Valdés-Solís, T., Fuertes, A.B., High-surface area inorganic compounds prepared by nanocasting techniques, *Materials Research Bulletin*, **2006**, *41*, 2187-2197.

[93] Karandikar, P., Patil, K.R., Mitra, A., Kakade, B., Chandwadkar, A.J., Synthesis and characterization of mesoporous carbon through inexpensive mesoporous silica as template, *Microporous and Mesoporous Materials*, **2007**, *98*, 189-199.

[94] Drage, T.C., Arenillas, A., Smith, K.M., Pevida, C., Piippo, S., Snape, C.E., Preparation of carbon dioxide adsorbents from the chemical activation of urea–formaldehyde and melamine–formaldehyde resins, *Fuel*, **2007**, *86*, 22-31.

[95] Hao, G.-P., Li, W.-C., Qian, D., Lu, A.-H., Rapid synthesis of nitrogen-doped porous carbon monolith for CO_2 capture, *Advanced Materials*, **2010**, *22*, 853-857.

[96] Sevilla, M., Valle-Vigón, P., Fuertes, A.B., N-doped polypyrrole-based porous carbons for CO_2 capture, *Advanced Functional Materials*, **2011**, *21*, 2781-2787.

[97] Meng, L.-Y., Park, S.-J., One-pot synthetic method to prepare highly N-doped nanoporous carbons for CO_2 adsorption, *Materials Chemistry and Physics*, **2014**, *143*, 1158-1163.

[98] Liu, Z., Du, Z., Song, H., Wang, C., Subhan, F., Xing, W., Yan, Z., The fabrication of porous N-doped carbon from widely available urea formaldehyde resin for carbon dioxide adsorption, *Journal of Colloid and Interface Science*, **2014**, *416*, 124-132.

[99] Liu, Z., Du, Z., Xing, W., Yan, Z., Facial synthesis of N-doped microporous carbon derived from urea furfural resin with high CO_2 capture capacity, *Materials Letters*, **2014**, *117*, 273-275.

[100] Balsamo, M., Budinova, T., Erto, A., Lancia, A., Petrova, B., Petrov, N., Tsyntsarski, B., CO_2 adsorption onto synthetic activated carbon: Kinetic, thermodynamic and regeneration studies, *Separation and Purification Technology*, **2013**, *116*, 214-221.

[101] Tseng, R.-L., Wu, F.-C., Juang, R.-S., Adsorption of CO_2 at atmospheric pressure on activated carbons prepared from melamine-modified phenol–formaldehyde resins, *Separation and Purification Technology*, **2015**, *140*, 53-60.

[102] Lee, J., Han, S., Hyeon, T., Synthesis of new nanoporous carbon materials using nanostructured silica materials as templates, *Journal of Materials Chemistry*, **2004**, *14*, 478-486.

[103] Liang, C., Li, Z., Dai, S., Mesoporous carbon materials: Synthesis and modification, *Angewandte Chemie*, **2008**, *47*, 3696-3717.

[104] Lu, A.H., Schüth, F., Nanocasting: A versatile strategy for creating nanostructured porous materials, *Advanced Materials*, **2006**, *18*, 1793-1805.

[105] Xu, B., Peng, L., Wang, G., Cao, G., Wu, F., Easy synthesis of mesoporous carbon using nano-$CaCO_3$ as template, *Carbon*, **2010**, *48*, 2377-2380.

[106] Pevida, C., Drage, T.C., Snape, C.E., Silica-templated melamine–formaldehyde resin derived adsorbents for CO_2 capture, *Carbon*, **2008**, *46*, 1464-1474.

[107] Sevilla, M., Fuertes, A.B., CO_2 adsorption by activated templated carbons, *Journal of Colloid and Interface Science*, **2012**, *366*, 147-154.

[108] Zhao, Y., Zhao, L., Yao, K.X., Yang, Y., Zhang, Q., Han, Y., Novel porous carbon materials with ultrahigh nitrogen contents for selective CO_2 capture, *Journal of Materials Chemistry*, **2012**, *22*, 19726-19731.

[109] Li, Q., Yang, J., Feng, D., Wu, Z., Wu, Q., Park, S., Ha, C.-S., Zhao, D., Facile synthesis of porous carbon nitride spheres with hierarchical three-dimensional mesostructures for CO_2 capture, *Nano Research*, **2010**, *3*, 632-642.

[110] Lakhi, K.S., Cha, W.S., Joseph, S., Wood, B.J., Aldeyab, S.S., Lawrence, G., Choy, J.-H., Vinu, A., Cage type mesoporous carbon nitride with large mesopores for CO_2 capture, *Catalysis Today*, **2015**, *243*, 209-217.

[111] Zhou, W., Bai, X., Wang, E., Xie, S., Synthesis, structure, and properties of single-walled carbon nanotubes, *Advanced Materials*, **2009**, *21*, 4565-4583.

[112] Su, F., Lu, C., Cnen, W., Bai, H., Hwang, J.F., Capture of CO_2 from flue gas via multiwalled carbon nanotubes, *Science of The Total Environment*, **2009**, *407*, 3017-3023.

[113] Lu, C., Bai, H., Wu, B., Su, F., Hwang, J.F., Comparative study of CO_2 capture by carbon nanotubes, activated carbons, and zeolites, *Energy & Fuels*, **2008**, *22*, 3050-3056.

[114] Su, F., Lu, C., Chen, H.S., Adsorption, desorption, and thermodynamic studies of CO_2 with high-amine-loaded multiwalled carbon nanotubes, *Langmuir*, **2011**, *27*, 8090-8098.

[115] Ye, Q., Jiang, J., Wang, C., Liu, Y., Pan, H., Shi, Y., Adsorption of low-concentration carbon dioxide on amine-modified carbon nanotubes at ambient temperature, *Energy & Fuels*, **2012**, *26*, 2497-2504.

[116] Boehm, H.P., Surface oxides on carbon and their analysis: A critical assessment, *Carbon*, **2002**, *40*, 145-149.

[117] Lopez-Ramon, M.V., Stoeckli, F., Moreno-Castilla, C., Carrasco-Marin, F., On the characterization of acidic and basic surface sites on carbons by various techniques, *Carbon*, **1999**, *37*, 1215-1221.

[118] Lagergren, S., About the theory of so-called adsorption of soluble substances, *Kungliga Svenska Vetenskapsakademiens Handlingar*, **1898**, *24*, 1-39.

[119] Ho, Y.S., McKay, G., Pseudo-second order model for sorption processes, *Process Biochemistry*, **1999**, *34*, 451-465.

[120] Zhao, A., Samanta, A., Sarkar, P., Gupta, R., Carbon dioxide adsorption on amine-impregnated mesoporous SBA-15 sorbents: Experimental and kinetics study, *Industrial & Engineering Chemistry Research*, **2013**, *52*, 6480-6491.

[121] Heydari-Gorji, A., Sayari, A., CO_2 capture on polyethylenimine-impregnated hydrophobic mesoporous silica: Experimental and kinetic modeling, *Chemical Engineering Journal*, **2011**, *173*, 72-79.

[122] Kumar, K.V., Sivanesan, S., Selection of optimum sorption kinetics: Comparison of linear and non-linear method, *Journal of Hazardous Materials*, **2006**, *134*, 277-279.

[123] Kumar, K.V., Sivanesan, S., Comparison of linear and non-linear method in estimating the sorption isotherm parameters for safranin onto activated carbon, *Journal of Hazardous Materials*, **2005**, *123*, 288-292.

[124] Ho, Y.-S., Second-order kinetic model for the sorption of cadmium onto tree fern: A comparison of linear and non-linear methods, *Water Research*, **2006**, *40*, 119-125.

[125] Langmuir, I., The constitution and fundamental properties of solids and liquids. Part I. Solids, *Journal of the American Chemical Society*, **1916**, *38*, 2221-2295.

[126] Ritter, J.A., Bhadra, S.J., Ebner, A.D., On the use of the dual-process langmuir model for correlating unary equilibria and predicting mixed-gas adsorption equilibria, *Langmuir*, **2011**, *27*, 4700-4712.

[127] García, S., Pis, J.J., Rubiera, F., Pevida, C., Predicting mixed-gas adsorption equilibria on activated carbon for precombustion CO_2 capture, *Langmuir:The ACS Journal of Surfaces and Colloids*, **2013**, *29*, 6042-6052.

[128] Myers, A.L., Prausnitz, J.M., Thermodynamics of mixed-gas adsorption, *AIChE Journal*, **1965**, *11*, 121-127.

[129] Frey, D.D., Rodrigues, A.E., Explicit calculation of multicomponent equilibria for ideal adsorbed solutions, *AIChE Journal*, **1994**, *40*, 182-186.

[130] Do, D.D., Adsorption Analysis: Equilibria and Kinetics, Imperial College Press, **1998**.

[131] Sochard, S., Fernandes, N., Reneaume, J.-M., Modeling of adsorption isotherm of a binary mixture with real adsorbed solution theory and nonrandom two-liquid model, *AIChE Journal*, **2010**, *56*, 3109-3119.

[132] Ruthven, D.M., Principles of Adsorption and Adsorption Processes, John Wiley & Sons, **1984**.

[133] Schell, J., Casas, N., Pini, R., Mazzotti, M., Pure and binary adsorption of CO_2, H_2, and N_2 on activated carbon, *Adsorption*, **2012**, *18*, 49-65.

[134] Deng, H., Yi, H., Tang, X., Yu, Q., Ning, P., Yang, L., Adsorption equilibrium for sulfur dioxide, nitric oxide, carbon dioxide, nitrogen on 13X and 5A zeolites, *Chemical Engineering Journal*, **2012**, *188*, 77-85.

[135] Ridha, F.N., Webley, P.A., Entropic effects and isosteric heats of nitrogen and carbon dioxide adsorption on chabazite zeolites, *Microporous and Mesoporous Materials*, **2010**, *132*, 22-30.

[136] Veneman, R., Kamphuis, H., Brilman, D., Post-combustion CO_2 capture using supported amine sorbents: A process integration study, *Energy Procedia*, **2013**, *37*, 2100-2108.

[137] Sjostrom, S., Krutka, H., Evaluation of solid sorbents as a retrofit technology for CO_2 capture, *Fuel*, **2010**, *89*, 1298-1306.

[138] Fauth, D.J., Gray, M.L., Pennline, H.W., Krutka, H.M., Sjostrom, S., Ault, A.M., Investigation of porous silica supported mixed-amine sorbents for post-combustion CO_2 capture, *Energy & Fuels*, **2012**, *26*, 2483-2496.

[139] Vinu, A., Ariga, K., Mori, T., Nakanishi, T., Hishita, S., Golberg, D., Bando, Y., Preparation and characterization of well-ordered hexagonal mesoporous carbon nitride, *Advanced Materials*, **2005**, *17*, 1648-1652.

[140] Vinu, A., Anandan, S., Anand, C., Srinivasu, P., Ariga, K., Mori, T., Fabrication of partially graphitic three-dimensional nitrogen-doped mesoporous carbon using polyaniline nanocomposite through nanotemplating method, *Microporous and Mesoporous Materials*, **2008**, *109*, 398-404.

[141] Xia, Y., Mokaya, R., Generalized and facile synthesis approach to N-doped highly graphitic mesoporous carbon materials, *Chemistry of Materials*, **2005**, *17*, 1553-1560.

[142] Lee, S.-Y., Park, S.-J., Determination of the optimal pore size for improved CO_2 adsorption in activated carbon fibers, *Journal of Colloid and Interface Science*, **2013**, *389*, 230-235.

[143] Andhariya, N., Chudasama, B., Mehta, R.V., Upadhyay, R.V., Nanoengineering of methylene blue loaded silica encapsulated magnetite nanospheres and nanocapsules for photodynamic therapy, *Journal of Nanoparticle Research*, **2011**, *13*, 3619-3631.

[144] Chen, C., Kim, J., Ahn, W.-S., Efficient carbon dioxide capture over a nitrogen-rich carbon having a hierarchical micro-mesopore structure, *Fuel*, **2012**, *95*, 360-364.

[145] Przepiórski, J., Skrodzewicz, M., Morawski, A.W., High temperature ammonia treatment of activated carbon for enhancement of CO_2 adsorption, *Applied Surface Science*, **2004**, *225*, 235-242.

[146] László, K., Tombácz, E., Josepovits, K., Effect of activation on the surface chemistry of carbons from polymer precursors, *Carbon*, **2001**, *39*, 1217-1228.

[147] Wang, L., Yang, R.T., Significantly increased CO_2 adsorption performance of nanostructured templated carbon by tuning surface area and nitrogen doping, *The Journal of Physical Chemistry C*, **2012**, *116*, 1099-1106.

[148] Pels, J.R., Kapteijn, F., Moulijn, J.A., Zhu, Q., Thomas, K.M., Evolution of nitrogen functionalities in carbonaceous materials during pyrolysis, *Carbon*, **1995**, *33*, 1641-1653.

[149] Olejniczak, A., Lezanska, M., Wloch, J., Kucinska, A., Lukaszewicz, J.P., Novel nitrogen-containing mesoporous carbons prepared from chitosan, *Journal of Materials Chemistry A*, **2013**, *1*, 8961-8967.

[150] Pevida, C., Plaza, M.G., Arias, B., Fermoso, J., Rubiera, F., Pis, J.J., Surface modification of activated carbons for CO_2 capture, *Applied Surface Science*, **2008**, *254*, 7165-7172.

[151] Zhu, B., Li, K., Liu, J., Liu, H., Sun, C., Snape, C.E., Guo, Z., Nitrogen-enriched and hierarchically porous carbon macro-spheres-ideal for large-scale CO_2 capture, *Journal of Materials Chemistry A*, **2014**, *2*, 5481-5489.

[152] Zhou, J., Li, W., Zhang, Z., Xing, W., Zhuo, S., Carbon dioxide adsorption performance of N-doped zeolite Y templated carbons, *RSC Advances*, **2012**, *2*, 161-167.

[153] Sayari, A., Belmabkhout, Y., Serna-Guerrero, R., Flue gas treatment via CO_2 adsorption, *Chemical Engineering Journal*, **2011**, *171*, 760-774.

[154] Chen, H., Sun, F., Wang, J., Li, W., Qiao, W., Ling, L., Long, D., Nitrogen doping effects on the physical and chemical properties of mesoporous carbons, *The Journal of Physical Chemistry C*, **2013**, *117*, 8318-8328.

[155] Mane, G.P., Talapaneni, S.N., Anand, C., Varghese, S., Iwai, H., Ji, Q., Ariga, K., Mori, T., Vinu, A., Preparation of highly ordered nitrogen-containing mesoporous carbon from a gelatin biomolecule and its excellent sensing of acetic acid, *Advanced Functional Materials*, **2012**, *22*, 3596-3604.

[156] Liu, Q., Shi, J., Zheng, S., Tao, M., He, Y., Shi, Y., Kinetics studies of CO_2 adsorption/desorption on amine-functionalized multiwalled carbon nanotubes, *Industrial & Engineering Chemistry Research*, **2014**, *53*, 11677-11683.

[157] Monazam, E.R., Shadle, L.J., Miller, D.C., Pennline, H.W., Fauth, D.J., Hoffman, J.S., Gray, M.L., Equilibrium and kinetics analysis of carbon dioxide capture using immobilized amine on a mesoporous silica, *AIChE Journal*, **2013**, *59*, 923-935.

[158] Caldwell, S.J., Al-Duri, B., Sun, N., Sun, C.-g., Liu, H., Snape, C.E., Li, K., Wood, J., Carbon dioxide separation from nitrogen/hydrogen mixtures over activated carbon beads: Adsorption isotherms and breakthrough studies, *Energy & Fuels*, **2015**, *29*, 3796-3807.

[159] Bakhtyari, A., Mofarahi, M., Pure and binary adsorption equilibria of methane and nitrogen on zeolite 5A, *Journal of Chemical & Engineering Data*, **2014**, *59*, 626-639.

[160] Bae, T.-H., Hudson, M.R., Mason, J.A., Queen, W.L., Dutton, J.J., Sumida, K., Micklash, K.J., Kaye, S.S., Brown, C.M., Long, J.R., Evaluation of cation-exchanged

zeolite adsorbents for post-combustion carbon dioxide capture, *Energy & Environmental Science*, **2013**, *6*, 128-138.

[161] Walton, K.S., Sholl, D.S., Predicting multicomponent adsorption: 50 years of the ideal adsorbed solution theory, *AIChE Journal*, **2015**, *61*, 2757-2762.

[162] Jeon, J.-K., Ihm, S.-K., Park, Y.-K., Kim, J.S., Kim, S.D., Kim, S., Kim, J.M., Kim, S.-S., Yoo, K.-S., Effect of isotherm selection on performance prediction of CO_2 PSA process, in: J.-S.C. Sang-Eon Park, L. Kyu-Wan (Eds.) Studies in surface science and catalysis, Elsevier, **2004**, 547-550.

[163] Yi, H., Li, F., Ning, P., Tang, X., Peng, J., Li, Y., Deng, H., Adsorption separation of CO_2, CH_4, and N_2 on microwave activated carbon, *Chemical Engineering Journal*, **2013**, *215–216*, 635-642.

[164] Zhou, X., Yi, H., Tang, X., Deng, H., Liu, H., Thermodynamics for the adsorption of SO_2, NO and CO_2 from flue gas on activated carbon fiber, *Chemical Engineering Journal*, **2012**, *200–202*, 399-404.

[165] Saha, B.B., Jribi, S., Koyama, S., El-Sharkawy, I.I., Carbon dioxide adsorption isotherms on activated carbons, *Journal of Chemical & Engineering Data*, **2011**, *56*, 1974-1981.

[166] Yi, H., Wang, Z., Liu, H., Tang, X., Ma, D., Zhao, S., Zhang, B., Gao, F., Zuo, Y., Adsorption of SO_2, NO, and CO_2 on activated carbons: Equilibrium and thermodynamics, *Journal of Chemical & Engineering Data*, **2014**, *59*, 1556-1563.

[167] Shen, C., Grande, C.A., Li, P., Yu, J., Rodrigues, A.E., Adsorption equilibria and kinetics of CO_2 and N_2 on activated carbon beads, *Chemical Engineering Journal*, **2010**, *160*, 398-407.

[168] Esteves, I.A.A.C., Lopes, M.S.S., Nunes, P.M.C., Mota, J.P.B., Adsorption of natural gas and biogas components on activated carbon, *Separation and Purification Technology*, **2008**, *62*, 281-296.

[169] Hornbostel, M.D., Bao, J., Krishnan, G., Nagar, A., Jayaweera, I., Kobayashi, T., Sanjurjo, A., Sweeney, J., Carruthers, D., Petruska, M.A., Dubois, L., Characteristics of an advanced carbon sorbent for CO_2 capture, *Carbon*, **2013**, *56*, 77-85.

[170] Hong, B.D., Slatick, E.R., Carbon dioxide emission factors for coal, in: Energy Information Administration, Quarterly Coal Report, Washington, DC, **1994**, pp. 1-8.

[171] Sakintuna, B., Yürüm, Y., Preparation and characterization of mesoporous carbons using a turkish natural zeolitic template/furfuryl alcohol system, *Microporous and Mesoporous Materials*, **2006**, *93*, 304-312.

[172] Elsayed, M.A., Hall, P.J., Heslop, M.J., Preparation and structure characterization of carbons prepared from resorcinol-formaldehyde resin by CO_2 activation, *Adsorption*, **2007**, *13*, 299-306.

[173] Pol, V.G., Shrestha, L.K., Ariga, K., Tunable, functional carbon spheres derived from rapid synthesis of resorcinol-formaldehyde resins, *ACS Applied Materials & Interfaces*, **2014**, *6*, 10649-10655.

[174] Wu, Y.-J., Yang, Y., Kong, X.-M., Li, P., Yu, J.-G., Ribeiro, A.M., Rodrigues, A.E., Adsorption of pure and binary CO_2, CH_4, and N_2 gas components on activated carbon beads, *Journal of Chemical & Engineering Data*, **2015**, *60*, 2684-2693.

[175] Rios, R., Correia, L., Bastos-Neto, M., Torres, A.E., Hatimondi, S., Ribeiro, A., Rodrigues, A., Cavalcante, C., Jr., de Azevedo, D.S., Evaluation of carbon dioxide–nitrogen separation through fixed bed measurements and simulations, *Adsorption*, **2014**, *20*, 945-957.

[176] Rios, R.B., Stragliotto, F.M., Peixoto, H.R., Torres, A.E.B., Bastos-Neto, M., Azevedo, D.C.S., Cavalcante Jr, C.L., Studies on the adsorption behavior of CO_2-CH_4 mixtures using activated carbon, *Brazilian Journal of Chemical Engineering*, **2013**, *30*, 939-951.

[177] Shao, X., Feng, Z., Xue, R., Ma, C., Wang, W., Peng, X., Cao, D., Adsorption of CO_2, CH_4, CO_2/N_2 and CO_2/CH_4 in novel activated carbon beads: Preparation, measurements and simulation, *AIChE Journal*, **2011**, *57*, 3042-3051.

[178] Suresh, S., Srivastava, V.C., Mishra, I.M., Isotherm, thermodynamics, desorption, and disposal study for the adsorption of catechol and resorcinol onto granular activated carbon, *Journal of Chemical & Engineering Data*, **2011**, *56*, 811-818.

[179] Guo, B., Chang, L., Xie, K., Adsorption of carbon dioxide on activated carbon, *Journal of Natural Gas Chemistry*, **2006**, *15*, 223-229.

[180] Hsu, S.-C., Lu, C., Su, F., Zeng, W., Chen, W., Thermodynamics and regeneration studies of CO_2 adsorption on multiwalled carbon nanotubes, *Chemical Engineering Science*, **2010**, *65*, 1354-1361.

[181] Wahby, A., Silvestre-Albero, J., Sepúlveda-Escribano, A., Rodríguez-Reinoso, F., CO_2 adsorption on carbon molecular sieves, *Microporous and Mesoporous Materials*, **2012**, *164*, 280-287.